



# MSc. Thesis in Civil Engineering

Faculty of Architecture, Civil and Environmental Engineering

## Design of a light-shaping adaptive facade using fiber-reinforced polymer materials

Baehr-Bruyère Joëlle

Supervised by:

Vassilopoulos Anastasios

Wienold Jan

Chamilothori Kynthia

Andersen Marilyne



## Table of contents

<b>GENESIS</b> .....	<b>4</b>
<b>INTRODUCTION</b> .....	<b>5</b>
<b>CONCEPT</b> .....	<b>7</b>
<b>CHAPTER I - DAYLIGHT PERFORMANCE</b> .....	<b>15</b>
<b>1 INTRODUCTION &amp; METHODOLOGY</b> .....	<b>15</b>
1.1 MODELING AND DAYLIGHT SIMULATIONS .....	16
1.2 METRICS .....	22
1.3 PERFORMANCE ASSESSMENT .....	25
<b>2 BASE PERFORMANCE</b> .....	<b>26</b>
2.1 OPEN AND CLOSED STATES .....	27
2.2 ADDING INTERMEDIATE STATES .....	36
<b>3 STATE CHOICE AND ANNUAL SCHEDULE</b> .....	<b>41</b>
3.1 PREPARING THE DATABASE .....	41
3.2 LOGIC OF THE STATE CHANGES .....	42
3.3 RESILIENCE OF THE SHADING SYSTEM TO WORKING AND SOCIAL SCENARIOS .....	44
<b>4 CONCLUSION OF CHAPTER I</b> .....	<b>48</b>
<b>CHAPTER II - STRUCTURAL DESIGN</b> .....	<b>50</b>
<b>1 REQUIREMENTS SPECIFICATION</b> .....	<b>51</b>
1.1 GEOMETRY .....	51
1.2 BEHAVIOR .....	51
1.3 LOADS .....	52
1.4 LIFESPAN AND DURABILITY .....	54
<b>2 PRE-DESIGN</b> .....	<b>55</b>
2.1 THEORETICAL BACKGROUND: 2D CALCULATIONS OF LAMINATED PLATE ELEMENTS .....	56
2.2 MODELING OF EXTERNAL LOADS AND SUPPORT CONDITIONS .....	58
2.3 STEPS IN THE STATIC CHECKS .....	60
2.4 CHOICE OF FIBERGLASS FABRIC TYPE .....	63
2.5 GOVERNING PARAMETERS IN THE DESIGN .....	67
2.6 CONCLUSION ON THE PRE-DESIGN & SHORTCOMINGS OF THE CLT .....	69
<b>3 FEA ANALYSIS</b> .....	<b>71</b>
3.1 MODELING COMPOSITES WITH ANSYS SOFTWARE .....	71
3.2 COMPARISON BETWEEN ANSYS AND CLT RESULTS .....	76
<b>4 LABORATORY TESTING</b> .....	<b>86</b>
4.1 SCALING .....	86
4.2 SPECIMENS FABRICATED .....	88
4.3 CHARACTERIZATION OF THE MATERIAL IN BENDING .....	90
4.4 CHARACTERIZATION OF THE MATERIAL IN PURE SHEAR .....	92

4.5	TORSION BREAK TEST .....	95
4.6	TORSION RELAXATION TEST .....	103
<b>5</b>	<b>CONCLUSION OF CHAPTER II.....</b>	<b>107</b>
<b>CHAPTER III - TOWARD A REAL IMPLEMENTATION: PENDING INVESTIGATIONS....</b>		<b>110</b>
<b>1</b>	<b>OPTICAL DESIGN .....</b>	<b>110</b>
1.1	TRANSMITTANCE OF FULL-SIZE FACADE ELEMENTS .....	110
1.2	CONTROL ON THE OPTICAL PROPERTIES .....	111
<b>2</b>	<b>MOTION'S COMPLEXITY AND ACTUATORS.....</b>	<b>114</b>
2.1	INDEPENDENTLY ROTATING BLINDS .....	114
2.2	MULTIPLE PIECES .....	115
<b>3</b>	<b>ENERGY SAVINGS .....</b>	<b>120</b>
3.1	ABOUT DAYLIGHT AND SOLAR HEAT GAINS.....	120
3.2	ABOUT (THE HIDDEN FACE OF) DAYLIGHT EFFICIENCY.....	122
<b>4</b>	<b>CONCLUSION OF CHAPTER III.....</b>	<b>124</b>
<b>CONCLUSION .....</b>		<b>125</b>
<b>ACKNOWLEDGMENTS .....</b>		<b>127</b>
<b>REFERENCES.....</b>		<b>128</b>
<b>APPENDIX I.....</b>		<b>131</b>
<b>APPENDIX II.....</b>		<b>132</b>
<b>APPENDIX III.....</b>		<b>137</b>
<b>APPENDIX IV .....</b>		<b>140</b>
<b>APPENDIX V.....</b>		<b>141</b>
<b>APPENDIX VI .....</b>		<b>144</b>
<b>APPENDIX VII .....</b>		<b>145</b>
<b>APPENDIX VIII .....</b>		<b>146</b>
<b>APPENDIX IX .....</b>		<b>147</b>
<b>APPENDIX X.....</b>		<b>148</b>
<b>APPENDIX XI .....</b>		<b>149</b>
<b>APPENDIX XII .....</b>		<b>151</b>

## Genesis

Light is immaterial, but light can change the way a space is perceived.

Light is an intangible structural element.



Figure 1 - Robert Irwin, Dawn to Dusk, 2016  
Picture: Alex Marks

The Light and Space artistic movement was one of the first to explore this duality by focusing on perceptual phenomena. Artists such as Robert Irwin focused their work on the spectator's experience of light under specific volume and scale conditions [1]. In his Dawn to Dusk installation, he played with natural light by directing its flow through the use of transparent, translucent or reflective materials.

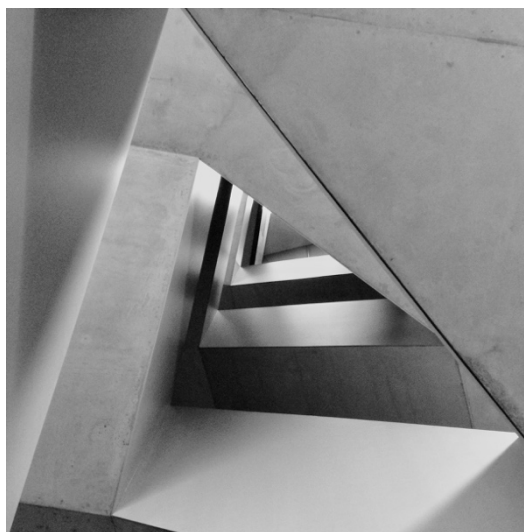


Figure 2 - Staircase, Chemin de Bérée 4a Lausanne , 2018  
Picture: Joëlle Baehr-Bruyère



Figure 3 – Tate Museum, London, 2018  
Picture: Joëlle Baehr-Bruyère

I am really sensitive to this potential of space structuration offered by light, especially natural light. As a civil engineer, I realized that it was quite often neglected in the guidelines for the design of buildings, whereas it plays a key role on how the occupants feel inside. So I started thinking of a practical implementation to bridge the gap between people's perceptions and quantifiable physical parameters that engineers can act on.

## Introduction

The facade has an ancestral envelope function, providing insulation against heat and cold and protecting the occupants from the natural elements like water and sun [2]. In the past decades, energy efficiency issues broadened this view. The Intergovernmental Panel on Climate Change (IPCC) showed in their last synthesis report that human was the main cause of current global warming [3]. Anthropogenic pressure on the ecosystem became a major issue and the construction industry had to face new challenges among which energy savings, energy storage measures and alternatives to fossil fuels.

In Switzerland, the law on energy [4] asks for a detailed energy concept in order to deliver building permits. The practical recommendations developed in the SIA norms 380-1 [5] and 380-4 [6] give a special emphasis on natural ventilation and natural lighting to reduce the energy demand. Similar considerations exist worldwide and feed into the development of adaptive kinetic facades. The distinguishing feature of these facades is the inclusion of passive or active environmental control by changing state, in order to make the best of real time local climatic conditions. As an example, researchers from ETH Zürich developed in 2016 the Adaptive Solar Facade (ASF) [7]. This system is composed by individually addressable modules with embedded photovoltaic solar cells. Those elements move to constantly adapt their orientation with the aim to maximize the generation of electricity while minimising the heating, lighting & cooling demand of the building.

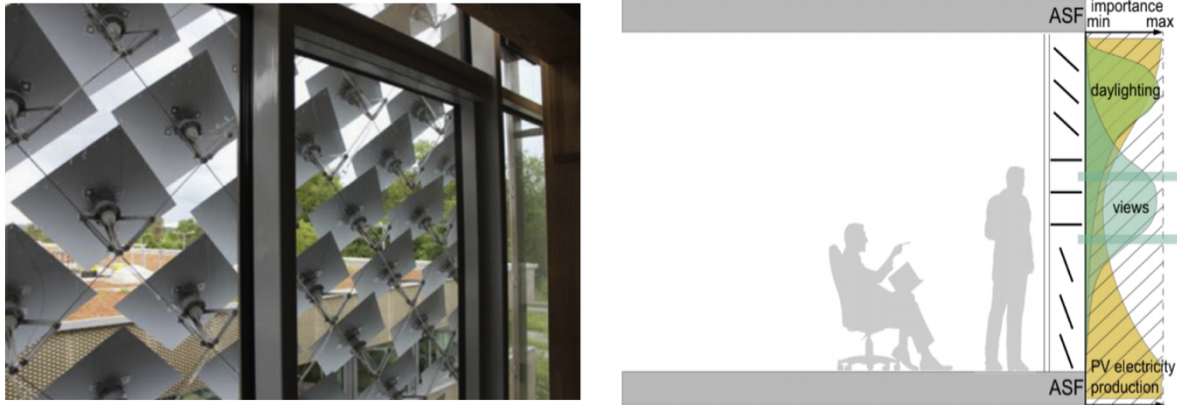


Figure 4 - The Adaptive Solar Facade, ETHZ, 2016

Architecturally speaking, the development of adaptive facades was fostered by the paradigm of biomimicry. Its design philosophy is to analyse and replicate mechanisms existing in nature, because they have been overcoming problems for billions of years [8]. Hence these mechanisms can be considered to be intrinsically sustainable solutions.

Today the facade is for the building what our skin is for us: an envelope acting like an interface sensitive to its environment. In this scope, biomimetic designs should be responsive not only to outdoor conditions but also to indoor conditions. With their multiple adaptive possibilities, kinetic facades offer a response to both changing climatic conditions and user requirements. Light, especially direct sunlight, is the core resource exploited by those evolutive shading systems. Daylighting control systems are of particular importance.

For example the Al Bahar Towers in Abu Dhabi have an outer structure that works like the petals of a flower. It closes during the hottest hours of the day to reduce solar gain and glare, and opens up when the sun sets and the desert air is cooler.

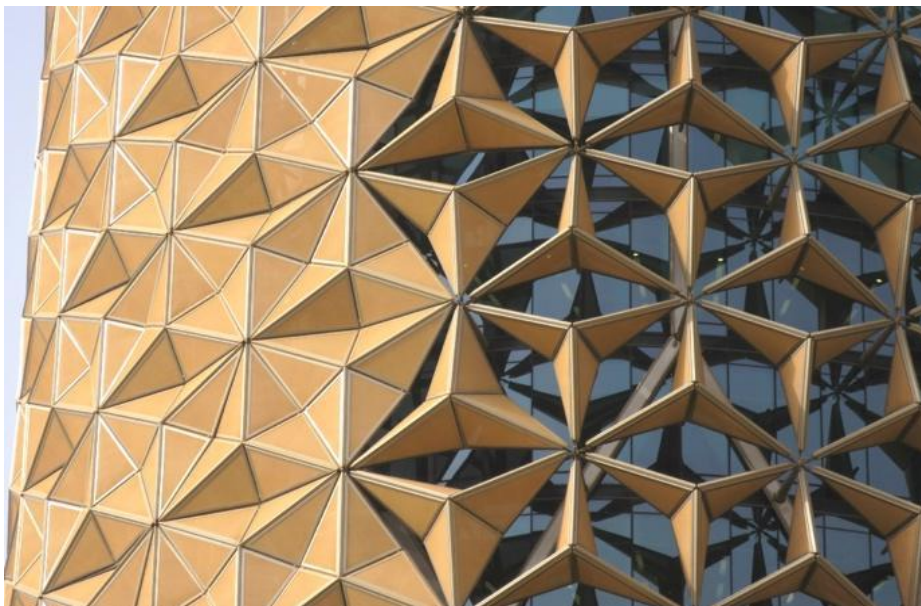


Figure 5 - Al Bahar Towers, Abu Dhabi

Existing applications demonstrate that highly integrated concepts are needed to combine functions that are sometimes contradictory. A recent study from the Sustainable Building Design Lab, Liège University Belgium [9] on the Al Bahar project points out an underestimation of the importance of assessing and validating the impact of the facade on indoor environmental quality and occupant satisfaction.

Although adaptive facades create a strong aesthetical identity on buildings, they are currently mostly developed to improve comfort and reduce energy demand. Regarding the daylighting performance, they are typically evaluated based on quantifiable physical parameters with little attention – for lack of evaluation criteria – given to subjective appreciation of the facade and the resulting daylight patterns [10]. Then what about the effect of the light entering a room through such a facade? What about the intensity, the repartition, the diffusion, the patterns created inside the building, and their impact on people? Indeed recent studies, e.g. from Abboushi & al. [11], highlighted the importance of qualitative factors such as visual interest when assessing the daylight performance of a space.

This thesis aims to complement conventional functions performed by existing daylighting control systems through the development of a new type of adaptive shading system which enhances the occupants' experience of the space. The work derives both conceptual and technical design processes of the adaptive facade system along with the development of related assessment methods. The shape of the facade elements can shift between different states to manage daylight repartition and glare, accordingly to the atmosphere people are seeking for. It explores kinetic facades in their entire potential to shape light by investigating both quantitative and qualitative levers of visual comfort. Creative expression recovers a meaningful place within building efficiency.

## Concept

Modern buildings are designed with ever wider openings. This characteristic means that the part of glazed surfaces in the envelope increases substantially, and so does the amount of solar radiation and daylight penetrating inside. These buildings are then a first pick target for the development of adaptive facades.

New office buildings are a typical example. The popularity of co-working is growing, following people's desire for a less formal, more flexible environment where they interact casually in large meeting areas [12]. Consequently, many companies choose to go for large open workspaces and to care about wellbeing of the employees as a key of their productivity. Today's office buildings seek for comfort and attractiveness. This turns them into a very challenging area of study for us.

We will especially study the case of the Foyer of the SG building, located at EPF Lausanne. It is indeed a very modular open workspace. The space is at the first floor, oriented to the East. It has a large continuous window of 2.36 meters height, topped by a concrete upper part of similar height. It is mostly empty in its base configuration and modulated according to the needs of the users. Currently it is used for groupwork, for architectural exhibitions, for conferences and as a social space for aperos, etc.

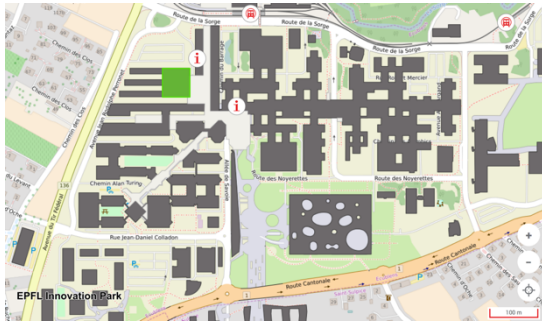


Figure 6 - Location of the SG building, EPFL map



Figure 7 - Indoor view of the Foyer (K. Chamilothori)

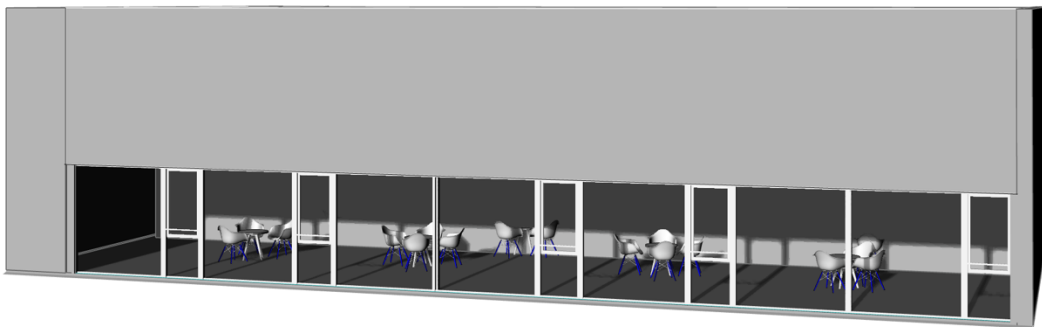


Figure 8 - 3D model of the SG Foyer

## A motion

In their 2015 experimental studies investigating the subjective evaluation of different shading systems, Omidfar & al. assessed that user's preference went to shading systems creating mid-complexity and high order patterns in office buildings [13]. Work carried out by Chamilothori & al. from 2016 to 2019 highlighted that irregularity in the spatial composition of the facade openings was indeed exciting but could be somehow distracting, so it was preferred for social spaces whereas uniformity was better suited for work [14],[15]. Also experimental studies from Abboushi & al. pointed out that the quality of the view to the outside was a key factor proved to enhance perceived visual comfort [11].

The above qualitative criteria have their importance when trying to identify the most efficient option for a light shaping kinetic facade. The optimum found by relying only on quantitative daylight metrics can be very different. An integrated design should address both.

It is usual to see buildings equipped with vertical blinds. What about their performance? Taking into account the need for sufficient daylight but also the glare prevention, vertical blinds were shown by Omidfar & al. to be the best performing in terms of useful daylight illuminance. However, these same blinds were rated as unappealing and uncomfortable by the users [13]. Striped patterns are more likely to cause visual discomfort because they have Fourier amplitude spectra that departs maximally from those of natural scenes (Wilkins, 2016), creating sunlight patterns with disturbing spatial frequency. Similarly, Abboushi & al. found that horizontal blinds applied in a real environment were the most negatively evaluated in terms of visual interest when the user was seated perpendicular to the window [11]. In contrast, less linear openings have been shown to lead to a

10% increase in evaluations of interest and excitement compared to vertical blinds [15], indicating important potential in this research direction.

→ Traditional vertical blinds were proven to be an efficient shading system but they are not attractive for people. This project aims to improve them, enhancing their qualitative performance without losing on the quantitative efficiency. Based on current knowledge from scientific literature review correlated to experimental findings in the context of the SG Foyer, the concept presented here rethinks the movement possibilities of the blinds to create more interesting forms and patterns. It introduces torsion as a new degree of freedom. When a rectangular facade element is twisted, its borders get curved. We thus expect the generated openings to improve perceptual impressions of the space [15].

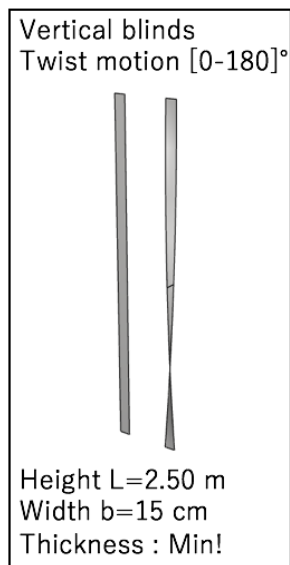


Figure 9 – Concept



Figure 10 – Design concept with variations from 0 to 180° in the rotation of the elements in a mockup model (1:5 scale)

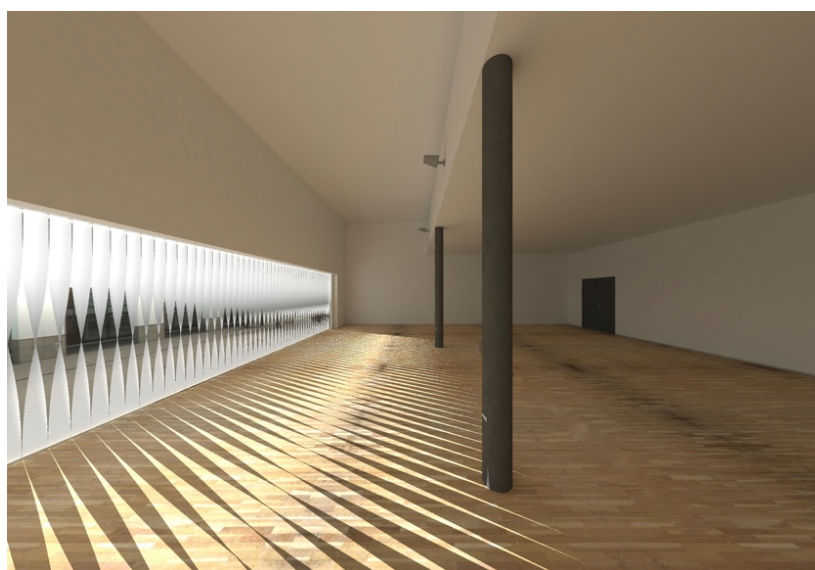


Figure 11 - Example space simulated at 9:00 on March 15<sup>th</sup> in sunny conditions with all slats tilted at 135

The blinds are held at both ends by supports that can rotate. If both the top and bottom support operate the same rotation we have a traditional vertical blind, rotating around its central axis. Now if the two supports operate different rotations, the element is twisted. The height results from the size of the window (2.36m) plus some margin for the fixation system. The width is a design choice (and is not a decisive parameter for the design calculations as we will see later in Chapter II). One of the goals will be to minimize the thickness so that the system does not disturb the view to the outside when it is open. The thickness is to be optimized according to structural stresses and strains. As a facade, the elements are located outside, meaning that they are subjected to natural elements such as wind and need to be “tough” enough to resist them. At the same time, the twist requires relatively “flexible” elements. Today mechanically actuated small rigid pieces are widely used in kinetic facades (see Fig.4 the ASF). Intrinsically “flexible” elements are still much fewer, however those elements reduce a lot the number and the complexity of the mechanical supports needed. This is explained mostly by the fact that it is technically complex to achieve both high resistance and large deformation capacity, even more so with complicated shapes.

## A material

Fiber Reinforced Polymers appeared in 1909 with the invention of Bakelite and became popular in the 30's with chemical development of resins, notably by the company DuPont®. They consist in a polymer matrix which is reinforced by casting fibers inside. Today the matrix is usually epoxy or polyester (or vinylester). Among the existing reinforcements, glass, carbon and aramid fibers are the most common. Originally used in the aviation industry for their lightweight properties (for a resistance comparable to metal), FRP materials are now developed for many new applications, “meant for performing a variety of functions apart from the primary structural function which provides structural functions such as strength, stiffness, stability while non-structural functions provides energy harvesting, self-healing capability, sensing and actuation and sometimes acts as a protective layer” [16].

Figures 12 and 13 show some examples of their first implementations in the design of “flexible” facade elements.

a)



b)



Figures 12 a&b- One Ocean, thematic pavilion EXPO 2012, SOMA architecture + Knippers Helbig Engineering, Yeosu 2012

The facade of the One Ocean pavilion is a system reproducing fish-like biological moving mechanism at the architectural scale by means of animated patterns (Fig. 12a). The elements, made of Glass FRP, are 3m to 14m high and 9mm thick. They resist Korean high wind loads while being highly elastically deformable. The principle relies on triggered instability: shell buckling is obtained by in-plane compression (Fig. 12b).

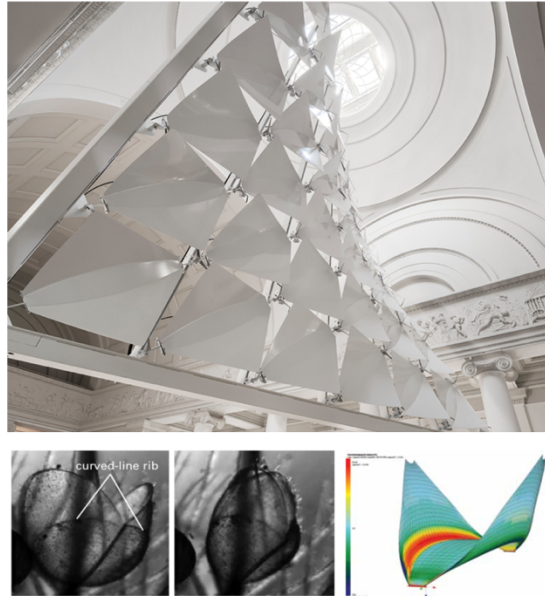


Figure 13 - FlectoFold, ITKE, Stuttgart 2016

The FlectoFold was developed at the Institute of Building Structures and Structural Design (ITKE) of Stuttgart. It is a modular elastic-kinetic facade shading system, made of FRP. The concept is biomimetic, inspired by the trapping mechanism of the *Aldrovanda* carnivorous plant. The module consists in several interacting surfaces, folds and ribs with different material characteristics. They define a stiff lens-shaped backbone and two lobes, so that a small motion of the support causes complex motion: a tiny stretching of the central part triggers a curve-line folding move, leading to a new equilibrium configuration in a position far different from the initial one [17]. It is similar to triggered elastic buckling in the Oce Ocean Pavilion.

In those two examples we do not have elements moving like rigid bodies anymore. The state-change motion of both systems is characterized by large elastic deformations. This apparent flexibility is due to a specific properties of FRP materials: their high strength-to-stiffness ratio. They define the range of elastic-kinetics. Figure 14 illustrates it by providing an overview through de materials used in structures today [18].

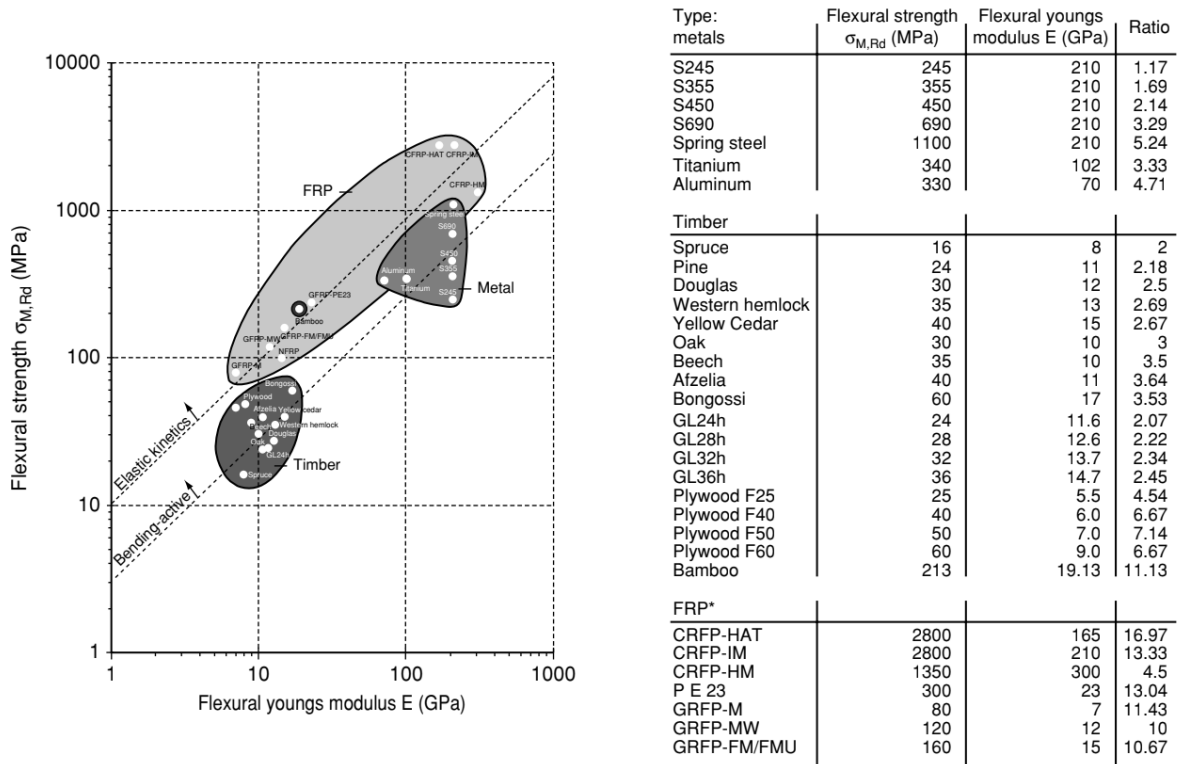


Figure 14 - Common building materials with ratio of strength  $\sigma_M$  (MPa) to stiffness E (GPa)

We saw that FRP materials had some “flexibility” inherent to their material properties and could consequently reach large deformation before failure. They also have an even more interesting characteristic: classical materials offer defined properties while FRPs bring the possibility to create the properties we need! This is possible thanks to the lamination fabrication process. Layers of reinforcement are disposed and impregnated with resin one by one, allowing to play on the orientation of the fibers to achieve different strength properties in any direction that requires it. It also allows to integrate productive elements such a solar cells, or core elements such as thermal insulation. FRPs are tailor-made materials. They allow free-formability, enhancing the architectural creativity with an infinity of design options. They also meet the current challenge of embedded multiple fonctionnalités.

The polymer resins, especially epoxy, exhibit good water and chemicals resistance properties over the lifespan while wood, steel or even concrete need regular care. Moreover, in our framework we can broaden the light-shaping possibilities by working with Glass FRPs, which keep some translucency, and play on optical properties, so that light can also be shaped when going through the elements and not only in between them like it is the case with opaque FRPs. Technically speaking, the choice of glass fibers is endorsed by their stability under the action of UV radiation. The choice of GFRP confirms the need for an epoxy resin as it should be able to deform at least as much as the fibers. To illustrate this Figure 15 shows the strains to failure of several fiber and resin types.

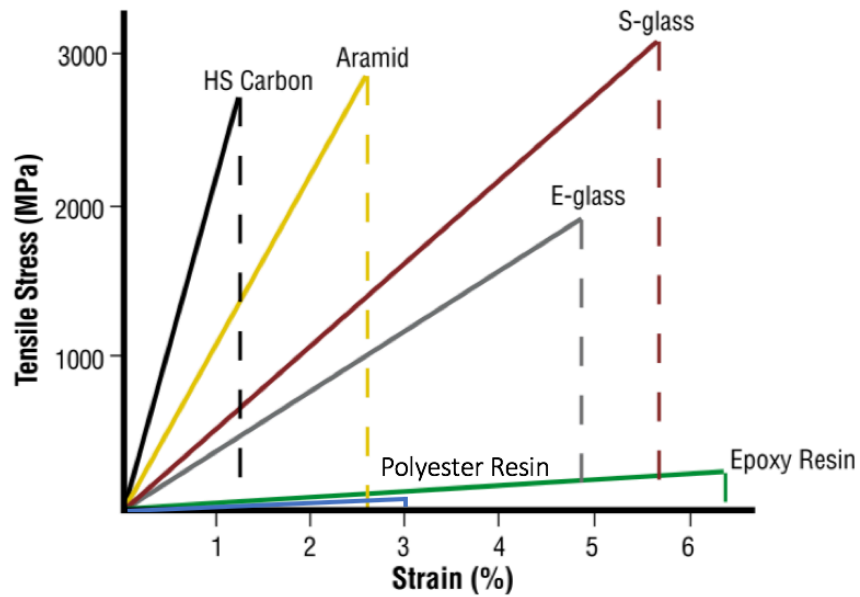


Figure 15 - Typical strains to failure of different reinforcement fibers and resins, adapted from [19]

FRPs allow to realize fully integrated concepts that fit the needs of each project. They adapt instead of giving a fixed feasibility framework, which is suited to the research philosophy of this project. This project aims to achieve core engineering and architectural visions, that depend on inputs from highly interrelated issues gravitating around. It is anything but a straightforward process.

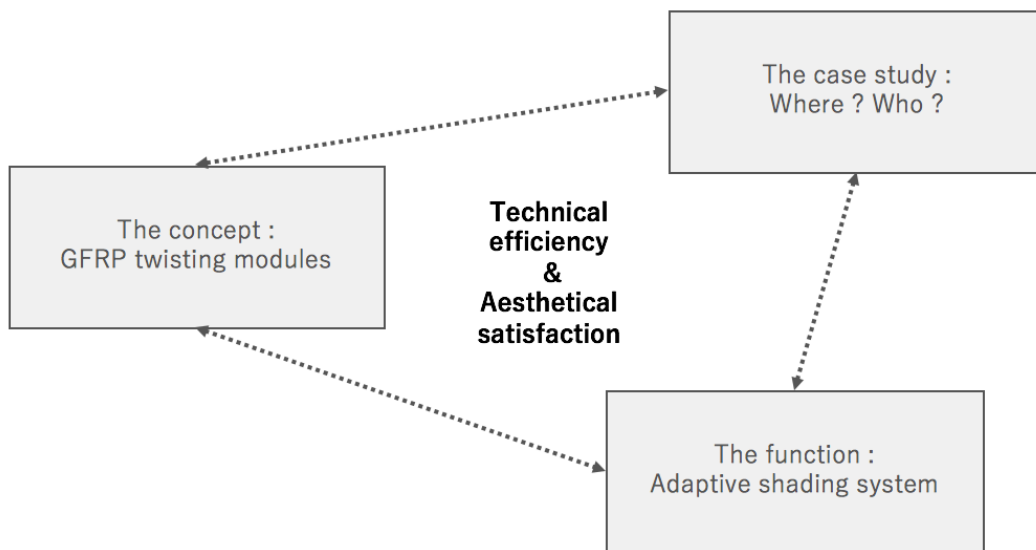
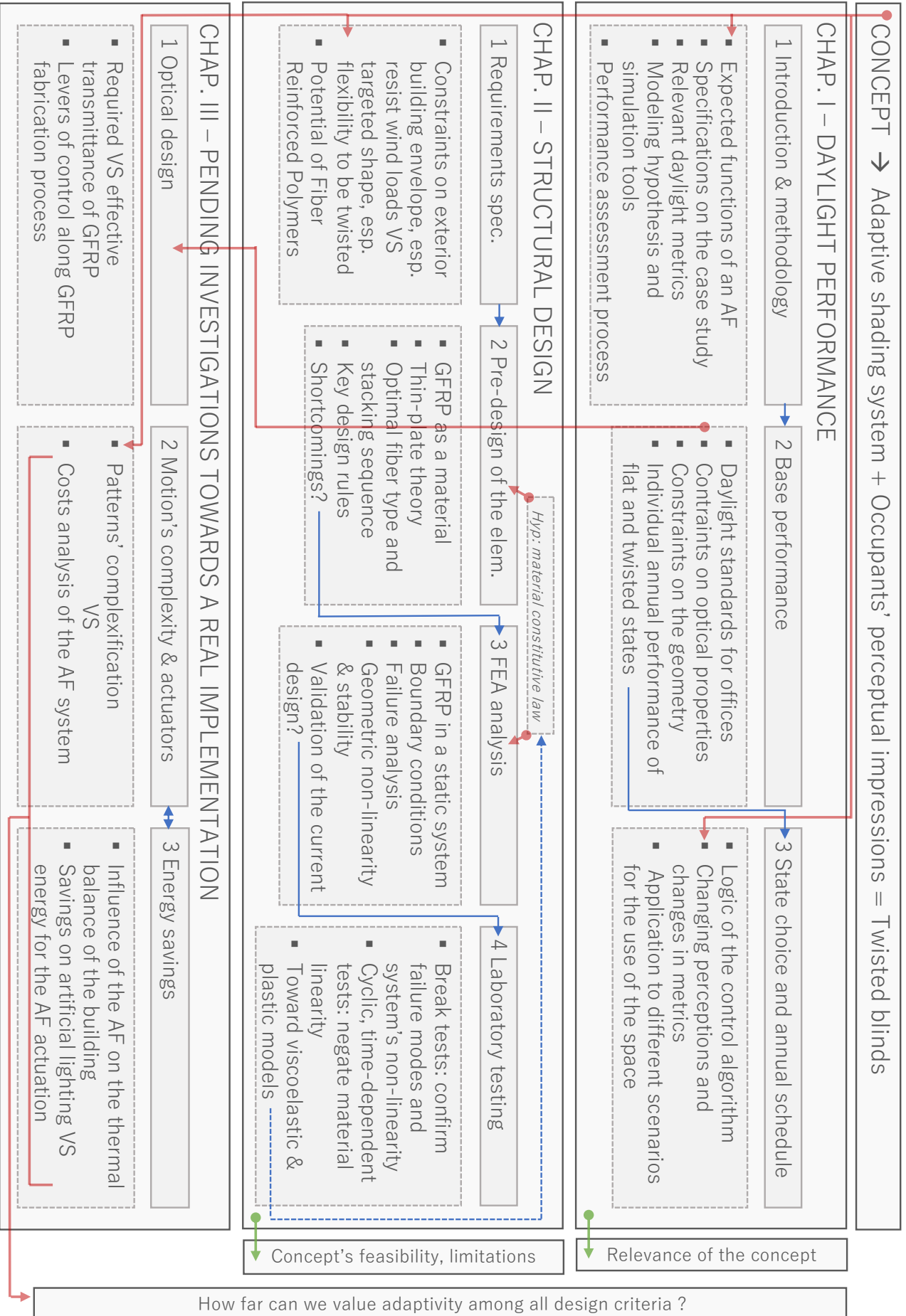


Figure 16 – Interrelated issues in the structure of the project

The following chapters derive the design process of this adaptive facade system. The shape of the facade elements is designed in order to improve both the occupants' visual comfort and their experience by taking advantage of natural daylighting. Composite materials are investigated for the technical implementation of such a facade system. The structural design of the composite elements is presented, as long as potential limitations and guidelines regarding further investigations needed to fully characterize the behavior of the resulting shading system.

# PROJECT MAPPING



# CHAPTER I

## DAYLIGHT PERFORMANCE

### 1 Introduction & methodology

This project develops a kinetic shading system that aims to increase the potential of conventional blinds by addressing the user's experience issue. It embraces the base function of a shading system (i.e. protecting against glare and allowing daylight penetration when glare is not problematic) and goes further by means of twisted configurations expected to improve perceptual impressions. Hence this system fulfills the following functions:

- As a shading device, the system should provide glare control, preserve a maximized view to the outside when in open position and block all direct light when closed.
- Visual comfort calls for a daylight management that ensures both spatial and temporal good repartition of the illuminance.
- Finally enhancing the appraisal of the space also means that the occupants can influence the shape of the openings and the resulting impressions of the space according to their needs.

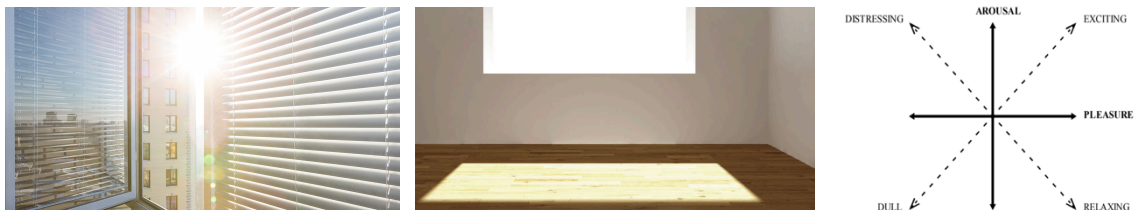


Figure 17 - Functions of the facade system: glare control, daylight management & space appreciation

The first two functions described above are expected from any shading system, while the third one is newly introduced as a requirement. Elements are designed to shift from a fully open state that maximizes the view out to a fully closed state that minimizes the incident solar radiation, with intermediate twisted states that allow partial view access while creating visual interest in the scene.

Adaptive kinetic facades fulfill their functions by means of motions: they change state. Different types of inputs can trigger a change. The pyramid in Figure 18 sorts the most common inputs by priority order.

First of all, the kinetic system is quite often combined with a pre-defined autonomous schedule of the blinds. This is the base schedule (3), calibrated using average local climatic conditions. This schedule is efficient on average.

Then the facade may have sensors and react in real-time to the changing environment, with conditions like "If a given point illuminance is over a given threshold, switch to position ...". This

second decision loop is based on the current real environmental conditions sensed by the facade, enhancing the biomimetic architectural response. This is daylight sensing (2).

Finally, the user has the “final say” and can shortcut the other decision loops in order to ask for a specific state. This is direct manual user control (1). When the kinetic facade design also aims at the occupant’s appraisal of the space, this third decision loop lets the user control the atmosphere/patterns inside the room.

The effective succession of states results from a mix of inputs, either scheduled or as uncertain as the user behavior could be.

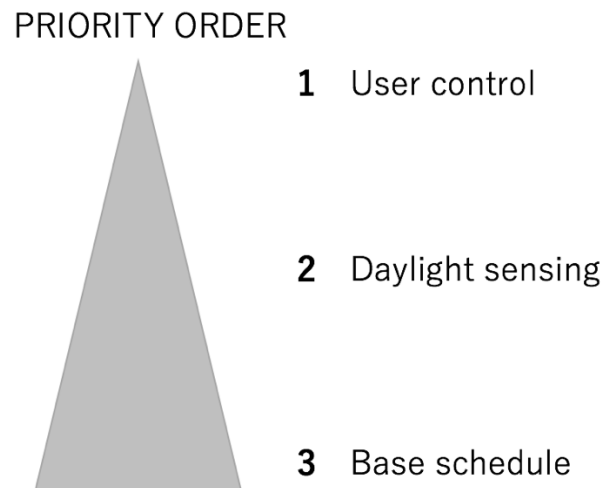


Figure 18 – General hierarchy of state change decision loops

This chapter steps into investigations about state choice and control system of the blinds. It proposes a daylighting performance assessment procedure and demonstrates the system’s efficiency and flexibility by applying it to two scenarios of use (working and socializing), each translated into different requirements on glare protection. The analysis is based on average local weather data, i.e. Geneva weather data (‘base schedule (3)’ on the pyramid Fig. 18). In a prospect of future development, sensors should be embedded in the facade so that real-time weather data replace the average data (‘daylight sensing (2)’ on the pyramid Fig. 18).

## 1.1 Modeling and daylight simulations

This section describes the modeling of the example space and the daylight simulation processes.

The SG foyer (in light blue in the plans Fig. 19 & 20) is 43.5 meters long for a depth of 11.2 meters. It is a large space that could host different groups of people with separate activities. In order to obtain daylight metric values comparable to the thresholds from standards, mainly calibrated for office spaces, we will run the simulations for a reduced zone (orange zone in the plans). We selected the South-East part because it was more critical than North-East in terms of having enough

illuminance regarding the walls geometry and the sunpaths in Appendix I. We assumed a usage area of max. 5.6m depth and 21.5m width to remain consistent with a “reference office” size [19].

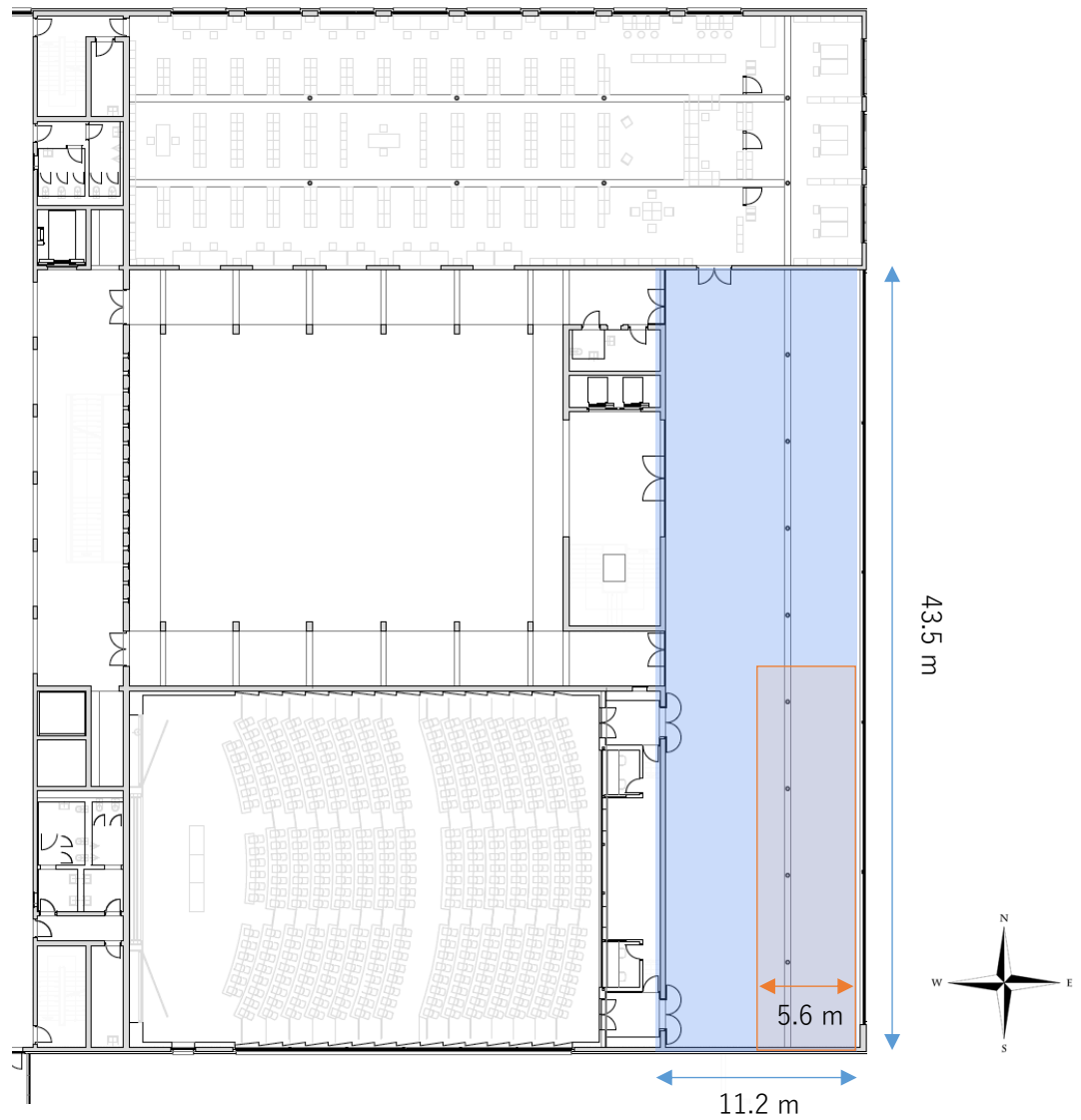


Figure 19 - Ground plan of the SG building (Scale 1:500)

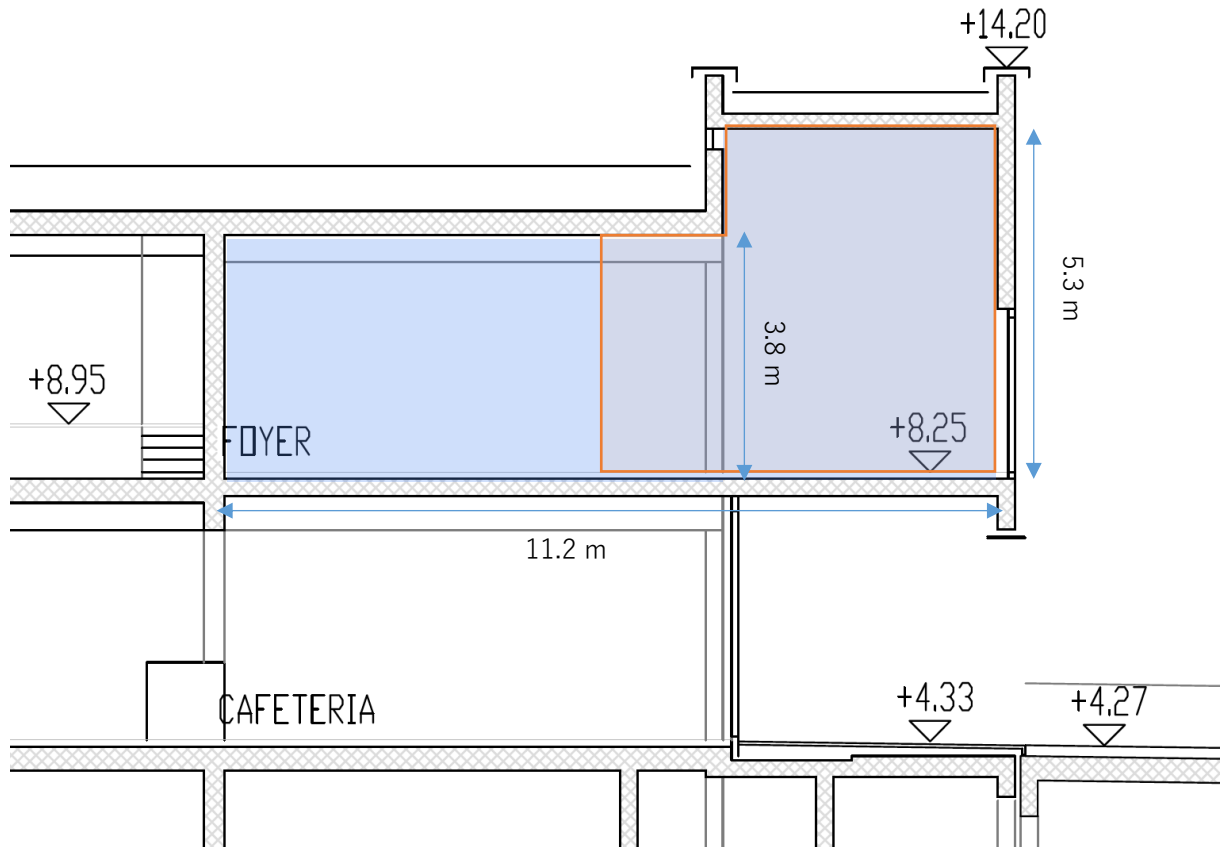


Figure 20 - Elevation cut through the SG foyer (Scale 1:100)

The modeling software Rhinoceros is used to create the 3D model of the space. The twisted blinds are parametrically defined in the Grasshopper plugin for Rhino3D, and the different configurations to test are added to the 3D model using the 'Bake' command. The Grasshopper file is reproduced in Figure 21 below. The inactivated (orange links) part allows to draw random patterns to be reproduced by the facade. We will go back to this in Chapter III while discussing independently rotating blinds.

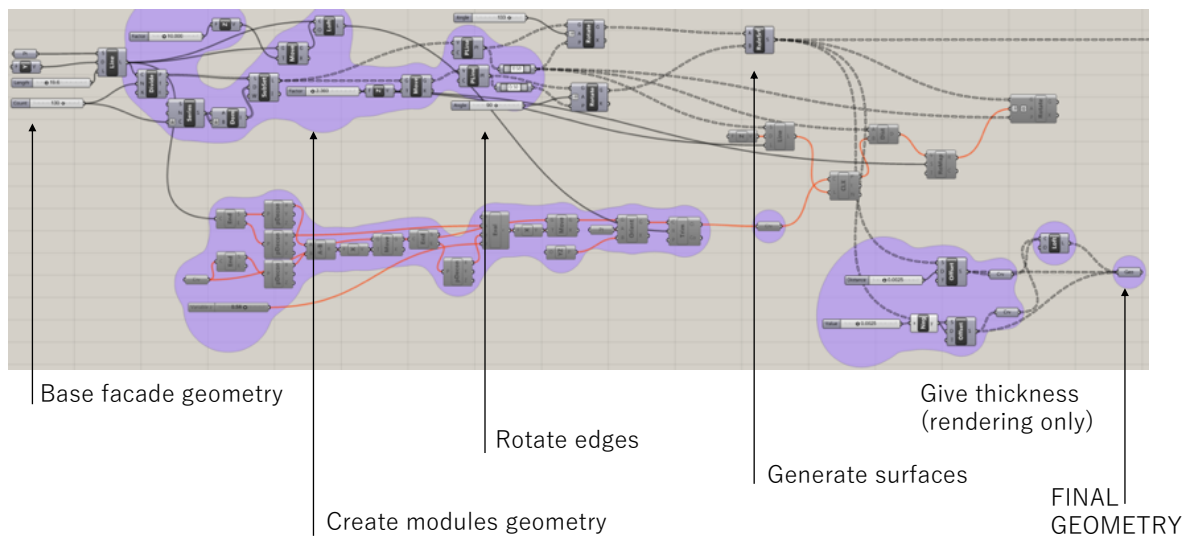


Figure 21 – Grasshopper file for the twisted blinds

All the surfaces (walls, roof, furnitures, glazings etc) are assigned optical material properties to be used by Radiance and the DIVA-for-Rhino plugin. Note that the existing glazing of the SG foyer is a solar control glazing with low transmittance (0.6). In our model we try to evaluate the performance of our kinetic facade, thus the material parameters of the glazing are set to normal ones (transmittance of 0.8). The optical properties of the blinds are investigated later on, in section 2 'Base performance'. They are modeled as purely translucent material without forward peak in Radiance data language i.e. specularity and roughness are zero. From the user manual of this software suite [20], "Trans is a translucent material, similar to plastic\*. The transmissivity is the fraction of penetrating light that travels all the way through the material. The transmitted specular component is the fraction of transmitted light that is not diffusely scattered. Transmitted and diffusely reflected light is modified by the material color. Translucent objects are infinitely thin".

\* "Plastic is a material with uncoloured highlights. It is defined by a red green and blue reflectance value, a specularity value and by a roughness value. A positive roughness value will display highlights (uncoloured by the materials modifier) but not show any reflections from other objects."

The trans primitive:				Acceptable values:		
modifier	trans	identifier		colour	[0:1],[0:1],[0:1]	Min 0, Max 1
0				black - white		
5	R G B spec rough	<-( Colour ) <-( specularity & roughness )		specularity	[0:1]	Min 0, Sug. max 0.07
	trans tspec	<-( transmission & transmitted specularity )		roughness	[0:1]	Min 0, Sug. max 0.02
				matte - satin		
				polished - low gloss		
				transmission	[0:1]	Min 0, Max 1
				opaque - transparent		
				transmitted specularity	[0:1]	Min 0, Max 1

Example:			
void	trans	identifier	
0		lamp_shade	
5	.7 .3 .2 0 0.05 .5 .5		

Table 1 - Meaning of Radiance material parameters (trans material)

Surface	Type	Reflectance	Specularity
Ceiling	plastic	94.5%	0
Floor	plastic	31.0%	0
Walls	plastic	93.5%	0
Glazing	glass	<b>Visual Transmittance 80%</b>	

Table 2 - Surfaces' optical properties, based on photometric and spectrophotometer measurements from Chamilothori

Finally, simulations are performed with the DIVA plugin for Rhino3D [21].

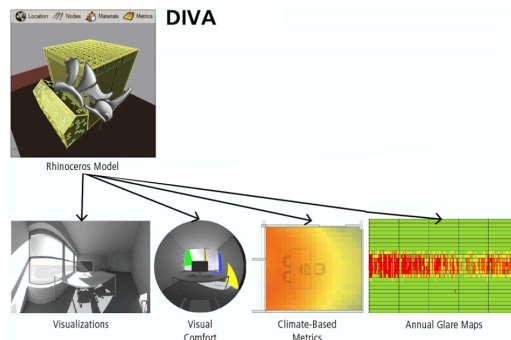


Figure 22 - Simulations possible with DIVA

Point-in-time visualizations coupled with false coloring of the scenes are useful to evaluate the luminance on the different surfaces and spot possible mistakes in the 3D model or the material assignment. They were used in the master thesis pre-study. Daylight factor calculated with an overcast sky is a good first hint of the “quantity” of daylight that penetrates a space, depending only on the geometry of the openings and material parameters. Grid-based simulations, taking into account local weather data, indicate the effective daylight availability inside the space by calculating the illuminance. This is stated by Daylight Autonomy or spatial Daylight Autonomy metrics. Finally glare tools allow to evaluate the glare probability for both specific viewpoints and specific sun positions all over the year.

The table below details the meaning of the resulting metrics. Next section (1.2 ‘Metrics’) links them to the recommendations from new european standards "Daylight in Buildings" EN17037:2019 [22] and "Blinds and Shutters" prEN14501:2019 [23].

Indicator	Threshold / Ranges	Details
Daylight Factor (DF)	<b>X%</b>	% of outside illuminance (overcast sky) that effectively enters the building
Daylight Autonomy (DA)	<b>X%</b> of o.h. > <b>Y</b> Lux	% of occupied hours when the illuminance is over a threshold (spatial average)
Spatial DA	<b>X%</b> of floor area > <b>Y</b> Lux for <b>Z%</b> o.h.	% of floor area with illuminance over the threshold during a given fraction of occupied hours
Daylight Glare Probability (DGP <sub>e&lt;5%</sub> )	< <b>p</b> for 95% o.h. (⇔ exceeds p less than 5% of o.h.)	Reflects the probability for a person to be dazzled during a given % of occupied hours

Table 3 - Daylight metrics evaluated by DIVA

All simulations were performed with typical Radiance simulation parameters described in Table 4. Specifically the -ab 3 setting means that the calculation takes into account sunbeams reflections in the limit of three bouncings. It underestimates a bit the illuminance especially at the back of the room. However the use of -ab 4 leads to highly time-consuming simulations.

<b>-ab</b>	<b>-ad</b>	<b>-as</b>	<b>-ar</b>	<b>-aa</b>
3	1000	20	300	0.1

Table 4 - Radiance calculation parameters

The Geneva IWEC weather files were downloaded from the energyplus.net website. “The IWEC data files are 'typical' weather files suitable for use with building energy simulation programs” [24]. The files derive hourly solar radiation and cloud amount information from 18 years of archived hourly weather data.

All the climate-based metrics are evaluated on a grid of sensor nodes set at a distance of 0.85m from the ground. Each node is representative for a piece of floor area (43cm\*38 cm in our model), for 611 nodes in total.

Glare simulations in DIVA-for-Rhino are performed for a given viewpoint, with hemispherical 'fisheye' vision. The EU standards precise that "the expected worst case position should be investigated. These positions are usually close to the facade and/or where you can expect view connection to a low sun position. If you fulfill the glare criteria for the worst case(s) within a space, it will comply with the utilized area of a space." [22]

The camera is set inside the room close to the window (2 meters behind, which is a great 1/3 of the depth of the area under study). The height is 1.56 m and corresponds to the mean eye-level of a standing person. We chose to study this position because of the mixed use of the space with few seated office work performed and because there were no additional surfaces at the seated eye-level that could make a meaningful difference as furnitures were not included. Regarding the azimuth of the camera, the choice was made knowing the East orientation of the building, to make sure that we included times when the sun was directly hitting the facade, i.e. during mornings, as visible on the scheme Figure 23 and the more precise 3D annual sunpath diagram including the building in Appendix I. The camera was rotated at 30° from the East (instead of 45° to get perfect South-East) so that the corner wall was not too much protective against the worst low bright sun situations. The choice of the point along the Y axis is debatable. It would have been worst to put it closer to the middle of the window, as some additional low morning sunrays would have been caught by the 180° view. We decided here to cover an average worst case.

Surrounding buildings are not added to the 3D model for daylight simulations as their shading influence would distort the performance evaluation of the shading system.

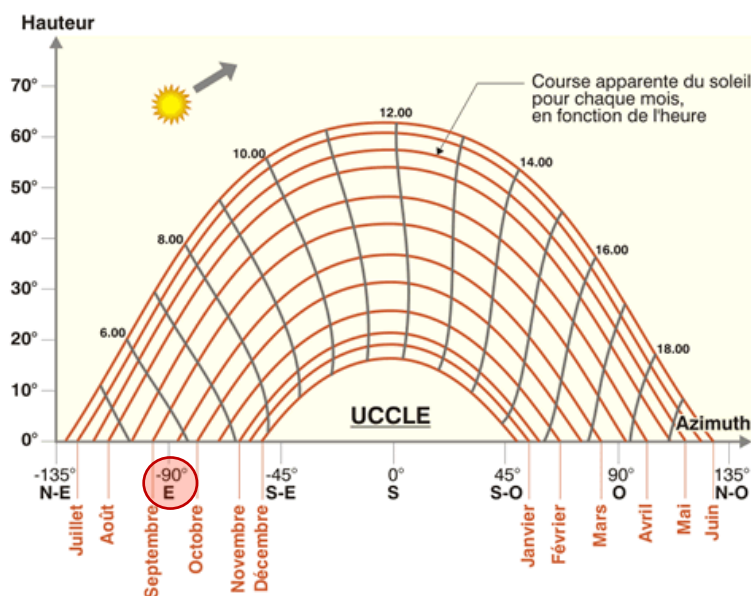


Figure 23 - Sunpath diagram: approximate position of the sun for an East oriented building in Europe (source: [www.energieplus-lesite.be](http://www.energieplus-lesite.be))

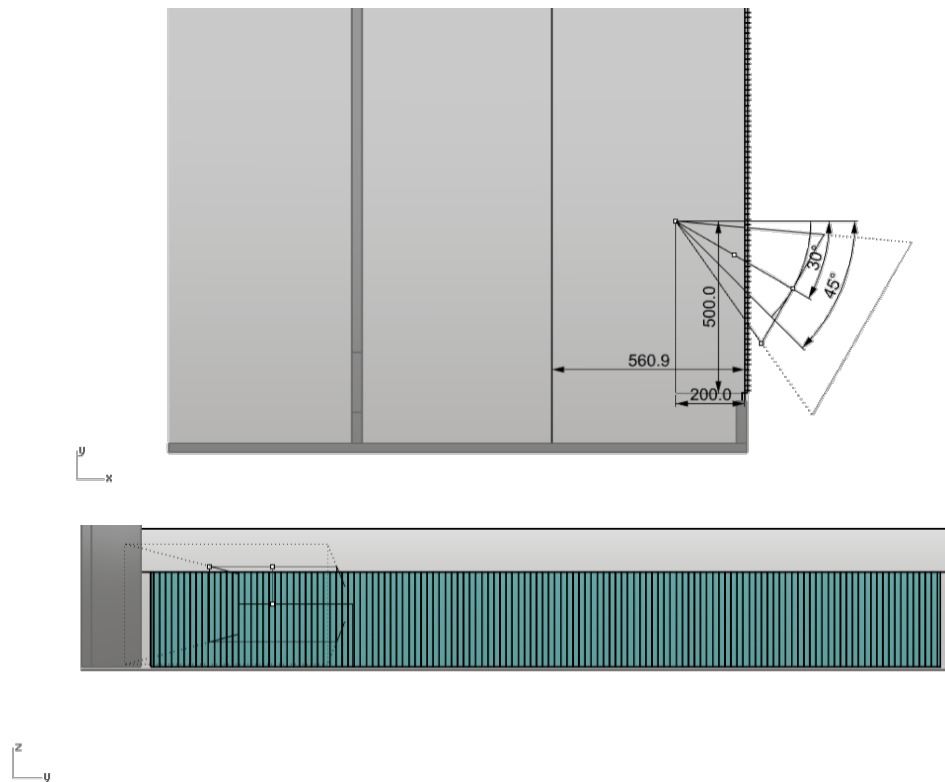


Figure 24 - Positioning of the camera for glare simulations. Top: plane view ; Bottom: front elevation view

## 1.2 Metrics

The evaluation of the daylight and glare protection performance is based on the standards "Daylight in Buildings" EN17037:2019 [22] and "Blinds and Shutters" prEN14501:2019 [23]. This section explains the purpose of the different metrics as well as their underlying assumptions.

Basically, two rules emerge as guidelines for the quantitative performance assessment:

**Rule 1** | The measurement of the illuminance aims at ensuring that we have ENOUGH daylight entering.

**Rule 2** | The study of the probable daylight glare aims at ensuring that we do not have TOO MUCH daylight entering.

The recommendations from EN17037:2019 "Daylight in [office] Buildings" are followed to quantify the target parameters **X**, **Y**, **Z** and **p** in Table 3 previously presented.

The first point (**1**) is to provide ENOUGH daylight:

**Table A.1 — Recommendation of daylight provision by daylight openings in vertical and inclined surface**

Level of recommendation for vertical and inclined daylight opening	Target illuminance $E_T$ (lx)	Fraction of space for target level $F_{plane, \%}$	Minimum target illuminance $E_{TM}$ (lx)	Fraction of space for minimum target level $F_{plane, \%}$	Fraction of daylight hours $F_{time, \%}$
Minimum	300	50%	100	95%	50%
Medium	500	50%	300	95%	50%
High	750	50%	500	95%	50%

NOTE Table A.3 gives target daylight factor ( $D_T$ ) and minimum target daylight factor ( $D_{TM}$ ) corresponding to target illuminance level and minimum target illuminance, respectively, for the CEN capital cities.

Table 5 - Table A.1 EN17037:2019

Daylight Provision (DP) is a spatial and temporal measurement of Daylight Autonomy among the hours when daylight is provided (understand during daytime). The EU standards state the daylight provision levels in terms of % of floor area and of % of hours when we have daylight condition inside the studied room. However DIVA states its metrics in terms of (% of floor area also and of) % of occupied hours. To convert occupied hours to daylight hours, we create a self-define “occupancy” schedule (.csv file containing a list of ‘0’=no and ‘1’=yes). In the weather data file, we sum direct and diffuse irradiation and return “1” (=daylight condition) if it is over the threshold of 20 W/m<sup>2</sup>, “0” otherwise. Then this list of 0 and 1 is used as the occupancy schedule in DIVA. Using this schedule, the sDA calculated by DIVA is the Daylight Provision and states how many nodes of the grid receive an illuminance greater that a target illuminance during at least half of the daylight hours over the year.



Figure 25 – Mapping of daylight hours all over the year (white cells)

Table 6 gives an idea of the minimum Daylight Factor we should achieve depending on the selected threshold for the Daylight Provision in Table 5. Table 7 does the same for the view outwards.

**Table A.3 — Values of  $D$  for daylight openings to exceed an illuminance level of 100, 300, 500 or 750 lx for a fraction of daylight hours  $F_{time, \%} = 50 \%$  for 33 capitals of CEN national members**

Nation	Capital <sup>a</sup>	Geographical latitude $\varphi$ [°]	Median External Diffuse Illuminance $E_{v,d,med}$	$D$ to exceed 100 lx	$D$ to exceed 300 lx	$D$ to exceed 500lx	$D$ to exceed 750lx
Switzerland	Bern	46,25	16000	0,6%	1,9%	3,1%	4,7%

Table 6 - Table A.3 EN17037:2019

**Table A.5 — Assessment of the view outwards from a given position**

Level of recommendation for view-out	Parameter <sup>a)</sup>		
	Horizontal sight angle	Outside distance of the view	Number of layers to be seen from at least 75% of utilized area: - sky - landscape (urban and/or nature) - ground
Minimum	≥ 14°	≥ 6,0 m	At least landscape layer is included
Medium	≥ 28°	≥ 20,0 m	Landscape layer and one additional
			layer is included in the same view opening
High	≥ 54°	≥ 50,0 m	all layers are included in the same view opening
<sup>a)</sup> For a space with room depth more than 4 m, it is recommended that the respective sum of the view opening(s) dimensions is at least 1,0m x 1,25m (width x height).			

Table 7 - Table A.5 EN17037:2019

The second point (2) is to prevent from having TOO MUCH daylight:

Glare (more precisely discomfort glare) is hard to quantify, as there is a part of subjectivity in the discomfort. Subjective rating scales are often used, like the DeBoer scale that ranges from 9 (just noticeable) to 1 (unbearable). The Daylight Glare Probability (DGP) is a metric that quantifies the percentage of people that experience discomfort glare in a given luminous scene.

$$DGP = c_1 \cdot E_v + c_2 \cdot \log\left(1 + \sum_i \frac{L_{s,i}^2 \cdot \omega_{s,i}}{E_v^{a_1} \cdot P_i^2}\right) + c_3$$

$E_v$ :	vertical Eye illuminance [lux]	$c_1 = 5.87 \cdot 10^{-5}$
$L_s$ :	Luminance of source [cd/m <sup>2</sup> ]	$c_2 = 9.18 \cdot 10^{-2}$
$\omega_s$ :	solid angle of source [-]	$c_3 = 0.16$
$P$ :	Position index [-]	$a_1 = 1.87$

Figure 26 - Calculation of the DGP (source J.Wienold, Comfort &amp; Architecture class)

The parameters of the formula have been calibrated based on behavioral studies on people performing office tasks under different natural light scenes and shading system conditions. The equation contains two effects. The first part relates to the vertical illuminance at the eye level, allowing to measure the glare even if there is not so much contrast (for example in very bright scenes). The second part quantifies the contrast between the light sources and their background, regarding their luminance and their position in the visual field.

Based on statistical studies [25], the standard EN17037:2019 defines glare thresholds as the probabilities that cannot be exceeded more than 5% of occupied hours. Then we are below those

values for 95% of the time. 0.45 is the limit for disturbing glare while 0.40 corresponds to perceptible glare and 0.35 to imperceptible glare.

**Table A.7 — Proposed different levels of threshold  $DGP_{e<5\%}$  for glare protection**

Level of recommendation for glare protection	$DGP_{e<5\%}$
Minimum	0,45
Medium	0,40
High	0,35

Table 8 - Table A.7 EN17037:2019

Note that for the glare evaluation, we use “true” occupied hours. It makes more sense to evaluate the glare probability during the time when the space is possibly used than during all the daylight hours. Also DGP categories in Table 8 are calibrated for this 8 A.M. to 6 P.M reference workday. Here is the annual map of occupied hours (set from 8 A.M. to 6 P.M.) ; the jump is due to the summer timeshift.



Figure 27 - Mapping of occupied hours all over the year (white cells)

### 1.3 Performance assessment

The technical performance of the twisting blinds is assessed according to widely recognized quantitative daylight metrics. The daylight factor, DF, gives an indication of the daylight performance of the space under overcast conditions. This simple metric is used in the following section (2) for an initial assessment of the base performance of the shading system with fully open blinds and to evaluate the influence of the composite material reflectance on this performance. To evaluate efficiency of the shading system regarding adequate annual illumination and glare protection we use the definitions of the annual daylight provision (DP) and the annual daylight glare probability ( $DGP_{e<5\%}$ ) described in section 1.2 ('Metrics'). While the DP takes into account local weather data during daylight hours (i.e. irradiance > 20 W/m<sup>2</sup>) and blind states to describe the performance of the space regarding daylight provision, the  $DGP_{e<5\%}$  value allows to determine the DGP value that is not exceeded more than 5% of the total occupied hours. For the evaluation of the control algorithm (section 3 'State choice and annual schedule'), we define an annual spatial

illuminance  $ASI_{50,50}$  concept, as the illuminance level reached over 50% of the floor area for 50% of the relevant time steps, i.e. when both occupancy and daylight conditions are fulfilled.

The qualitative perceptual improvement brought by the twist (and its creative potential) is stated based on findings on the topic mentioned in the 'Concept' section, especially the latest studies from Chamilothori [15]. The investigation of people's subjective response to 6 facade patterns, among which vertical strips and skewed strips visible in the images below, showed that changing from vertical to skewed facade elements significantly increased how interesting the space was perceived (an increase of 1.09 units on a 11-points scale) and how exciting (an increase of 1.05 units). The twisted blinds resemble those skewed vertical elements, hence we make the assumption that the effect on the perceptual impressions of the people is similar. The twisted states are considered to generally increase the pleasantness and visual interest of the space. Further studies should address occupants' responses to these twisted blinds and differentiate slight variations (e.g. more open at the top, or at the bottom, influence of the width and of edges curvature etc).

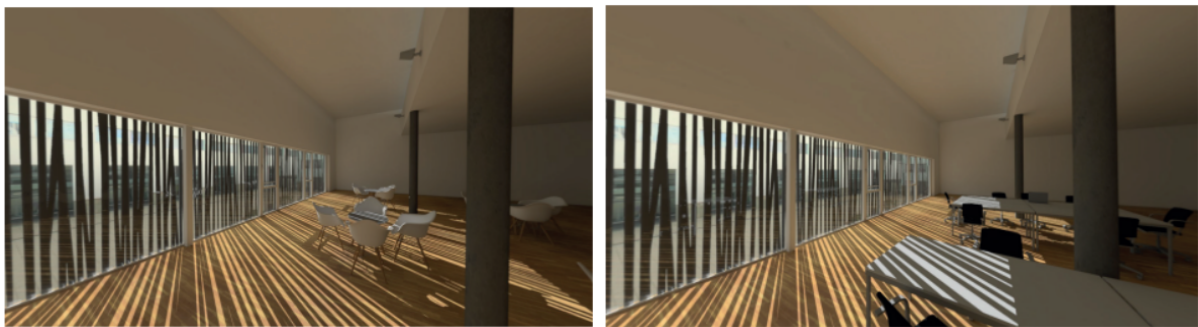


Figure 28 - Illustration of the space with the skewed facade variation for a clear sky with low sun angle and both social context (left) and working context (right). From [15].

To sum up, the paradigm is: *knowing that the proposed kinetic facade has a more pleasant shape than vertical blinds, if we prove that it can be satisfying in terms of quantifiable indicators, we demonstrate that it performs better on the overall.*

In section 2 ('Base performance') we define minimum requirements imposed on the system. It concerns the optical behavior of the material, characterised by feasible ranges of optical properties, especially the transmittance and the reflectance. Those parameters have direct influence on the shading system base function, meaning that the closed state must provide glare protection while the open state must ensure good daylight provision. Then we investigate the specificities of different intermediate twisted states by looking individually at their annual performance too.

In section 3 ('State choice and annual schedule') the facade states are combined through a control algorithm to assess the daylight performance of the kinetic shading system's behavior as a whole. We will show that it is possible to design an efficient yearly schedule with visually interesting (twisted) configurations, and investigate the influence of the context (working or social) on the schedule.

## 2 Base performance

In this section we point out adequate optical properties based on the performance expected from the open and closed states of the blinds. We impose those states to satisfy the *Medium* office

work recommendation level of the EU standard EN17037:2019. Once the transmittance and the reflectance are fixed, we analyze individually the daylight performance of a set of representative states, detailed Figure 29 right after. Schematic visualizations of those states covering the facade can be found in Appendix II.

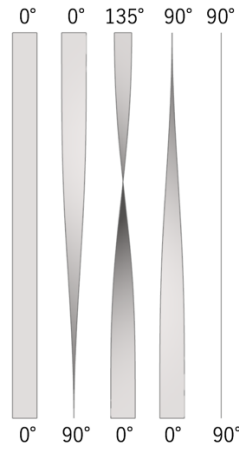


Figure 29 – The different blinds’ states investigated in details; illustration for a single element that changes shape through rotations at the top or at the bottom

## 2.1 Open and closed states

### 2.1.1 Efficiency of the closed state

Closed blinds define the zero for respectively the top and bottom rotation. This state is referred as 0-0° .

Medium office work recommendation level of the EU standards corresponds, according to Table 8, to an annual  $DGP_{e<5\%} \leq 0.40$ . To protect from glare we need (in the 100% closed position) to block direct light hitting the modules. It ideally means to achieve 0 direct transmittance, which is consistent with glare protection classes  $\geq 2$  in Table 9 after.

We also want to take advantage of using GFRP compared to traditional blinds (made of aluminium for instance). GFRP is not opaque, and we will design it such that even when totally closed, the facade still acts like a source of (diffuse) light. In others terms, we are looking for a translucent material, commonly defined as allowing light to pass through but diffusing it so that persons, objects, etc on the opposite side cannot be seen clearly. Consequently we want to maximize diffuse transmittance of the material, at least to a certain extent. The total transmittance (direct+diffuse) should not exceed 15% to 20% (Table 10).

**Table E.2 — The marerial porperties and glare protection classes**

Class	Influence on visual comfort				
	0	1	2	3	4
	very little effect	little effect	moderate effect	good effect	very good effect

Table 9 - Table E.2 prEN114501:2019

**Table E.3 — Glare control classification given EN 14501 according to the visual transmittance properties  $\tau_{v,n-a}$  and  $\tau_{v,n-diff}$**

$\tau_{v,n-diff}^b$	$\tau_{v,n-n}^a$					
	$\tau_{v,n-n} = 0,00$	$0,00 < \tau_{v,n-n} \leq 0,01$	$0,01 < \tau_{v,n-n} \leq 0,02$	$0,02 < \tau_{v,n-n} \leq 0,03$	$0,03 < \tau_{v,n-n} \leq 0,05$	$\tau_{v,n-n} > 0,05$
$\tau_{v,n-diff} \leq 0,03$	4	4	3	3	1	0
$0,03 < \tau_{v,n-diff} \leq 0,06$	4	3	2	2	1	0
$0,06 < \tau_{v,n-diff} \leq 0,10$	4	3	2	1	0	0
$0,10 < \tau_{v,n-diff} \leq 0,15$	3	2	1	1	0	0
$0,15 < \tau_{v,n-diff} \leq 0,20$	2	2	1	1	0	0
$0,20 < \tau_{v,n-diff} \leq 0,25$	1	1	0	0	0	0
$0,25 < \tau_{v,n-diff}$	0	0	0	0	0	0

<sup>a</sup>  $\tau_{v,n-n}$  is the normal/normal light transmittance  
<sup>b</sup>  $\tau_{v,n-diff}$  is the normal/diffuse light transmittance

Table 10 - Table E.3 prEN114501:2019

The reflectance of the material should be optimized according to the effectively reached transmittance, keeping in mind the equation linking transmittance, reflectance and absorption:

$$T + R + A = 1$$

For a transmittance about 15%, a low reflectance often implies a pretty high absorption and the luminance of the diffuse surface gets too high inside. In the other hand a very high reflectance would bring glary direct light when the blinds are twisted. As a first approach we will accept reflectances playing around 50%.

Figure 30 provides the annual glare map for the configuration without blinds, as a reference. The camera was set as detailed in section 1.1 ('Modeling and daylight simulations').



Figure 30 - Annual mapping of the daylight glare probability without blinds (x axis: months (days) – y axis: hours)

The DGP not exceeded during more than 5% of the occupied hours (Figure 30) is  $DGP_{e<5\%} = 0.89$ . A shading system is definitely necessary, especially on the morning when our East oriented building receives direct sun. NB: The annual glare map should be symmetric (because the annual sun path is). It was found here that the difference, for ex. between May and July, was due to the Geneva weather dataset.

Below (Figure 31) is the annual glare map with 0-0° closed blinds for a 15% transmittance (and 50% reflectance). The 0-0° position prevents intolerable glare as the DGP is never higher than 0.45 during the year. Furthermore  $DGP_{e<5\%} = 0.35$ , which is below the 0.40 medium threshold defined.



Figure 31 - Annual mapping of the daylight glare probability with 15% transmittance and 50% reflectance blinds in closed position (x axis: months (days) – y axis: hours)

However we locally see on the map orange (but no red) time steps. From April to July, glare levels in the morning exceed 0.40. A solution could be to adapt the optical parameters i.e. reducing the transmittance if we really want to perform better on those time steps, as in Figure 32 below. Here (Geneva climate) the frequency of occurrence of disturbing glare is acceptable so the decision on the transmittance is maintained free. Nevertheless note that in very sunny countries, a high occurrence of disturbing glare would be expected and would make mandatory to lower the transmittance.

Figure 32 shows the annual glare map for a 10% transmittance (and still 50% reflectance).  $DGP_{e<5\%} = 0.28$ , indeed we see that we avoid any perceptible glare all year long.

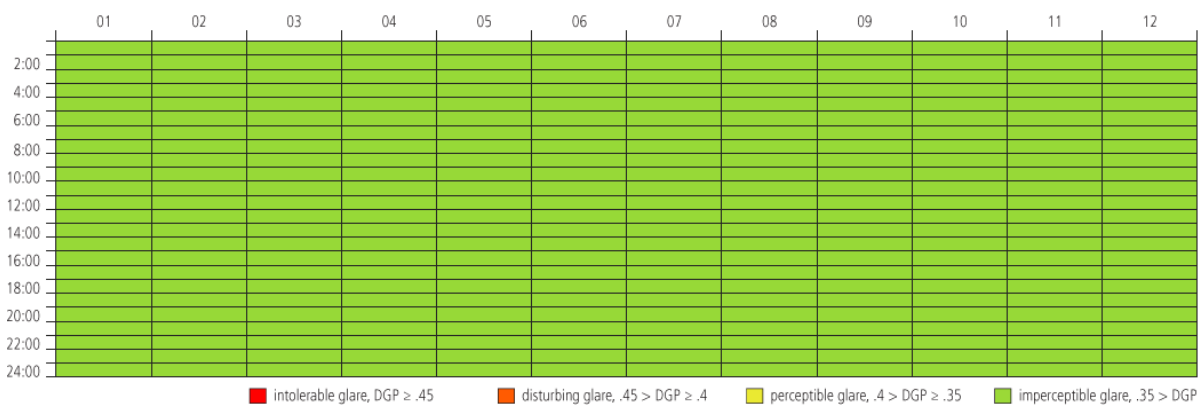


Figure 32 - Annual mapping of the daylight glare probability with 10% transmittance and 50% reflectance blinds in closed position (x axis: months (days) – y axis: hours)

**Conclusion**

Achieving glare protection class 3 requires to limit to 15% the visual transmittance of the GFRP material and to avoid any direct transmittance.

**2.1.2 Efficiency of the open state**

Open blinds state is referred as 90-90° .

Concerning the view outwards (please refer to Table 7), medium recommendation level of the EU standards is completed as the window of the SG foyer goes from bottom to top of the room.

Regarding Daylight Provision (DP), an illuminance of 500 lux should be reached for 50% of the floor area and during 50% of daylight hours, as well as a minimum illuminance of 300 lux for 95% of the floor area and 50% of daylight hours, to comply with the medium recommendation recalled in Table 11 below.

Level of recommendation for vertical and inclined daylight opening	Target illuminance $E_T$ (lx)	Fraction of space for target level $F_{plane, \%}$	Minimum target illuminance $E_{TM}$ (lx)	Fraction of space for minimum target level $F_{plane, \%}$	Fraction of daylight hours $F_{time, \%}$
Minimum	300	50%	100	95%	50%
Medium	500	50%	300	95%	50%
High	750	50%	500	95%	50%

NOTE Table A.3 gives target daylight factor ( $D_T$ ) and minimum target daylight factor ( $D_{TM}$ ) corresponding to target illuminance level and minimum target illuminance, respectively, for the CEN capital cities.

Table 11 – ‘Recommendation of daylight provision by daylight openings in vertical and inclined surface’ - Table A.1 EN17037:2019

We should achieve a daylight factor  $DF \geq 3.1\%$  with our selected threshold for the DP (please refer to Table 6). Table 12 below provides DP evaluations for the configuration without blinds, as a reference, and with open blinds (90-90°), for both  $DP[500lux]_{50\%}$  and  $DP[300lux]_{50\%}$ .

Results show that the *Medium* recommendation is not reached, with  $DP[500lux]_{50\%} = 48\% < 50\%$ . The blinds’ open state cuts too much light if it is kept fixed all year long. This is mainly because of the East orientation, catching direct sun only in the morning and with a small azimuth to the facade’s plane. Even without the shading system, the room has  $DP[500lux]_{50\%} = 82\% < 100\%$ . We should consider the technical design of the supports so that the blinds can be removed at some times, for example sliding them to the edges of the facade by means of steel rails. Without such a system, the fixed open blinds nonetheless comply with the *Minimum* recommendation, i.e.  $DP[300lux]_{50\%} = 78\% > 50\%$  (see also the daylight provision maps in Appendix V, further explained in 2.2.3).

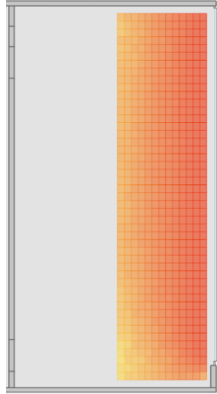
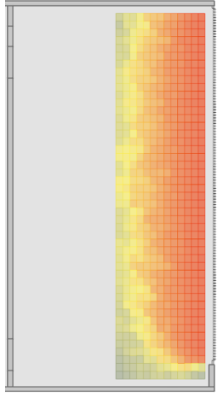
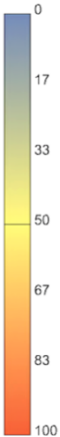
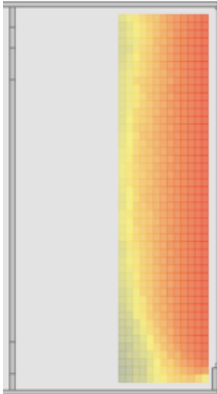
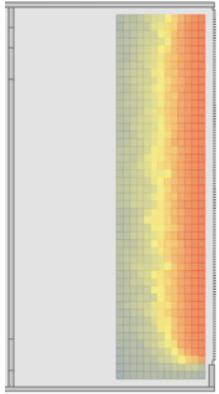
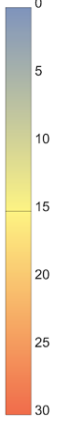
Blinds position	No blinds (ref.)	90-90	
<b>DP[300lux]<sub>50%</sub></b>	100 %	(50<) 78 % (<95)	
<b>DP[500lux]<sub>50%</sub></b>	82%	<b>48% (&lt;50)</b>	
Repartition for DP[300lux] <sub>50%</sub>			<p>Colorscale (% of daylight hours)</p> 
Repartition for DP[500lux] <sub>50%</sub>			
<b>DF</b>	7.61%	4.27%	<p>(% of outdoor illuminance)</p> 
Repartition for DF			

Table 12 – Evaluation and visualization of the Daylight Provision and Daylight Factor for blinds in the 90-90° open state, in comparison with a reference state without blinds.

About the Daylight Factor, we satisfy easily 3.1%, as the open position (90-90) achieves a mean DF of 4.27%. Note that in the base state, without blinds, this DF reaches 7.61%. The reduction due to rectangle open geometry is  $\frac{7.61-4.27}{7.61} * 100 = 43.8\%$ . This is independent of the width of the blinds.

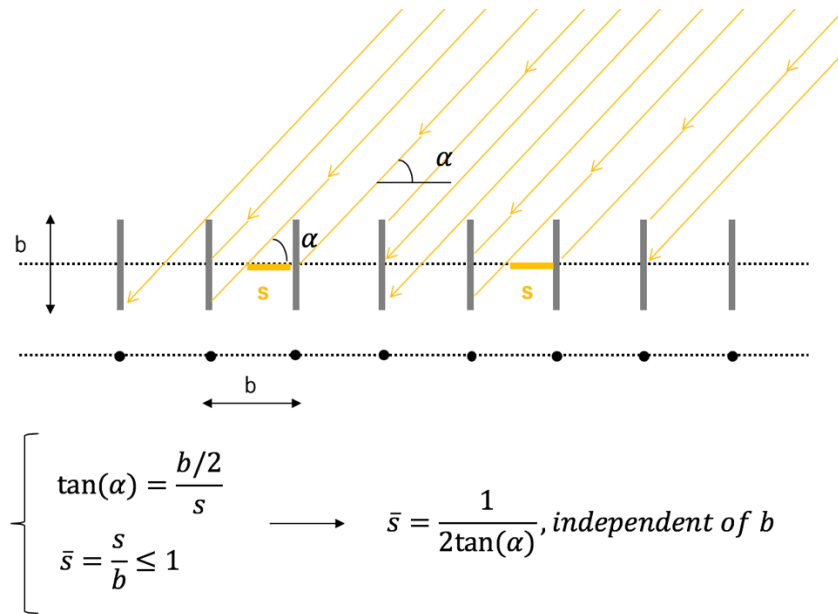


Figure 33 - The effective opening ratio  $\bar{s}$  (for incident light with azimuth  $\alpha$ ) is independent of the blinds' width, as long as the blinds are all rotated in the same way.

The reflectance is involved in the “light catching” mechanism when the blinds are open. We need a minimum reflectance to ensure that enough light is reflected inside when the system is open. To identify suitable boundaries for GFRP material, we investigate the impact of the reflectance on the Daylight Factor with 15% transmittance materials and respectively 20, 35, 70 and 85% reflectances:

Configuration	90-90, r=0%	90-90, r=20%	90-90, r=35%	90-90, r=50%	90-90, r=70%	90-90, r=85%
DF [%]	3.73	3.92	4.08	4.27	4.53	4.73

Table 13 - Impact of a change in the reflectance on the Daylight Factor, for 15% transmittance materials

Mean DF evolution according to the blinds reflectance ( $\tau = 15\%$ )

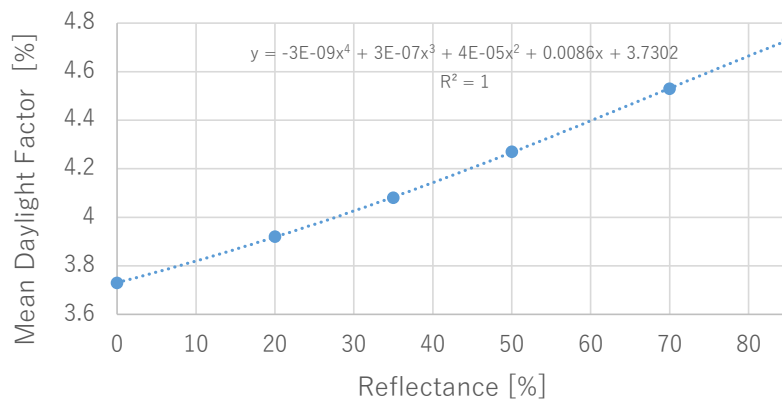


Figure 34 – Sensitivity of the Daylight Factor to a change in the facade elements reflectance (15% transmittance, 90-90° state)

The sensitivity of the DF to the reflectance is small: a 30% change in reflectance leads to a relative 4.75% change in DF value, i.e. playing in the [35-65]% reflectance range will vary the DF in the [4.08-4.48]%. Furthermore all the points exceed the DF=3.1% *Medium* requirement.

## Conclusion

The findings of this section showed that the blinds' modeling with 15% diffuse Transmittance and 50% Reflectance is adequate for the present application.

The 'material.rad' script for Radiance is the following:

```
#15/50:
void trans transluc_15_50
0
0
7 0.65 0.65 0.65 0 0 0.2308 0
```

Chapter III section 1 will investigate how to effectively control the GFRP optical properties.

### 2.1.3 About the use of opaque material

The use of an opaque material like plastic i.e. transmittance 0% and reflectance 100% would obviously enhance the light penetration in the open states, as after light passing straight in between blinds, the second main catching mechanism involved is light entrance after a hit on the blinds. The GFRP blinds becomes however interesting in the partially or fully closed states, when the main catching mechanism involved is light diffused through the blinds.

	Open (90-90)		Closed (0-0)	
	t15_r50	t0_r100	t15_r50	t0_r100
t <sub>transmittance</sub> _r <sub>reflectance</sub>				
Daylight Factor	4.27	4.73	0.93	0
DP[300lux]50% [%]	78	99	7	0
DP[500lux]50% [%]	48	51	0	0

Table 14 - Comparison between fully opaque and partially translucent materials

### 2.1.4 Practical considerations

Concerning the practical implementation of the facade, a central issue is to achieve a 100% closed position, without direct light passing between the elements. To do so there are several options:

-Option type 1: some light can enter but after several bounces, so that it is diffuse light. This options requires thick and/or offset modules.

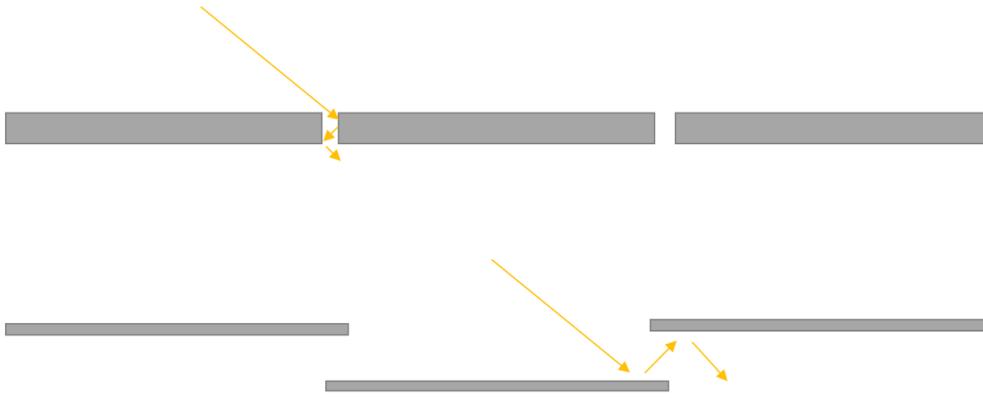


Figure 35 - Thick modules (top) ; offset modules (down)

- Option type 2: no light enters between the modules. This is achieved by adding jointing elements filling the gaps or by introducing a small overlap of the modules.

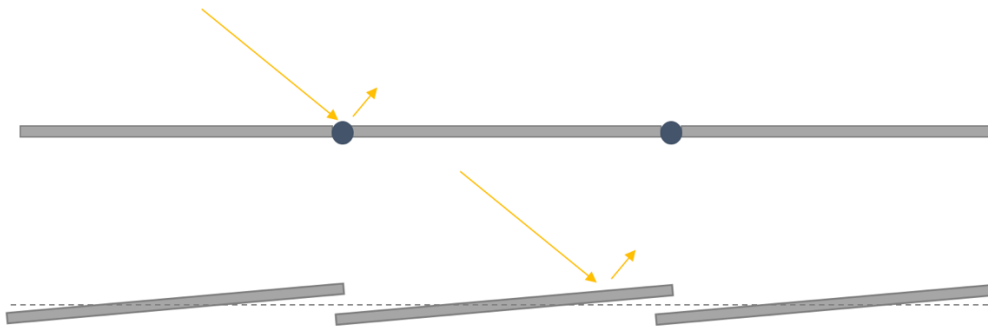


Figure 36 - Modules with joints (top) ; overlapped modules (down)

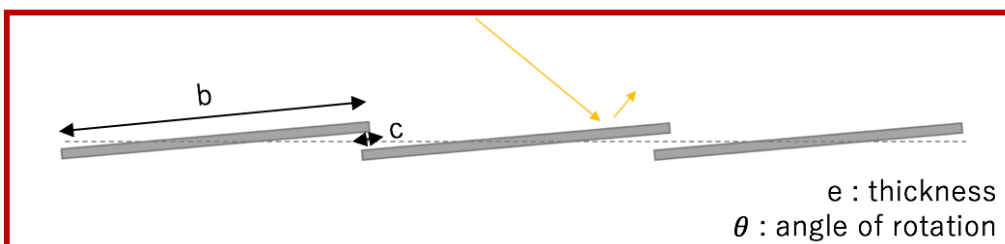
We want to maximize the view out when the modules are open, hence the thick modules solution is discarded. The offset modules solution is discarded too because it changes a lot the architectural concept. We will use a type 2 option.

The joints option involves carefulness regarding thermal dilatancy. Admitting an expansion coefficient  $\alpha = 3 * 10^{-5} K^{-1}$  for GFRP and a uniform  $\Delta T = \pm 20 K$ , it creates a lateral thermal expansion  $\Delta \epsilon = \pm 20 * 3 * 10^{-5} * 0.15 = 9 * 10^{-5} m$  per module along the width. This is reasonable. However, joints create opaque vertical lines that are maybe not very attractive visually.

We currently opt for the overlap option, with a geometrical condition on it: all the modules centers must stay on the same horizontal line. Hence the minimum angle should be such that

$$\tan(\theta) * (b - c) > e$$

with e the thickness, b the width and c the overlap length.



Examples of numerical values:

Overlap c	Thickness e	With b	Min angle $\theta$
1 cm	1 cm	15 cm	4.09°
0.5 cm	1 cm	15 cm	3.95°

Table 15 - Restrictions on the overlap between the modules

A 1:5 scaled mockup was made to have a clearer understanding of eventual issues raised by the overlap when the blinds are twisted. It is also a useful tool for light patterns trials.

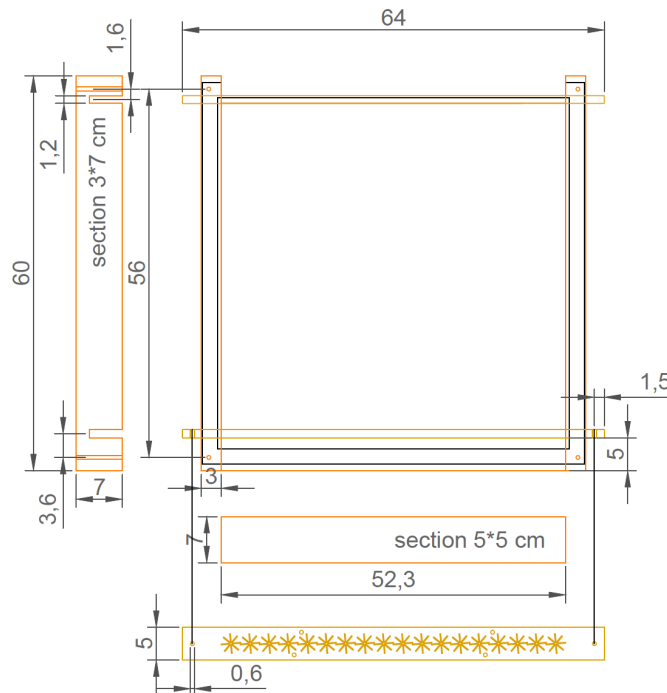


Figure 37 - Sketch of the mockup structure

The setup is a wooden frame which can hold 1:5 GFRP strips fabricated at the CClab. It plugs into an experimental black-box setup already available at the LIPID lab (black lines on the sketch). The existing setup has an aluminium frame with interior area of 54\*54cm plus a 3mm thick internal layer, 2cm wide borders and four steel rods of  $d=6\text{mm}$  &  $L=6\text{cm}$  centered in the corners.

The wooden frame has massive wood pieces that insert into the steel rods and MDF thin layers in which we drilled slots to insert the GFRP strips. The slots have a “star” shape that allows to achieve multiple orientations to twist lamellas:  $0^\circ$  ,  $45^\circ$  ,  $90^\circ$  . The lamellas are  $H=50\text{cm}$  (+5cm to insert them through the slots). They are dragged from the top through the upper frame piece and lay on the lower one.

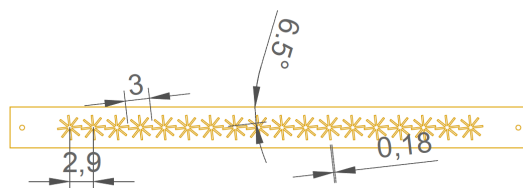


Figure 38 - Detail of the multi-oriented slots (top view)

Here is what it looks like.



Figure 39 - Mockup trials. Note that on the picture taken from the inside of the blackbox (left and right), strips made of woven reinforcement are on the left and strips made of mat reinforcement are on the right. The view in between the elements is realistic but the view through them is not. The total transmittance values measured on the above mat and woven GFRP strips are higher (resp. 54% and 65%), especially the direct part - Pictures J. Baehr-Bruyère.

## Conclusion

We cannot have several consecutive lamellas twisted at 180° . Because of the overlap introduced, they are touching each other at one end (see the two pieces in the middle in Fig. 39 above). For investigations regarding the daylighting control system, the highest rotation considered will be 135° .

## 2.2 Adding intermediate states

### 2.2.1 Individual annual daylight performance of the different blinds' state

Below are summarized the annual daylight glare probabilities and daylight provision metrics for a selection of possible blinds' states (**15%** transmittance, **50%** reflectance). The view access is also evaluated\* for the same viewpoint as the DGP and a perspective view (150° horizontal & 120° vertical). \*by counting white pixels in a daylight simulation with uniform sky, -ab 0 and opaque blinds

The maps are sorted in increasing protection, i.e. decreasing DGP and DP. The following blinds orientations are chosen to have an overview. They are noted in the format top rotation - bottom rotation, 0° being parallel to the facade's plane. Annual glare maps and illustrations regarding daylight provision are provided in Appendices III and IV. Annual daylight provision maps were developed by the author, in the same vein as glare maps plotted by DIVA. They can be found in Appendix V. The combination of DGP and DP maps provides an intuitive visual tool to capture the behavior of the different states.

Selected states:

- 0° - 0° (fully closed)
- 0° - 90° (partially open at the bottom)
- 180° - 0° (fully twisted)
- 135° - 0°
- 90° - 0° (partially open at the top)
- 90° - 90° (fully open)

<b>Blinds position</b>	<b>No blinds (ref.)</b>	<b>90-90</b>	<b>90-0 *</b>	<b>135-0 **</b>	<b>180-0 **</b>	<b>0-90 *</b>	<b>0-0</b>
<b>DGP<sub>e&lt;5%</sub></b>	0.89	0.59	0.53	0.46	0.37	0.37	0.35
<b>DP[300lux]<sub>50%</sub></b>	100 %	78 %	64 %	62 %	41%	35%	7 %
<b>DP[500lux]<sub>50%</sub></b>	82%	48%	39%	39%	24%	21%	0%
<b>View access</b>	100%	33%	45%	30%	22%	45%	0%

\*clockwise rotation

\*\*counter-clockwise rotation

Table 16 - Annual daylight glare probability and daylight provision for the studied states, noted 'top rotation - bottom rotation' and sorted in increasing protection i.e. decreasing DGP. The view access information stands for the same viewpoint as used for DGP.

The case without blinds is a reference case for the maximum daylight provision in the room. The 0-0° case confirms that the facade system ensures its light-blocking function when closed, while being still a bit luminous compared to classical opaque elements. The 0-90° blocks the light on the upper part, giving rise to a short band with high illuminance close to the window (see Appendix IV) which is not the most useful, but this state is still interesting because it allows to keep a part of the facade open (view access) while we would fully close at 0-0° only for extremely glary cases. Indeed it was shown that without systematic closing of the blinds is poorly accepted by the occupants [26].

The state 90-0° blocks the light on the lower part, allowing for a better (deeper) light penetration across the room. The 90-90° is even better at homogenizing the daylight repartition across the year (see Appendices IV & V). Finally, the 180-0° configuration blocks direct light on the top and bottom parts of the window. It achieves a glare protection identical to the 0-90° state (DGP=0.37), for a better daylight provision but nevertheless highly restricting the view access (compared to 0-90° state). In the same vein, the 135-0° state provides better glare protection than the 90-0° for an equal daylight provision. The out-of-plane curved shape of elements twisted further than 90° seems to "catch" to the inside a greater part of the incident light, while a twist up to 90° performs better in terms of view access. It brings up the question if the blinds should be "open" to optimize the view out or to optimize how sunlight is coming in.

Further characterization of the phenomenon would require to use ray-tracing methods, to study the 3D light bouncing between the curved surfaces of the blinds. Such investigations should be complemented by a multiple-positions analysis, as the view out is strongly dependent on the position of the observer!

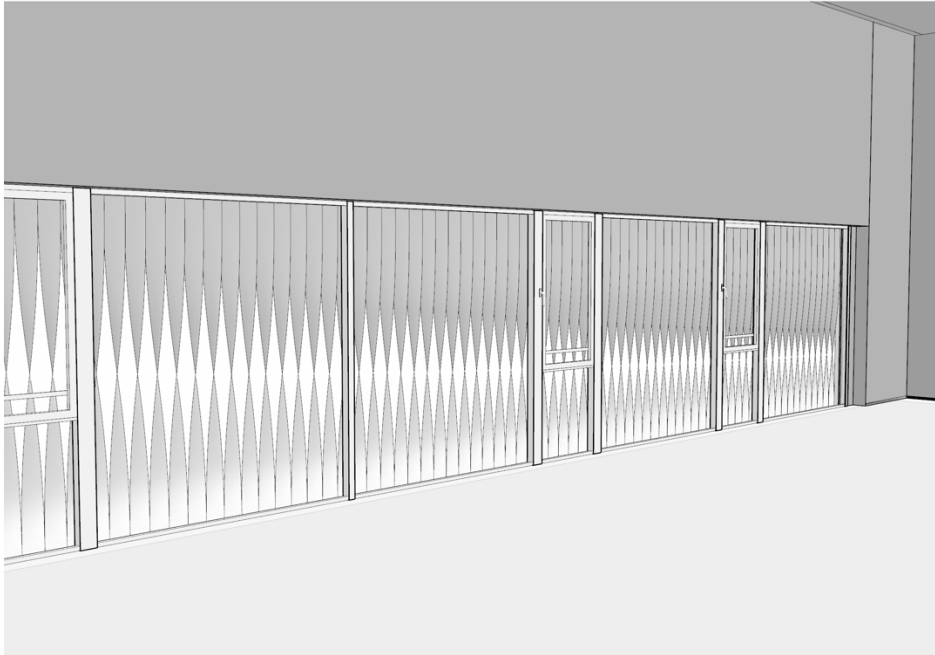


Figure 40 – ‘The view out is strongly dependent on the position of the observer’  
Side observer with blinds in the 0-135° position

In view of the implementation of a choice function, we see that multiple parameters can be involved in the performance assessment, with complex mutual dependencies amongst themselves. There is no absolute ‘best state’, the different parameters must be valued on a case-by-case basis according to user needs.

### 2.2.2 Clockwise or counter-clockwise twist

A performance comparison of both 90-0 and 0-90 states, rotated once clockwise and once the other way round, lead to the conclusion that clockwise rotation is better for this case study and orientation. Indeed, DGP annual metric of both tested states performs better with the clockwise rotation, for similar DP. Corresponding DGP colormaps are provided in Appendix III.

Blinds position	90-0 *	90-0 **	0-90 *	0-90 **
DGP <sub>e&lt;5%</sub>	<b>0.53</b>	0.62	<b>0.37</b>	0.43
DP[300lux] <sub>50%</sub>	<b>64 %</b>	64 %	<b>35 %</b>	37 %

\*clockwise rotation

\*\*counter-clockwise rotation

Table 17 – Influence of the rotation direction on the individual annual daylight performance.

Once direct rays in between the blinds are avoided, the glare is due to sunrays directly reflected by the blinds toward some people’s eyes. Specularity and roughness material values being set to zero in radiance, all the light hitting the blinds is then equally reflected in all directions as diffuse light. With clockwise rotation the users are more likely to see the transmitting face of the blinds, while they tend to see the reflecting face with counter-clockwise rotations so they face higher illuminance levels. In a model that would include specularity and roughness, another important parameter would be the tilt angle. Counter-clockwise rotations leads to largest tilt angle than clockwise rotations, hence tending to reflect the ray more to the inside. It is possible that the reduction in DGP with clockwise rotation would be even greater than measured here. Also the orientation of the overlap





Figure 43 - Illuminance dataset (.ill file) transformed into annual daylight provision map

From this point, we have annual mapping of the performance for the different configurations of the blinds. We recall the initial objective: ensuring that we have enough daylight but not too much. Basically, for each timestep we would intuitively select a blind configuration which is green both in the sDA and DGP maps. Example is given below for the 135-0° configuration. After 11:00 A.M., this state ensures both a protection against disturbing glare and an illuminance greater than 300 lux for more than 75% of the floor area.



Figure 44 - Annual DGP map for the 135-0° configuration, material t=15% r=50% (x axis: months (days) – y axis: hours)

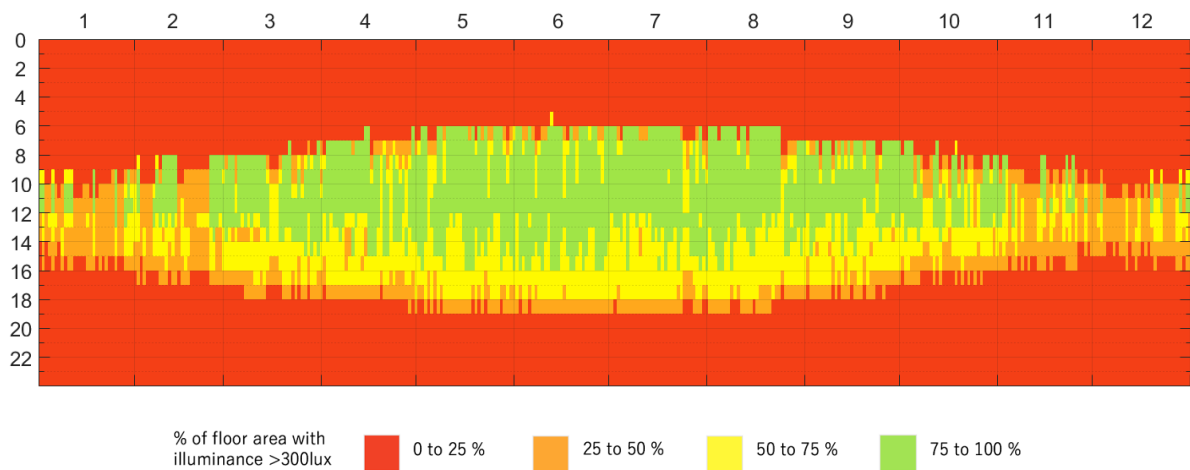


Figure 45 - Annual DP map for the 135-0° configuration, material t=15% r=50% (x axis: months (days) – y axis: hours)

The colormaps are a nice educational tool. They allow the facade designer to capture the facade's behavior, especially for twisted states that create not so obvious light bouncings. Future prospects could be to plot the maps according to real-time weather conditions and to implement them in the user interface. The glare and illuminance thresholds defining the **green** zones are doomed to be adjusted according to the needs, e.g. involving the current use of the space, user sensitivity, perceptual effects...

## 3 State choice and annual schedule

This section explains how we build a dynamic schedule for the blinds in order to optimize their orientation during the day, across the whole year. The work is performed with Excel and Matlab softwares. The state choice function and related performance check conditions are detailed. A custom function is developed to optimize the choice of the facade state for every hourly time step. Perceptual impressions are involved in the decision by associating potential occupant activities of working and socializing to specific changes on daylight metrics.

### 3.1 Preparing the database

Hourly data were simulated in advance for all states and stored in a database. Both Annual Glare and Annual Daylight Provision simulations were run with DIVA-for-Rhino for configurations from Figure 29. We use Excel macros written in the Visual Basic developer tool for the aftertreatment of glare and illuminance datasets.

#### 3.1.1 Daylight glare probability datasets

The '.dgp' files recording the  $DGP_{e<5\%}$  at each time step are kept as is.

#### 3.1.2 Direct sun datasets

We created a file indicating for each time step if there is direct sun or not on the camera sensor (see Fig. 24 the selected viewpoint for the DGP evaluation) by simulating the exact sun position with -ab0 and measuring the illuminance on the sensor. Whenever the file indicates a non-zero value, there is direct sun on the sensor. Incoming direct sun leads to a high DGP value, however the direct sun datasets complement the DGP ones to be sure to discard disturbing direct sun occurrence.

It is also a way to correct possible errors introduced by the interpolation in the DGP calculation. Indeed, calculations are done for a set of 65 sun positions representing the yearly sun paths. When it comes that the time step under study does not match one of those 65 positions, the output value is a weighted average of the 4 closest positions and the distance between the current sun position studied and those closest positions. Hence it might happen that people are effectively dazzled by direct sun while the 4 positions used for averaging corresponds to sunrays hitting the blinds so that the point-in time DGP value is underestimated.



Figure 46 - Illustration of the interpolation problematic in the DGP calculation

NB: in our case the analysis of the direct sun datasets finally showed that there were only very few hours with incoming direct sun, which was caused by the distance from the viewpoint to the facade and the orientation of the facade (all sun positions  $>20^\circ$  were in any case not visible). We deduced that the high DGP values we had resulted mainly of the vertical illuminance caused by the diffuse scattering and less by the direct sun and the mentioned interpolation problematic.

### 3.1.3 Illuminance datasets

Figure 42 (section 2.2.3 'Understanding the making of the maps') shows '.ill' datasets. To implement the state choice algorithm of the autonomous schedule, we treat illuminance data in a slightly different and more mathematical way than for the colormaps: for each hourly time step, i.e. lines in the '.ill' file, we calculate the median illuminance across the 611 sensor nodes, i.e. the lux level reached by 50% of floor area. By doing so, we define a spatial illuminance concept 'SI<sub>50%</sub>'.

## 3.2 Logic of the state changes

State changes are triggered by conditional loops managing the actuation of the facade. The code outputs a list of the type "Month/Day/Hour<sub>i</sub> ↔ State<sub>j</sub>," and evaluate the annual performance of the schedule it established.

The function includes three simultaneous conditions to satisfy at each hourly time step: (1) maximizing SI<sub>50%</sub> i.e. the work plane illuminance reached by at least 50% of the floor area, while (2) avoiding direct sun penetration, and (3) limiting the point-in time DGP to a maximum ("cut-off") value chosen according to the studied scenario. The point-in-time cut-off DGP is selected according to the targeted annual DGP performance  $DGP_{e<5\%,annual}$ . Both working and social usages could be addressed by changing this threshold, as the discomfort glare perception is highly influenced by the difficulty of the task performed, in a way that people performing demanding intellectual work are less tolerant towards glare [27][28].

Excel Datafiles obtained from DIVA simulations and VBA macro treatment are an input for the Matlab code. For each hourly time step, they contain the  $DGP_{e<5\%}$  and the SI<sub>50%</sub> values, and so all over the year, for all the blinds configurations in the database. There are many time steps during which the blinds' position does not really matter, for example at night. To optimize the computation time, the default configuration is open, i.e. blinds rotated at 90-90° and the state choice is

performed only when it is relevant. Relevant time steps are time steps when both those two conditions are fulfilled: **a** | we have a daylight condition (irradiation > 20 W/m<sup>2</sup>) AND **b** | the building is occupied (8AM to 6PM)}.



Figure 47 - Mapping the relevant time steps (white cells) all over the year. NB: superposition of Figures 25 and 27

### [detailed structure of the ‘Schedule’ function]

An upper boundary is defined for the point-in-time glare as a cutoff value i.e. we ensure that  $DGP_{e<5\%} < cutoff$  at each (relevant) time step. We develop the choice of this boundary with examples in 3.3.

- For each relevant time step the following loops happen in the subfunction ‘statechoice.m’:
  - if even with closed blinds  $DGP_{e<5\%} > cutoff$  then set the state to “closed” at this time step and go to the next time step.
  - otherwise check among all the states in the database the ones that satisfy  $\{DGP_{e<5\%} < cutoff \text{ AND direct sun is avoided}\}$  and record them as admissible states. Note that we have, for sure, at least one feasible state here: the closed state, that always prevents direct sun.
  - among the admissible states, pick the one that maximizes  $SI_{50\%}$ . Record it as the scheduled configuration for this time step, along with the corresponding  $DGP_{e<5\%}$  and  $SI_{50\%}$  values.
  - go to the next time step.
- Once the above loops ran for the whole year, i.e. with have a ‘Schedule’ vector containing the succession of chosen blinds state:

$$\text{“Month/Day/Hour}_i \Leftrightarrow \text{State}_i\text{”}$$

along with the corresponding  $DGP_{e<5\%}$  and  $SI_{50\%}$ , the annual performance can be evaluated in the subfunction ‘annualperformance.m’. We calculate the annual daylight glare probability  $DGP_{e<5\%,annual}$  as the 95<sup>th</sup> percentile of the  $DGP_{e<5\%}$  values. We also look at the Annual Spatial Illuminance level that is reached across (at least) 50% of the floor area for (at least) 50% of the relevant time steps (occupancy during daylight hours):  $ASI_{50\%(of\ floor\ area),50\%(of\ relevant\ time\ steps)}$ , resumed as  $ASI_{50,50}$ , which is the 50<sup>th</sup> percentile of the  $SI_{50\%}$  values.

During the afternoon, due to the East orientation, the blinds can stay open all the time without glare. The indicator  $ASI_{50,50}$  exhibits few variations, staying around 500 lux. Indeed it mainly

reflects the performance of the 90-90° state (521lux). To better interpret the schedule's influence, the same indicator is calculated taking only into account time steps before 12:00.

- If the annual indicators are not satisfying for the intended use of the shading system, we must adapt the  $DGP_{e<5\%}$  *cutoff* condition, tightening it up or relaxing it. NB: directly imposing a cutoff value equal to the annual value to be reached would be too conservative.

### 3.3 Resilience of the shading system to working and social scenarios

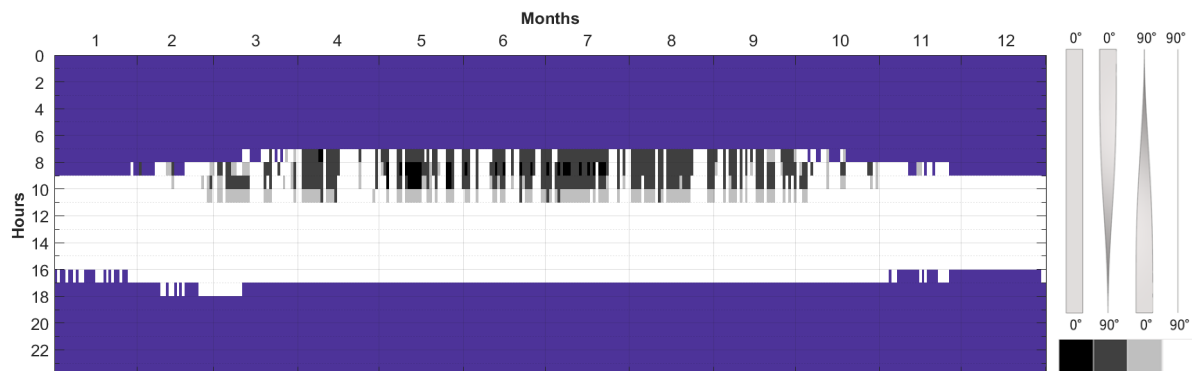
In this section we illustrate the state control algorithm with some examples scenarios, modeled by specific variations of the intolerable glare threshold.

Let's start simple, with a database containing 4 possible states:

- open, 90-90°
- open only at the top, 90-0°
- open only at the bottom, 0-90°
- closed, 0-0°

**Scenario 1** | The space is used as a working space.

We have to make a first “guess” for the intolerable glare threshold.  $DGP_{e<5\%}$  *cutoff* is set to 0.45, relying on EN17037:2019 [22] (cf. Table 8). We obtain the following schedule:

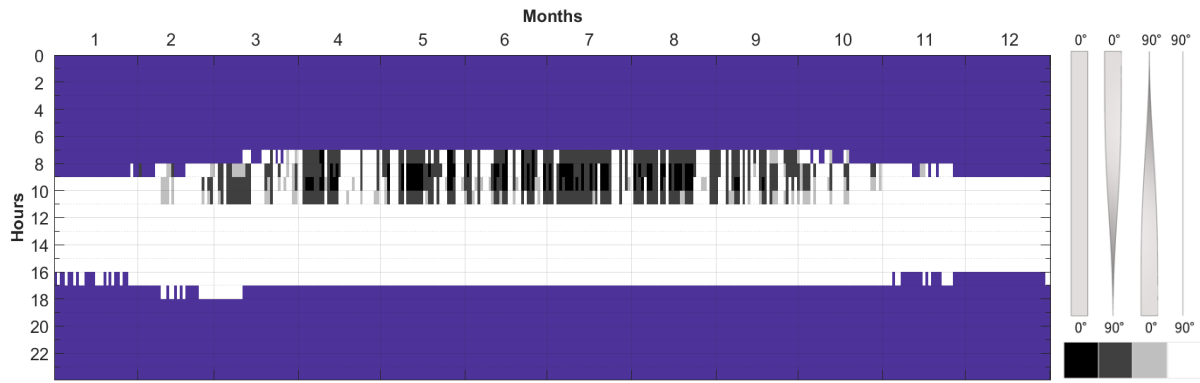


$$DGP_{e<5\%,annual} = 0.431, \quad ASI_{50,50} = 519 \text{ lux}, \quad ASI_{50,50,morning} = 894 \text{ lux}$$

Figure 48 - Variations in the annual state-change controls observed for an admissible point-in-time DGP=0.45 and 4 possible states

There are very few times when we need to completely close the blinds. The twisted state closed at the top does a great job protecting from glare while letting some diffuse light penetrate through the GFRP translucent material. From 10:00 to 11:00 A.M., the configuration open at the top makes a good transition state, as the sun is high and in between S-E and S orientations, still hitting the facade.

According to the same standards, the annual DGP should not exceed 0.40 for an office workspace. This is reached by lowering the cutoff condition to 0.42. The schedule becomes:



$$DGP_{e<5\%,annual} = 0.398, \quad ASI_{50,50} = 519 \text{ lux}, \quad ASI_{50,50,morning} = 855 \text{ lux}$$

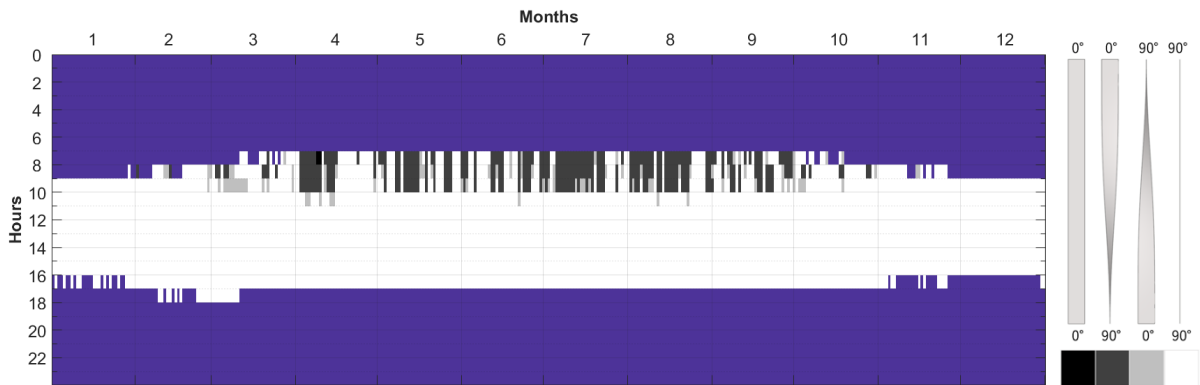
Figure 49 - Variations in the annual state-change controls observed for an admissible point-in-time DGP=0.42 and 4 possible states

We see that we need to close more often, and that the top-open (90-0) state is not particularly relevant. The top closed (0-90) state continues to be a satisfying state, avoiding to close for the whole morning.

**Scenario 2** | The intended use of the space goes more to socializing activities.

In a social situation, people are less inconvenienced by glare as they can move and orient themselves freely into the room and they are also more indulgent as they do not have to perform complicated reflexive tasks. To model this situation, we modify again the  $DGP_{e<5\%}$  cutoff. According to statistical studies of the glare rating in offices from Wienold ([25], especially the table 7.2 p.70), 0.45 is the lowest limit for intolerable glare (in offices) while 0.60 is the uppermost.

The DGP cutoff is increased to 0.50:

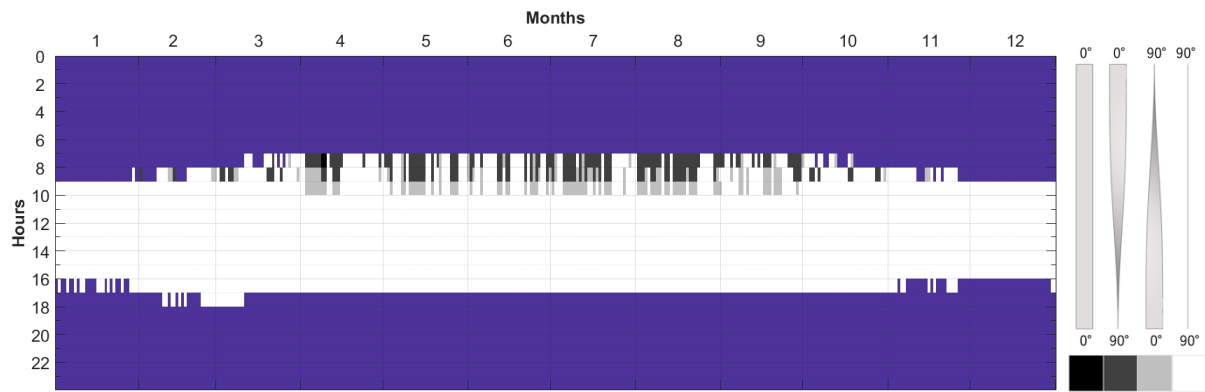


$$DGP_{e<5\%,annual} = 0.471, \quad ASI_{50,50} = 519 \text{ lux}, \quad ASI_{50,50,morning} = 924 \text{ lux}$$

Figure 50 - Variations in the annual state-change controls observed for an admissible point-in-time DGP=0.50 and 4 possible states

Almost only one twisted configuration is used (top-closed). There is no need to totally close anymore.

And testing with a DGP cutoff up to 0.55:



$$DGP_{e<5\%,annual} = 0.503, \quad ASI_{50,50} = 519 \text{ lux}, \quad ASI_{50,50,morning} = 925 \text{ lux}$$

Figure 51 - Variations in the annual state-change controls observed for an admissible point-in-time DGP=0.55 and 4 possible states

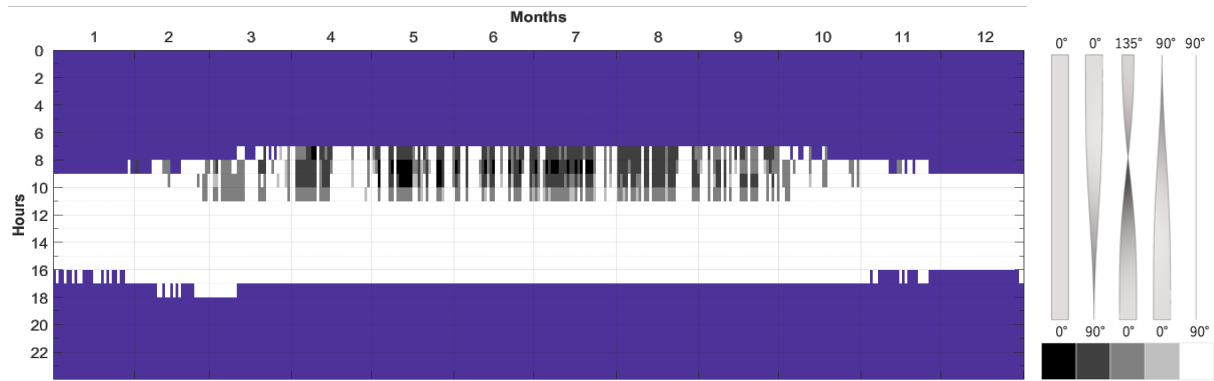
Both twisted configurations are used, which is positive, but the annual DGP increases (up to 0.50 which is definitely unacceptable!) without benefit on the illuminance compared to the previous situation. We reach the point at which constraints on visual comfort are so weak that having an adaptive shading system is questionable.

Up to now we proved that such a twisting facade system performs well in daylight management for a workspace. We also identified that the twist makes even more sense when some constraints are relaxed, as a characteristic of a social use of the space ( $DGP_{e<5\%} \text{ cutoff} \in [0.45 - 0.50]$ ). For this range, it is interesting to enrich the database of twisted states. We add the 135-0 configuration, expected to have a performance in between the top-closed and bottom-closed states (please refer to Table 16 in section 2.2.1 ‘Individual annual daylight performance of the different blinds’ state’).



Figure 52 - Newly introduced state: 0.135°

DGP cutoff set to 0.45, with 5 possible states:

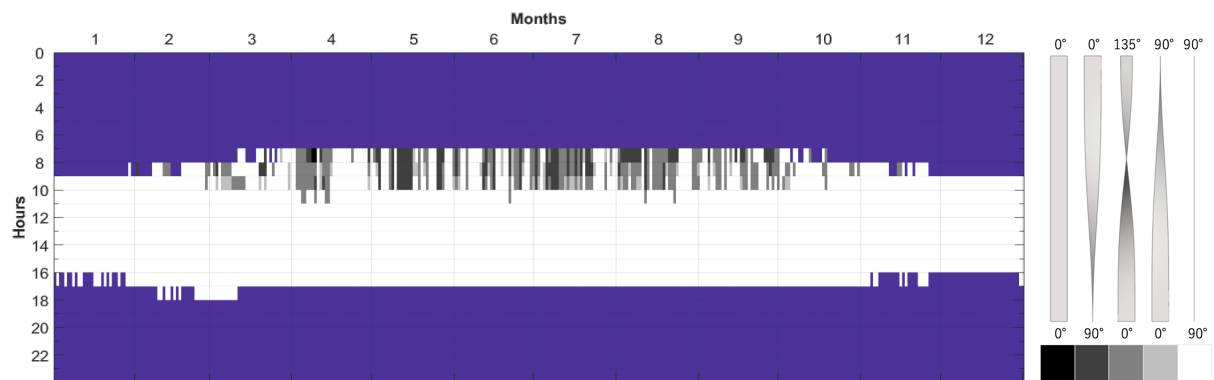


$$DGP_{e<5\%,annual} = 0.428, \quad ASI_{50,50} = 521 \text{ lux}, \quad ASI_{50,50,morning} = 953 \text{ lux}$$

Figure 53 - Variations in the annual state-change controls observed for an admissible point-in-time DGP=0.45 and 5 possible states

Compared to the 4-states database, the transition state newly introduced improves the metric  $ASI_{50,50,morning}$  from 894 to 953 lux while the DGP is similar, about 0.43 (see Fig. 48).

DGP cutoff increased to 0.50:



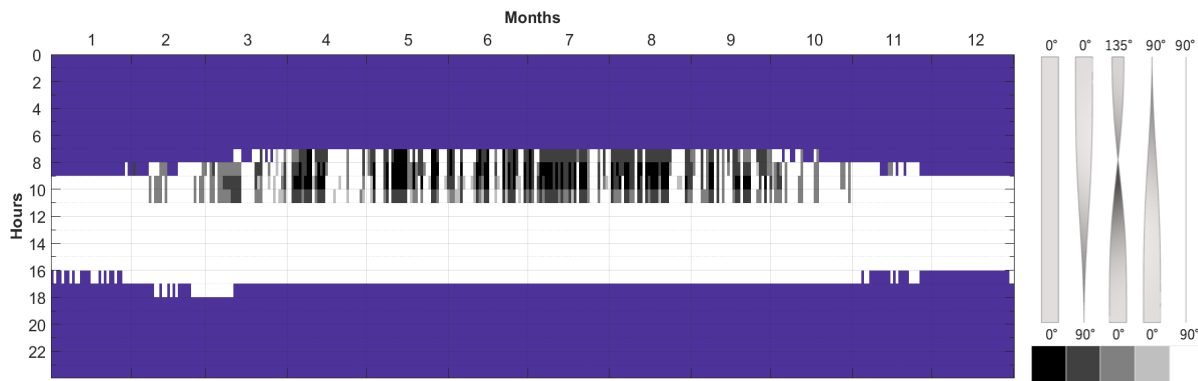
$$DGP_{e<5\%,annual} = 0.481, \quad ASI_{50,50} = 521 \text{ lux}, \quad ASI_{50,50,morning} = 953 \text{ lux}$$

Figure 54 - Variations in the annual state-change controls observed for an admissible point-in-time DGP=0.50 and 5 possible states

The same comment as for Figure 51 stands: we reach the point when constraints on visual comfort are so weak that having an adaptive shading system is questionable. However the schedule from Figure 51 had only 4 possible states and a lower DGPcutoff (0.55) leading to higher annual glare, for a final  $ASI_{50,50,morning} = 925 \text{ lux}$  lower than the 953 lux here.

It highlights the benefit of multiplying the intermediate states to efficiently cover the diversity of the situations. This benefit can also be attested by a comparison between the schedules with resp. the 4-states and 5-states databases when we impose to meet the workspaces standards i.e.  $DGP_{e<5\%,annual} \leq 0.40$ . Please refer to Figure 49 for the 4-states database. Figure 55 below plots the schedule for the 5-states one.

DGP cutoff set to 0.41 (threshold suitable to meet  $DGP_{e<5\%,annual} \leq 0.40$ ):



$$DGP_{e<5\%,annual} = 0.396, \quad ASI_{50,50} = 521 \text{ lux}, \quad ASI_{50,50,morning} = 911 \text{ lux}$$

Figure 55 - Variations in the annual state-change controls observed for an admissible point-in-time DGP=0.41 and 5 possible states

$ASI_{50,50,morning}$  is improved from 855lux (Figure 49) to 911 lux, for a same annual DGP!

## 4 Conclusion of Chapter I

Appropriate optical material properties were investigated first, to take advantage of GFRP translucency while ensuring an adequate performance of the open and closed states of the blinds, based on the medium recommendation level from standard EN17037:2019 [22] regarding daylight provision (DP) and achieving a "good effect" regarding glare protection according to prEN14501:2019 [23] (glare control class 3). It required to limit the visual transmittance to 15% and to avoid any direct transmittance. Results using a material with 15% transmittance showed that the closed state (0-0) sufficiently prevents from discomfort glare ( $DGP_{e<5\%}=0.35$ , i.e. below the medium recommendation level of 0.40), while GFRP remains luminous compared to classical opaque elements. The influence of the reflectance was investigated for the daylight provision in the open state (90-90): a change in reflectance value from 35% to 65% resulted in a change of the DF from 4.1% to 4.5%. Given this low sensitivity a reflectance value of 50% was selected. Following these findings, a material with 15% transmittance and 50% reflectance was applied to the shading system elements for the calculation of the annual daylight performance of each state in an annual basis. Regarding the rotation direction of the twisted states, it must be chosen so as the user (who needs to be protected against glare) faces the transmitting face of the blinds rather than the reflecting one. A set of 5 representative states was selected, from open to closed positions with 3 intermediates twisted states covering the spread of Daylight Glare Probability and Daylight Provision metrics in between the 2 extreme states. It appeared that playing on the curvatures of twisted elements influences the light penetration, for identical protection. Those complex mutual dependencies could be a whole topic to study, possibly complexified by additional parameters such as the view access, etc. In this work, state choices in annual actuation schedules of the shading system were performed through a dedicated optimization function. It included three simultaneous conditions to satisfy at each time step, i.e. maximizing  $SI_{50\%}$  under the constraint to avoid direct sun penetration and to limit the point-in time DGP to a maximum "cutoff" value. This cutoff was varied according to the targeted usage of the space.

This work showed that with this new adaptive facade a balance between glare protection and daylight provision could be achieved. The range of states of the shading allows to adjust to users' needs without systematically closing the blinds, where automatic closing was shown to be poorly accepted by the occupants [26]. Using GFRP materials leads to more (diffuse) light penetration in the closed or partially closed states compared to opaque material, intrinsically reducing the overall electrical lighting. However, energy savings for the lighting have to be seen in relation to the thermal effects of the facade, i.e. solar heat gains in summer and, to a lesser extent, in relation to the electrical consumption of the facade's actuators. This topic is developed in Chapter III. The kinetic system also adapts to different types of usage, showing its potential for social functions of the space, which can allow less severe quantitative requirements regarding glare prevention. Following the findings in [15], the twisted states were considered to generally increase the pleasantness and visual interest of the space. Further studies should address occupants' responses to variations in these twisted blinds.

The potential of the kinetic system has been demonstrated for average weather data and characteristic twisted states. Going back to the control pyramid presented in Fig. 18, the Schedule function would be operational with real-time data collected by sensors instead of average climatic data. About the intermediate states, a mix of flat-rotated-only configurations would be expected to perform great as well, as traditional vertical blinds do. A schedule mixing flat and twisted states is also conceivable.

The user control is not limited to the blinds opening or closing. It is worth developing a smart interface, where the user might say "now I would prefer more interesting patterns" (even if it technically sacrifices some visual comfort), or "now I would prefer to maximize my visual comfort". Going even further, the user would input an atmosphere parameter like "focus", "cosy", "cool",... and the system would adapt its decision function accordingly. The association of perceptual impressions to some changes in daylight metrics is a first step towards the integration of the qualitative performance in smart facade controllers. This was typically done with the tolerable point-in-time  $DGP_{e<5\%}$  limit, varying it to model either working or social atmospheres. However, regarding perceptual components, the prediction of the desired state is a complex and highly user-dependent issue. As highlighted in [10], "AF must go through a soft-landing process [...] to customize and adapt the AF technology to users' needs and expectations." User-specific data are needed to perform the customization. Data are collected by showing the users several possibilities and asking about their preferences. This could be done either at the commissioning of the adaptive facade during R&D processes or by means of immersion in virtual reality scenes, on a similar approach than the one conducted by Chamilothoni & al. [29]. Given all the possible intermediate twisted states and the variability of user-specific data, it becomes impossible to "handwrite" straightforward conditions for the blinds' actuation. The use of self-learning multi-objective algorithms as decision functions could help a lot [30]. Multi-objective algorithms use Pareto's optimization, i.e. they select a front of optimal under the simultaneous constraint of several objective functions. Especially evolutionary genetic algorithms (e.g. NSGA-II) produce a population of solutions, submit them to the previously explained Pareto's optimization and perform genetic mutations of the population according to the results, repeating the process from one generation to the next until no better solution is found.

# CHAPTER II

## STRUCTURAL DESIGN

Glass fiber reinforced polymers (GFRP) are made of layers of fiberglass fabric cast into resin. They were preselected for their resistance to environmental attacks, e.g., rain and UV-radiation, along with the customization of their structural performance through the choice of fibers' types and orientations. In addition, they may also exhibit some translucency.

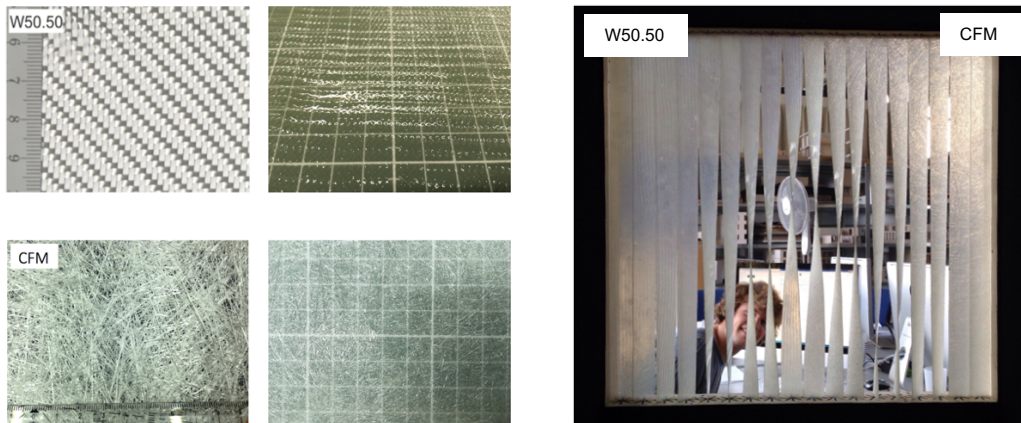


Figure 56 - Reinforcement fibers (left) ; Reinforcement fibers just impregnated with resin (center) ; Resulting laminates after the cure, here cut into strips for the mockup purpose (right)

In its base-state, the adaptive GFRP module has a rectangular shape similar to traditional Californian blinds. Our goal is to twist it so that we can achieve multiple configurations, allowing more or less light to enter the building while creating surprising facade patterns. In this section we detail the structural design process of the facade modules.

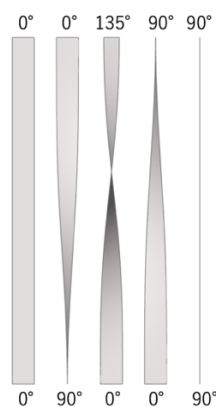


Figure 57 - Reminder: the different blinds' states investigated

Investigations of the structural behavior are firstly conducted for a torsional angle from 0 to 180° , the latter being the upper boundary of the twist technically achievable (cf. the overlap issue developed in Chapter I section 2.1.4 'Practical considerations'). Structural feasibility analysis uses plate's theory and calculations implemented by hand for a pre-design, complemented afterward by

a Finite Element Modeling analysis, highlighting phenomena specific to the entire system, i.e. to the combination of specific material, loads and support conditions. Lastly, laboratory testing processes are developed to validate the characterization of the system's torsional behavior, including broader range than  $180^\circ$  .

# 1 Requirements specification

This section specifies the requirements for the design of the facade modules.

## 1.1 Geometry

- Module height:  $H_{ref} = 2.5 \text{ m}$ .
- The width is indicatively set to  $b = 15 \text{ cm}$  for architectural purposes. We will see later that the calculations are independent of it, except for the torsional load that will be applied with the mechanical actuators.
- We want the elements to be very thin so that they won't obstruct the view when the system is fully open ( $90-90^\circ$  ). The structural design will target the minimum thickness necessary to meet the requirements defined right after.

## 1.2 Behavior

We design a non-structural facade, meaning that it is not part of the building load-bearing system. Nevertheless we have to control the structural behavior in terms of stresses and strains:

- Efforts:  
On one hand the element needs to resist along its length the bending moment due, mainly, to the wind pressure.  
On the other hand we want to lower as much as possible the torsional moment needed to achieve a  $180^\circ$  angle of twist. So we do not want the element to resist torsion (and torsional shear strain), but we have to ensure it does support related shear stresses so that no shear failure happens.
- Deflections:  
We will rely on the criterion from SIA 260 'Basis of Structural Design'. The SIA260:2013 norm [31] stipulates that the maximum admissible horizontal deflection regarding the 'Aspect' of the elements is  $H/250$  (Table 18). This corresponds to:

$$w_{\max} = H/250 = 2500/250 = \mathbf{10 \text{ mm}}$$

'Aptitude au fonctionnement' criterion in Table 18 is left aside as the facade is not part of the building load-bearing system.

État-limite	Conséquences des effets des actions		
	irréversibles	réversibles	réversibles
	Cas de charge		
	rare (20)	fréquent (21)	quasi permanent (22)
Aptitude au fonctionnement – Éléments incorporés à caractère fragile – Éléments incorporés à caractère ductile – Utilisation et exploitation	$u \leq h/500$ <sup>1) 2)</sup>	$u \leq h/200$ <sup>1)</sup> $u \leq H/300$	
Aspect			$u \leq h/250$ <sup>1)</sup>
<sup>1)</sup> Déplacement horizontal dû aux actions variables. <sup>2)</sup> Si des éléments incorporés réagissent de manière particulièrement sensible aux déformations de la structure porteuse, il faut prévoir avant tout la prise de mesures constructives contre les dommages, en plus ou à la place des mesures découlant de la procédure de dimensionnement.			
Les déplacements horizontaux sont déterminés selon les normes SIA 262 à 266.  Des valeurs limites différentes pour les déplacements horizontaux peuvent être convenues en accord avec les exigences d'utilisation. Elles doivent être inscrites dans la base du projet. En particulier pour les ponts roulants, des exigences plus élevées peuvent être envisagées.			

Table 18 - Standard values for horizontal displacements of walls, frames and columns (Table 4 SIA 260)

### 1.3 Loads

The external loads acting on such facade are:

- Applied torsion

Our objective is to reach a maximum 180° rotation over the length of the element. Considering an actuation system able to fully introduce torsional moment at the ends, the sollicitation  $T$  [N.m] is constant over the element and so the curvature  $\chi$  [ $m^{-1}$ ]:

$$T = G * J * \chi$$

with  $GJ$  [ $N.mm^2$ ] the torsional stiffness, depending on the element geometry and layers properties. Then  $\chi$  is the total rotation  $\theta$  [rad] divided by the length of the element  $L$  [m]:

$$\chi = \frac{\theta}{L}$$

- Wind loads

As we design facade elements, they are subjected to the effects of the wind and transmit them to the loadbearing structure. We model them as a static equivalent wind pressure, according to the SIA261:2014 norm [32]:

Dynamic pressure (SIA 261 6.2.1.1):

$$q_p = c_h q_{p0}$$

with  $q_{p0} = 0.9 \text{ kN/m}^2$  (SIA 261 Appendix E)

Coefficient accounting for the repartition profile of the wind:  $c_h = 1.6 \left[ \left( \frac{z}{z_g} \right)^{\alpha_r} + 0.375 \right]^2$

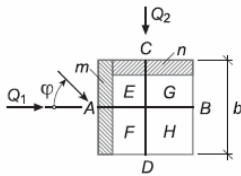
Lausanne can be considered as a Cat. IV location and the building height is  $z = 15$  m from the ground.

Catégorie de terrain	Exemples	$z_g$ [m]	$\alpha_r$
II	rive lacustre	300	0,16
IIa	grande plaine	380	0,19
III	localité, milieu rural	450	0,23
IV	zone urbaine étendue	526	0,30

Table 19 - Gradient height  $z_g$  and terrain roughness exponent  $\alpha_r$  (Table 4 SIA 261)

So we have  $c_{r1} = 0.83$  [-], and  $q_p = 0.75$  kN/m<sup>2</sup>.

Characteristic wind load:  $q_k = c_{pe}q_p$



$\varphi$	Coefficients de pression																Coefficients de force		
	$c_{pe}$								$c_{pe}$			$c_{pi}$					$c_{f1}$	$c_{f2}$	$c_{f3}$
	Surface d'application								Surface localisée			Ouvertures prépondérantes sur les côtés					Surface de référence		
	A	B	C	D	E	F	G	H	m	n	o	rép.	A	B	C	D	$b \cdot h$	$d \cdot h$	$d \cdot b$
0°	0,7	-0,25	-0,35	-0,35	-0,5	-0,5	-0,25	-0,25	-0,85	-0,45	-0,8	0,15/ 0,21	0,7	-0,25	-0,35	-0,35	0,95	0	-0,38
15°	0,55	-0,25	-0,2	-0,35	-0,5	-0,55	-0,25	-0,3	-0,85	-0,45	-1,0	$\pm 0,15$	0,55	-0,25	-0,2	-0,35	0,8	0,15	-0,4
45°	0,4	-0,4	0,4	-0,4	-0,45	-0,45	-0,45	-0,25	-0,85	-0,85	-0,45	$\pm 0,1$	0,4	-0,4	0,4	-0,4	0,8	0,8	-0,4
90°	-0,35	-0,35	0,7	-0,25	-0,5	-0,25	-0,5	-0,25	-0,45	-0,85	0,45	$\pm 0,15$	-0,35	-0,35	0,7	-0,25	0	0,95	-0,38
$\hat{c}_{pe} = -2,0$																$c_{fr} = 0$			

Table 20 - Factors for  $h : b : d = 0.3 : 1 : 1$  to  $0.05 : 1 : 1$ , flat roof (SIA 261 Table 31)

The closer shape of building proposed by the norm is a flat building with  $h : b : d = 0.3 : 1 : 1$  to  $0.5 : 1 : 1$  with a flat roof. The worst combination would happen for a wind with  $\phi = 0^\circ$  (Table 20).

Both pressure and respectively suction are applied on every element on their outer, and respectively inner, side. Here we can reasonably suppose that the suction affects only the loadbearing structure of the building. Hence the coefficient of pressure is calculated such that:

$$c_{pe} = c_{pe,A,pressure}$$

$$c_{pe} = 0,7 \text{ [-]}$$

Finally, the applied wind load is:

$$q_k = c_{pe}q_p = 0.7 \cdot 0.75 = 0.525 \text{ [kN/m}^2\text{]}$$

Assumption: the elements are designed to resist to the characteristic value of the load, even if it should be multiplied by a load factor of 1.5 to obtain design value according to SIA 260. We do so because our modules are not part of the load-bearing system so we accept a less severe requirement. A detailed dynamic study of the element would be required to check for the undesired vibrations that could damage the elements and reduce the comfort of the users of the building. It calls for fluid mechanics airflow and turbulence modeling.

The wind can act on any twisted configuration between [0-180° ].

We model 3 relevant ones for the pre-design: 0-0° , 0-90° and 0-180° , as follows:

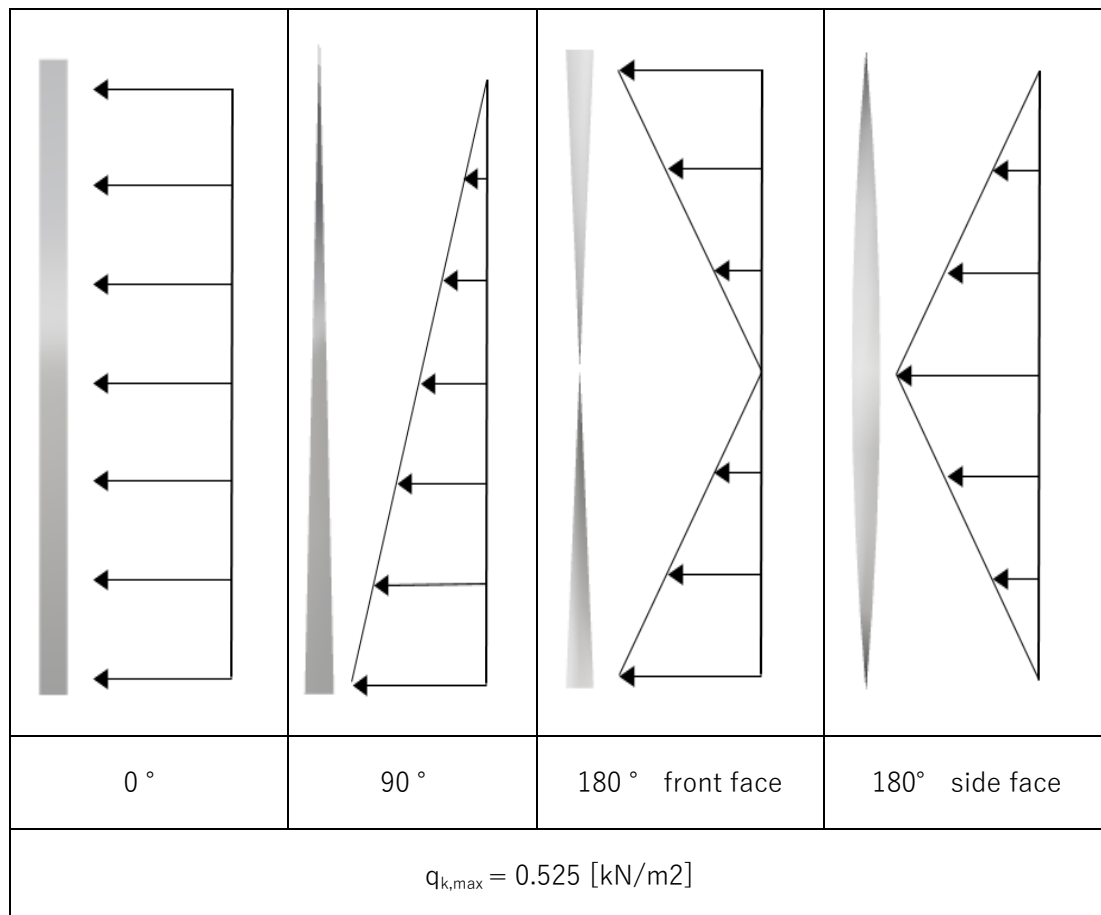


Figure 58 - Wind loadcases

- The ruin of the elements in case of a fire is admitted as they are not part of the loadbearing structure.
- Accidental load case such as a bird's impact is neglected.

## 1.4 Lifespan and durability

These facade elements must satisfy complementary sustainability requirements:

- As the GFRP material is an electrical insulator, preventive action must be taken to avoid the ruin of the elements in case of a storm. Also, if fire load case is structurally neglected, potential ignition and flame propagation along with toxic smokes must remain below

standardized limits (e.g. NFPA 285 ‘Standard Fire Test Method for Evaluation of Fire Propagation Characteristics of Exterior Wall Assemblies Containing Combustible Components’).

- The temperature variations in Switzerland are high, so icy cycles may happen. Thus, a hydrophobic matrix is desired to ensure the durability of the elements. Otherwise, formation of ice into the material could damage the internal structure of the elements. In Lausanne, the minimal average temperature is about  $-3.2^{\circ}\text{C}$  in January and the maximal average temperature is about  $24.5^{\circ}\text{C}$  in July. So we have  $\Delta T \approx 30\text{ [K]}$ . Thermal influence on the mechanical properties must be taken into consideration.
- Actuators monitor the environmental conditions and control the opening of the modules. The facade can also change state when users ask for it. By correlating the daylight conditions to the working hours and the more social uses of the SG Foyer, we roughly estimate that the system would achieve (in average) 4 closure-opening torsion cycles per day. A long-term behavior study would be relevant regarding those cycles along the lifespan.

Part of the requirements defined there are fulfilled by the choice of appropriate matrix and fiber types. Fiberglass reinforcement material is chosen for this use. Carbon fibers are far more resistant but are also 5 to 10 times more expensive than glass fibers. The study [33], partly recalled in section 2.4, proved that it was not justified to use it. Aramid fibers are in-between glass and carbon in terms of cost and strength, but they can deteriorate when subjected to UV radiation. We use epoxy resin as it is able to deform more than the glass fibers whereas polyester cannot. Epoxy also exhibits better adhesive properties and is less damaged by water.

The remaining requirements need to be transposed into quantitative properties we can play on like the type of reinforcement (roving, woven fabric, mat ...) and its elastic properties ( $E$ ,  $G$ , ...) as well as other relevant properties like cost, weight, environmental impact, ...

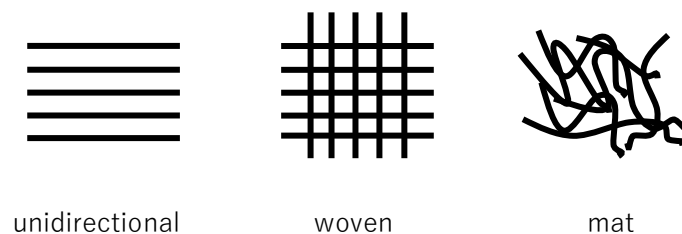


Figure 59 - Schematic representation of the different fabric types

We will now provide a deeper analysis of the structural behavior.

## 2 Pre-design

FRP laminates are made of a sequence of layers of fiber fabric into resin, called laminae, stacked together. A lamina thus corresponds to one layer of {fibers+resin}. We used the Classical Lamination Theory (CLT) to perform a first structural analysis, i.e. to calculate strains and stresses, layer-by-layer when loads are applied on the elements. A Matlab code combined with an Excel material database were developed to automate the calculations, allowing to explore the possibilities offered by composites in this facade element design. A linked Excel sheet contains a material database with stiffness and strength properties. In the Matlab interface, the user must provide

informations about the chosen material, the geometry of the element, the stacking sequence (number of layers and orientation) and the twisting angle. Then the code performs all the verifications.

## 2.1 Theoretical background: 2D calculations of laminated plate elements

### [Implementation of the CLT in a Matlab code as a base tool to calculate strains and stresses for any configuration and layer properties]

The CLT is valid under the following assumptions:

- Each lamina is orthotropic (see Fig. 62).
- Each lamina is homogeneous.
- Plane sections remain plane during deformation  $\rightarrow \gamma_{xz} = \gamma_{yz} = 0$ .
- The laminate is thin and loaded only in its plane (plane stress state)  $\rightarrow \sigma_z = \tau_{xz} = \tau_{zy} = 0$ .
- Displacements are continuous and small.
- Each lamina is elastic.
- There is no delamination between successive laminae.

Provided the material properties of each lamina, their orientation and their thickness, the CLT allows us to build the stiffness matrix  $K = \begin{bmatrix} A & B \\ B & D \end{bmatrix}$  of any FRP laminate, to explicit the constitutive law ruling its mechanical behavior. Material properties needed for each lamina are the following:

$E_{11}$ : tensile modulus in the fibers' (principal) direction

$E_{22}$ : tensile modulus in the transverse direction

$G_{12}$ : shear modulus

$\nu_{12}$ : major Poisson ratio

$\sigma_{11,max,t}$  = X: tensile strength in the fibers' (principal) direction

$\sigma_{11,max,c}$  = X': compressive strength in the fibers' (principal) direction

$\sigma_{22,max,t}$  = Y: tensile strength in the transverse direction

$\sigma_{22,max,c}$  = Y': compressive strength in the transverse direction

$\tau_{12,max}$  = S: shear strength

And the constitutive law of the FRP laminate is written 'summing' the contributions of all laminae:

$$\begin{Bmatrix} n_x \\ n_y \\ n_s \\ m_x \\ m_y \\ m_s \end{Bmatrix} = \begin{bmatrix} A_{xx} & A_{xy} & A_{xs} & B_{xx} & B_{xy} & B_{xs} \\ A_{xy} & A_{yy} & A_{ys} & B_{xy} & B_{yy} & B_{ys} \\ A_{xs} & A_{ys} & A_{ss} & B_{xs} & B_{ys} & B_{ss} \\ B_{xx} & B_{xy} & B_{xs} & D_{xx} & D_{xy} & D_{xs} \\ B_{xy} & B_{yy} & B_{ys} & D_{xy} & D_{yy} & D_{ys} \\ B_{xs} & B_{ys} & B_{ss} & D_{xs} & D_{ys} & D_{ss} \end{bmatrix} \begin{Bmatrix} \varepsilon_x^0 \\ \varepsilon_y^0 \\ \varepsilon_s^0 \\ k_x \\ k_y \\ k_s \end{Bmatrix}$$

$$A_{ij} = \sum_{k=1}^n \bar{Q}_{ij}^{(k)} (z_k - z_{k-1})$$

$$B_{ij} = \frac{1}{2} \sum_{k=1}^n \bar{Q}_{ij}^{(k)} (z_k^2 - z_{k-1}^2)$$

$$D_{ij} = \frac{1}{3} \sum_{k=1}^n \bar{Q}_{ij}^{(k)} (z_k^3 - z_{k-1}^3), \quad i,j = x,y,s.$$

[A] is the extensional stiffness matrix

[B] is the coupling stiffness matrix

[D] is the flexural stiffness matrix

The left hand side is the vector of external loads applied on the element. Note that they are forces by unit of width:  $n$ [N/m'] and  $m$ [N.m/m']. That's why section 1.1 ('Geometry') says that calculations are independent of the width  $b$ . They are written in small letters to be differentiated from total forces written in capital letters (e.g.  $M_x = m_x * b$ ).

In our case only  $M_x$  (wind) and  $M_s$  (torsion) are schematically acting as follows:

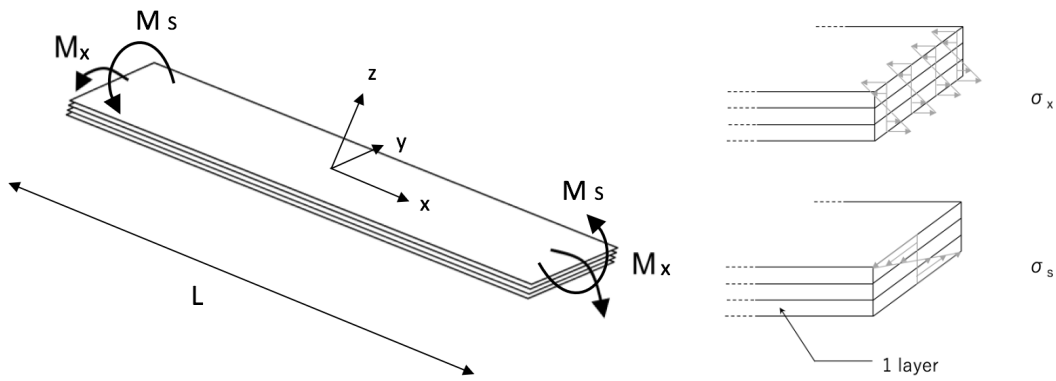


Figure 60 – External forces acting on the laminate and schematic representation of the stresses generated in a section cut

The  $z_k$  [m] are the plies top surface and bottom surface coordinates, starting with the first layer put on the lamination table. Be careful that  $z=0$  is the middle of the laminate (mid-plane).

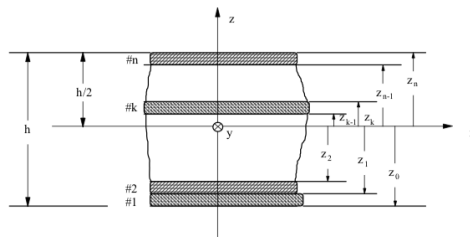


Figure 61 - Coordinates of the plies

The  $\overline{Q}_{ij}$  are the  $i,j$  coefficients of the transformed reduced stiffness matrix of each ply  $k$ . They are calculated starting with the reduced compliance matrix  $[S]_{local}$  of a ply in its principal axis (local axis):

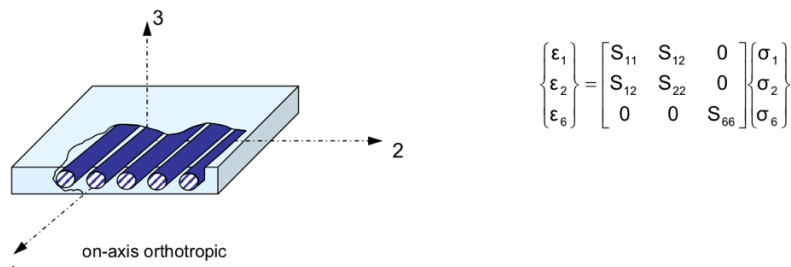


Figure 62 - Orthotropy of the matrix  $[S]_{local}$

$$\begin{aligned} S_{11} &= 1/E_1 \\ S_{22} &= 1/E_2 \\ S_{12} &= -\nu_{12}/E_2 \\ S_{66} &= 1/G_{12} \end{aligned}$$

This compliance matrix is then transformed in the axis of the laminate (global axis):

$$[S]_{global} = [T]' * [S]_{local} * [T]$$

with  $[T]$  written below and  $\theta$  the angle between the ply principal axis (fibers direction) and the laminate main axis.

$$[T] = \begin{bmatrix} m^2 & n^2 & 2mn \\ n^2 & m^2 & -2mn \\ -mn & mn & m^2 - n^2 \end{bmatrix} \quad \begin{aligned} m &= \cos(\theta) \\ n &= \sin(\theta) \end{aligned}$$

Then the  $[Q]_{global}$  matrix is the reversed  $[S]_{global}$  matrix.

The right hand side of the constitutive law is the vector of mid-plane strains and curvatures. Knowing them we can calculate global strains in each ply:

$$\begin{Bmatrix} \varepsilon_x \\ \varepsilon_y \\ \varepsilon_s \end{Bmatrix} = \begin{Bmatrix} \varepsilon_x^0 \\ \varepsilon_y^0 \\ \varepsilon_s^0 \end{Bmatrix} + z \begin{Bmatrix} k_x \\ k_y \\ k_s \end{Bmatrix}$$

And global stresses for each ply, using the transformed reduced stiffness matrix of the desired ply:

$$\begin{Bmatrix} \sigma_x \\ \sigma_y \\ \sigma_s \end{Bmatrix} = \begin{bmatrix} \bar{Q}_{xx} & \bar{Q}_{xy} & \bar{Q}_{xs} \\ \bar{Q}_{xy} & \bar{Q}_{yy} & \bar{Q}_{ys} \\ \bar{Q}_{xs} & \bar{Q}_{ys} & \bar{Q}_{ss} \end{bmatrix} \begin{Bmatrix} \varepsilon_x \\ \varepsilon_y \\ \varepsilon_s \end{Bmatrix}$$

Finally we need the local stresses for each ply, meaning the stresses along the principal directions of each ply:

$$\begin{Bmatrix} \sigma_1 \\ \sigma_2 \\ \sigma_6 \end{Bmatrix} = [T] \begin{Bmatrix} \sigma_x \\ \sigma_y \\ \sigma_s \end{Bmatrix}$$

We will compare those local stresses to the failure strength values, see the failure criterion explanation in following section 2.3 ('Steps in the static checks').

## 2.2 Modeling of external loads and support conditions

### [Incremental calculation of the torsional moment to apply to reach the desired deformation (angle of rotation of 180° )]

From section 1.3 ('Loads') we have  $T = G * J * \chi$ . G and J being constant for a given rectangular laminate, the torsional moment  $T$  is a linear function of the torsional curvature  $\chi$ . However this

relation stands for uniaxial torsion and has to be adapted in order to use the CLT, as this theory stands for infinite plates and studies a ‘small’ piece of those plates.

In the CLT, the torsional curvature  $k_s$  is the out-of-plane displacement of a ‘small’ (infinitesimal) piece of plate, hence it is the double of the torsional angle derivative:  $k_s = 2 \frac{d\theta}{dx}$  and for our case where  $\frac{d\theta}{dx}$  is constant,  $k_s = 2\chi$ .

In the CLT, the torsional moment  $m_s$  (or  $m_{xy}$  in the coordinates system from Figure 63) is distributed on the four edges of a ‘small’ plate piece and calculated by unit of width. Unidirectional torsion is the same that redistributing it on two edges only, the two other ones being free edges. We have  $T = 2 * m_s * b$ , with  $b$  [m] the width of the element.

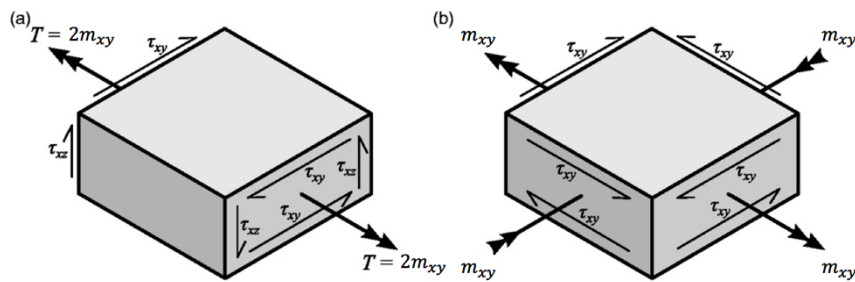


Figure 63 – Schematic representation of the shear stresses for (a) the case of uniaxial torsion (b) torsional moments in the CLT. Adapted from [34]

We need to determine the torsion that will act on our element (its plate equivalent) for the different rotated load cases defined in Fig. 58. It depends on the constitutive law of the laminate, i.e. its stiffness matrix. Starting from no torsion at all, we increase the moment  $m_s$  step by step in the force vector and calculate the strain  $k_s$  at each step by inverting the  $[K]$  matrix, until we reach a total angle of rotation of  $\theta = 180^\circ$  ( $\pi$  rad), which corresponds to  $k_s = 2 * \frac{\pi}{L}$  [rad.m<sup>-1</sup>] where L is the height of the module. Note that the effective support reaction is the torsional moment  $T = 2 * m_s * b$ .

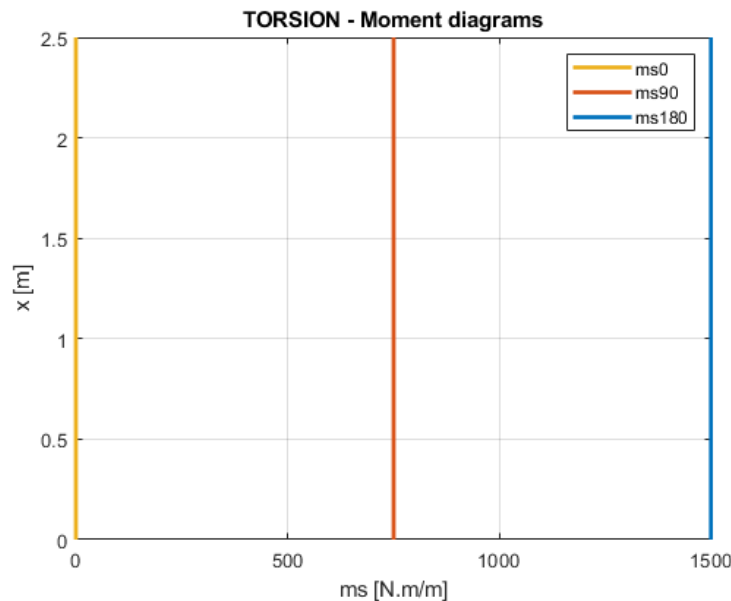


Figure 64 – Evolution of torsional moment ms along the x position on the element for 0° , 90° & 180° states (e.g. here with 24 unidirectional layers of material 2 from Table 21)

### [Calculation of the bending moments resulting from the wind pressure]

The effect of the wind has to be modeled according to the bending moment it creates. We cannot apply directly the pressure load because it acts out of plane and falls outside of the CLT framework.

Our facade module is represented as a simply supported beam. We have the following equations for the bending moments:

$$0^\circ : m_x = q * \frac{L*x-x^2}{2}$$

$$90^\circ : m_x = q * \frac{L*x-x^3/L}{6}$$

$$180^\circ \text{ face: } m_x = q * \frac{L*x-2x^2+4x^3/L}{4} \text{ for } x \in [0;L/2], \text{ symmetric for } x \in [L/2;L]$$

$$180^\circ \text{ side: } m_x = q * \frac{3L*x-4x^3/L}{12} \text{ for } x \in [0;L/2], \text{ symmetric for } x \in [L/2;L]$$

Those moments are independent of the laminate's constitutive law.

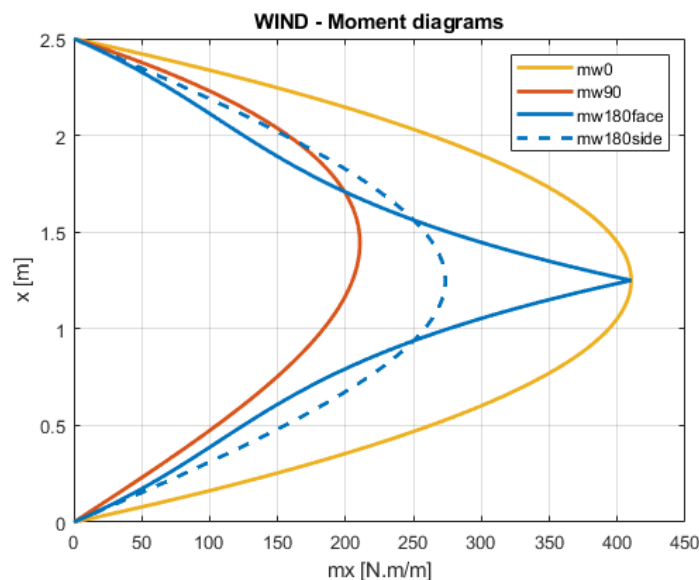


Figure 65 – Evolution of bending moment  $m_x$  due to the wind along the  $x$  position on the element, for  $0^\circ$ ,  $90^\circ$  &  $180^\circ$  states (simply supported static system)

## 2.3 Steps in the static checks

### [Superposition of the wind load case and the torsional load case to plot the results in failure criterion and check that we do not exceed strength limits]

The FRP material is modeled as linear elastic until failure, allowing to 'sum' the effects of different load types calculated separately. Stresses and strains resulting from the superposition of flexural and torsional actions are calculated in many cuts along the element length. For the failure criterion we need to plot the stresses in the most critical section, which is at mid-span.

We use the Tsai-Wu failure criterion to predict the failure. As a quadratic failure criterion it takes into account the interaction between the different stress components. Failure occurs when the criterion reaches 1, i.e. the following expression is null:

$$F_{11}\sigma_1^2 + F_{22}\sigma_2^2 + F_{33}\sigma_3^2 + F_{44}\sigma_4^2 + F_{55}\sigma_5^2 + F_{66}\sigma_6^2 + 2(F_{12}\sigma_1\sigma_2 + F_{13}\sigma_1\sigma_3 + F_{23}\sigma_2\sigma_3) + F_1\sigma_1 + F_2\sigma_2 + F_3\sigma_3 - 1 = 0$$

Under plane stress state, it simplifies to the following expression:

$$F_{11}\sigma_1^2 + F_{22}\sigma_2^2 + F_{66}\sigma_6^2 + 2F_{12}\sigma_1\sigma_2 + F_1\sigma_1 + F_2\sigma_2 - 1 = 0$$

The failure components  $F_1, F_2, F_{11}, F_{22}, F_{66}$  are expressed as functions of the failure strengths  $X, X', Y, Y' & S$ :

$$F_1 = \frac{1}{X} - \frac{1}{X'} ; F_2 = \frac{1}{Y} - \frac{1}{Y'} ; F_{11} = \frac{1}{XX'} ; F_{22} = \frac{1}{YY'} ; F_{66} = \frac{1}{S^2}$$

$F_{12}$  is calculated according to Tsai-Hahn's theory:  $F_{ij} = -\frac{1}{2}\sqrt{F_{ii}F_{jj}}$

The failure criterion can be represented as a 3D surface. If the points corresponding to the stresses across the laminate are inside this surface, it is safe. If they reach it, we have a failure.

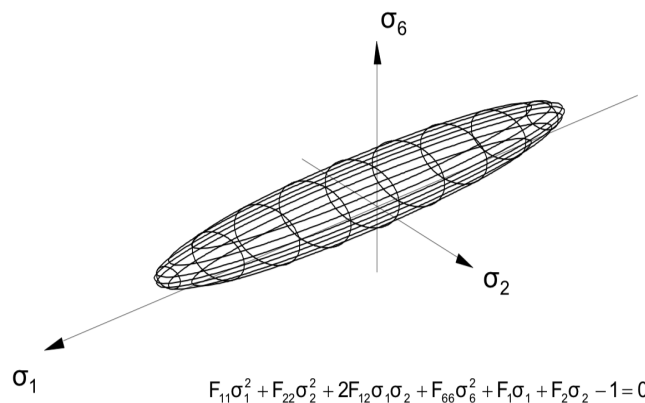


Figure 66 - 3D representation of the failure criterion for plane stress-state

**[Ensure that the deformations are acceptable (lower than the limit deflection)]**

The bending curvature is the second derivative of the deflection:  $k_x = -\frac{d^2w}{dx^2}$

For isotropic beams, we have the following kinematic relation:  $\frac{d^2w}{dx^2} = -\frac{M_x}{EI}$  and the calculation of the deflection results from the double integration of the moment. For example for a simply-supported beam under uniform load  $q$ ,  $w_{max} = \frac{5qL^4}{384EI}$ , and for a fixed-fixed beam  $w_{max} = \frac{qL^4}{384EI}$ .

In a laminate, this is not valid anymore. For simple stacking sequences, it is possible to derive a relation between the effective elastic modulus of the element  $E_x$  and the elastic modulus of one ply  $E_1$  in order to use the equations of isotropic beams.

But in a broader general case, we need to go back to the relation  $k_x = -\frac{d^2w}{dx^2}$  and integrate twice the expression of the curvature along the length of the module to obtain the deflection.

$$w_x(x) = \iint_0^x k_x dx^2$$

Note that if couplings\* occur,  $k_x$  could be influenced by the torsional moment  $m_\zeta$  and not only be a function of  $x$ .

\* The coupling issue in the laminates is explained in details in [33]. For this special case study we will see that we only use orthotropic material along one of its principal axis (only layers of fabric at  $0^\circ$  respectively to the fibers' main orientation). It is a sufficient condition to avoid couplings.

**[Check that the ranges of extensional and shear strains reached by the plies stay in the elastic domain, below the region where microcracks are expected to form]**

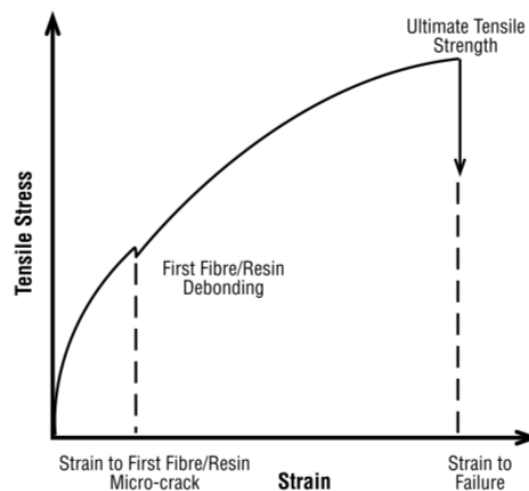


Figure 67 - Typical FRP stress-strain graph, from [18]

In a first approach we will rely on the following conservative elastic strain limits:

$$\varepsilon_{x,e|} = 2\% \text{ for tension and compression along the } x \text{ axis}$$

$$\varepsilon_{s,e|} = 1.5\% \text{ for shear}$$

These are based on tension tests performed during the Advanced Composites in Engineering Structures course and shear tests described by Kashaba in [35].

**[Finally iterate on the stacking sequence so that the last three points of the static checks section are all satisfied]**

## 2.4 Choice of fiberglass fabric type

Many types of glass fabrics are commercially available. Three different ones (see Fig. 68) are investigated to identify the best suited for the studied application.

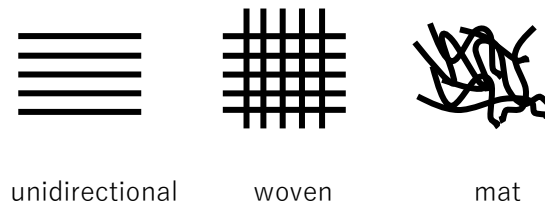


Figure 68 - Reminder: Schematic representation of the different fabric types

The analysis required to know material stiffness and strength properties of a lamina (fibers+resin). Compared to traditional materials like steel or wood, for which resellers provide tables of guaranteed properties, composites' properties are highly dependent on the fabrication process and precision (e.g. excess resin or slight misalignment of fibers have great influence on the properties). The following material properties database was constructed based on typical ranges found in specialized technical literature. It includes cost, ply thickness and mechanical properties.

Index	Material Name	Material	Cost [CHF/m <sup>2</sup> ]	Ply thickness [mm]	E11 [GPa]	E22 [GPa]	G12 [GPa]	v12 [GPa]	X [Mpa]	X' [Mpa]	Y [Mpa]	Y' [Mpa]	S [Mpa]
1	(UD) T300/5208	Gr/Ep	50	0.125	181	10.3	7.17	0.28	1500	1500	40	246	68
2	(UD) Scotchply 1002	Gl/Ep	8	0.5	38.6	8.27	4.14	0.26	1062	610	31	118	72
3	W50.50	Gl/Ep	10	0.5	19.55	19.55	2.85	0.19	440	425	440	425	40
4	CFM	Gl/Ep	4	0.5	9.34	9.34	3.51	0.33	30	30	30	30	15

Table 21 - List of materials investigated in the pre-design

Material 1: unidirectional fabric of carbon\* fibers, reinforcement weight  $\sim 300 \left[ \frac{g}{m^2 \cdot layer} \right]$ , 6K

\* This material is tested to illustrate the irrelevance of using carbon fibers in this facade application.

Sources:

- Elastic constants: Advanced Composite Course, Lecture 4
- Failure stresses: Advanced Composite Course, Lecture 6
- Price: Castro Composites catalog: <https://www.castrocompositesshop.com>

Material 2: unidirectional fabric of glass fibers, reinforcement weight  $\sim 425 \left[ \frac{g}{m^2 \cdot layer} \right]$

Sources:

- Elastic constants: Advanced Composite Course, Lecture 4
- Failure stresses: Advanced Composite Course, Lecture 6
- Price: Castro Composites catalog: <https://www.castrocompositesshop.com>

Material 3: woven fabric of glass fibers, reinforcement weight  $\sim 600 \left[ \frac{g}{m^2 \cdot layer} \right]$

Sources:

- Elastic constants: Aida Cameselle-Molares, Anastasios P. Vassilopoulos, Thomas Keller. *Experimental investigation of two-dimensional delamination in GFRP laminates*. Engineering Fracture Mechanics, Volume 203, 2018, Pages 152-171.
- Failure stresses: Mechanical Properties of Carbon Fibre Composite Materials, Fibre / Epoxy resin (120° C Cure), Performance COMPOSITES Ltd: [http://www.performance-composites.com/carbonfibre/mechanicalproperties\\_2.asp](http://www.performance-composites.com/carbonfibre/mechanicalproperties_2.asp)
- Price: Castro Composites catalog: <https://www.castrocompositesshop.com>

Material 4: chopped strand mat of glass fibers, reinforcement weight  $\sim 600 \left[ \frac{g}{m^2 \cdot layer} \right]$

Sources:

- Elastic constants: Aida Cameselle-Molares, Anastasios P. Vassilopoulos, Thomas Keller. *Experimental investigation of two-dimensional delamination in GFRP laminates*. Engineering Fracture Mechanics, Volume 203, 2018, Pages 152-171.
- Failure stresses: CCLab experience
- Price: Swiss-Composites catalog

Ply thickness:

- Glass/Epoxy plies have a thickness around 0.5 mm
- Graphite/Epoxy plies are around 0.125 mm

This study follows a semester project [33] realized as a pre-investigation in the context of the Advanced Composites in Engineering Structures course. The aim was to identify the main structural design parameters that ruled rectangular FRPs subjected to bending and torsion, and their influence when varied. A broad parametrical analysis was developed, in which the length of the modules was a variable along with the reinforcement material and the stacking sequence of the plies. Three parameters can be critical for the design: the deflection, the shear stresses and the shear strains. For elements smaller than 0.5m, the shear stress and strain are decisive while the deflection remains rather small. The solution is to turn the outer layers at  $\pm 45^\circ$  so that they carry the shear in tension/compression. For higher lengths, the three critical parameters show up simultaneously ; adding  $\pm 45^\circ$  layers to solve shear issues conflicts with the other design requirements, as it makes the element harder to twist and creates a loss of bending stiffness. A hierarchy is needed among the different requirements. Elements longer than 3m are out of the range of this study, stability issues would prevail and stand for the introduction of intermediate supports.

In the context of this thesis, the kinetic facade elements must cover  $H_{ref} = 2.5 \text{ m}$  and the deflection criterion is prioritized. An element needs to both resist along its length the bending moment due to the wind pressure and allow torsional shear to happen, while ensuring that shear failure is not reached. Laminates made of layers stacked with  $0^\circ$  orientation are prioritized for this application so that the maximum tensile modulus occurs along the X direction and the minimum shear modulus occurs along the transverse Y direction.

As mentioned we expected the deflection  $w$  to be decisive as the elements were quite long (think about the dependence on  $L^4$  for isotropic beams). For each fabric material in the database Table 21, we firstly investigated plies stacking sequence so as the deflection is lower than the limit value to identify the number of  $0^\circ$  layers required, and then derived the maximum rotation  $\theta_{max}$  that this sequence could undergo without reaching failure (admissibility of torsional shear stress and strain) in order to ensure an operative facade. We recall that the maximal deflection allowed by SIA260:2013 norm was  $w_{max} = \frac{Height}{250}$ . The width  $b$  was kept equal to 15 cm ;  $b$  was only involved to determine the necessary twisting moment to apply with the actuators at the end of the calculation process.

We started making the hypothesis that the elements were like simply-supported beams. It is highly conservative but allows to derive analytically the moments because the system is isostatic. However this model lead to a disproportionate number of plies to satisfy the deflection criterion. It is necessary to model the elements as they are: fixed-fixed beams, embedded at their ends into steel clamps from the actuation mechanism. To avoid calculation of hyperstatic moment under

complicated wind load cases, we made the following assumption: the deflection of the real system can be derived by dividing the deflection of the simply-supported system by a factor 5. This factor comes from the well known relations for isotropic beams under uniform load  $q$  (simply-supported  $w_{max} = \frac{5qL^4}{384EI}$ ; fixed-fixed  $w_{max} = \frac{qL^4}{384EI}$ ). For the  $0^\circ$  wind load case (critical for the deflection) and the  $0^\circ$  -only sequences (specially orthotropic laminate) that we have, this factor is exact. Then the maximum deflection allowed by the Matlab code is  $\frac{Height}{250} * 5$ .

We obtain the following layers combinations for fabrics in Table 21:

Material	1	2	3	4
Cost	50 CHF/m <sup>2</sup>	8 CHF/m <sup>2</sup>	10 CHF/m <sup>2</sup>	4 CHF/m <sup>2</sup>
Sequence	[0° (*57)]	[0° (*24)]	[0° (*30)]	-
Nb <sub>layer</sub>	57	24	30	-
Thickness	7.5 mm	12 mm	15 mm	-
$\theta_{max}$	130°	165°	130°	-
T <sub>180°</sub>	163.2 N.m	399.6 N.m	604.5 N.m	-

Table 22 - Results for the reinforcement materials in the database from Table 21

We didn't go further with the material 4 (CFM) because its E modulus and shear strength were too low to achieve solutions with acceptable thickness and rotation capacity. Unidirectional E-Glass (material 2) required a bit less layers in comparison with the woven E-Glass (material 3), as it showed higher stiffness along the X direction and so lower deflection. But a higher E modulus does not always mean less layers. We can notice that the carbon variation (material 1) required twice as many layers than the E-Glass products. This is due to the ply thickness of the carbon which is 3.5 times smaller than the ones made of E-Glass. Even if the Young modulus of carbon plies is 4 to 5 times higher than the one of glass plies, we needed some inertia to activate some tensile/compressive strength and limit the deflection under wind load. The materials were consequently not limited by their strength but by the total thickness of the element that is necessary to provide flexural stiffness (E\*I) and respect the criterion regarding the maximal deflection. Moreover, carbon fibers exhibited a high G modulus, limiting  $\theta_{max}$  to lower rotations than glass material, and had a cost 5 times higher than glass fibers. Among fiberglass, woven also limited the maximum rotation allowed as a thicker laminate was needed for the deflection compared to unidirectional fiberglass, moreover leading to an increase of 25% in the necessary amount of raw material and an increase of 50% in the mechanical torque.

Regarding the number of layers needed and the cost per unit surface, the material 2 is the most promising. Right below we provide failure criterion check, deflection check and elastic strains assessment for this unidirectional Glass/Epoxy laminate made of 24 layers at  $0^\circ$  for a 2.5m height. The max deflection allowed is  $w_{max}=2500/250*5=50\text{mm}$ . To satisfy the structural requirements we must stay into the ellipses.

The stiffness matrix of this laminate is in the form  $A_s B_0 D_s$  (i.e. specially orthotropic laminate [36]):

$$[K] = \begin{bmatrix} 4.7E + 08 & 2.6E + 07 & 0 & 0 & 0 & 0 \\ 2.6E + 07 & 1.0E + 08 & 0 & 0 & 0 & 0 \\ 0 & 0 & 5.0E + 07 & 0 & 0 & 0 \\ 0 & 0 & 0 & 5.6E + 03 & 3.1E + 02 & 0 \\ 0 & 0 & 0 & 3.1E + 02 & 1.2E + 03 & 0 \\ 0 & 0 & 0 & 0 & 0 & 6.0E + 02 \end{bmatrix}$$

Both local stresses and strains are calculated for the bottom, middle and top points of each layer of the laminate, and so for the different twist cases defined (0°, 90°, 180°) and their associated wind load (Fig.58). As all the layers are identically oriented at 0°, the local axis 1 resp.2 matches the X resp. Y direction of the global reference axis in which the loads are defined. Hence  $\sigma_1$  reflects the magnitude of bending and  $\sigma_6$  the one of torsional shear (note that relations are that simple because we do not have couplings). Both  $\sigma_1$  and  $\sigma_6$  reach their maximum in the outer layers, as those stresses increase with the distance from neutral axis (see Fig.60). In this simple configuration we can write directly:

$$\sigma_1 = \frac{M_x}{I} * z \text{ and } \sigma_6 = \frac{M_s}{J} * 2z$$

where the geometrical properties I and J are respectively the inertia and the torsion constant.

The legend for the stress & strain plots is always the same, the different dots correspond to points respectively at the bottom, the middle and the top of each layer, for the load cases defined in 1.3.

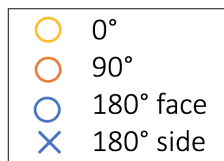
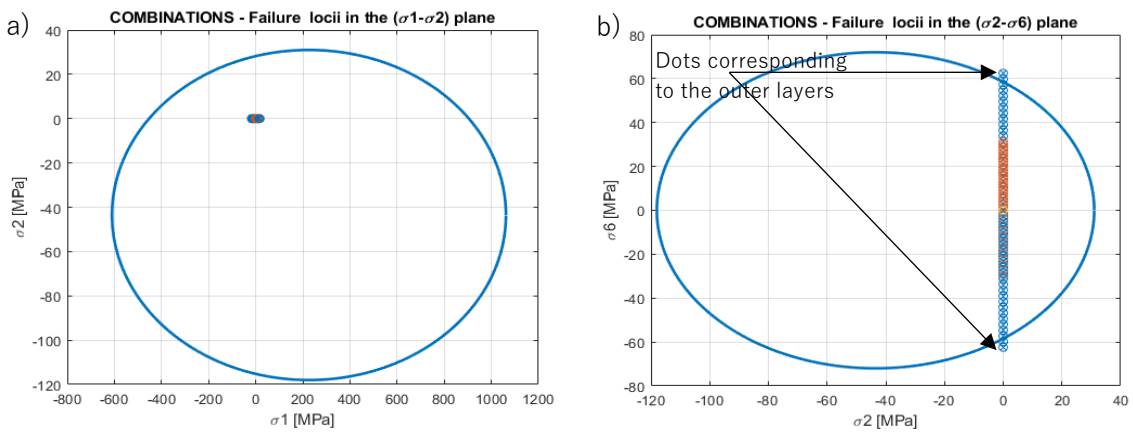
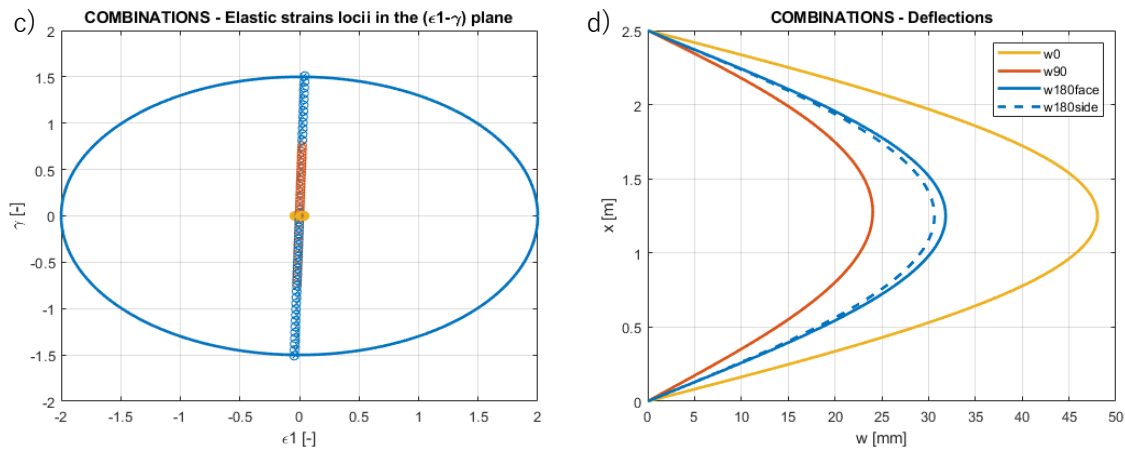


Figure 69- Legend of the plots.





Figures 70 a to d - Results with Material 2 for L=2.5 m (a)Top left: Failure criterion  $\sigma_1$ - $\sigma_2$  – (b)Top right: Failure criterion  $\sigma_2$ - $\sigma_6$  – (c)Bottom left: elastic strains limit – (d)Bottom right: deflections

The deflection under the  $0^\circ$  load case is decisive in the number of layers needed. However if we look at the  $\sigma_1$  values we observe that we are far from exploiting the material strength in tension/compression. Some core layers are not solicited at all. It confirms that it is worthless to use fibres with greater resistance like carbon, the point is really the inertia and consequently the relation between the number of layers and the thickness of the laminate.

The laminate does not support the shear stresses and strains due to the  $180^\circ$  case (blue dots outside the ellipses). The maximum rotation  $\theta_{max}$  is restricted to  $165^\circ$  ; at this point we exploits 100% of the shear resistance on the outer layers.

## 2.5 Governing parameters in the design

A sensitivity analysis is provided afterwards for unidirectional fiberglass laminates to resume the governing parameters and their influence respectively on the maximum deflection reached and the maximum rotation allowed. 3D plots investigate typical ranges of material properties and element thickness, while 2D cuts made in those previous plots correspond to the pre-designed element, i.e. 24 unidirectional layers of E-Glass material 2 (cf Table 22).

Bending stiffness EI is involved in the element's deflection:

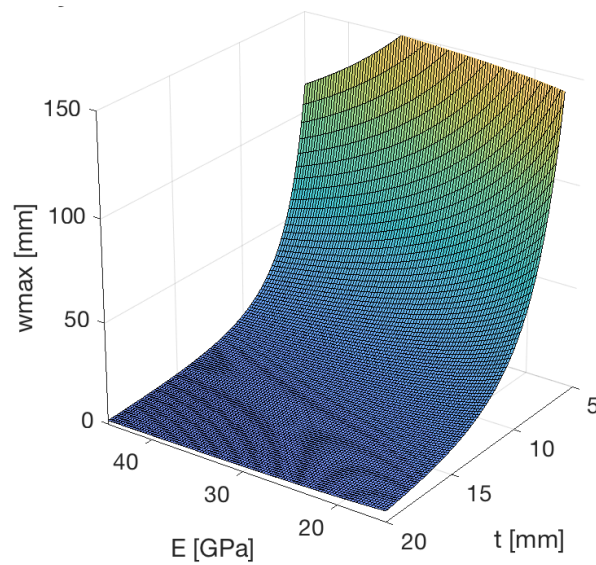
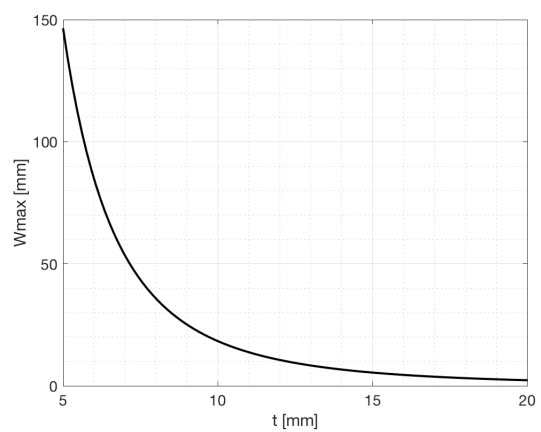
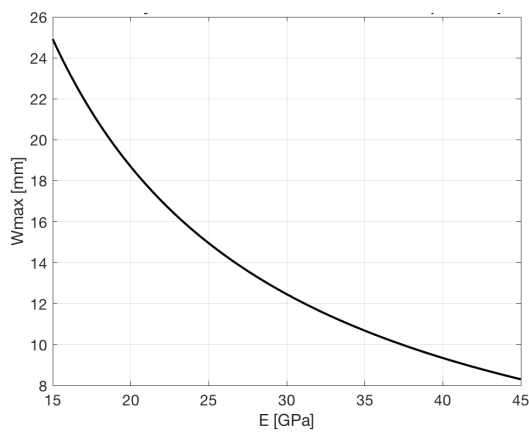


Figure 71 - Sensitivity of the maximum deflection to the E modulus and to the thickness for an unidirectional fiberglass laminate (with  $q=0.525\text{kN/m}^2$ ;  $L=2.5\text{m}$ )



Figures 72 a&b - Sensitivity of the maximum deflection to (a) the E modulus ( $t=12\text{mm}$ ), (b) the thickness ( $E=35\text{GPa}$ )

Both an increase in the E modulus and in the thickness decreases the deflection, however an increase in thickness has higher efficiency as  $w = f\left(\frac{1}{E}\right)$  while  $w = g\left(\frac{1}{t^3}\right)$  (with  $f = \frac{qL^4}{384I}$  and  $g = \frac{qL^4}{384E/12}$ ).

Torsional stiffness GJ is involved in the element's rotational capacity:

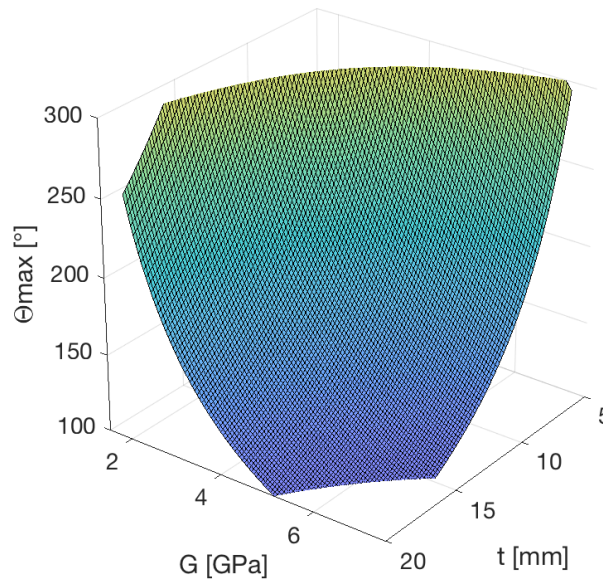
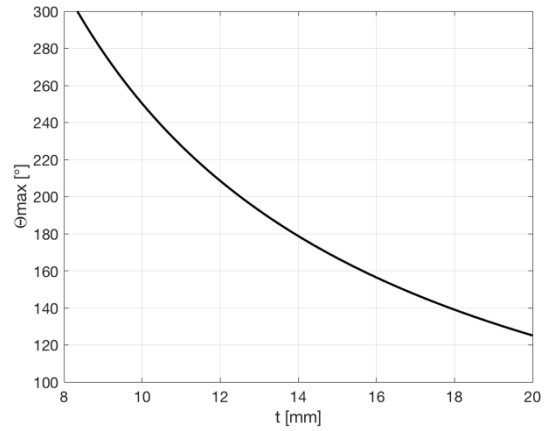
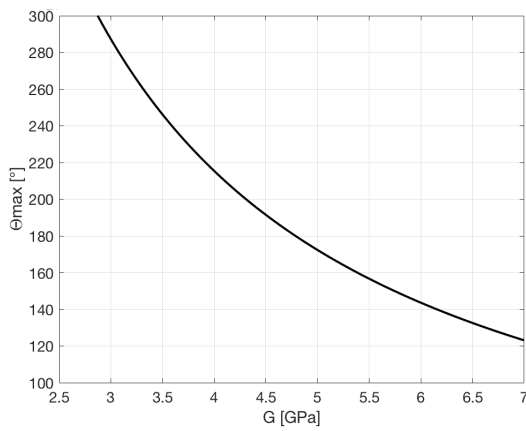


Figure 73 - Sensitivity of the maximum rotation to the G modulus and to the thickness for an unidirectional fiberglass laminate (with  $\tau_{max}=60\text{Mpa}$  ;  $L=2.5\text{m}$ )



Figures 74 a&b- Sensitivity of the maximum rotation to (a) the G modulus ( $t=12\text{mm}$ ) , (b) the thickness ( $G=4.14\text{GPa}$ )

Both a decrease in the G modulus or in the thickness increases the rotation capacity in the same way (i.e. the form of the mathematical relation is identical) as  $\theta_{max} = f\left(\frac{1}{G}\right) = g\left(\frac{1}{t}\right)$  (with  $f = \frac{\tau_{max}L}{t} * \frac{180}{\pi}$  and  $g = \frac{\tau_{max}L}{G} * \frac{180}{\pi}$ ).

## 2.6 Conclusion on the pre-design & shortcomings of the CLT

The Classical Lamination Theory allowed us to identify appropriate material and stacking sequence for the facade elements, providing an understanding of the stresses and deformations. Unidirectional glass fibers stacked at  $0^\circ$  are the most promising. The minimum thickness for 2.5m

long pieces is about 12mm, for a maximum rotation about  $165^\circ$ . Governing trends for the design of unidirectional laminates are synthesized in four points:

- **The  $0^\circ$  load case (uniform wind, no twist) is always decisive for the maximum deflection.**
  - **The  $\theta_{\max}$  load case (triangular wind) is always decisive for the maximum shear stresses and strains, occurring in the outer layers.**
  - **A decrease of the deflection is achieved by adding more layers at  $0^\circ$ , increasing the thickness and so the bending stiffness 'EI'**
  - **A decrease in the shear stress and strain, for a same total rotation, is achieved by removing layers to decrease the thickness of the laminate, decreasing the torsional stiffness 'GJ'**
- The thickness is contradictorily involved in deflection and rotation design criteria.**

The numerical results obtained must be consolidated because, firstly, some of the hypothesis of the CLT validity framework were overtaken, and secondly this theory cannot account for local phenomena or non-linear behavior, as it calculates linear elastic stresses and strains.

The following tables list the main questioned hypothesis and potential 'hidden' phenomena, depending on the action type (bending under wind load or applied torsion). The wind action is quiet small in terms of magnitude of stresses (cf plots Fig. 74), the GFRP elements should fully respond in linear elasticity and the deflection calculated by the CLT should be accurate. The only complementary investigation needed would be the support detailing so that we prevent local stress concentrations and possible resulting damages in force introduction zones.

Regarding the torsion however, several hypothesis are violated as the element undergoes large deformations. When applying efforts on a previously deformed structure (i.e. the structure's shape is now far different from its initial shape) non-linearity of the response can occur for geometrical reasons, because physical and mechanical properties of the deformed structure are different. The equilibrium equations\* must be solved taking into account the deformed configuration. Thin structures are well-known to show geometrical non-linearity [37].

\* *stresses emerging in a body equilibrate external force acting on this body*

In structural mechanics, non-linearity can also be caused by the material itself. Composites are often modeled as elastic (i.e. deformations are reversible) and linear (i.e. stresses grows proportional to strains) up to failure as fiber-driven failure are mainly brittle and common applications target extremely stiff pieces. However here the torsional behavior is driven by both sheared fibers and the epoxy matrix. It is not excluded that large deformations could trigger non-linear viscoelastic behavior of the matrix, acknowledged to be a common time-dependent behavior of thermosetting polymers like epoxy ([38] chapter 10), or could even lead to permanent plastic irreversible strains.

Study of force introduction close to the supports also holds for torsion. Influence of hyperstatic support conditions (fixed-fixed) requires attention too, as it is not known yet for systems in torsion and can interact with the two types of non-linearities previously mentioned.

CLT hypothesis	Potential shortcoming	External action in question
Infinite thin plate, plane stress-state (through-thickness stresses $\sigma_z, \tau_{yz}, \tau_{xz}$ assumed to be 0)	Support conditions, side effects & arising stress redistributions	Wind, Rotation
Small deformations, plane sections remain plane	Geometrical non-linearity	Rotation
Linear elasticity	Material non-linearity	Rotation

Table 23 - Phenomena falling outside the framework of the CLT while being relevant regarding the problem studied

NB: method used in 2.2 ‘Modeling of external loads and support conditions’ to introduce resp. flexural and torsional moments was necessary but not sufficient to account properly for supports conditions (no account for side-effects).

### 3 FEA analysis

#### 3.1 Modeling composites with ANSYS software

##### 3.1.1 Background of Finite Elements Analysis

Finite Element Analysis (FEA) relates to the computational modeling of complex behavior of structural or fluid systems and their solving by means of Finite Element Methods (FEM). FEM is a mathematical modeling that allows for a numerical solving of the problem, broadly used in the field of structural and mechanical engineering to investigate the distribution of field variables (e.g. stresses, displacements,…) across solid bodies subjected to external actions (e.g. forces, temperature,…). The solid geometry is assigned material properties and is discretized into small elements. Those finite elements are connected to each other but only in some points called nodes. The whole (finite elements and related connectivity information) forms the mesh.

External loads are discretized as well and applied to the concerned nodes. Basically, FEM solves for the nodal displacements  $\{u^e\}$  of a finite element and approximates the displacement field of this finite element by a linear combination of interpolation function, with interpolation coefficients usually equal to the nodal displacements such that:

$$\{F^e\} = [K^e]\{u^e\}$$

$[K^e]$  element stiffness matrix

$\{F^e\}$  vector of element’s equivalent forces

$\{u^e\}$  vector of element's nodal displacements

Knowing the connectivity of the nodes, those element governing equations are then assembled to build system equations, 'summing' the contribution of all finite elements, in order to solve for the whole solid displacement field. A global relation  $\{F\} = [K]\{u\}$  is obtained for the whole structure. Boundary conditions such as constrained displacements and rotations are applied on the corresponding degrees of freedom (DOF) and the global relation is inverted (nb: specific methods exists to avoid time-consuming direct inversion [39]). Finally, based on the displacements calculated, elemental strains and stresses are calculated using constitutive relations.

FEM does not solve the strong form, also called the differential form, of the equilibrium but its integrated form on a finite element, called the weak form. The solution is approximated, as it is true 'in average' on each small element. The precision of the mesh (element size and type) has a great importance regarding the approximation of the field variables through the solid and so the accuracy of the results. It requires experience to optimize element choice and refine the mesh geometry only in regions where it is necessary so that computation time is not wasted. Considerations on the mesh quality are further developed in Appendix VI. Different element types exist (2D like bar, triangle, quadrilateral..., 3D like pyramid, hexahedra,...), they have different number of nodes and the nodes have different translational and rotational degrees of freedom (from 2 up to 6 DOF per node). Hence the element choice greatly impacts the interpolation functions.

It exists a plethora of FEA programs commercially available. However, only a few of them include features capable of specifically analyzing composite materials. Softwares like ANSYS® or Abaqus™ can be cited among others.

ANSYS is a suite of products that interact together to perform the analysis from geometrical input and meshing to solution calculation and results treatment. It is based on the APDL script language (ANSYS Parametric Design Language). The user can perform operations directly entering code command lines ('classic' mode) or by means of an interface ('workbench' mode) that manages to convert user's requests into APDL code. We used the latter mode as the most intuitive one, nevertheless the classic mode is recommended for a transparent control of the calculations.

### 3.1.2 Modeling steps with the different ANSYS components system

FEA steps are subdivided into pre-processing, processing and post-processing steps.

Pre-processing represents about 70% of the effort when performing FEA structural design, and even more in this thesis as the software was self-learnt.

Pre-processing is achieved with the 'Ansys Composite Pre-Processing' (ACP Pre) component system.

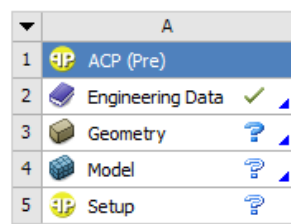


Figure 75 - Ansys Composite Pre-Processing component system

The ‘Engineering Data’ resource is filled with either material properties available in Ansys database or user-defined ones. We now use a material from Ansys database, as it contains all the 3D orthotropic linear elastic properties i.e. elastic constants E, G &  $\nu$ , limit strengths and limits strains. We choose ‘ANSYS Epoxy E-Glass Wet’ as it is the closest one from material selected in the pre-design (material 2 from Table 21). The geometry of the element is defined into the ‘Space Claim’ modeler (2D geometry, the thickness is defined later).

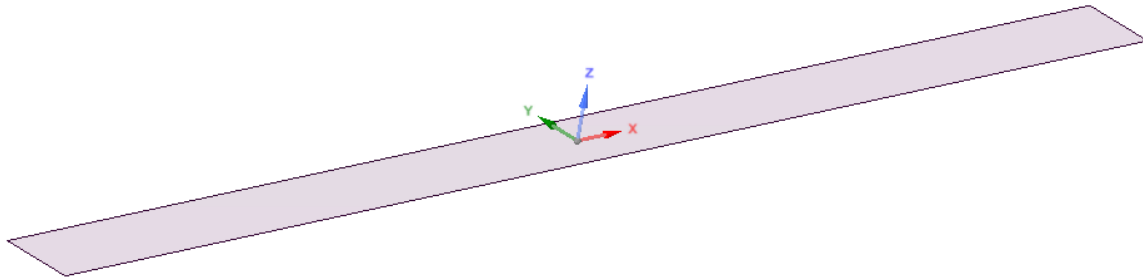


Figure 76 - Geometry and coordinates system definition in Space Claim

The ‘Model’ edition step including loads and support conditions is done in a ‘Static Structural’ component system, which calls for the core ‘ANSYS Mechanical’ package. For now a dummy thickness is assigned to the geometry and a mesh is created. We must define fabrics, plies and stacking sequence in ACP Pre. A new fiberglass single layer type (‘Fabric’) is created with the ‘Epoxy E-Glass Wet’ material. This layer is assigned a thickness of 0.5mm. Its mechanical properties are resumed in the following polar plot:

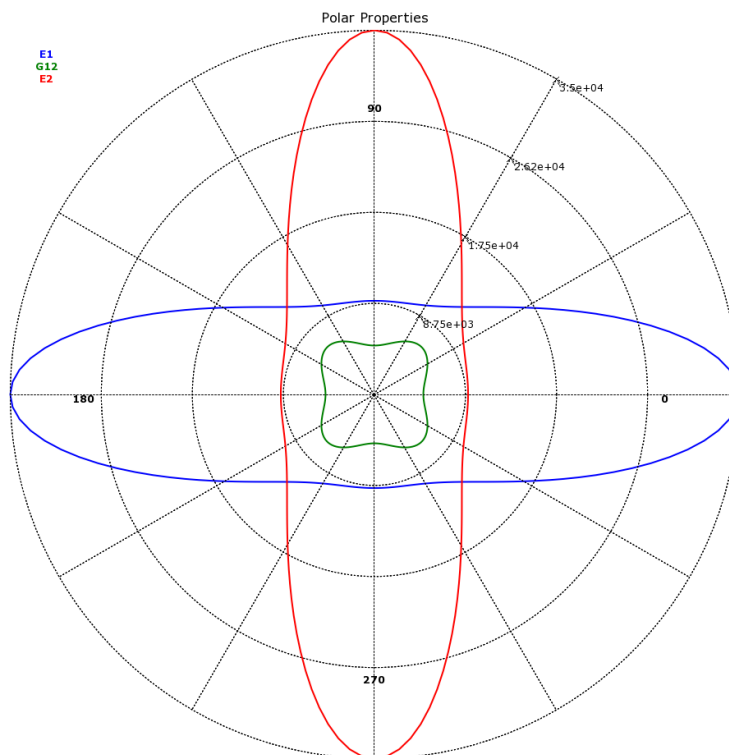


Figure 77 - Polar representation of the in-plane elastic constants for an unidirectional ply of ‘Epoxy E-Glass Wet’ material ; angles are relative to a rotation from the main principal direction (0° ) which is the fibers’ direction

A ‘Rosette’ (i.e. a local coordinates system) is created, with principal direction x along the length of the rectangular element, and attached to the rectangular geometry, the whole becoming an

'Oriented Selection Set' which defines the area to be used for the layup definition: composite layers will be applied to this area, with orientations defined relatively to the rosette's direction meaning that plies with fibers directed parallel to this rosette coordinates system are oriented at 0°. Plies are created in the 'Modeling Groups' subsection, here oriented at 0° and with fabric material previously defined. We now have a shell model. Solid modeling i.e. volumic modeling, is obtained by extrusion of the shell model along the surface's normal direction. Quadrilateral solid mesh elements are used ('SOLID185'). Those elements include midside nodes, so that they can reconstruct quadratic fields across the element's thickness and avoid the well know shear locking problematic that occurs in linear mesh elements, unable to model the curvature.

The ACP Pre 'Setup' is finally plugged into the 'Static Structural' analysis component. Detailed tree structures of those components are provided in Appendix VII.

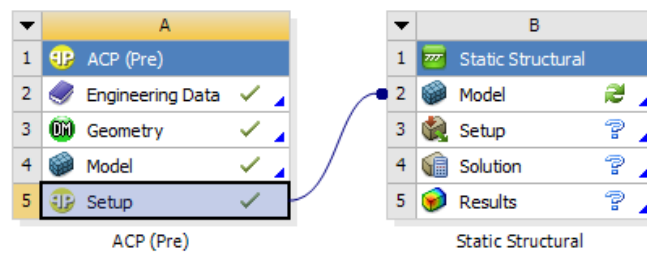


Figure 78 - Static Structural system component and data inherited from ACP Pre

'Setup' is pursued in 'Static Structural'. Boundary conditions and loads are added. Supports are defined along the short ends edges (or faces for solid modeling). Supports' behavior is set to 'Rigid'. In 3D, a support has 6 degrees of freedom: 3 displacements 'u' and 3 rotations 'r' along resp. X,Y,Z (or 3 forces and 3 moments if expressed in terms of support reactions). With two ends supports, the maximum number of unknowns is 12. We have 6 equilibrium equations, hence we must block at least 12-6=6 DOF to prevent rigid bodies motions (i.e. to have an isotastic, simply-supported, structure) and 6 more to have an hyperstatic fixed-fixed structure as determined in section 2.4. For supports, DOF are controlled one-by-one in the 'Remote displacement' panel. Torque is applied as a boundary condition, by imposing a rotation rX different from 0. This rotation is 'Ramped', increasing linearly from 0° to the final value on a 30 seconds time interval. This allows us to mimic the real facade actuation and to obtain plots of the Torque-Rotation relation. Half of the rotation is equally applied at each end to have a homogeneous repartition along the length. Also note that in Table 26 we free the longitudinal displacement X at one end to allow axial retraction during the twist, otherwise the restrained strain creates undesired tensile stresses in the body (detailed in Fig. 89 & 91). Wind pressure is applied as a surface load, along the (-Z) global direction, because the wind direction stays the same while the module is twisted.

End 1: 'Remote displacement'		End 2: 'Remote displacement 2'	
uX	free	uX	<b>0</b>
uY	<b>0</b>	uY	<b>0</b>
uZ	<b>0</b>	uZ	<b>0</b>
rX	free	rX	free
rY	free	rY	free
rZ	free	rZ	<b>0</b>

Table 24 – Boundary conditions for a simply-supported 3D GFRP beam

End 1: 'Remote displacement'		End 2: 'Remote displacement 2'	
uX	<b>0</b>	uX	0
uY	0	uY	0
uZ	0	uZ	0
rX	<b>0</b>	rX	<b>0</b>
rY	<b>0</b>	rY	<b>0</b>
rZ	<b>0</b>	rZ	0

Table 25 - Boundary conditions for a fixed-fixed 3D GFRP beam

End 1: 'Remote displacement'		End 2: 'Remote displacement 2'	
uX	<b>free</b>	uX	0
uY	0	uY	0
uZ	0	uZ	0
rX	<b><math>\theta/2</math></b>	rX	<b><math>-\theta/2</math></b>
rY	0	rY	0
rZ	0	rZ	0

Table 26 - Boundary conditions for a twisted fixed-fixed 3D GFRP beam with released axial displacement

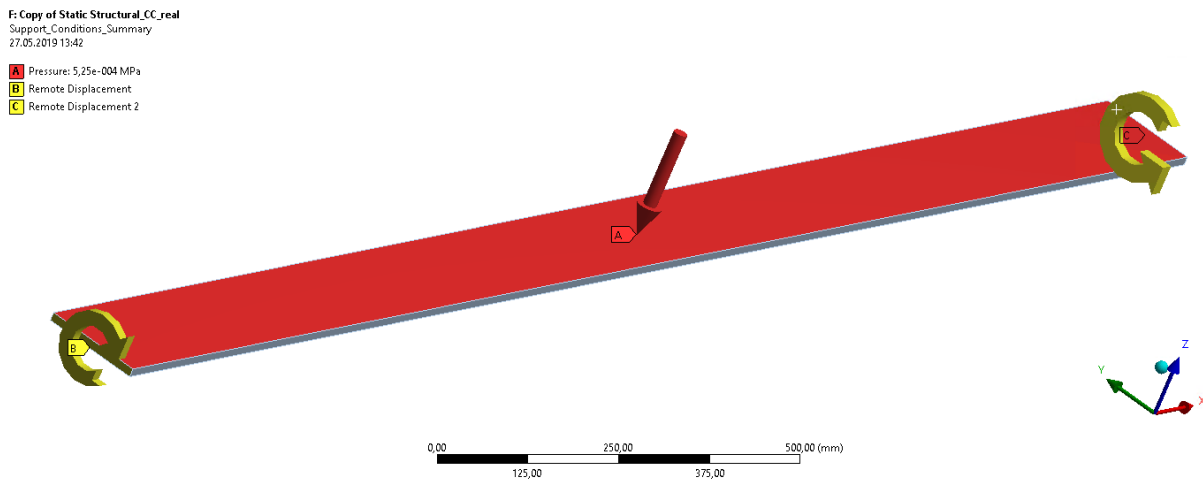


Figure 79 – Application of boundary conditions and loads

'Analysis Settings' are configured to allow for large deformations and take them into account in the solving process, meaning that the calculation will include potential geometrical non-linearity by iteratively solving the equilibrium equations for the successive deformed configurations of the structure (Newton-Raphson algorithm).

Processing represents about 5% of the effort when performing FEA structural design. The difficulty is to iterate on pre-processing parameters so that the software converges in an acceptable computing time.

Post-processing represents the remaining 25% of the effort when performing FEA structural design. For general post-processing operations like visualization of deformations, we used directly 'Mechanical'. More composite-specific visualizations like stresses within the different layers are then performed with 'Ansys Composite Post-Processing' (ACP Post). Calculation of the Tsai-Wu failure criterion was implemented in the 'Solution' panel.

### 3.2 Comparison between ANSYS and CLT results

In the first place, we will study separately the bending and the torsion to compare results provided by ANSYS to results obtained by the CLT. A separate study assumes that the superposition principle holds for the load combination, this is to be discussed afterwards.

The full-scale element is modeled (H=2.5m).

For unidirectional orthotropic laminae stacked at 0° the stiffness matrix [K], built with the classical lamination theory, simplifies. Couplings disappear, especially the flexural-torsional coupling. It ends up with the following linear constitutive law:

$$\begin{Bmatrix} 0 \\ 0 \\ 0 \\ m_x \\ 0 \\ m_s \end{Bmatrix} = \begin{bmatrix} A_{xx} & A_{xy} & 0 & 0 & 0 & 0 \\ A_{xy} & A_{yy} & 0 & 0 & 0 & 0 \\ 0 & 0 & A_{ss} & 0 & 0 & 0 \\ 0 & 0 & 0 & D_{xx} & D_{xy} & 0 \\ 0 & 0 & 0 & D_{xy} & D_{yy} & 0 \\ 0 & 0 & 0 & 0 & 0 & D_{ss} \end{bmatrix} \begin{Bmatrix} \varepsilon_x^0 \\ \varepsilon_y^0 \\ \varepsilon_s^0 \\ k_x \\ k_y \\ k_s \end{Bmatrix}$$

From which we derive:  $m_x = D_{xx} * k_x + D_{xy} * k_y$  and  $m_s = D_{ss} * k_s$

As mentionned, we now use a theoretical material 'ANSYS Epoxy E-Glass Wet' from Ansys database. We also extract the 2D properties required by the Matlab code from this database to perform the comparison:

Properties of Outline Row 10: Epoxy E-Glass Wet			
	A	B	
1	Property	Value	
2	Density	1,85E-09	mm^-3 t
3	Orthotropic Secant Coefficient of Thermal Expansion		
8	Orthotropic Elasticity		
9	Young's Modulus X direction	35000	MPa
10	Young's Modulus Y direction	9000	MPa
11	Young's Modulus Z direction	9000	MPa
12	Poisson's Ratio XY	0,28	
13	Poisson's Ratio YZ	0,4	
14	Poisson's Ratio XZ	0,28	
15	Shear Modulus XY	4700	MPa
16	Shear Modulus YZ	3500	MPa
17	Shear Modulus XZ	4700	MPa
18	Orthotropic Stress Limits		
19	Tensile X direction	780	MPa
20	Tensile Y direction	31	MPa
21	Tensile Z direction	31	MPa
22	Compressive X direction	-480	MPa
23	Compressive Y direction	-100	MPa
24	Compressive Z direction	-100	MPa
25	Shear XY	60	MPa
26	Shear YZ	35	MPa
27	Shear XZ	60	MPa
28	Orthotropic Strain Limits		
29	Tensile X direction	0,0244	
30	Tensile Y direction	0,0038	
31	Tensile Z direction	0,0038	
32	Compressive X direction	-0,015	
33	Compressive Y direction	-0,0125	
34	Compressive Z direction	-0,0125	
35	Shear XY	0,015	
36	Shear YZ	0,012	
37	Shear XZ	0,015	

Figure 80 - 3D material properties of 'ANSYS Epoxy E-Glass Wet' material

Material Name	Material	Ply thick. [mm]	E11 [GPa]	E22 [GPa]	G12 [GPa]	v12 [GPa]	X [Mpa]	X' [Mpa]	Y [Mpa]	Y' [Mpa]	S [Mpa]	$\epsilon_{el}$ [%]	$\gamma_{el}$ [%]
ansysWet	GI/Ep	0.5	35	9	4.7	0.28	780	480	31	100	60	2.44	1.5

Table 27 - 2D material properties extracted from the 'ANSYS Epoxy E-Glass Wet' database of properties

For ANSYS simulations, solid modeling is used and a quadrilateral mesh is imposed ('Face Meshing'), with 'Element size' 10mm along the short edges of the the facade module and 25mm along the longer ones.

### 3.2.1 Bending

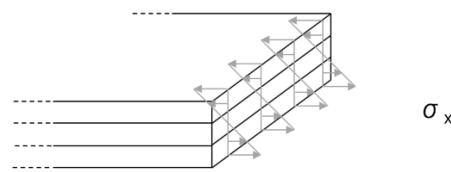


Figure 81 - Reminder: schematic representation of bending normal stresses

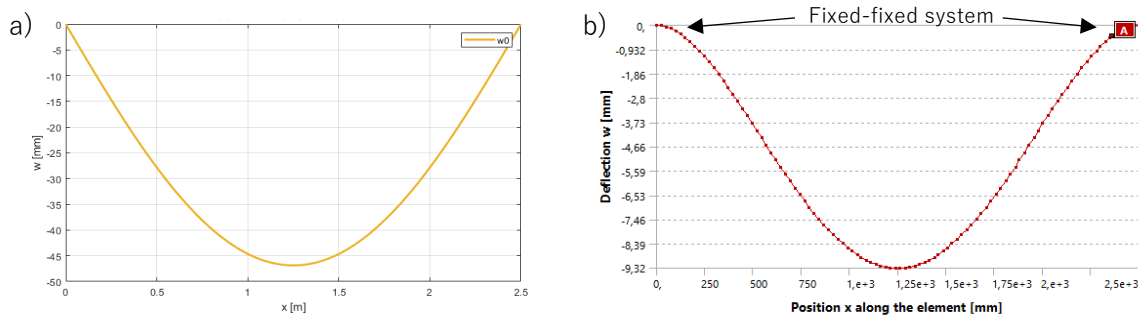
First let's estimate how many UD layers we need to satisfy the maximum deflection criterion. We recall that in the Matlab code the system is modeled as simply-supported and we apply a factor 5 on the  $w_{adm}$  limit to account for the real fixed-fixed system, that is why  $w_{adm}=50\text{mm}$ .

We need 25 layers, so that  $w_{max, simply\ supported}=46.9\text{mm}$ , i.e.  $w_{max, fixed-fixed} = w_{max, simply\ supported} / 5 = 9.40\text{mm}$

According to ANSYS, with the following support conditions,  $w_{max} = 9.32\text{mm}$ .

End 1: 'Remote displacement'		End 2: 'Remote displacement 2'	
X	free	X	0
Y	0	Y	0
Z	0	Z	0
rX	0	rX	0
rY	0	rY	0
rZ	0	rZ	0

Table 28 - Boundary conditions, element under wind load  $q=0.525\text{kN/m}^2$



Figures 82 a&b – (a)CLT and (b)ANSYS prediction of the deflection under  $0^\circ$  wind load case using 25 layers of 'Epoxy E-Glass Wet' material (L=2.5 m)

3.2.2 Torsion

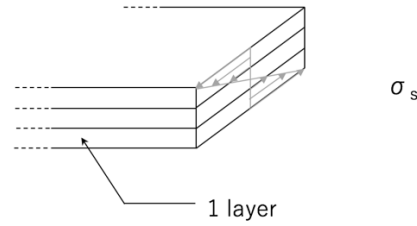
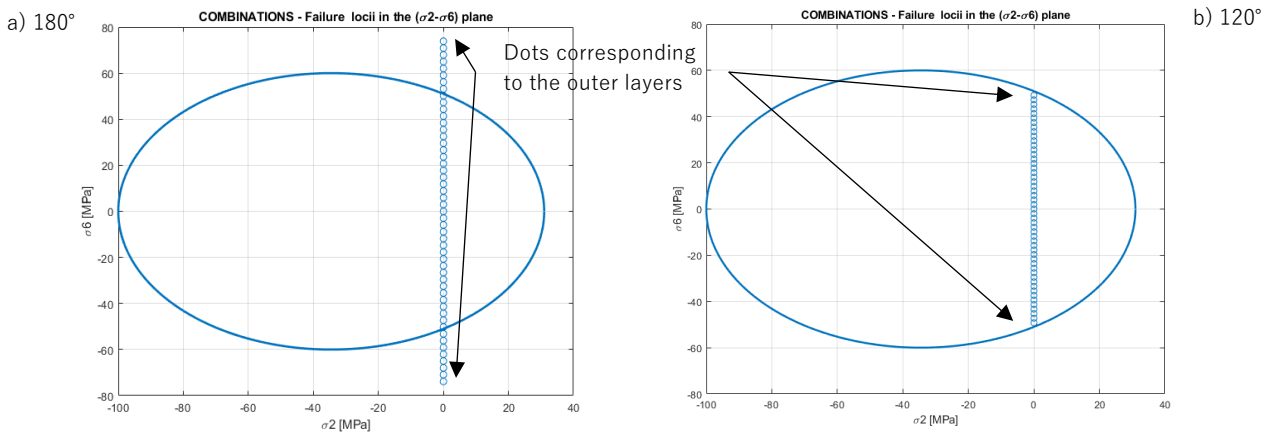


Figure 83 - Reminder: schematic representation of in-plane shear torsional stresses

Calculations performed with Matlab (CLT) for 25 layers of ‘AnsysWet’ material showed that we cannot reach 180° without shear failure, the maximum allowed rotation being 120° \* to stay in the ellipse (Figure 84).

\*against 165° with material 2 from database Table 21 ; mainly because of the increase in thickness from 24 to 25 layers



Figures 84 a&b – CLT prediction of 2D Tsai-Wu failure criterion using 25 layers of ‘Epoxy E-Glass Wet’ material (L=2.5 m), for (a) 180° rotation, (b) 120° rotation – Projection of the criterion in the  $\sigma_2$ - $\sigma_6$  plane.

Simulation is performed with ANSYS to validate this evaluation of the maximum  $\theta$  angle acceptable on the 1:1 full-size element. FEM confirms that the limit  $\theta_{lim} \approx 120^\circ$  is conservative;  $\theta_{lim,FEM} \approx 140^\circ$

End 1: ‘Remote displacement’		End 2: ‘Remote displacement 2’	
X	free	X	0
Y	0	Y	0
Z	0	Z	0
rX	70°	rX	-70°
rY	0	rY	0
rZ	0	rZ	0

Table 29 - Boundary conditions in FEM analysis, element under 140° torsion

The Tsai-Wu failure criterion (cf. section 2.3) is now evaluated in 3D:

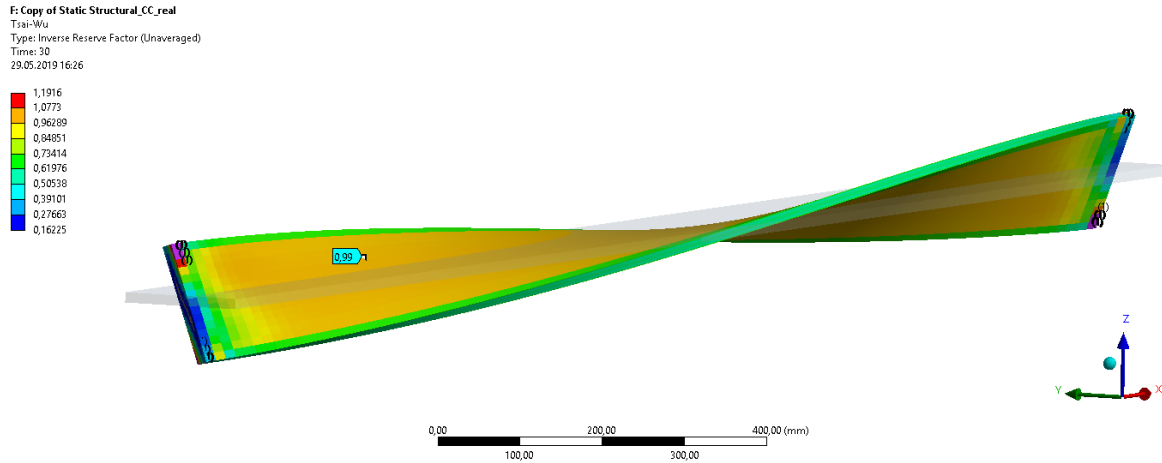


Figure 85 - ANSYS evaluation of Tsai-Wu failure criterion in 3D for a 140° rotation on an element made of 25 layers of 'Epoxy E-Glass Wet', L=2.5 m (results visualization for the outer layers)

At 140°, shear-driven failure is reached on the outer layers, the failure criterion being equal to 1.0 (orange central zone, see also the shear stresses Figure 86 hereafter). For now we do not pay attention to the 1.19 value occurring in the corners. Failure is reached here because of predominant normal stresses as shown later in Figure 88. Mesh refinement is needed to accurately evaluate the magnitude of the phenomenon.

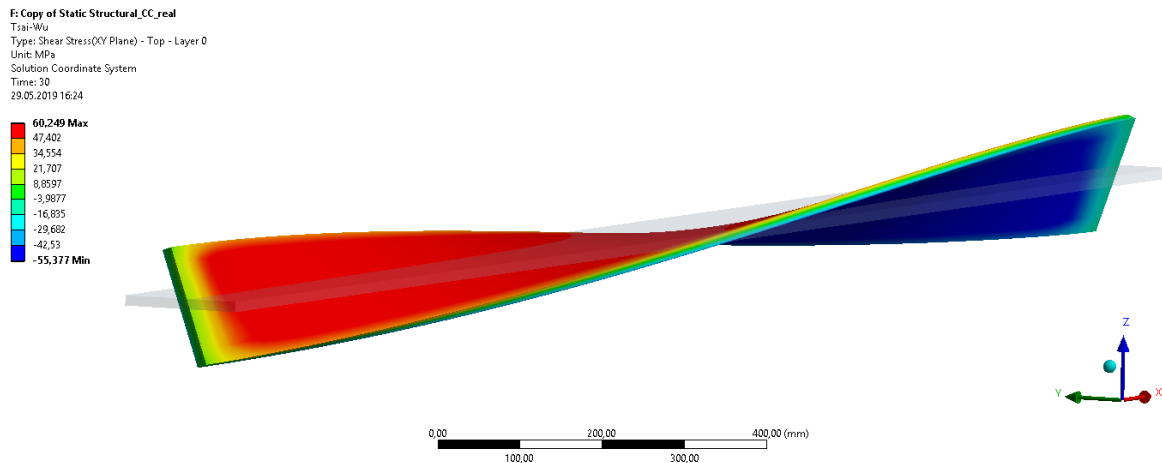


Figure 86 - ANSYS evaluation of in-plane shear stresses for a 140° rotation on an element made of 25 layers of 'Epoxy E-Glass Wet', L=2.5 m (results visualization for the outer layers)

Far from edges, the in-plane shear ( $\tau_{12} = \tau_{xy}$ ) is similar to the CLT forecast. Note that the extreme values are not symmetrical on Fig. 86 because the values are calculated for the top points on each layer. Close to the free edges, the in-plane shear must be zero as in cannot 'exit' the body. Equilibrium is ensured by the emergence of transverse shear stresses ( $\tau_{13} = \tau_{xz}$ ), see figure 87 below. Evaluation of Tsai-Wu criterion considering only 2D stresses misses stresses concentrations and rearrangement (and predicts failure slightly earlier), showing once again that CLT analysis was not capable of integrating this phenomenon.

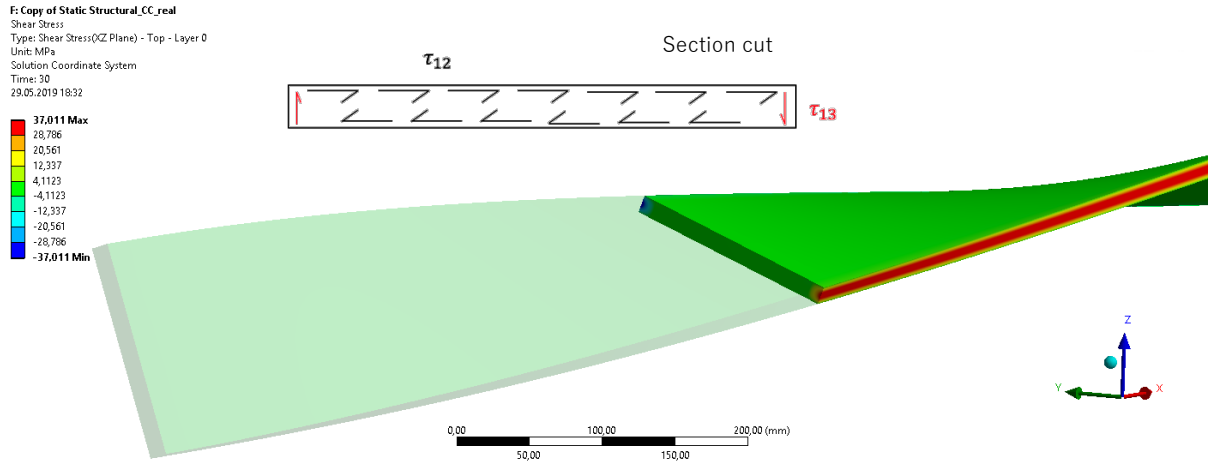


Figure 87 - ANSYS evaluation of transverse shear stresses for a 140° rotation on an element made of 25 layers of 'Epoxy E-Glass Wet', L=2.5 m (results visualization in a vertical cut through the body)

Far from the supports, the body is subjected to axial compression close to the center and axial tension close to the edges (Fig. 88). We mentioned in section 3.1.2 ('Modeling steps') the need to free the longitudinal displacement  $u_x$ . Fig. 89 plots axial normal stresses when locking  $u_x$ . A global tension increase ( $\sim +35\text{Mpa}$ ) is effectively affecting the body. With  $u_x$  free, total axial retraction is 2.28mm (Fig. 90)

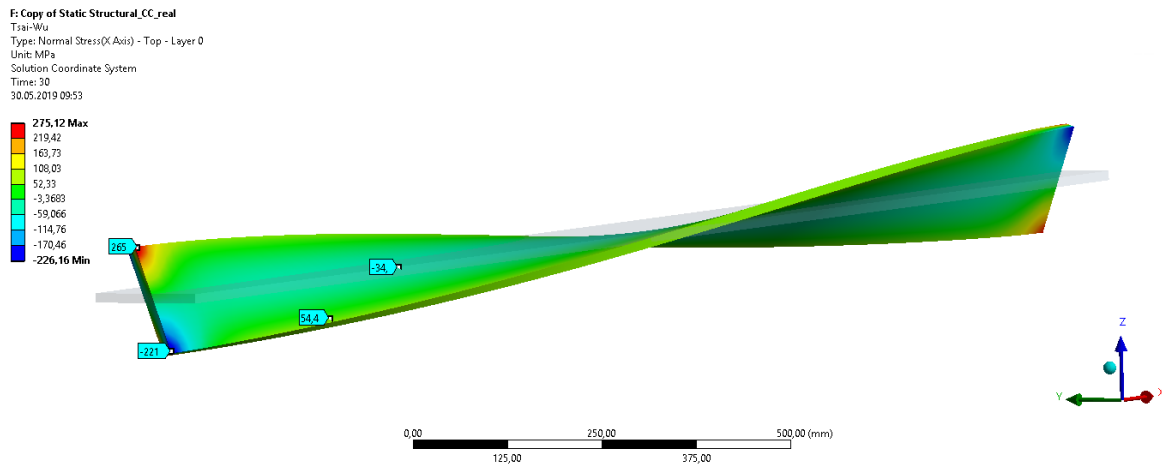


Figure 88 - ANSYS evaluation of axial normal stresses for a 140° rotation on an element made of 25 layers of 'Epoxy E-Glass Wet', L=2.5 m (results visualization for the outer layers,  $u_x$  free at one end)

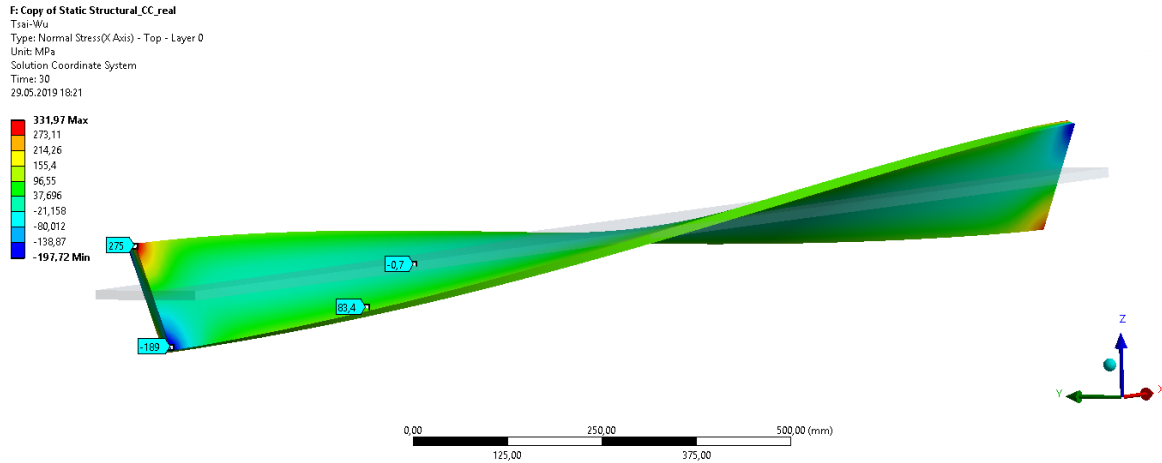


Figure 89 - ANSYS evaluation of axial normal stresses for a 140° rotation on an element made of 25 layers of 'Epoxy E-Glass Wet', L=2.5 m (results visualization for the outer layers, uX locked)

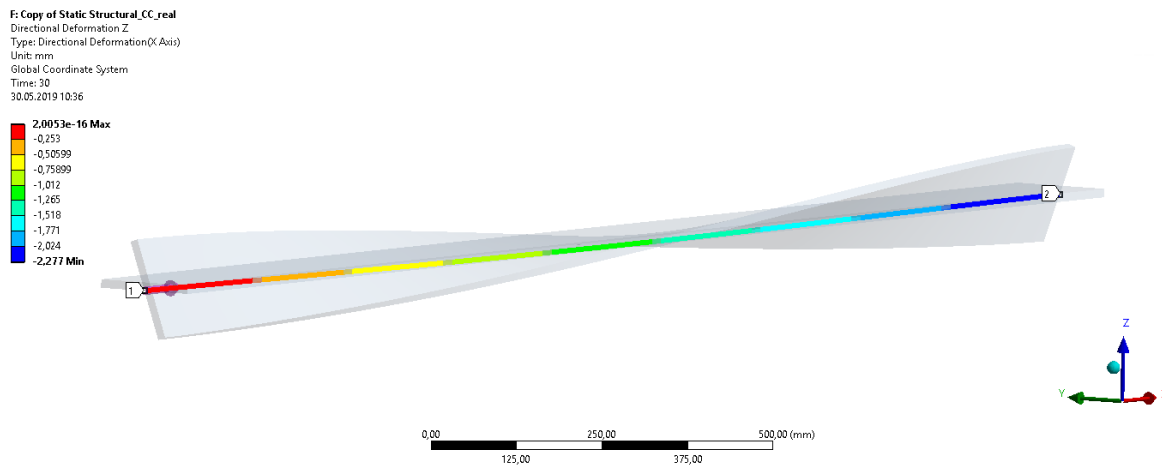


Figure 90 - ANSYS evaluation of axial retraction for a 140° rotation on an element made of 25 layers of 'Epoxy E-Glass Wet', L=2.5 m (results visualization along the neutral axis, uX free at one end)

Lastly, ANSYS calculation in large deformations highlighted the start of a torsional buckling behavior. The element slowly bends out-of-plane when twisted. For a 140° rotation, Figure 91 after shows an out-of-plane maximum deflection of 6.63mm. (NB: It would not help a lot to lock uX, o-o-p deflection would still be 5.59 mm). This o-o-p deflection is undesired, moreover because it has the same magnitude and potentially the same direction (depending on the rotation direction) as the o-o-p deflection due to wind load. Only calculation methods accounting for the effects of large deformations can predict instability.

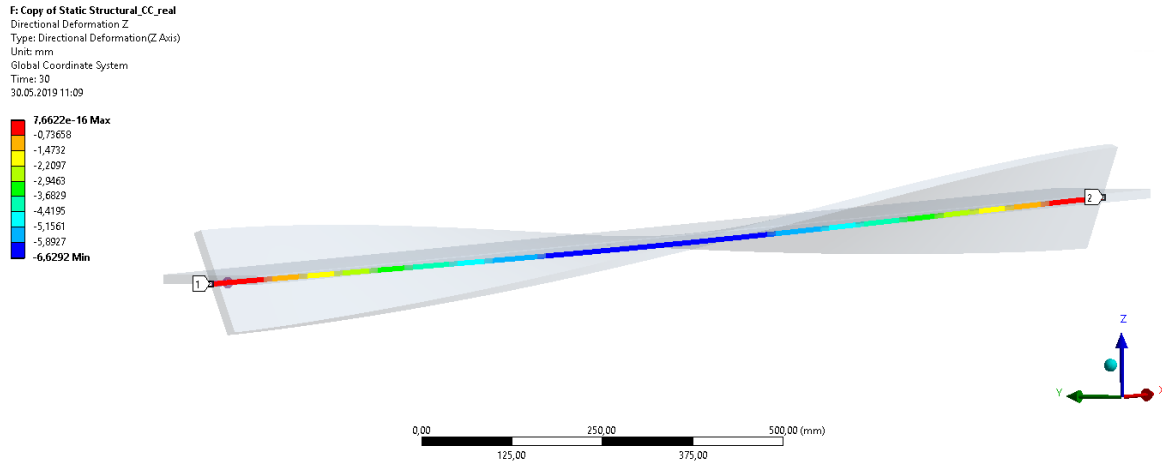


Figure 91 - ANSYS evaluation of o-o-p deflection (torsional buckling) for a 140° rotation on an element made of 25 layers of 'Epoxy E-Glass Wet', L=2.5 m (results visualization along the neutral axis, uX free at one end)

### 3.2.3 Bending & Torsion

In this section both pressure and twist are applied on the element. The support conditions are identical to Table 29. The support moment reaction has 2 components, expressed in the coordinates system from Figure 76 as  $M_x^*$  (torsion) and  $M_y^*$  (bending).

*\*WARNING: ANSYS names the moments according to the axis of rotation (torsion  $M_x$ ) while plate theories like CLT name the moments by unit of width according to the axis of deformation (bending  $m_x$ ).*



Figure 92 – Support reaction (resulting moment) when the element is subjected to a 140° rotation and wind pressure, L=2.5 m

Calculation of the 3D Tsai-Wu criterion barely changes, from 0.99 (only torsion) to 1.02 (torsion and wind). Wind loads indeed generate stresses in the order of 5% of the related strength limit while torsion generates shear stresses reaching the related strength limit.

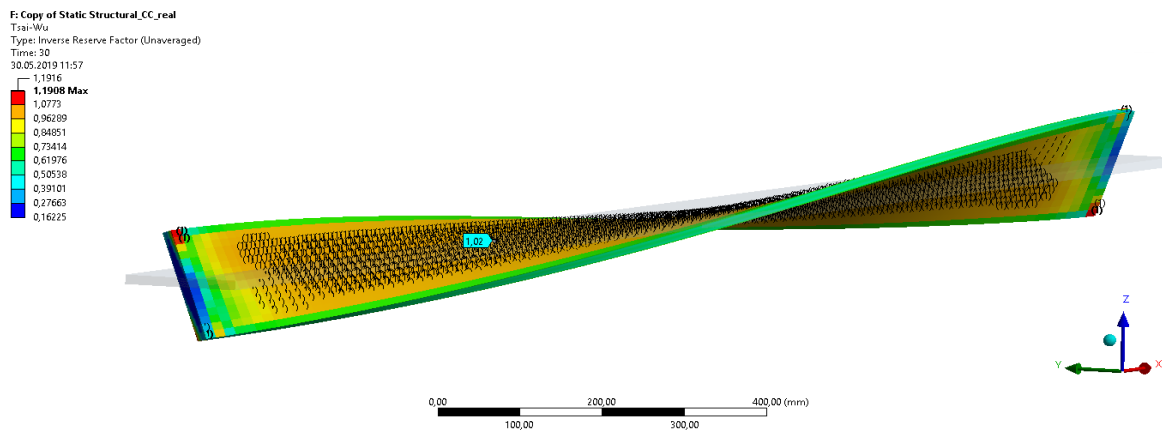


Figure 93 - ANSYS evaluation of Tsai-Wu failure criterion in 3D for a 140° rotation and wind pressure on an element made of 25 layers of 'Epoxy E-Glass Wet', L=2.5 m (results visualization for the outer layers)

Failure is still driven by the in-plane shear. The pressure has no effect on the in-plane shear stress repartition (identical to Fig. 86). Regarding normal longitudinal stresses, the bending introduces a maximum  $\pm 15\text{MPa}$  axial stress in the body (Fig. 94, to be compared with normal longitudinal stresses on Fig. 88).

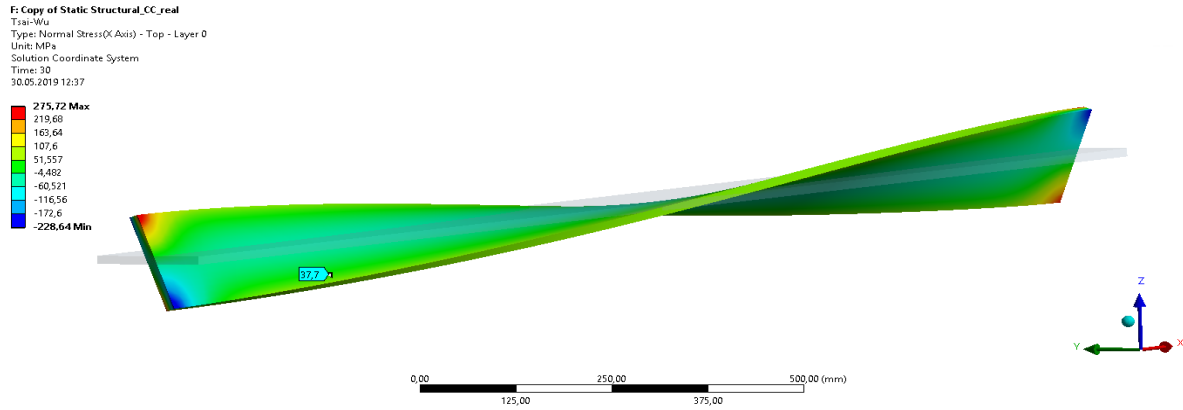


Figure 94 - ANSYS evaluation of axial normal stresses for a  $140^\circ$  rotation and wind pressure on an element made of 25 layers of 'Epoxy E-Glass Wet',  $L=2.5\text{ m}$  (results visualization for the outer layers,  $u_x$  free at one end)

The total out-of-plane deflection is plotted in Figure 95 below. Since we accounted for the deformed shape in equilibrium calculations, the superposition principle does not hold. The maximum deflection is  $w_{\text{max}}=7.15\text{mm}$  while summing separate effects of wind load and torsion (including buckling) would have predicted twice as much ; the pressure actually prevents part of the torsional buckling (see Fig. 96 after)! NB: the total axial retraction is unchanged, still  $2.28\text{mm}$ .

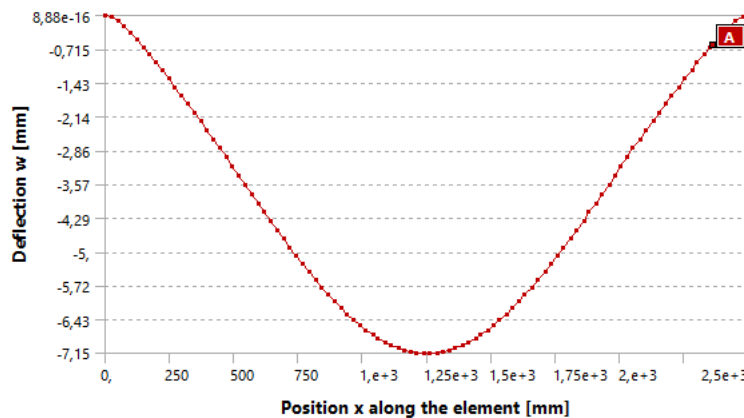


Figure 95 - ANSYS prediction of total o-o-p deflection for a  $140^\circ$  rotation and wind pressure on an element made of 25 layers of 'Epoxy E-Glass Wet',  $L=2.5\text{ m}$  (results along the neutral axis,  $u_x$  free at one end)

Figure 96 details the evolution of the maximum deflection for a rotation from  $0^\circ$  to  $140^\circ$  (rotation capacity), measured along the neutral axis and quantified as a percentage of the decisive maximum deflection i.e. the one reached when wind pressure acts normal to closed blinds. The black curve (torsion only) stands for o-o-p deflection due to the described buckling. For small rotations the total o-o-p deflection (torsion+wind) decreases as the wind load becomes triangular (recall Fig. 58 in section 1.3) and buckling's influence is small. For larger rotation instability and pressure interact in a way that results in a stabilized o-o-p deflection, which never exceeds the decisive situation.

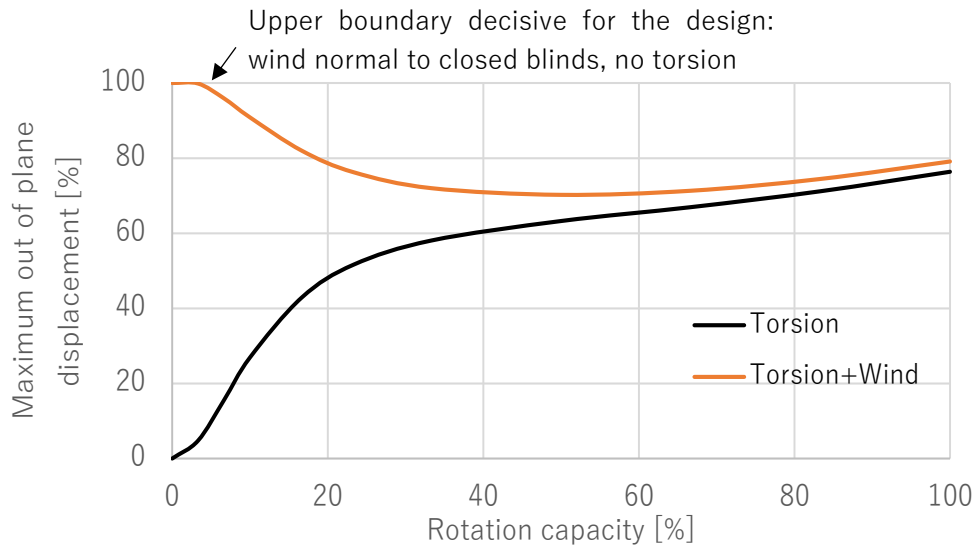


Figure 96 - Growth of the maximum o-o-p displacement along the neutral axis for an increasing rotation (up to the rotation capacity i.e. 140°) evaluated in % of the deflection value reached for wind pressure normal to closed blinds, based on ANSYS calculations for an element made of 25 layers of 'Epoxy E-Glass Wet',

The last point investigated is the relation between the angle of rotation and the torque that the facade's actuators will need to apply to reach it, i.e. the support reaction in torsion ('M<sub>x</sub>' in ANSYS notation):

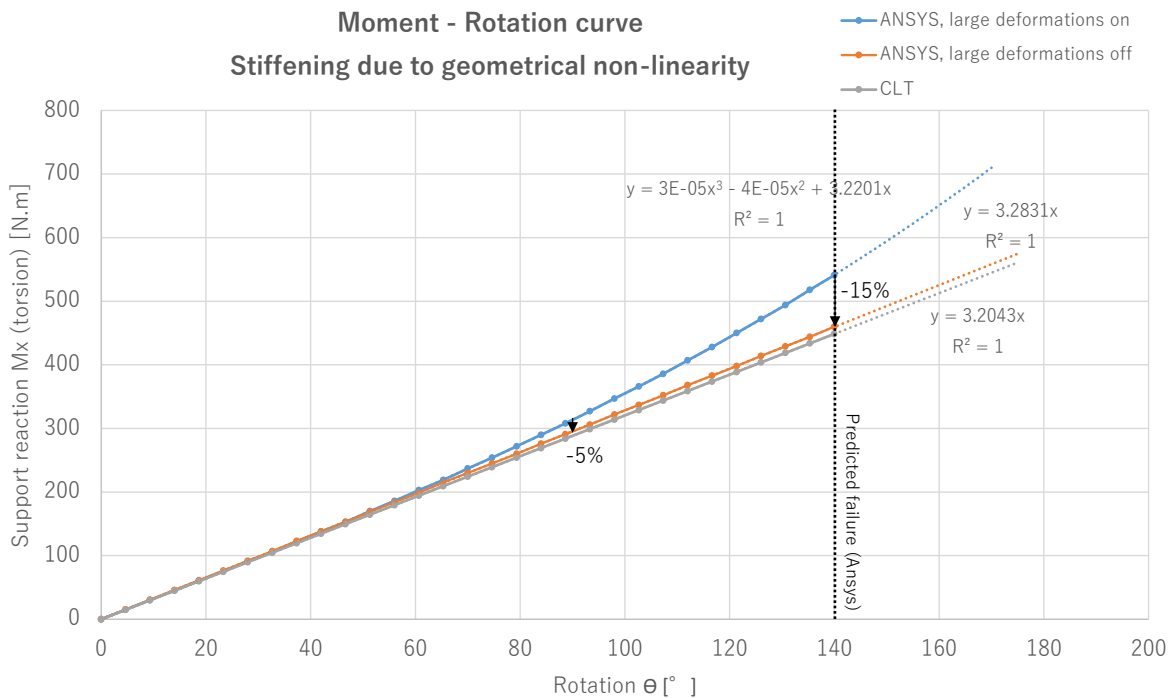


Figure 97 - Evolution of the support torque reaction for an increasing rotation angle: comparison between predictions from the CLT and ANSYS, with and without accounting for large deformations, for an element made of 25 layers of 'Epoxy E-Glass Wet', L=2.5 m.

We observe a 2.5% increase in the linear elastic slope obtained from ANSYS (solid modeling and real geometry) and obtained from the CLT (2D infinite plate).

However the most remarkable is the curve accounting for large deformations! The latter curve is not linear contrariwise of predictions from the CLT ( $T = 2 * b * m_s = 2 * b * D_{ss} * k_s$ ), we observe a stiffening behavior as the rotation increases. This is a consequence of large deformations that trigger geometrical non-linearity. Ignoring large deformations underestimates the torque by 5% for  $\theta = 90^\circ$  and up to 15% for  $\theta = 140^\circ$ . This stiffening effect is even greater when the GFRP element cannot retract axially (Fig.98 below).

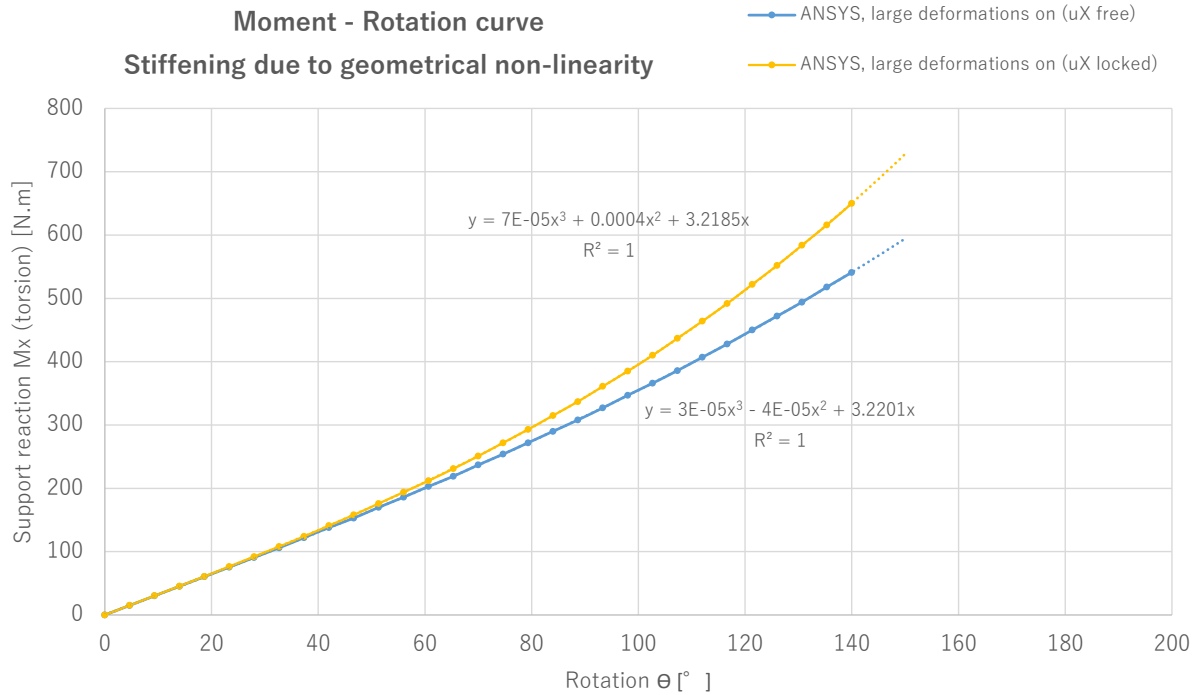


Figure 98 - Evolution of the support torque reaction for an increasing rotation angle: comparison of ANSYS calculations (large deformations) when locking the axial displacement or not, for an element made of 25 layers of 'Epoxy E-Glass Wet', L=2.5 m.

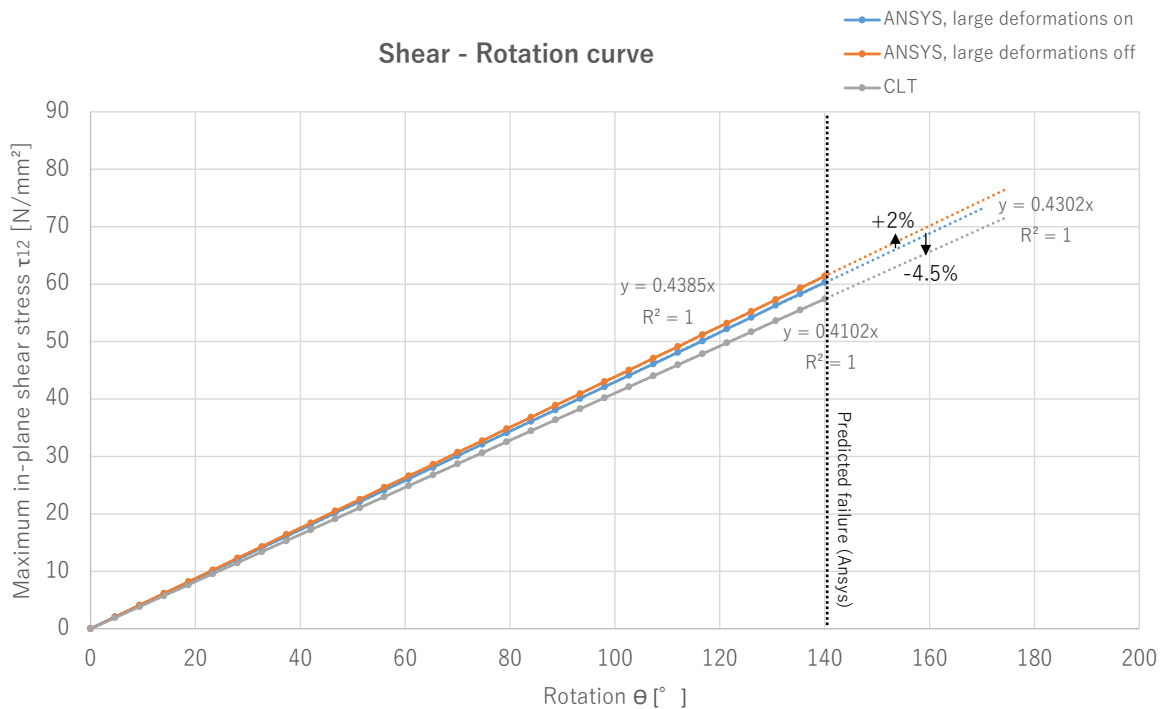


Figure 99 - Evolution of the maximum shear stress for an increasing rotation angle: comparison between predictions from the CLT and ANSYS with and without accounting for large deformations, for an element made of 25 layers of 'Epoxy E-Glass Wet', L=2.5 m.

Figure 99 represents the evolution of the maximum shear stresses induced by the torsion (on the outer layers) corresponding to the support reactions in Figure 97. Regarding shear stresses, all curves are close. In details, we observe again an increase in the linear elastic slope obtained from ANSYS (solid modeling and real geometry) compared to the CLT (2D infinite plate). Accounting for large deformations leads to 2% decrease of shear stresses, probably because of the deformed shape. However stresses are calculated for all the three curves according to a linear elastic constitutive law, and present comments are of interest only if this behavior is validated (which is not the case, see the discussion to come in section 4.5 'Torsion break test').

## 4 Laboratory testing

Composite solid modeling and FEM analysis performed taking into account effective boundary conditions and geometrical non-linearity showed a stiffening behavior of the system. A laboratory testing procedure was developed by the author in order to validate the torsional behavior suggested by the FEA. Tests were performed on 1:5 scaled elements. The first objective was to obtain experimental Torque-Rotation ( $T-\theta$ ) curves and fit a mathematical model to them in order to compare with ANSYS results, especially looking at the polynomial degree of the curve. A dedicated torsion test setup was built, reproducing the boundary conditions from Table 26. The second objective was to validate the range of rotations in which torsion breaks the element, i.e. when material strength is reached, and to observe the failure processes. Indeed both CLT and FEM calculations assumed a classical linear elastic behavior to calculate the stresses after solving for the deformations, while based on results from torsion break tests this hypothesis will be invalidated as it appeared that microdamages and permanent deformations occurred. The author carried out additional torsion relaxation tests to investigate non-elastic & non-linear effects.

GFRP specimens were fabricated to perform the tests. Unfortunately the laboratory could not have access to a material identical to the ANSYS fabric. Moreover hand-lamination allows only for a limited control on the amount of resin and small changes in thickness have a great impact on the laminate's mechanical properties (cf. the sensitivity analysis in section 2.5, especially Fig. 71 to 74). The author performed 3-points bending tests and shear tests beside the main procedure, so as to characterize the E-modulus and the in-plane shear strength of the laminated specimens, respectively impacting the bending and the torsional behaviors.

### 4.1 Scaling

For practical feasibility reasons, we worked on a scaled model. We chose to go from the 1:1 rectangular geometry to a 1:5 rectangular geometry, which was the mockup size (geometrical scaling).

However this is to take carefully, a geometrical scaling does not necessarily ensure a structural scaling, i.e. the behavior of the smaller elements is not ensured to be the same as the behavior of the bigger element. We must check if there is a possible structural scaling.

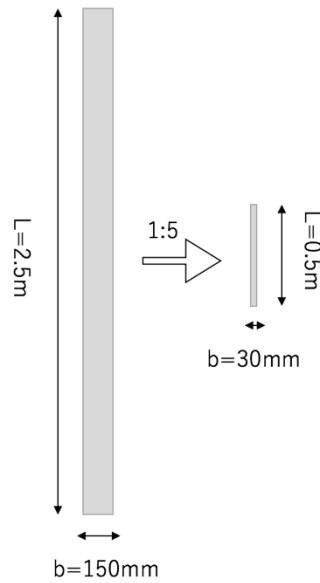


Figure 100 - 1:5 geometrical scaling of the facade modules

The required number of layers (and so the thickness of the laminates) is proportional to the length of the element because of the deflection criterion, applied as first design requirement:

$$\left\{ \begin{array}{l} w_{max} = \frac{q \left[ \frac{kN}{m^2} \right] * b * L^4}{384EI} = \frac{q \left[ \frac{kN}{m^2} \right] * \mathring{b} * L^4}{384E * \frac{\mathring{b} * t^3}{12}} \\ w_{lim} = \frac{L}{250} \end{array} \right.$$

$$w_{max} = w_{lim} \Rightarrow \frac{L}{t} = cst$$

Normal stresses are identical for both real-scale and reduced models (regarding the small flexural load the material is linear elastic):

$$\sigma_{1,max} = \frac{M_{bending}}{W} = \frac{q * \frac{L^2}{12}}{\frac{t^2}{6}} = \frac{q * L^2}{2t^2} = cst \text{ if } \frac{L}{t} = cst$$

As long as the behavior stays in the linear elastic domain, shear stresses generated by the torsional load are a linear function of the rotation. The maximum shear stress, occurring on the outer surfaces, is:

$$\tau_{max} = G * \chi * t = G * \frac{d\theta}{dx} * t = G * \frac{\theta}{L} * t$$

With  $t$  the total thickness of the laminate:  $t = t_{lamina} * n_{laminae}$ . For the full-scale element it comes:

$$\tau_{max,1:1} = G * \frac{\theta}{L} * t_{lamina} * n_{laminae,1:1}$$

We previously showed that the number  $n_{laminae}$  of layers required to satisfy the deflection criterion increases linearly with the length  $L$  of the modules:  $n_{laminae} = k * L$  where  $k$  is a constant.

For the 1:5 scaled element, it comes:

$$\tau_{max,1:5} = G * \frac{\theta}{L} * t_{lamina} * \frac{n_{laminae,1:1}}{5} = \tau_{max,1:1}$$

In-plane elastic maximum shear stresses are identical for both real-scale and reduced models, as long as the the material is in its linear elastic domain.

### Conclusion:

In the linear elastic domain, structural design of full-scale GFRP modules can be derived from analyzing 1:5 scaled elements, both bending and torsional behavior are accurately reproduced, i.e. identical stresses are generated.

About expected non-linearities, their mathematical form should be identical, however their magnitude won't be. This stands also for stress redistributions close to supports and edges, expected to have greater magnitude for bigger elements. However their influence on the failure criterion (Tsai-Wu) is neglectible regarding shear-driven failure (section 3.2.2).

## 4.2 Specimens fabricated

Two GFRP plates have been fabricated at the Composite Construction Laboratory. Rectangular strips (660mm\*30mm) are then cut into the plates. They were made a bit longer than the 500mm required by a 1:5 scaling in order to ensure sufficient extra-length for the grips in testing fixtures.

With previous ANSYS calculations using 'ANSYS Epoxy E-Glass Wet' theoretical material and a ply thickness of 0.5mm we estimated that 5 layers were necessary for the 1:5 element. Fabrics with properties as close as possible from those ones were picked at the lab, among the fabrics available. However we recall here that, along with the E modulus, the thickness of the laminate also plays a major role in the bending and torsional behavior. That's why we tried to slightly adapt the number of layers according to the material density and the lamination technique.

- The first plate is made of 6 layers of [V-type]<sup>1</sup> material. Hand lamination technique is used. The corresponding strips are named V1 to V4.

<sup>1</sup> Unidirectional E-glass fiber fabrics (EC 9-68), w=425 gr/m<sup>2</sup> (<https://www.swiss-composite.ch/pdf/Produkteuebersicht.pdf>)

- The second plate is made of 5 layers of [C-type]<sup>2</sup> material. (Despite a lower density, this material is thicker than the V material). Vacuum assisted resin infusion technique is used. The corresponding strips are named C1 to C5.

<sup>2</sup> Unidirectional E-glass fiber fabrics (Tissa), w=410 gr/m<sup>2</sup> (<http://www.tissa.ch/i4Def.aspx?tabindex=0&tabid=582&lang=en>)

The hand-made lamination process is the following: the first step is to cut pieces of fibers according to our needs, in terms of dimensions and fiber directions. Then we prepare the matrix mix: epoxy resin (Biresin CR83, Sika®) and hardener (Biresin CR83-2, Sika®) are mixed in 3:1 proportions in weight. The table has to be perfectly horizontal. It is covered with a material (plastic sheet here) protecting it (which can also be chosen to give a specific texture to the laminate) and if necessary sprayed with release agent (HP7, Marbocote Ltd.) so that the laminate won't stick once cured. We position the first layer of glass fibers (the reinforcement material) and saturate it with a first coat

of the cold-curing resin (the matrix material). Rollers are used to obtain homogeneous impregnation. We repeat this process layer by layer until we reach the required thickness/number of layers.

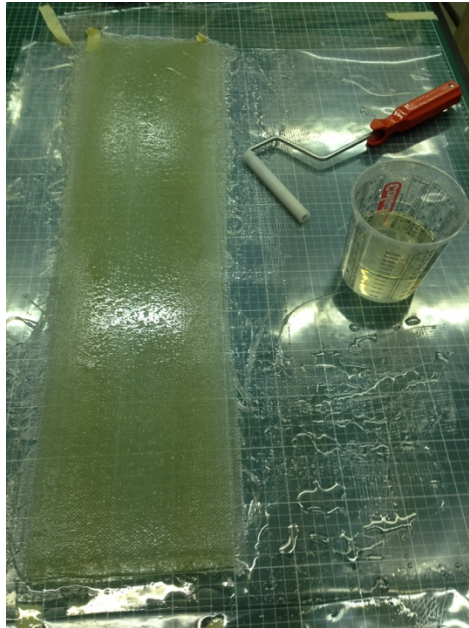
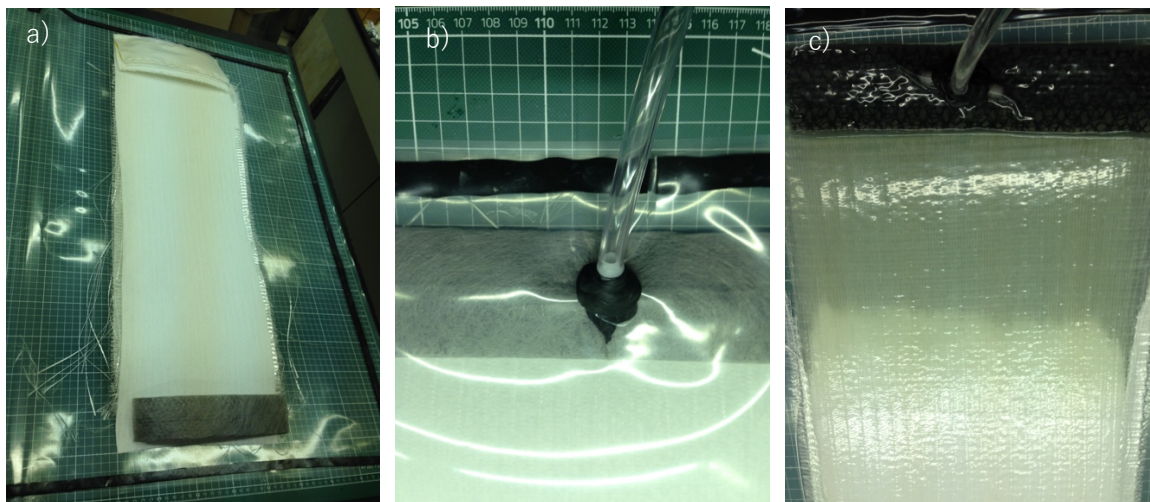


Figure 101 - Hand-lamination (V-type specimens): layers of fabric are impregnated one by one with the matrix mix, excess is evacuated with the roll – Picture J.Baehr-Bruyère.

Vacuum infusion technique differs from hand lamination as the layers of fabric are stacked together without resin on a plastic bag that will be sealed with tape. A bleeder recovers the layers of fabric to absorb excess resin during the process. Once the bag sealed, a tube connected to a pump sucks the air out, progressively replaced by the resin. This technique leads to thinner plies than hand lamination.



Figures 102 a to c - Vacuum infusion technique, (a) Layers are stacked together without resin, a diffuser and an absorber are added to then ensure a good spread of the resin, (b) Insertion of the tube for the resin and sealing of the vacuum bag, (c) Resin impregnation process - Pictures J. Baehr-Bruyère.

For both techniques the laminates need at least 24h curing at ambient temperature, before finalizing the cure in the oven. In case of vacuum infusion, the ambient temperature cure is done under maintained vacuum condition (or at least 15-20h on the 24h). After 24h cured, the plates are

removed from the lamination table and put into the oven for 6 hours at 70° C to obtain a fully completed cure. Finally the pieces are cut with a high-pressure waterjet sanding machine to realize strips.

### 4.3 Characterization of the material in bending

Young modulus of the specimens was estimated by means of three point bending tests performed on an universal electromechanical testing machine (LFM C50kN). The experimental setup and support conditions are presented in Figure 103 below. The length between the supports is  $L = 42$  cm. The specimens were loaded until a load  $P = 10$  N, definitely staying in the elastic domain of the material. The experiment is displacement-controlled. The displacement is increased at speeds  $V_c=0.5$  mm/s and  $V_v=0.1$  mm/s resp. for C-type and V-type specimens. Load and relative vertical displacement of the machine are recorded.

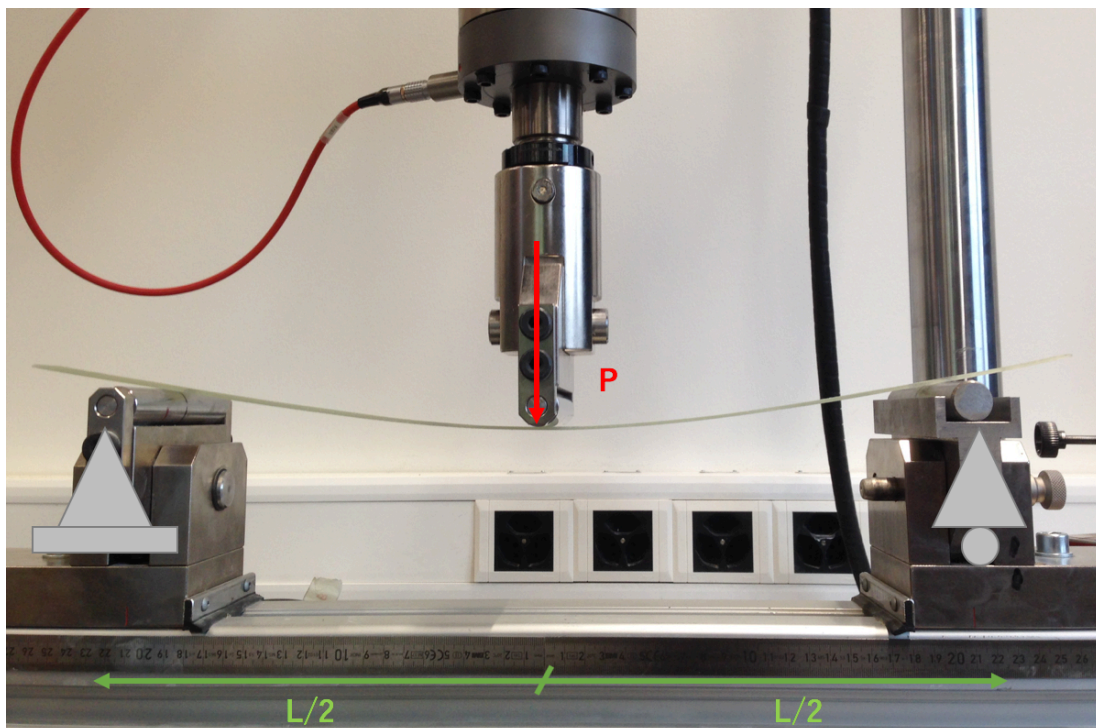


Figure 103 - Experimental setup for the 3-points bending test - Picture J.Baehr-Bruyère.

Results dataset are plotted and the slope is estimated with a linear regression. The Load-Displacement curves are in Appendix VIII. Example for sample C1:

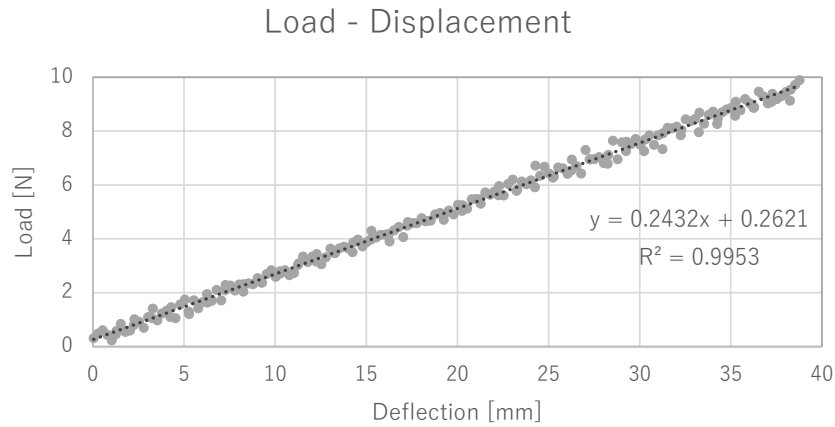


Figure 104 - Experimental load-displacement curve from 3-points bending test on sample C1

The laminates are unidirectional, the deflection at mid-span is calculated as  $w = \frac{PL^3}{48EI}$  where E is the Young modulus and I the inertia of the cross-section:  $I = \frac{bt^3}{12}$ . We derive  $E = \frac{PL^3}{w*48I}$ , with  $\frac{P}{w} = s$  the slope of the elastic Load-Displacement curve obtained from the 3 Points Bending test. The Table 30 below summarizes the results for the tested specimens.

Specimen	V1	V2	V3	V4	C1	C2	C3	C4	C5
Mean total thickness t [mm]	2.65	2.70	2.93	2.70	1.80	1.80	1.77	1.73	1.80
Mean layer thickness $t/n_{layers}$ [mm]	0.44	0.45	0.49	0.45	0.36	0.36	0.35	0.34	0.36
E modulus [Gpa=kN/mm <sup>2</sup> ]	-	-	22.7	25.9	25.7	-	-	27.5	23.8
Bending stiffness EI [kN.mm <sup>2</sup> ]	-	-	1'427.3	1'274.6	375.4	-	-	356.5	346.7

Table 30 - E-modulus measured with the 3-points bending test and calculated bending stiffness

All samples have similar E modulus, globally  $E \sim 25$  Gpa.

We would have expected to reach  $E \sim 35$  Gpa under those lamination conditions. The glass fabrics available at the lab are not stiff enough to be directly compared to the 1:5 scaled Ansys model. However the bending stiffness V of V samples is the same than for the theoretical ANSYS material:  $EI_{th} = \frac{35*30*(5*0.5)^3}{12} = 1367.2 \text{ kN.mm}^2$ , demonstrating again how a small variations in thickness counterbalances the too low E and stiffens the element. V-type samples satisfy bending criterion under wind load.

Following the rule of mixtures:

$$E_1 = V_f * E_f + (1 - V_f) * E_m$$

And given standard Young modulus values for E-glass unidirectional fabric and epoxy resin:

$$E_f = 70 \text{ GPa}, E_m = 3.5 \text{ GPa}$$

We can estimate fiber and matrix volumic fractions ( $V_f$  and  $V_m$ ) for the theoretical material:

For  $E_1 = 35 \text{ GPa}$ ,  $V_f = 47.4\%$  and  $V_m = 52.6\%$ , which is closer from ranges obtained by hand-lamination. Indeed the hand-lamination process usually leads to fractions ~35to50% fibers and ~50to65% resin while vacuum infusion process leads to ~65% fibers and ~35% resin.

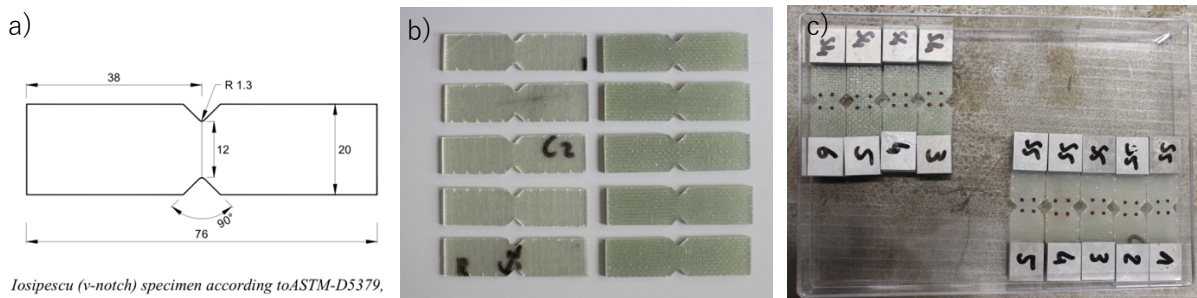
NB: considering the latter comment, we would have expected a higher E with the vacuum infusion process. It is probable that the E of the V-type fabric is greater than the E of the C-type fabric.

#### 4.4 Characterization of the material in pure shear

It is not possible to obtain directly the shear resistance from measurements during a torsion test. Even though the shear strain could be measured by gluing orthogonal gauges on the specimens, the shear stress cannot. The determination of the  $\{\gamma_{12} - \tau_{12}\}$  relation in torsion would require a reverse analysis with finite elements and iterations to approach numerically the observed physical behavior.

To obtain the value of the material shear strength  $\tau_{12,max}$ , pure shear tests were run following the Iosipescu test method and performed with a MTS 25kN universal testing machine. The machine has an integrated load cell that applies a vertical force. The experiment is displacement-controlled, such that the vertical displacement of the machine is 0.01mm/s.

The samples are cut in the C2 and V1 strips (cf. Table 30). They have the following normed shape:



Iosipescu (v-notch) specimen according to ASTM-D5379.

Figures 105 a to c - Shear test specimens, (a) Standardised Iosipescu shear test specimen, from [40], (b)&(c) Cut and preparation of the C-type and V-type specimens

As the samples were cut in thin GFRP strips, thick aluminium tabs were glued at the end to increase the contact surface in the load transfer zone of the setup Figure 106. Dots were printed at the center of the specimens, at the corners of a square of size 6mm, to measure the shear strain by a video extensometer (Sony XCLU100 CCD camera). Snapshots are also recorded every 10 seconds.

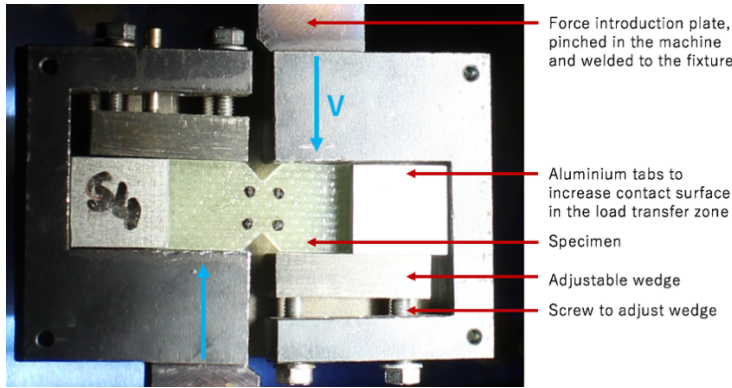


Figure 106 - Shear test setup, initial state - Picture J.B.B.

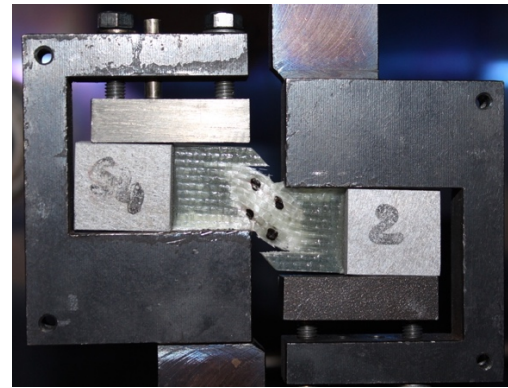


Figure 107 - Shear test setup, final state - J.B.B.

The calculation of the angular shear deformation  $\gamma$  is explained below:

$$\gamma = \alpha + \beta, \text{ with } \alpha \approx \tan(\alpha) = AA'/AC \text{ and } \beta \approx \tan(\beta) = DD'/CD$$

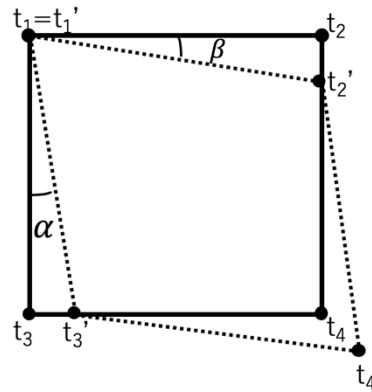
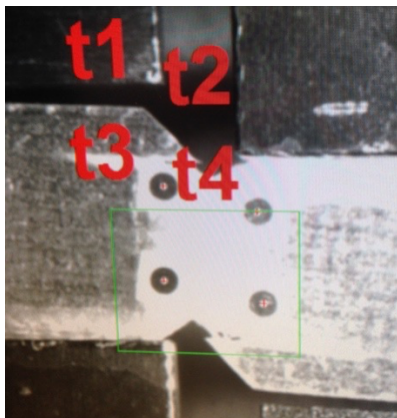


Figure 108 – Principle of the measurement of the angular shear deformation by means of video extensometer

The shear stress is obtained by dividing the vertical load by the cross-section area at the notch location:  $\tau = \frac{V}{t \cdot b_{notch}}$ , with  $b_{notch} = 12 \text{ mm}$ . The  $G_{12}$  modulus can be calculated from the slope of the elastic region of the shear stress-strain curve:  $\tau = G \cdot \gamma \Leftrightarrow G = \frac{\tau}{\gamma}$ . The torsional stiffness of the 1:5 strips ( $b=30\text{mm}$ ) is calculated afterwards. Stress-Strain results for the tested samples are provided in Table 31 below and plots are provided in Appendix IX. Empty columns refer to defective samples.

Specimen	Sv1	Sv2	Sv3	Sv4	Sv5	Sv6	Sc1	Sc2	Sc3	Sc4	Sc5
t [mm]	2.65	2.65	2.65	2.65	2.65	2.65	1.80	1.80	1.80	1.80	1.80
$\tau_{12,max}$ [Mpa]	>52	-	-	58.5	60.8	61.5	59.0	61.1	59.8	56.7	-
$G_{12}$ [Gpa]	1.0	-	-	0.9	1.71	1.0	1.30	0.46	0.60	0.65	-
Torsional stiffness GJ [kN.mm <sup>2</sup> ]	183.9	-	-	171.4	319.2	187.9	76.1	26.6	35.0	38.1	-

Table 31 – Results from shear tests. 'Sv' stands for a V-type sample, 'Sc' stands for a C-type sample.

Example plot is given below for sample Sv5 in figure 109.

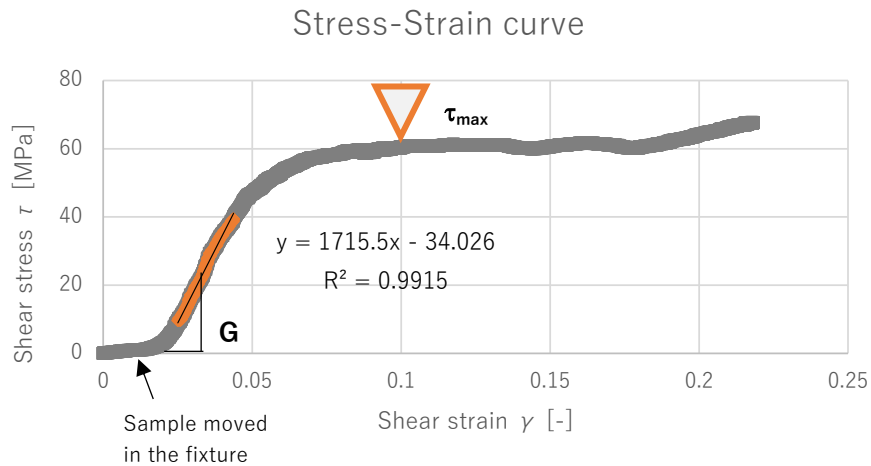


Figure 109 - Experimental stress-strain curve from pure shear test on sample Sv5

All samples have similar shear strength,  $S = \tau_{12,max} \cong 60 \text{ MPa}$ . This is consistent with the ‘ANSYS Epoxy E-Glass Wet’ (cf. Table 27). It is not surprising that both V and C type materials have the same shear strength, as behavior and failure are mainly matrix-driven and the same resin mix was used for both. Figure 110 shows typical damages in the specimens after failure. Failure mode is mixed and starts from the notch region, that is the weakest: firstly a brittle axial split occurs in the matrix due to stress concentration in the notch, along with small damages of the matrix in the central zone. Then the small cracks join to form bigger ones along the fiber/matrix interface. Sometimes the loading block directly pushes on the sample instead of the aluminium tabs and provoques compressive crushing.

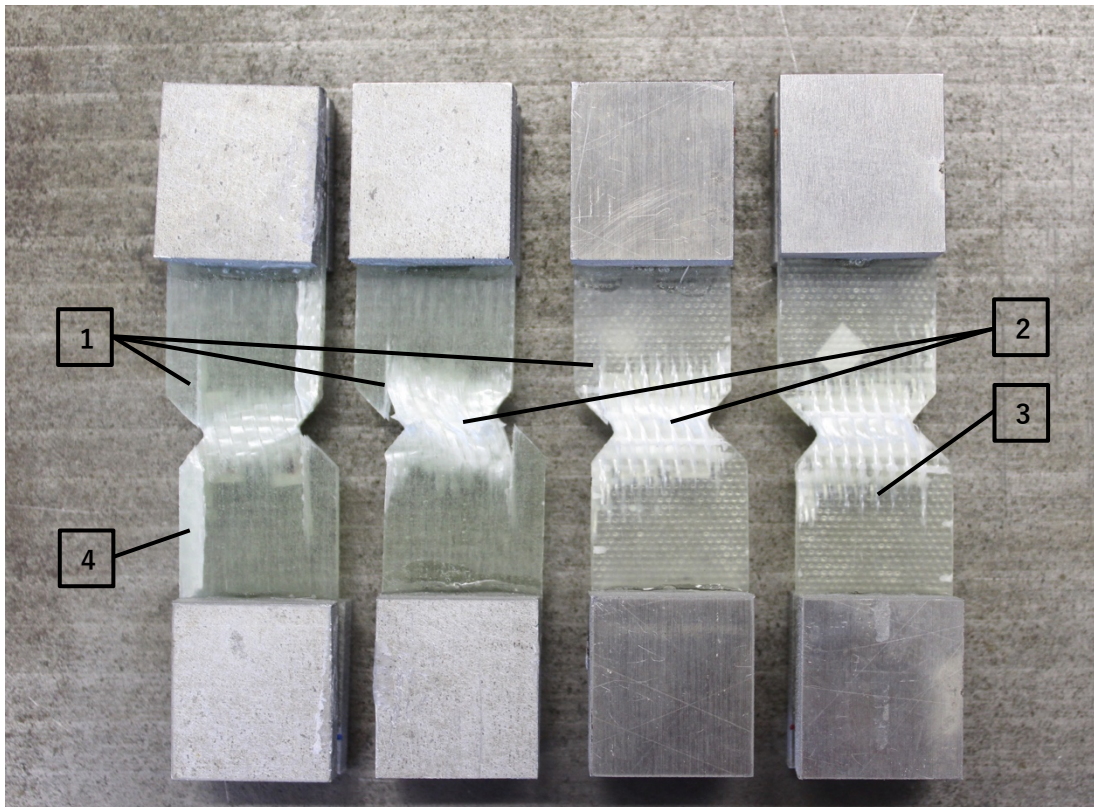


Figure 110 - Typical failure observed on the specimens (left: V-type ; right: C-type). Numbers refers to the modes in Fig.111 - Picture J. Baehr-Bruyère

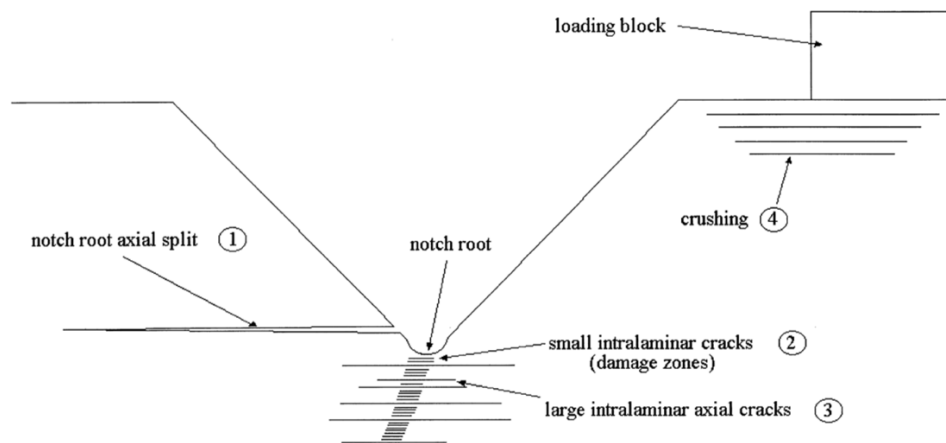


Figure 111 - Failure modes observed with the Iosipescu shear test, from [41]

Theoretically, the  $G$  modulus ( $G_{12}$ ) can be derived from the slope of the shear stress-strain curve in the elastic domain:  $G = \tau/\gamma$ . The  $G$  values calculated, resumed in previous Table 31, are extremely low, between 0.5 and 2.0 Gpa. This is not consistent with expectations, around 5 Gpa for unidirectional GFRP laminates. The fixture was not well adapted for thin samples. The aluminium tabs glued to increase the contact zone prevented the samples to tip over during loading but some sliding and out-of-plane deformations occurred, skewing the shape of the curves. This is visible on the experimental curves in Appendix IX. The fixture is suited for thicker samples, typically 10 to 15 mm thick.

#### 4.5 Torsion break test

A special fixture was designed and built with the help of the civil engineering technicians in order to perform torsion tests on the specimens. The element is clamped at each end in between steel plates, themselves tightened by screws. The whole is linked to a steel rod. On the right side the rod can rotate freely ; this is where the external torsion is applied, by means of a crotch. On the left side the rod can rotate too except that it ends up with a perpendicular steel bar, itself leaning on two load cells. When some torsion is applied, one of the load cell (depending on the sense of rotation) undergoes compression. The torque (support reaction) is calculated as the compression force multiplied by the lever arm in between the supports, i.e. 100mm. The total rotation of the specimens is measured by an inclinometer magnetised to the right side rod. All data is collected and visualized with the software CatMan.

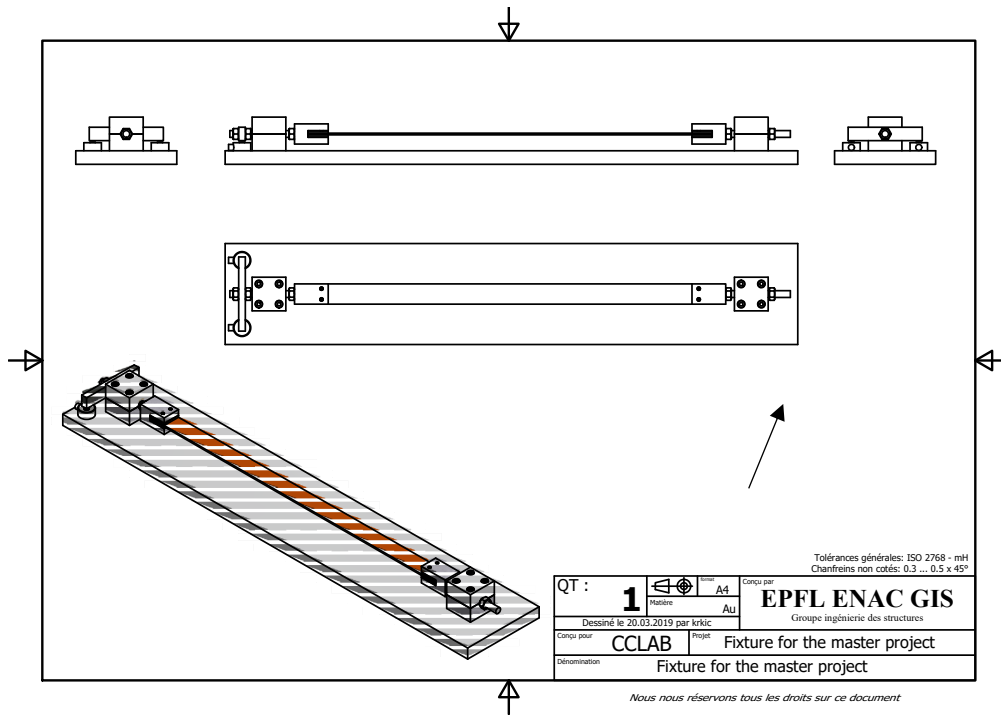
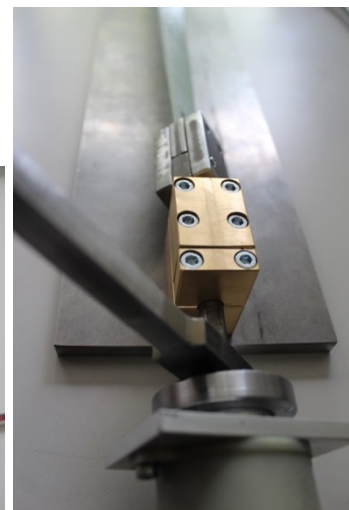
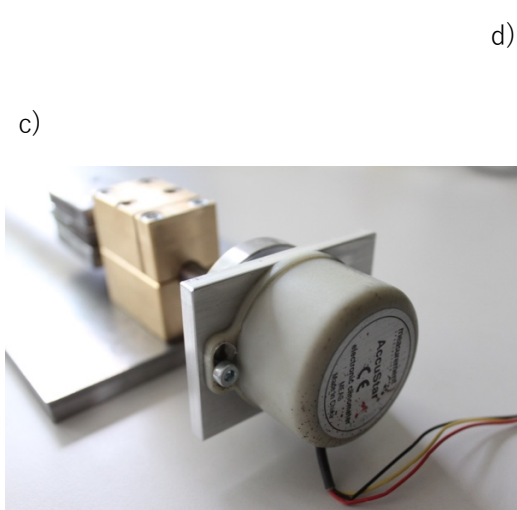


Figure 112 - Technical sketch of the torsion test fixture developed for the project - Courtesy of EPFL ENAC GIS



Figures 113 a to d – (a)Torsion test fixture (b)load cells (c)inclinometer and (d)crotch tool used to rotate the element – Pictures J.B.B

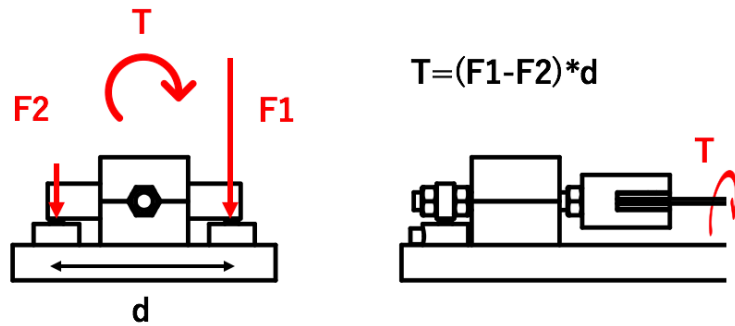
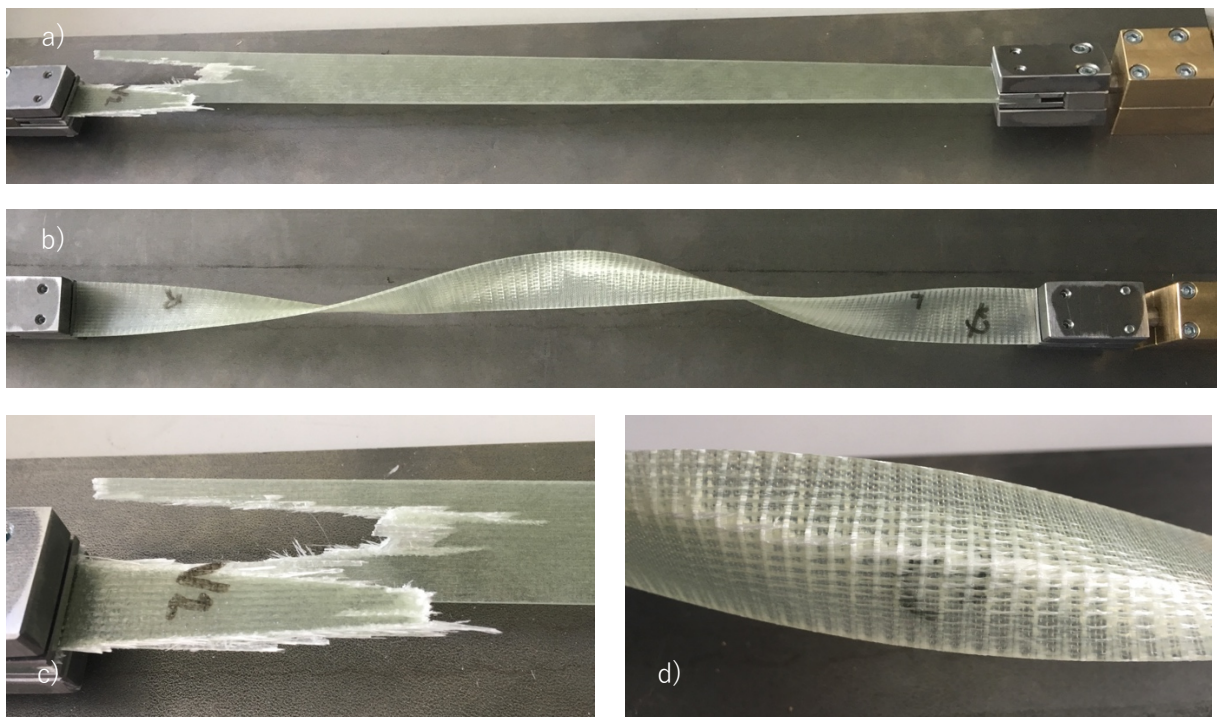


Figure 114 - Calculation of the torque based on the measurement of the forces in the load cells

At the beginning of each test both load cells and the inclinometer are set to zero. Performed measurements are relative to this zero. Data is recorded with a 0.1sec time step. NB: the inclinometer can perform a maximum 120° rotation ; additional screws allow to block the system during a test in order to reset the inclinometer and continue twisting.

Torsion break tests are performed on strips V2 and C3. Below are pictures of the failure modes followed by plots of the experimental results:



Figures 115 a to d – (a)&(b) Failure modes of resp. specimen V2 at the top and C3 at the bottom, (c)&(d) Zoom on the damaged zones - Pictures J. Baehr-Bruyère

Specimen V2: Failure occurred due to stress concentration in the support zone. The failure was brittle. At the edges of the support, the laminate failed in both transverse crushing of the matrix and tension/compression in the longitudinal fibers. In the force introduction zone, fibers failed either in tension or in shear along the stress propagation path. This is a mixed failure mode, that must be seen in relation to this specific system, i.e. this is not a failure mode typical of the material itself.

Specimen C3: We observed a global torsional buckling response and a progressive matrix-driven failure. Shear failure occurred in the matrix and progressed through the layers. During the same

time, transverse bindings failed in tension. When the interface (or interphase, Fig. 116) was reached, the fibers were on their own to carry the shear load and could not transfer it along the element anymore.

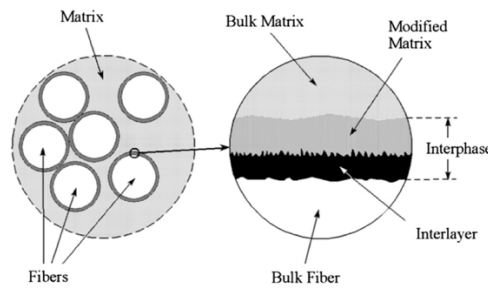


Figure 116 - Outline of the fiber/matrix interphase, from [42]

Figures 117 and 118 hereafter plot the experimental results of those two torsion break tests. The blue curves correspond to the collected measurements. For V2 brittle failure occurred for a 394° rotation. For C3 the failure was progressive and the sample finally macro-cracked for a 363° rotation.

A similarly scaled GFRP element was simulated in ANSYS (i.e. five layers of ‘Epoxy E-Glass Wet’ UD material and a specimen length simulated at 630mm to be consistent with laboratory specimens V2 and C3). Mathematical models were fitted to the experimental and ANSYS torque curves. All required a polynomial fit with degree 3 to obtain acceptable regression coefficients R<sup>2</sup>. The fit equations are provided below, where T is the torque in N.mm and θ the rotation in ° :

$$T_{V2} = 0.0003 \theta^3 - 0.0219 \theta^2 + 37.281 \theta$$

$$T_{C3} = 0.0003 \theta^3 + 0.0025 \theta^2 + 10.901 \theta$$

$$T_{ANSYS} = 0.0003 \theta^3 - 0.0007 \theta^2 + 20.368 \theta$$

The initial part of the curves is linear (no geometrical or material non-linearity in the behavior), as the deformations are small and the material is elastic. The [0-90° ] range is used to estimate the initial slope s by linear regression. The G modulus is derived from this slope:  $T = G.J.\chi$  with  $J = \frac{bt^3}{3}$  and  $\chi = \frac{\theta[^{\circ}] * \frac{\pi}{180}}{L}$  the curvature, L being the length between the supports,  $L = 630 \text{ mm}$ .

$$\text{It leads to } G = \frac{T}{\chi} * \frac{1}{J} = \frac{T}{\theta[^{\circ}]} * \frac{180}{\pi} * \frac{L}{J} = s * \frac{180}{\pi} * \frac{L}{J}$$

Specimen	Theoretical material (ANSYS)	V2	C3
Thickness t [mm]	2.50	2.70	1.77
Slope s [N.mm/° ]	-	38.8	12.8
G <sub>12</sub> [Gpa]	4.7	7.1	8.3
<b>Torsional stiffness GJ [kN.mm2]</b>	<b>734.4</b>	<b>1401.2</b>	<b>461.3</b>

Table 32 – Study of the linear range of torsion break tests and comparison with the torsional characteristics of the theoretical material ‘ANSYS Epoxy E-Glass Wet’

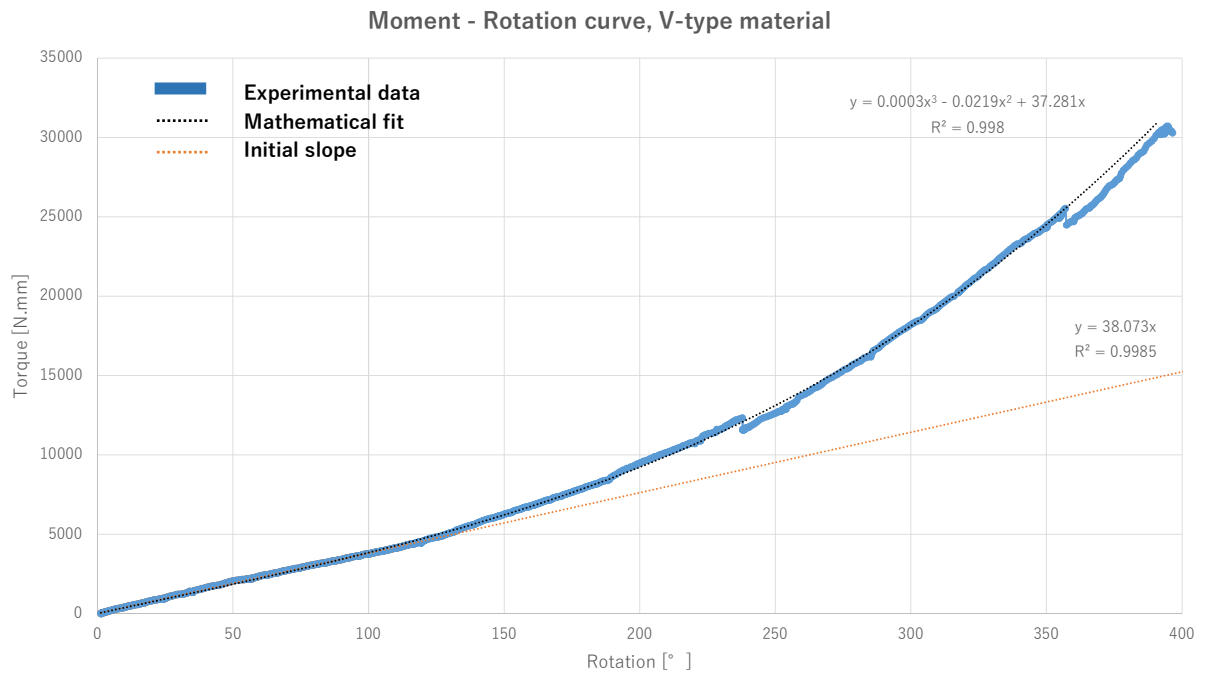


Figure 117 – Torsion break test: evolution of the torque force in sample V2 for an increasing rotation angle (speed: 5° /sec)

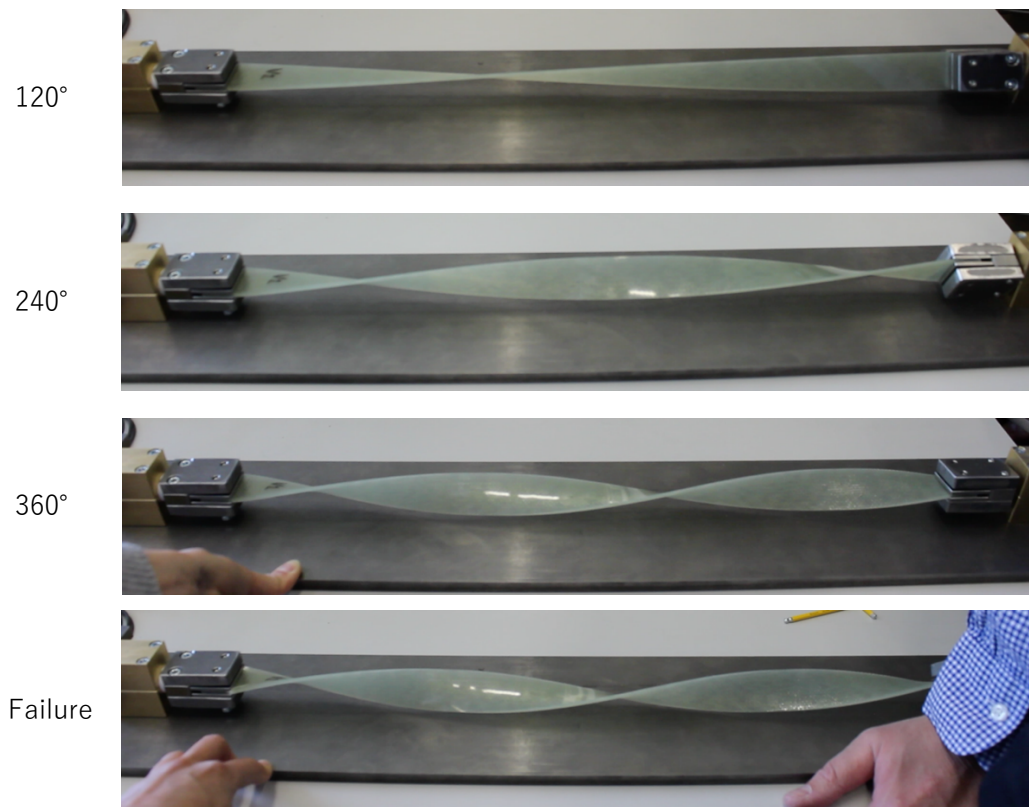


Table 33 - Torsion break test: rotation steps for sample V2 - Pictures J. Baehr-Bruyère

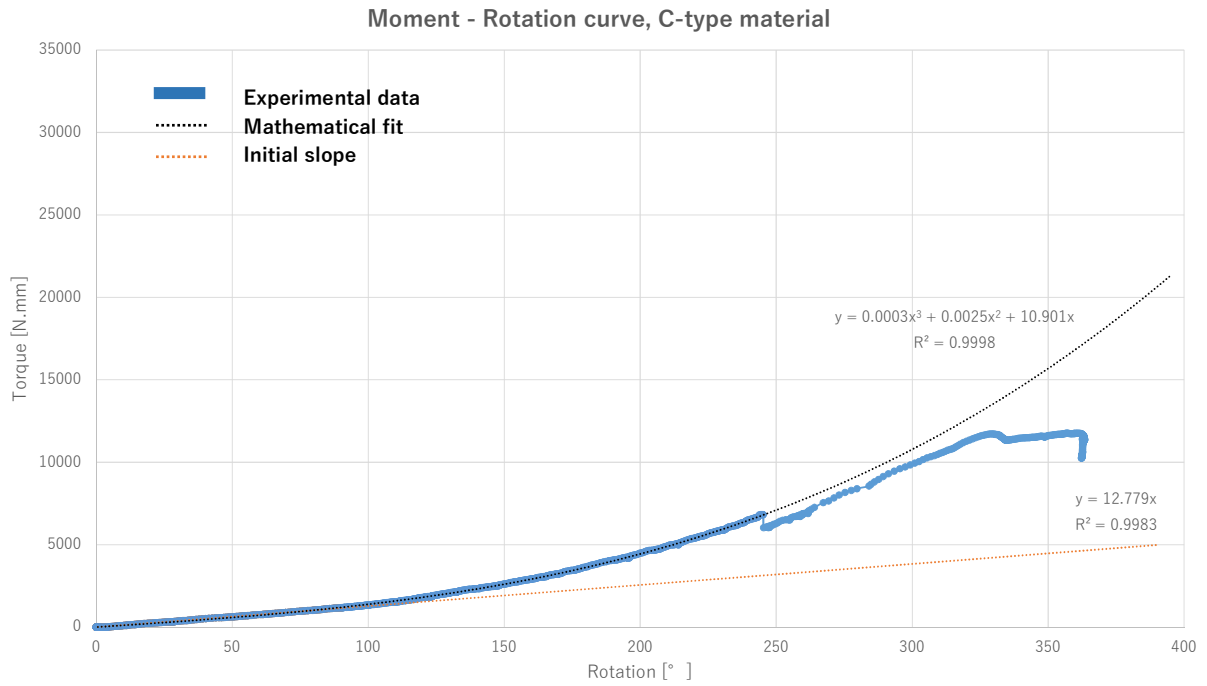


Figure 118 - Torsion break test: evolution of the torque force in sample C3 for an increasing rotation angle (speed: 6.5° /sec)



Table 34 - Torsion break test: rotation steps for sample C3 - Pictures J. Baehr-Bruyère

The experiments confirm the cubic relation between the applied torque force and the rotation highlighted by ANSYS calculations accounting for large deformations (see section 3.2.3, Fig. 97). We recall from section 4.1 ('Scaling') that the magnitude of those geometrical non-linear effects measured on real-scale and mockup elements cannot be compared as is.

The two experimental curves (Fig. 117 and 118) and the calculated ANSYS curve are superposed, Figure 119 hereafter. The hierarchy of the curves is in agreement with the different torsional stiffnesses from Table 32. For rotations higher than 90° , the cubic term in the equation starts governing. Experiments confirm the characterization of geometrical non-linearity highlighted in Fig. 97section 3 ('FEA analysis') when comparing ANSYS results to CLT results for the full-size element. Again, be aware that this behavior is a property of the studied geometry and boundary conditions, not of the material itself.

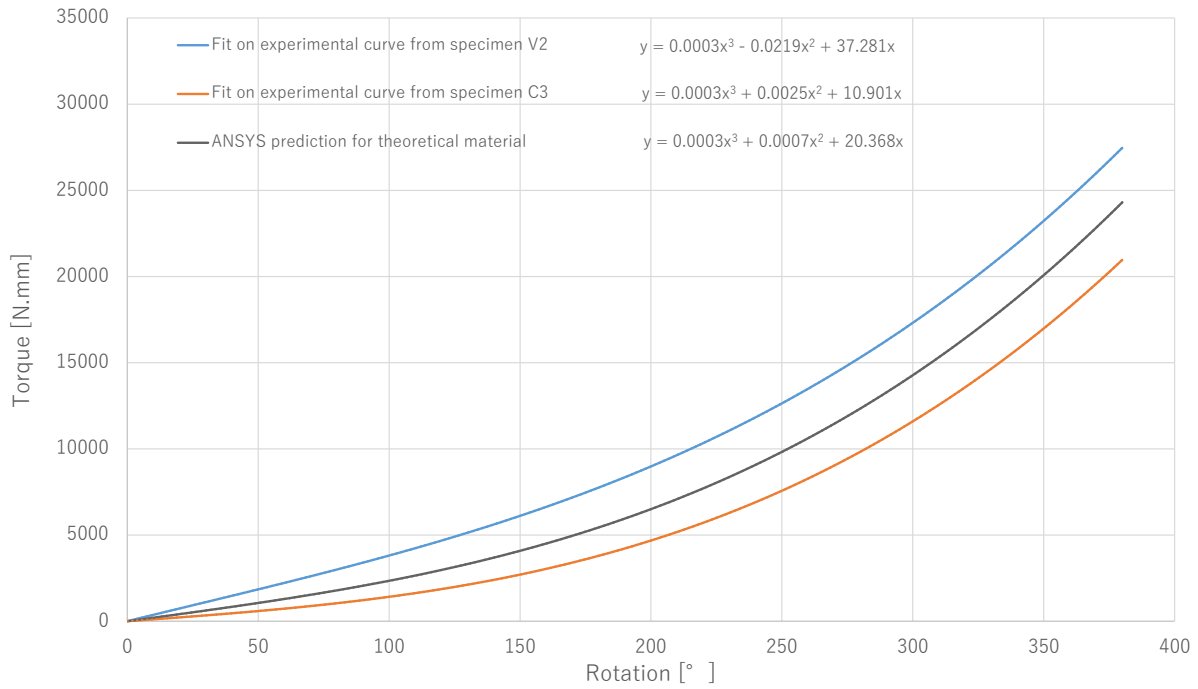


Figure 119 – Superposition of the torque-rotation curves obtained from either a mathematical fit on experimental data from torsion break test (samples V2 and C3), either from FEA analysis with ANSYS on theoretical material.

The shear strength of both V and C type materials was measured in section 4.3 (‘Characterization of the material in pure shear’):  $\tau_{12,max} \cong 60 \text{ MPa}$ . Knowing the shear strength, a quick estimation of the maximum achievable rotation can be calculated, by hand.

$$\theta_{max} = \frac{\tau_{12,max} * L}{G * t} * \frac{180}{\pi} [^\circ]$$

The estimation is made by hand as we cannot simulate the laboratory specimens in Ansys because too many material parameters remain unknown to run simulations. As discussed regarding Fig. 99 in section 3.2.3, if GFRP indeed behaves in linear elasticity when twisted the shear stresses calculated under the ‘thin plate’ hypothesis deviate from FEA results by less than 5%. Moreover, we demonstrated in section 4.1 (‘Scaling’) that mockup laminates designed with a scaled number of layers were subjected to identical stresses as real-scale laminates (L=2.5m), as long as the material is linear elastic. Hence for the theoretical material, the maximum rotation is the one determined with FEA calculations on the full-size element (see 3.2).

Specimen	Theoretical material	V2	C3
Estimated rotation at failure	140°	114.6°	147.4°
Effective rotation at failure (break test)	-	394°	363°

Table 35 – Comparison between expected and measured maximum rotations at failure

It jumps out, the elements can support rotations higher than expected! (3.4 times higher for V2 and 2.4 times higher for C3).

→ **The linear elasticity hypothesis is not valid for GFRP material subjected to high torsional shear strain.**

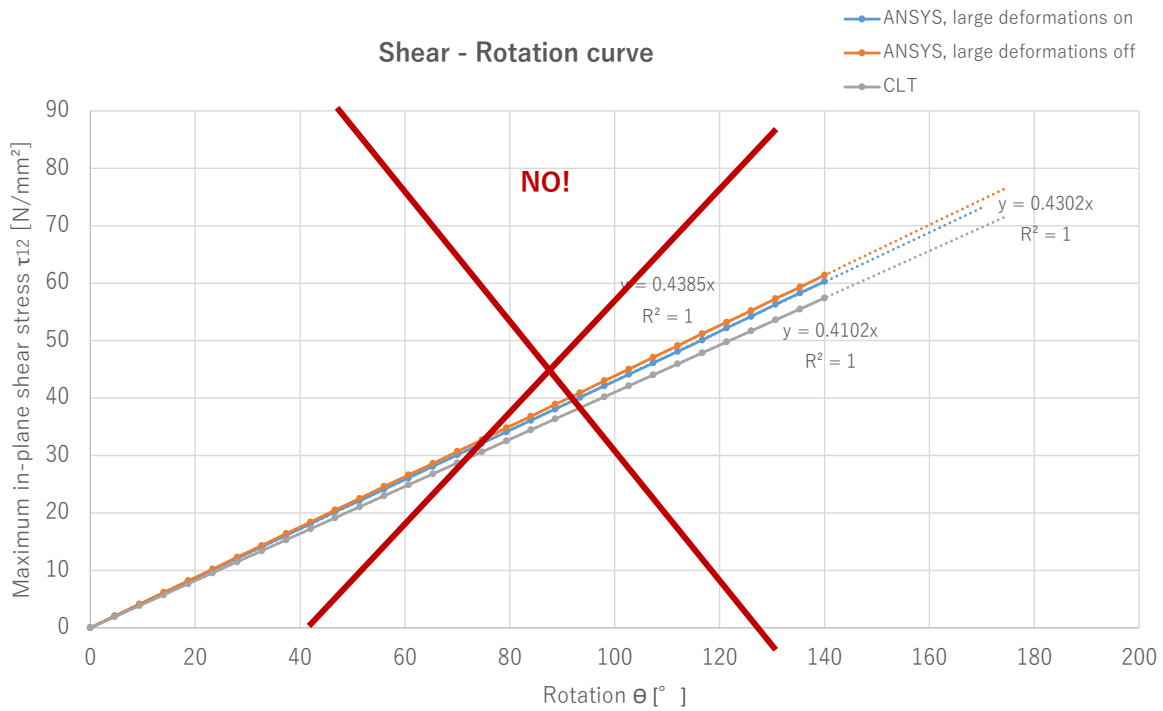


Figure 120 - The linear elasticity hypothesis is not valid for GFRP material subjected to high torsional shear strain.

Calculations of shear stresses (CLT, ANSYS) performed until here are not valid and visibly lead to an anticipated prediction of failure. If the newly exhibited rotation capacity sounds like a good new, it also means that the material exhibits some plasticity, which the author imagine in relation to the polymeric nature of the matrix and probable permanent rearrangements of its micro-structure. No scientific literature was found on this specific topic, despite a broad reading. The author suggests to concentrate further efforts on the implementation of a damage model to account for the progressive microdamage and softening of the material in the modeling of the structural behavior. A typical form of continuous damage model is the following:

$$C = C_0(1 - D)$$

where C is an elastic constant (would be the stiffness modulus G in our case) and D is the damage factor. D could be dependent on the shear strain in our case, and other parameters; D must be derived from physical measurements.

Along with this characterization, undesired effects driven by permanent changes affecting the material have to be quantified. Looking closer at the torsion break test curves Fig. 117 and 118, potential undesired effects show up. We notice some jumps in the measurements. Every 120°, the system is locked at the current rotation to reset the inclinometer. This process takes time, around 1 minute. The higher the rotation (and the torque load), the higher the jump. This behavior is typical from relaxation, i.e. a reduction of the stresses under constant deformation. Along with creep, relaxation is a time-dependent behavior typical of viscoelastic materials.

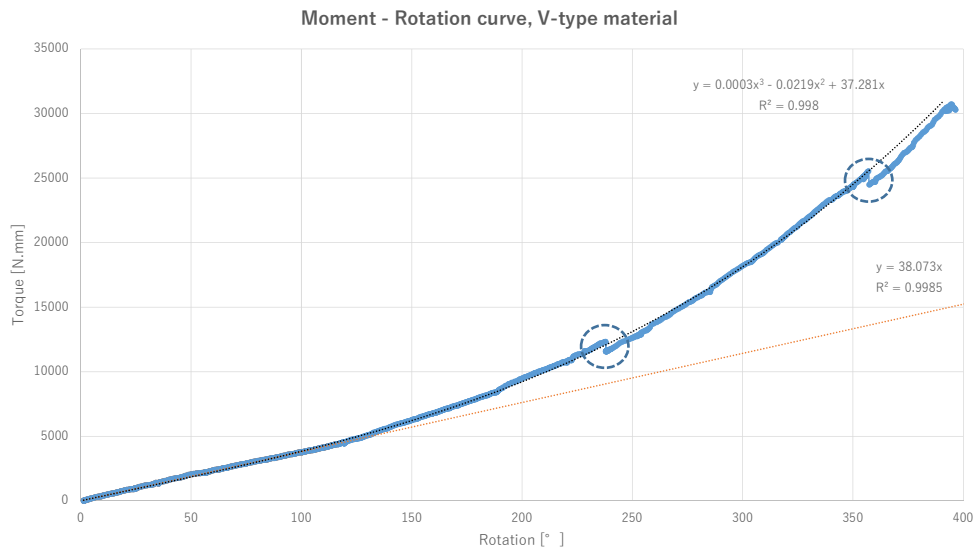


Figure 121 - Relaxation 'jumps' every 120° (system paused and locked) during torsion break test

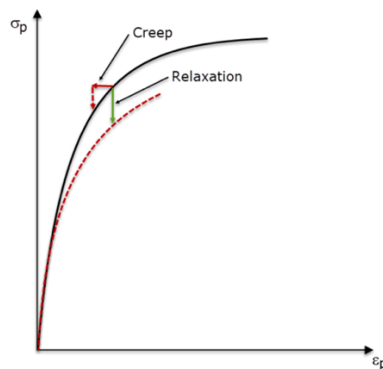


Figure 122 - Illustration of relaxation and creep phenomena

(source: <https://www.dlubal.com/fr/support-et-formation/support/base-de-connaissance/001529>)

## 4.6 Torsion relaxation test

The author developed torsion relaxation tests to confirm properly the occurrence of relaxation and characterize it. The setup is identical to torsion break test (section 4.5). The elements, originally flat, are placed in the fixture and measurements are initialized. C-type specimens were used. According to torsion break tests, the behavior of V-type material is reasonably expected to be similar regarding relaxation.

Test 1 investigates the response to several load levels (i.e. rotations of 45,90 & 135° ). Each level is maintained during 30 minutes, locking the fixture by means of the dedicated screws. The sample is unloaded previous to loading to the next level. The load history is detailed in Figure 123 and the resulting Torque-Rotation diagrams are provided Figure 124.

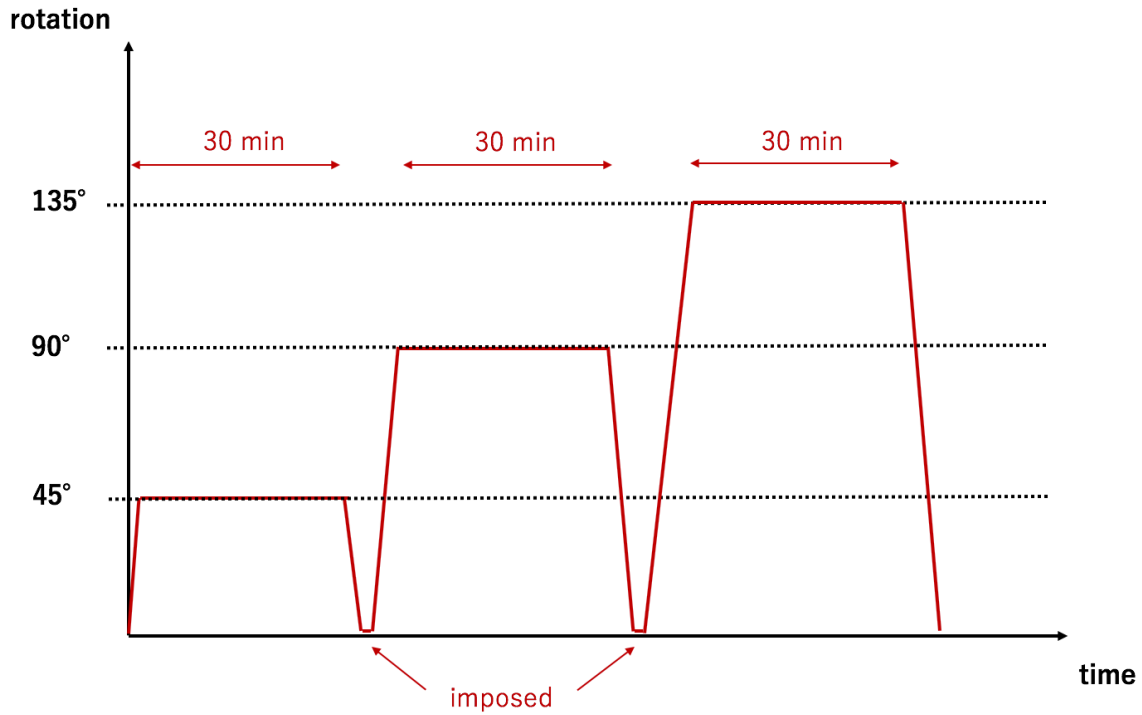


Figure 123 - Torsion relaxation test 1: history of imposed deformation

Cyclic loading with increasing maximum load

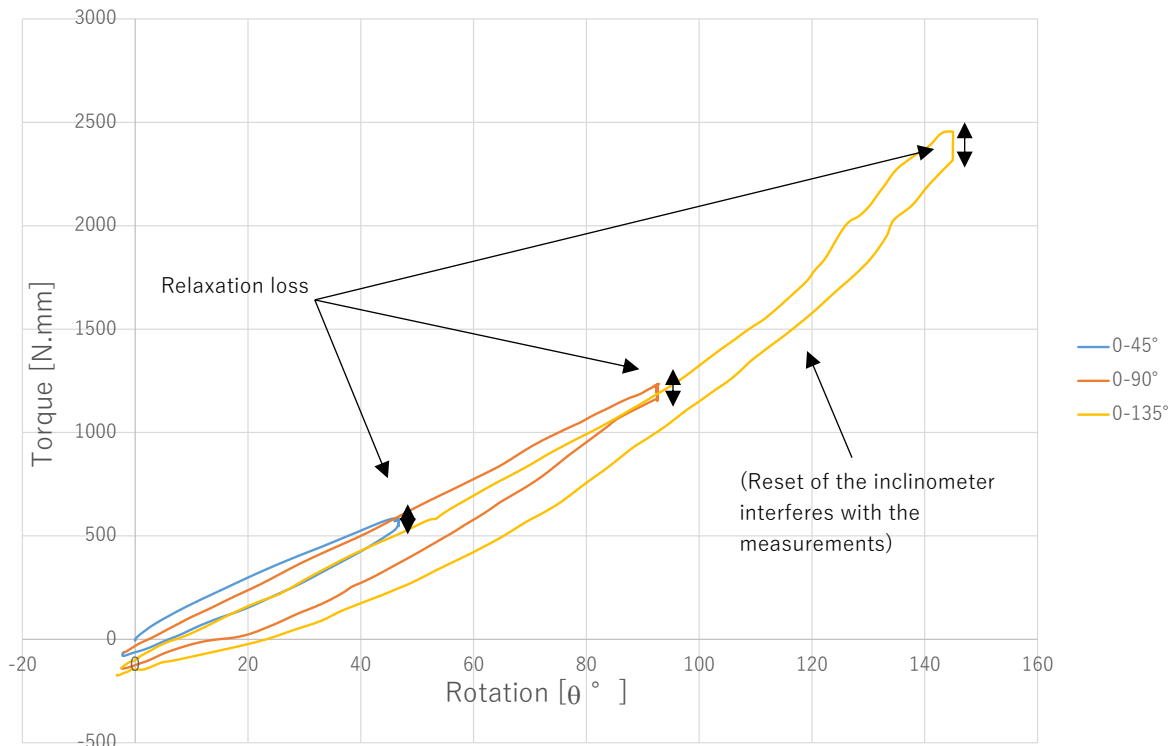


Figure 124 - Torsion relaxation test 1: relaxation losses for a C-type sample loaded and unloaded three times up to 45, 90 and 135°

All the three curves from test 1 have similar initial slope, there is no loss of stiffness induced by the cyclic loading which is a good point. Torque-Rotation relation is linear for the loadings up to 45° and 90° , while the 135° level highlights the cubic ( $x^3$ ) stiffening behavior described in the analysis of torsion break tests. Note that for the 135° level corrections were made to take into account the

reset of the inclinometer (maximum range  $120^\circ$  , hence the curve becomes messy after this point). Relaxation is visible: the torque diminishes under constant deformation during the locked stages. The absolute torque loss increases with the deformation level, however the loss is rather stable in terms of percentage of the torque value: 5.2%, 5.7% & 5.5% for resp. the first, second and third cycles. Permanent deformations seems to occur, as an extra, reversed, torque is needed to get the element back to its  $0^\circ$  flat state. Apparent permanent deformation also increases with each cycle (lots of experimental data are needed to say more on the increase).

Test 2 performs cyclic loading from  $0^\circ$  to  $90^\circ$  . The element is twisted up to  $90^\circ$  and locked in this position. After 5 minutes, screws are released and the sample is brought back to  $0^\circ$  by the operator, who controls the speed by hand with the crotch. Finally the operator removes the crotch and the sample is free to rotate. This two-steps release allows to differentiate elastic strain (i.e. can be recovered) from permanent strain. The process is repeated 3 times (cycles 1 to 3), the load history is detailed in Figure 125 and the resulting Torque-Rotation diagrams are provided Figure 126.

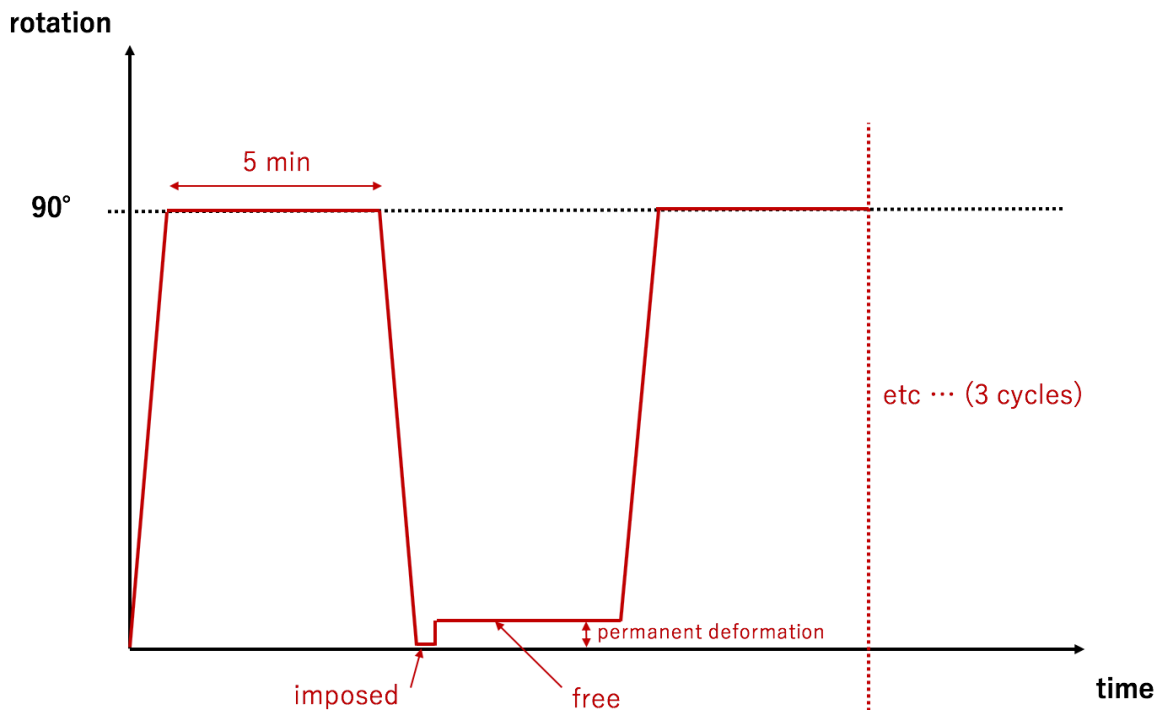


Figure 125 - Torsion relaxation test 2: history of imposed deformation

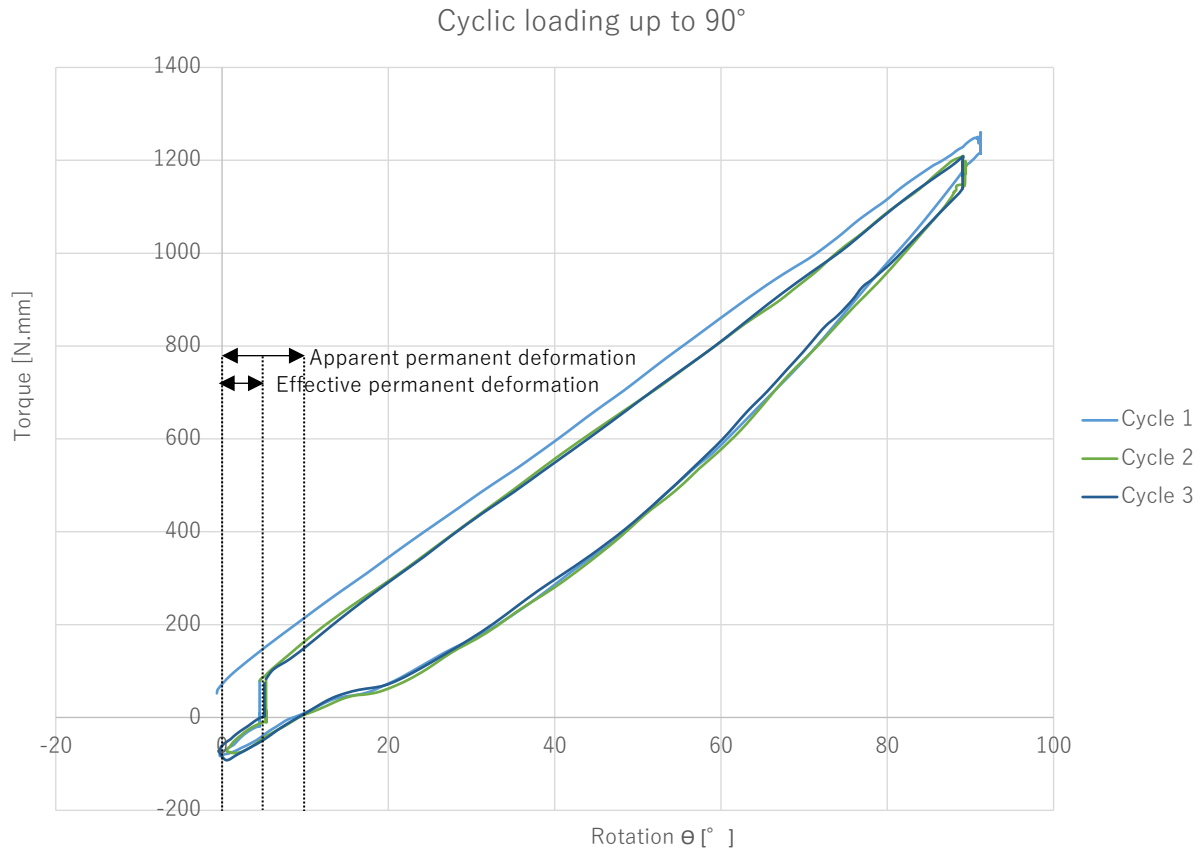


Figure 126 - Torsion relaxation test 2: relaxation losses and effective permanent strains for a C-type sample loaded and unloaded three times up to 90°

Test 2 confirms that the behavior is linear up to 90° (i.e. straight loading path) but not elastic (i.e. permanent strain remains after unloading). Micro-damages leading to permanent deformation depends on the stress history of the specimen. We see on Figure 128 that permanent strain is created only during the first cycle, as the following cycles are not 'pushing' the material further. The same reverse torque as observed with test 1 is needed to bring the specimen to 0°. However if the operator releases the rotation control, meaning that he stops applying an external force, the specimen recovers linearly 50% of the apparent permanent deformation in a 4 seconds time lapse, corresponding to a recovery rate of 1.25° /sec. The recovery is pretty instantaneous regarding the 5 minutes time lapse when the specimen is free. Longer-term recovery may exist, however being quite small, and we do not have appropriate experimental setup to measure it yet. Here we get an upper boundary of the permanent deformation, as we only allowed for short-time recovery.

Note that for both test 1 and 2, corrections were made to the raw data in order to account for the effect of the fixture. Indeed the locking process introduces friction forces in the rotating rod (picture (d) Figure 113). As long as the screws are tied, the torque force resulting from friction is directly supported by the steel piece; when the screws are released, part of this force is transferred to the left support through the element, creating an increase in the torque measured by the load cell. See in Appendix X for an example diagram previous to corrections and more explanations.

Those experiments brought evidence of the visco-elastic behavior of the material (relaxation). A fine quantification of relaxation losses would need a fixture with precise displacement control and modeling of the error due to friction. With the current setup, the magnitude of the error introduced

by hand control of the displacement, friction in the fixture and reset of the inclinometer can reach the magnitude of the torque loss itself when no correction is done. The experiments also brought evidence of the occurrence of plastic permanent deformations. Their magnitude depends on the largest strains (largest rotation) faced by the sample in its loading history. The recovery capacity was estimated to 50% of the permanent deformation for 90° rotation cycles.

## 5 Conclusion of Chapter II

The twisting facade concept lies as it were with the physical utopia of achieving simultaneous stiffness and flexibility. Both the material choice and the structural behavior of the system were investigated to engineer a feasible technical solution. The design involved wind loads acting on the facade along with the torque introduced in the modules by actuators rotating them. According to the SIA260:2013 [31], the static equivalent of the dynamic wind pressure for Lausanne's location resulted in a characteristic value  $q_k=0.525[\text{kN/m}^2]$ . The torque force was calculated in a later stage, as it depended on the constitutive law of the selected material and the magnitude of the imposed rotation. No load factors were applied to the characteristic values as the facade was not part of the loadbearing structure of the building.

Regarding the field of building and facade construction, composite (fiber reinforced polymers) materials were selected because they offered a way to design specific structural responses depending on the direction and the type of solicitation. Especially, glass fiber reinforced polymers (GFRP) were selected for their resistance to water and UV-radiation, and consistency in terms of strength for the studied application. Structural aim was to resist axial bending due to wind loads while allowing large torsional deformations. A pre-design identified unidirectional E-glass fibers stacked at 0° (resp. to the bending direction) to be the most promising option. This type of laminate belongs to the 'specially orthotropic' category and exhibits uncoupled bending and torsional behaviors. Relying on SIA261:2014 [32], the criterion  $w_{\max}=L/250=10[\text{mm}]$  was imposed on the maximum deflection, the latter being associated to wind acting normal to closed blinds and decisive for the number of plies needed. Indeed deflection depends on the bending stiffness  $EI$ , itself largely influenced by the thickness ( $I=f(1/t^3)$ ). For 2.5m long pieces, a minimum of 25 plies was necessary for a total thickness about 12mm. Consequently, satisfying the deflection criterion restrains the rotation capacity as  $\theta_{\max}=f(1/t)$ . Special care should be taken to consolidate this design criterion, as the underlying aim is to prevent disruptive 'shaking' of the facade with the wind, and to value an increase in the allowed rotation against an increase in the 'wind performance'. In this scope, eventual issues regarding cyclic loading and/or long-term behavior must be included.

To analyze the composite laminates, the commonly used Classical Lamination Theory (CLT) was implemented first. It is an analytical 2D thin-plate theory, which only considers thickness, stacking sequence and fiber orientation as input parameters to calculate the stiffness matrix  $K$  of any laminate (no specified length or width, no supports etc). Evaluating strains and stresses in different sections along a structural element goes back to pre-calculate by hand the reduction of external efforts at this specific location, which was done successfully for an equivalent isostatic GFRP beam but became complicated for the overall analysis of hyperstatic fixed-fixed beam, and impossible when it came to account locally for side-effects. Moreover, large torsional deformations outreached the validity framework of this theory. The author shifted to a numerical Finite Element Analysis.

FEM analysis was performed with ANSYS, using composite solid modeling and taking into account effective boundary conditions. The author transcribed in details the hypothesis and guidelines for the pre-processing, as part of the self-learning of the software. The rotation was increased step-by-step in the solving process in order to compute equilibrium equations taking into account the increasingly deformed shape of the structure. FEM confirmed the CLT estimation of the maximum deflection ( $w_{\max,CLT} = 9.4\text{mm}$ ,  $w_{\max,FEM} = 9.3\text{mm}$ ) and the general nature of the failure driven by in-plane shear stresses  $\tau_{xy}$  influencing more than 95% of the failure criterion, however the implementation of uniaxial torsion in the CLT underestimated the maximum rotation ( $\theta_{\max,CLT} = 120^\circ$ ,  $\theta_{\max,FEM} = 140^\circ$ ). Moreover, the FEM accounted for support conditions along with the 3D evaluation of Tsai-Wu failure criterion, pointing out high stresses concentrations in the supports zones, which are likely to bring unexpected failure. FEM also justified to allow the axial retraction to avoid a global tensioning of the element. Finally FEM pointed out the start of a torsional buckling (out-of-plane deviation by 6.6mm from the element's axis for  $\theta_{\max,FEM}$ ). Large deformations triggered geometrical non-linearity associated to an increase in the force needed to rotate the element that has deviated, visible on the Torque-Rotation curves. Ignoring large deformations underestimated the necessary torque up to 15% for  $\theta = 140^\circ$ . Given the existence of non-linearity, separate calculation and later superposition of the wind and torsion effects is not valid. Indeed pressure simultaneously applied actually prevented part of the torsional buckling.

A laboratory testing procedure was conducted for 1:5 scaled elements, on a fixture built to reproduce the defined support conditions i.e. a fixed-fixed system with axial displacement released. When comparing the real behavior of the system to the expected behavior, experimental Torque-Rotation (T- $\theta$ ) curves exhibited the same cubic polynomial shape as predicted by FEM calculations. It confirmed the characterization of the geometrical non-linearity affecting the system, as a property of the studied geometry, loads and boundary conditions (not of the material itself). Regarding the rotation achieved at failure, the specimens supported a full turn ( $360^\circ$ ) while they were expected to break a bit before half a turn (around  $140^\circ$ ) according to a linear elastic constitutive law. Failure mechanism was triggered by progressive torsional buckling when no anticipated failure occurred in the supports zones. These findings invalidated the use of such a linear elastic law to model the material's behavior when subjected to high torsional shear strains. The newly exhibited rotation capacity is advantageous but also means that the material exhibits some rearrangements of its micro-structure in relation to the polymeric nature of the matrix. Confirmation of non-elastic and non-linear effects was brought by cyclic and time-dependent tests. A relaxation of the torque force occurred, by about 5.5%, when  $45^\circ$ ,  $90^\circ$  and  $135^\circ$  rotations were imposed to the system and maintained during 30 minutes. Relaxation brought evidence of the visco-elastic behavior of the material. Cyclic tests also exhibited the occurrence of plastic permanent deformations, which magnitude depends on the largest strains (largest rotation) faced by the sample in its loading history. The apparent permanent deformation was estimated to  $10^\circ$  for  $90^\circ$  rotation cycles, with 50% recovery capacity of the permanent deformation at the release of the element and recovery rate  $1.25^\circ / \text{sec}$ .

The author suggests to concentrate future efforts on the implementation of a constitutive law that accounts for the progressive microdamaging and softening of the material in the modeling of the torsional behavior, as well as their time-dependency. Constitutive equations will be calibrated based on laboratory physical measurements and used to estimate the parameters of such a damaging law. Those parameters will then replace the current linear elastic constants in the finite element analysis. Strains and stresses calculated by FEM will be compared to the physical measurements to iterate on the calibrated law, and so until both FEM calculations and experiments match. This process is called reverse analysis.

In the prospect of demonstrating that viscoelastic and plastic effects range in acceptable boundaries regarding the intended use of the facade and its lifespan, these effects could be integrated and partly prevented or counterbalanced at early stages. It is well known that creep is for instance integrated into the design of concrete or wooden structures by means of initial camber, or that relaxation loss is balanced during the tensioning process of prestressed steel.

# CHAPTER III

## TOWARD A REAL IMPLEMENTATION: PENDING INVESTIGATIONS

This project was not developed following economical guidance to design a marketable product. The philosophy was to investigate the structural utopia of having both stiff and flexible twisting facade modules, previously shown to be promising as a shading system enhancing perceptual effects. When coming to the pragmatic feasibility, it obviously has shortcomings to address.

Based on the conclusions following chapters I and II, this chapter provides an overview of pending practical issues such as optical properties mastering, thermal influence of the facade and impact of the actuation technology on the cost, in a care to be realistic of the further steps towards the achievement of a functional product.

### 1 Optical design

#### 1.1 Transmittance of full-size facade elements

It was shown that the GFRP material of the blinds should not exceed 15% diffuse visual transmittance and avoid direct transmittance (Chapter I section 2.1.1 'Efficiency of the closed state'). In his thesis at CCLab [43], C. Pascual ran many physical measurements and calibrated a model of the total transmittance of GFRP laminates made of unidirectional and woven fiberglass fabrics. The model expresses the transmittance as a function of the reinforcement weight. All the details about the physical model are provided in the chapters 2 & 3 of his work. Here we highlight the analytical form of the expressions:

$$T_{total} = T_{0,total} * (1 - L(w)) , \text{ where } L(w) = 1 - (1 - L_{ref})^{w/w_{ref}} , T_0 \text{ and } L_{ref} \text{ being constants.}$$

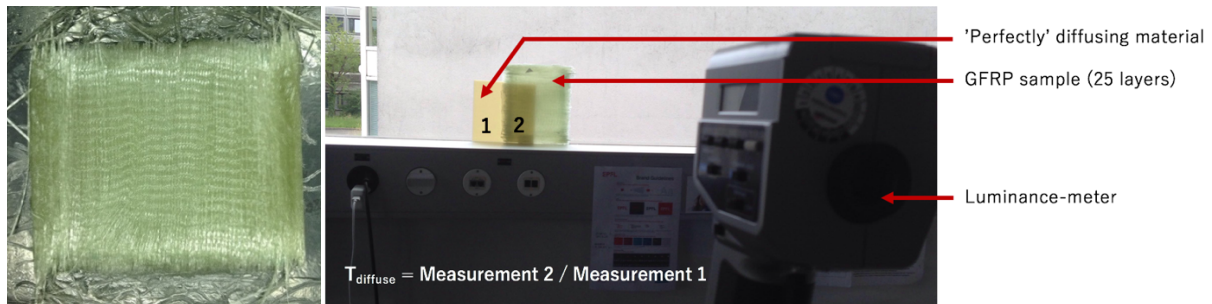
$w \left[ \frac{g}{m^2} \right]$  is the reinforcement weight and  $L [-]$  the loss of transmittance

The diffuse transmittance has the form  $T_{dif} = T_{total} * (1 - e^{-a*w})$  ,  $a$  being constant.

To meet structural requirements defined in Chapter II we need 25 layers of unidirectional fabric. A 15cm\*15cm specimen made of 25 layers of C-type material (reinforcement weight  $w=410$  [g/m<sup>2</sup>.layer]) was fabricated at the CCLab by hand-lamination technique. Detailed fabric properties and fabrication processes can be found in Chapter II section 4.2. Optical properties were measured at LIPID.

With reinforcement weight  $w=410$  [g/m<sup>2</sup>.layer], the theoretical total transmittance of an element made of 25 layers should be 26.6% ([43], equations 2.11 & 2.12). The direct part is zero with this amount of layers, which is a good point ([43], equation 3.21). Measurements on hand-laminated specimen with C-type reinforcement material (the same material as used for the calibration of the

transmittance model in [43]) showed a 27.5% diffuse transmittance, which makes a relative 3.4% difference with the expectation.



Figures 127 a&b – (a)15cm\*15cm specimen made of 25 layers of C-type material (b)quick transmittance measurement setup

Nevertheless, we have to implement measures to meet the 15% transmittance goal. The reflectance goal ( $\sim 50\%$ ) matters less (Chapter I section 2.1.2 ‘Efficiency of the open state’) but should be diffuse as well. Right after are provided some ideas to match optical needs.

## 1.2 Control on the optical properties

### 0| Play with the fibers

As explained shortly before, C.Pascual showed that a drop of transmittance occurs with increasing fiber reinforcement weight  $w$  [43]. This statement is valid when there is no perfect mismatch of refractive index between the fibers and the resin, which is most of the time the case with unavoidable air inclusion during the fabrication process. Otherwise, with perfect matching, the transmittance is independent on  $w$ . In our case we do not want to add more layers than the structurally necessary ones. Hence playing on this is not sufficient.

### 1| Play with the resin

It seems complicated to use something else than epoxy because it is the most suitable for structural purpose and durability. There is an option to add something in the resin mix, also in the prospect to increase the mismatch of refractive indexes between fibers and resin originally having equal indexes. Figure 128 quantifies the transmittance drop when the indexes are mismatched. Note that refractive indexes are wavelength dependent, hence too important mismatches can give a “coloured” appearance to the diffuse light.

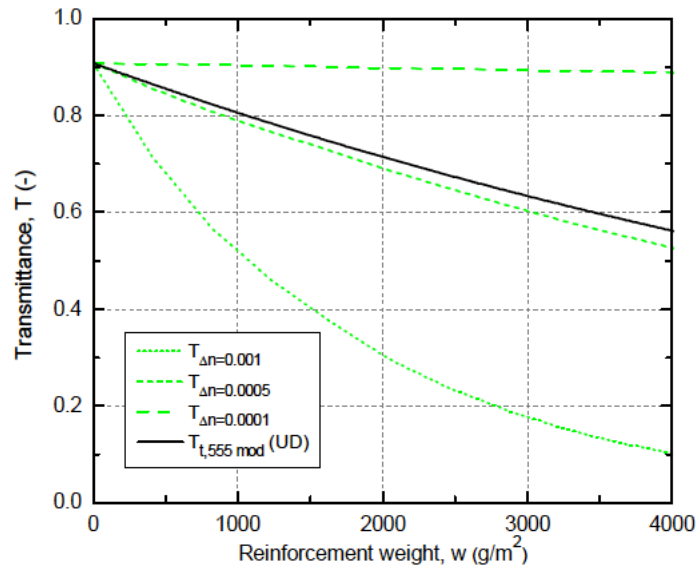


Figure 128 - Evolution of the transmittance for different mismatches of the refraction index  $\Delta n$ , from [43]

## 2| Give a matte finish

This option is mostly interesting to ensure diffuse reflection of the light instead of direct when the blinds are open. It can be achieved either with a textured mold, an acid matting post-treatment or a sanding post-treatment. It is difficult to add non-structural layers as coatings, except if the material resists the shear stresses (which are maximum on the outer surfaces of the laminate).

## (3| Opaque GFRP)

This would prove to be counterproductive as we chose to use glass for the opportunity to keep some ambient light through the blinds even when they are closed.

Regarding the transmittance, option **1|** was investigated by adding drops of tinting pigments into clear epoxy resin. Biresin® white and black ColorPaste from Sika were used, either separately or mixed to obtain greys. White is expected to increase the light reflection while black is expected to increase the absorption. Resin mix was made of epoxy resin (Biresin CR83, Sika®) and hardener (Biresin CR83-2, Sika®) mixed in 3:1 proportions in weight, identically to the GFRP specimens. Dyes were added afterward in the resin mix, in volumic proportions around 1:10'000 for 1 unit of dye (i.e. a 0.05 mL drop of dye is added with a pipette to 500 mL of resin mix). The thickness of the samples was made as identical as possible, equal to 12mm. Luminance was measured with each sample in a small integrating sphere to evaluate the drop of transmittance relatively to the transmittance of the reference (clear resin). Results are plotted Figure 131.

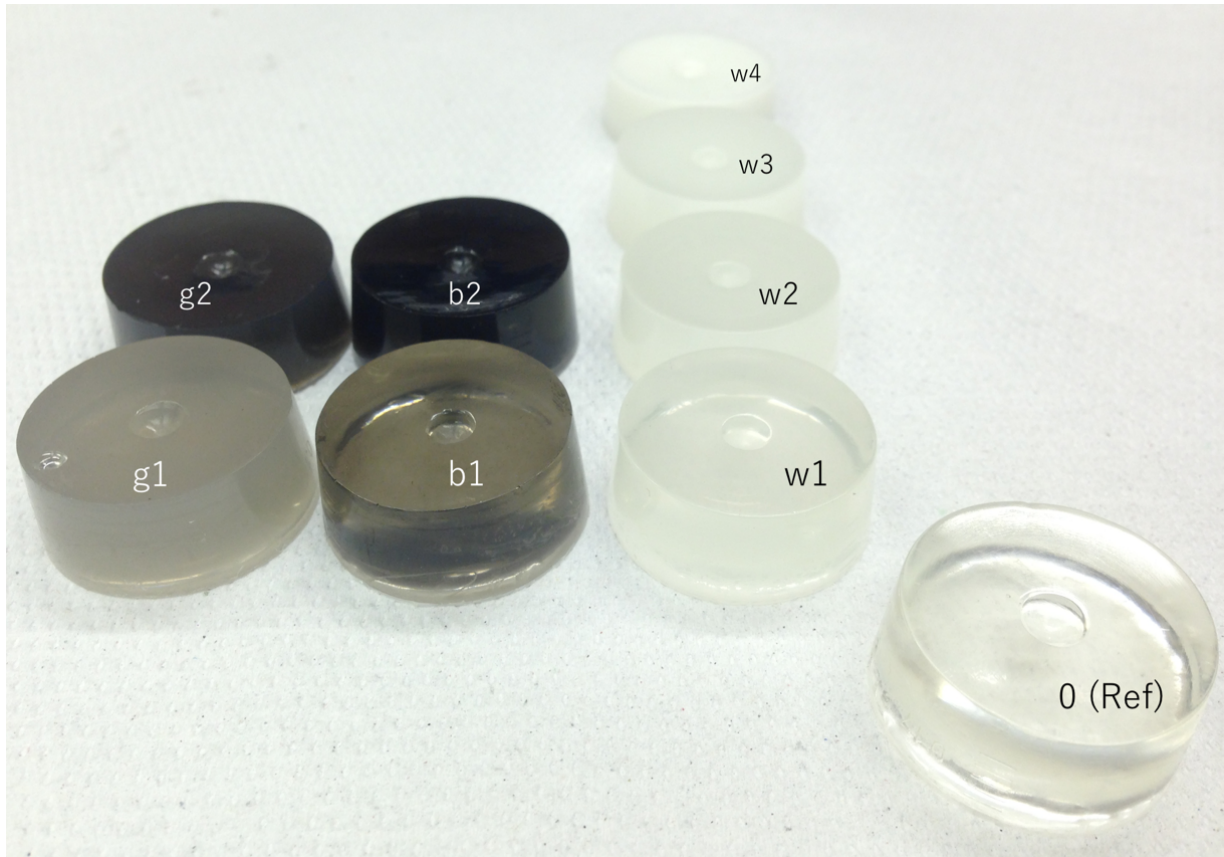


Figure 129 - Resin specimens dyed with white, black or both b&w color pigments

SAMPLES	WHITE					
	Units of dyes	0	1	2	3	4
BLACK	0	0 (Ref)	w1	w3	w3	w4
	1	b1	-	g1	-	-
	2	b2	-	g2	-	-
	3	-	-	-	-	-
	4	-	-	-	-	-

Table 36 – Concentration of white and black dyes in the different resin samples

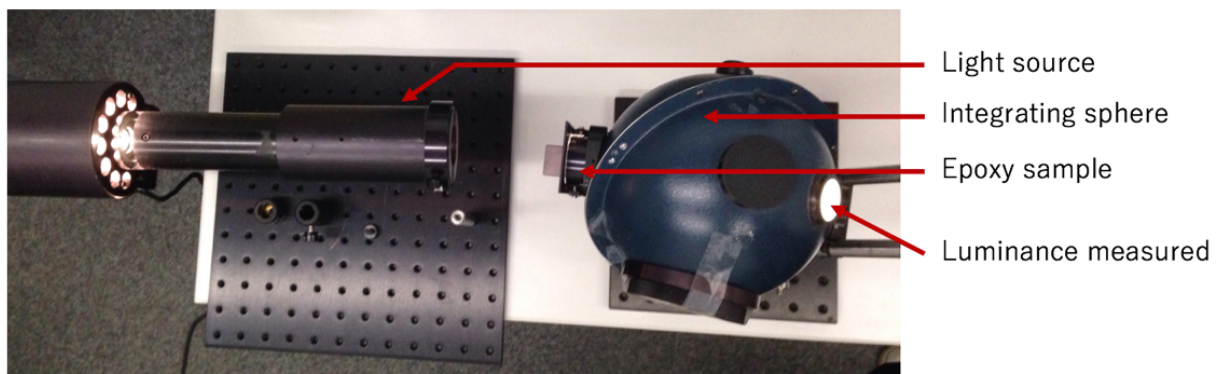


Figure 130 – Integrating sphere setup for luminance measurements



Figure 131 - Drop in the transmittance measured on dyed samples of resin compared to a reference sample of clear resin

The pursued drop of transmittance is about 50% for the GFRP elements (from current 27.5% to targeted 15%). Figure 131 above shows that it is either achievable with concentration  $10^{-4}$  [mL of dye/mL of resin mix] of black dye or  $1.5 \cdot 10^{-4}$  of white dye for 12 mm thick epoxy samples. Black pigment is more efficient at lowering the transmittance but looks also more 'cristal clear' while white pigment looks more translucent on Figure 129. Surprisingly black pigment loses its efficiency when mixed to the white to obtain greys. Influence of the color on reflectance and absorption needs further investigations, as well as interaction between pigments and fibers.

Optical properties of the laminates are also influenced by the surface's roughness. Values of total transmittance measured on GFRP strips from the mockup (Appendix XI) were 25% lower than theoretical values calculated with Pascual's equation for those same elements. Those strips' surface had been polished during the high pressure sandcut process.

Finally, optical properties can be highly angle-dependent. Measurement at 2 different angles  $\alpha=30^\circ$  and  $\alpha=45^\circ$  on GFRP strips from the mockup (Appendix XI) showed that the material was not Lambertian. The luminance of the raw (not textured) surface was not isotropic, whereas the apparent brightness of a Lambertian surface to an observer is the same regardless of the observer's angle of view.

## 2 Motion's complexity and actuators

### 2.1 Independently rotating blinds

In chapter I, autonomous annual schedules of the blinds were established including intermediate twisted states for the purpose of enhancing occupants' perceptual impressions. The control algorithm was evaluated for a given viewpoint aimed to be an average worst case for the glare and facade elements all subjected to the same motions. The prospect to broaden the analysis to multiple positions in the room raises the question of having independently moving blinds. It would

allow a finer level of daylighting control in the different zones of the room, and multiply the customization possibilities!

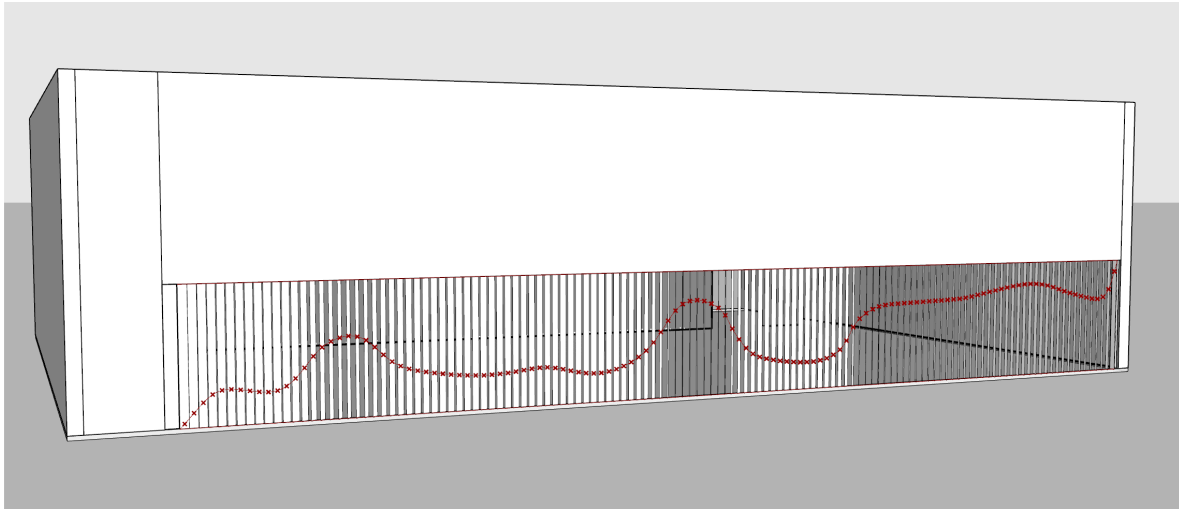


Figure 132 - Use of a control curve to independently control the rigid rotation of the blinds: creating open or closed zones with flat blinds (0-0° ).

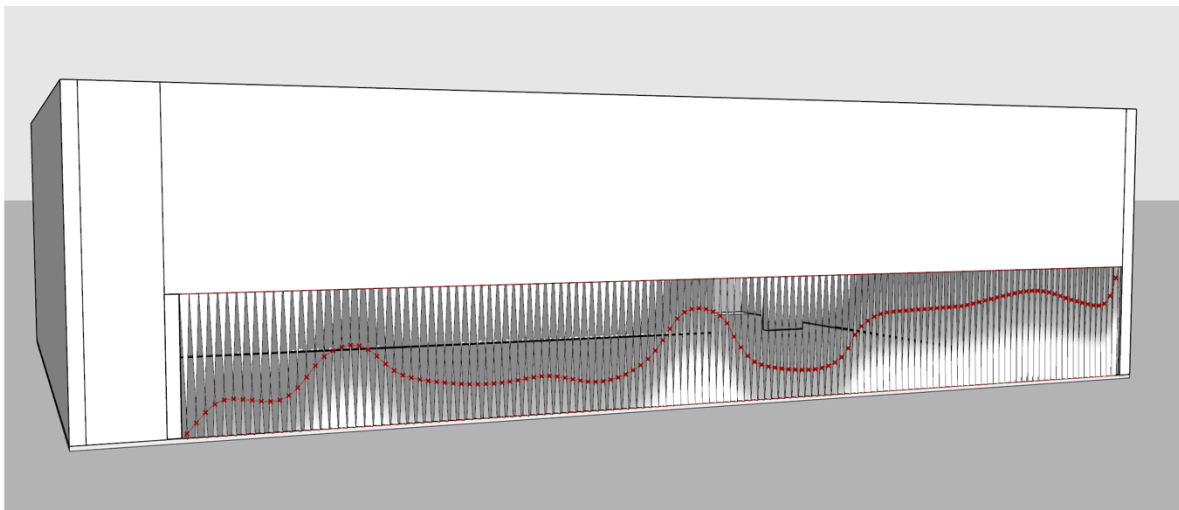


Figure 133 - Use of a control curve to independently control the rigid rotation of the blinds: playing further with the pleasantness of the facade, here with bottom twisted blinds (0-90° ).

## 2.2 Multiple pieces

The minimum thickness for 2.5m long pieces has been shown to be about 12mm. We can wonder if this is satisfying or if it is too much to ensure a pleasant view out when the kinetic facade is open. Moreover, regarding previous considerations on independently moving blinds, what comes out when extending the concept to independently moving pieces along the facade's height?

In the following, we study the implications of using shorter (therefore thinner) elements. The objective is to have one element or a group of elements that cover a slice (width  $b=0.15\text{m}$ ) of a  $H_{\text{ref}}=2.5\text{m}$  tall facade. The "facade slice" concept is illustrated in the Figure 134 below. We investigate variations from 1 to 4 pieces per facade slice. The maximum total rotation required along

$H_{ref}$  is  $\theta_{max}=135^\circ$ . In case of multiple pieces (height  $H_i$ ), the rotation is assumed to be equally partitioned so that  $\theta_{i,max}=\theta_{max} * H_i / H_{ref}$ .

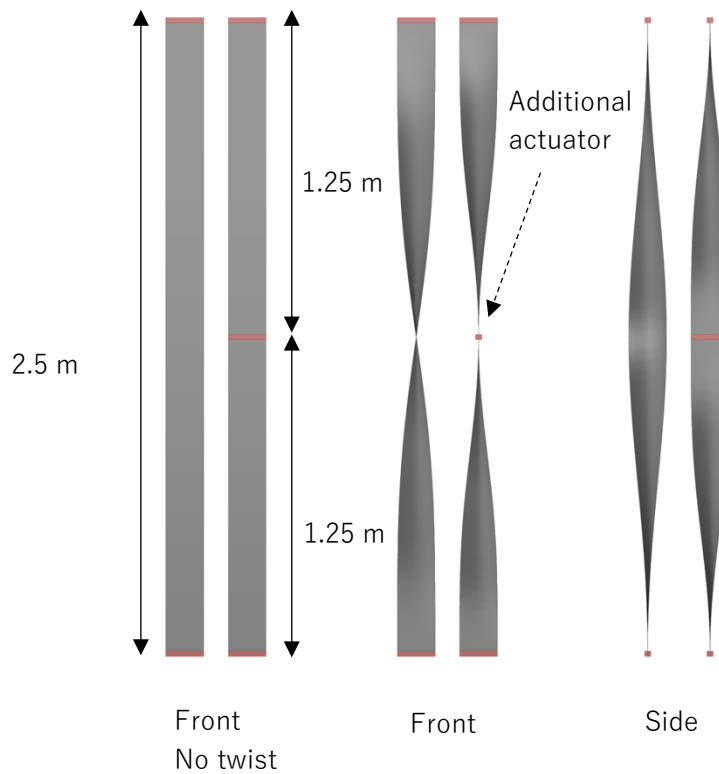


Figure 134 - Illustration of the facade slice concept with 1 element of H=2.5m and 2 elements of H=1.25m

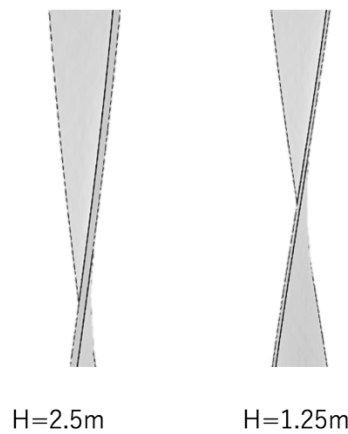


Figure 135 - Influence of the element height H on the thickness and the view obstruction

Once we want to compare design options that vary the height of the elements and so the number of elements needed to cover the facade, we should define the optimization function. The different variations are compared in terms of cost.

The parameters influencing the final price of the dynamic facade are:

- the surface of reinforcement material
- the volume of resin
- the number of actuators and their mechanical power

### Cost of the fiber reinforcement

We calculate the number of layers required to construct one element of a certain length. The equivalent surface for building a  $H_{ref} = 2.5\text{ m}$  tall facade slice is calculated afterwards.

The computation of the cost of the surface of reinforcement needed for one “facade slice” is given by:

$$C_{\text{reinforcement}} = N_{\text{layer}} * \text{cost}_{\text{fibres/m}^2} * b * H_{\text{single\_element}} * (H_{\text{ref}} / H_{\text{single\_element}})$$

$$\Leftrightarrow C_{\text{reinforcement}} = N_{\text{layer}} * \text{cost}_{\text{fibres/m}^2} * H_{\text{ref}} * b$$

### Cost of the resin

- We recall that the assumed ply thickness for GFRP is  $t_{\text{single\_ply}}=0.5\text{mm}$ .
- Based on products from the supplier Swiss Composite:
  - UD fiberglass fabric: 8 CHF/m<sup>2</sup>
  - Epoxy resin L-20: 423 CHF/20 kg
  - Hardener: 131 CHF/5 kg
  - The mixture rule for the resin / hardener is 100:25.
- The density of the epoxy resin is approx. 1.2 g/cm<sup>3</sup>

So we can obtain the volumetric price of the resin:

$$\text{cost}_{\text{resin/m}^3} = (423 + 131)/(20+5) \text{ [CHF/kg]} * 1,2\text{E}3 \text{ [kg/m}^3\text{]} = 26.6 \text{ [kCHF/m}^3\text{]}$$

For a volume fraction of resin about 50%, the required volume of resin for one “facade slice” is:

$$C_{\text{resin}} = N_{\text{layer}} * 0.5 * t_{\text{single\_ply}} * \text{cost}_{\text{resin/m}^3} * H_{\text{ref}} * b$$

$H_i$ [m]	$2.5 = H_{ref}$	$1.25 = H_{ref}/2$	$0.833 = H_{ref}/3$	$0.625 = H_{ref}/4$
$\theta_{i,max}$ [°]	135°	67.5°	45°	33.75°
$N_{b_{layer}}$ [-]	25	12.5	8.33	6.25

Table 37 – Variations investigated in the number of GFRP pieces per facade slice and respective maximum rotation and number of fiberglass layers required

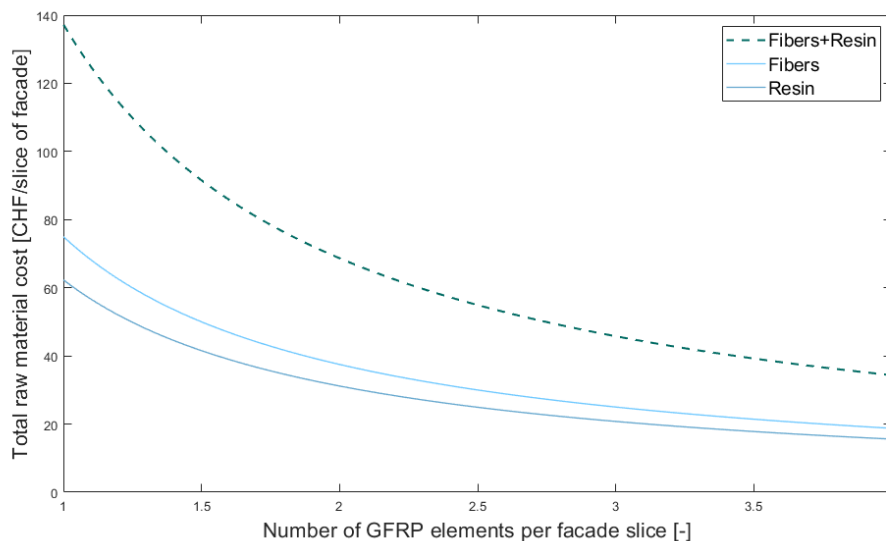


Figure 136 – Evolution of the total cost for raw material (fibers and resin) according to the number of pieces per facade slice

Considering only raw material, the facade slice cost is inversely proportional to the height  $H_i$  of the pieces. The variation with one element per slice is the most expensive, with a raw material cost of 137.325[CHF/slice] i.e. 366[CHF/m<sup>2</sup>] of facade.

NB: Regarding the prevalence of thickness over stiffness in the inertia (decisive parameter, see Chapter II sections 2.5 and 2.6), layers in the middle of the composite element are more like filler material than load bearing layers. It would be interesting to study options having cheaper materials in the core of the laminate to increase the inertia for a cheaper final cost, independently of the number of pieces per slice.

However, multiplying the pieces increases the number of motors required to actuate the facade. The price of such actuators depends on their mechanical power. We calculated the maximum torque force necessary (i.e. the torque force to achieve  $\theta_{i,max}$ ) using ANSYS to account for torsional stiffening with large deformations.

$H_i$ [m]	2.5= $H_{ref}$	1.25= $H_{ref}/2$	0.833= $H_{ref}/3$	0.625= $H_{ref}/4$
$Nb_{required\_motor}$ [-]	2	4	6	8
$T_{max}$ [N.m]	507.8	226.4	147.6	109.8

Table 38 - Variations investigated in the number of GFRP pieces per facade slice and respective maximum torque and number of actuators required

### Price of the actuators

In a first approach, based on market available products able to provide high continuous torque force at low rotation speed, hydraulic orbital motors were identified. Prices found on the market, (1USD~1CHF) ranged around the following amounts:



Figure 137 – Hydraulic orbital motor  
(source: <http://www.orbitalmotors.net/orbital-motor-tech-specs.php>)

Max. Continuous Torque [N.m]	100	600
Motor price per unit [CHF]	50	300

Table 39 – Market prices of hydraulic orbital motors  
(source: prices study on <https://www.alibaba.com/> as suppliers never show prices on their official websites)

For the studied application we reasonably model the price of a motor, called  $cost_{single\_motor}$ , as proportional to the mechanical power (torque):  $cost_{single\_motor} = T_{max} * cost_{mechanical}$ . According to Table 39 above,  $cost_{mechanical} = 0.5$  [CHF/N.m].

The number of actuators per 2.5m long facade slice is:

$$Nb_{required\_motor} = (H_{ref} / H_{single\_element}) * 2$$

And the cost of motors for one facade slice:

$$C_{motor} = Nb_{required\_motor} * cost_{single\_motor}$$

### Total cost of the facade slice

The estimation of the cost of one facade slice is finally calculated for each variation as:

$$C_{\text{slice\_facade}} = C_{\text{reinforcement}} + C_{\text{resin}} + C_{\text{motor}}$$

By plotting continuous curves, we admit that the number of layers and motors could be different from integers, as this study is quantitative and aims to give a first approximation of the final price of the elements.

### Comparison of the variations

Under the current hypothesis on  $\text{cost}_{\text{mechanical}}$  (0.5 CHF/N.m) the cost of the actuators governs the total cost of the facade. For a single element per facade slice, it represents about 80% of the total cost, the total cost being 645[CHF/slice] i.e. 1720[CHF/m<sup>2</sup>] of facade. This total cost decreases to about 1263[CHF/m<sup>2</sup>] for the 4-pieces variations. However the decrease is very sensitive to the hypothesis on the linear relation  $\text{cost}_{\text{single\_motor}} = T_{\text{max}} * \text{cost}_{\text{mechanical}}$ .

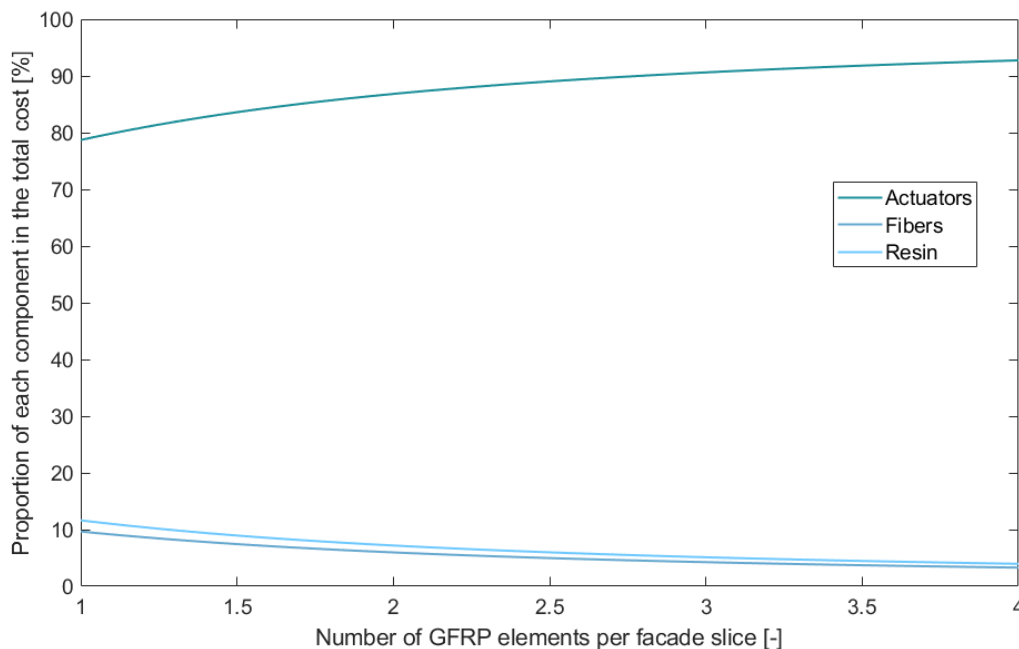


Figure 138 - Evolution of actuators, fibers and resin costs part in the total cost according to the number of pieces per facade slice

In a prospect of R&D processes succeeding in making and optimizing a dedicated mechanical solution for the actuators, we varied the  $\text{cost}_{\text{mechanical}}$  parameter from 0.5 to 0.05 to identify when the expenditures for the actuators decreased to an acceptable part of the total cost. Results are captured by the following 3D graph:

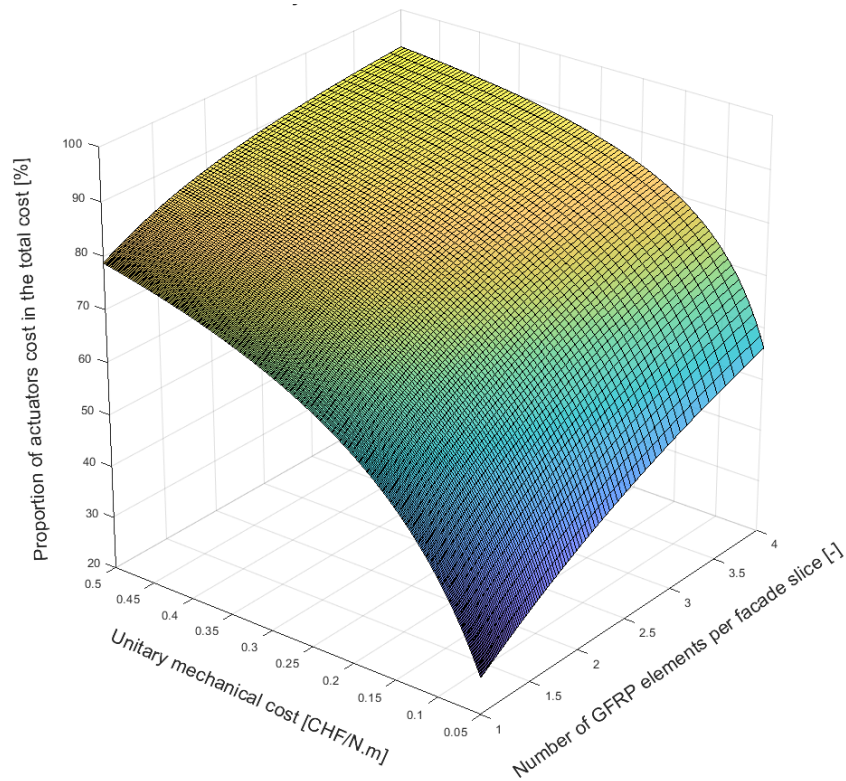


Figure 139 – Sensitivity of the proportion of actuators cost to a future decrease of the unitary mechanical cost

From  $\text{cost}_{\text{mechanical}}=0.14\text{CHF/N.m}$ , the actuators cost becomes less than 50% of the total cost for the variation with one element per slice. Multiple pieces solutions with 2 and 3 pieces become cost-effective, i.e. actuators cost  $<50\%$  (arbitrary) respectively from  $\text{cost}_{\text{mechanical}}=0.11$  and  $0.08$  CHF/N.m, while the 4 pieces variations still takes 56% of expenditures for  $\text{cost}_{\text{mechanical}}=0.05$  CHF/N.m.

## 3 Energy savings

The kinetic facade can adapt its state to provide glare control while minimizing as much as possible the reduction of the illuminance. Such a system reduces the energy consumption for lighting, as the occupants do not need to totally close the blinds all the time and use artificial light instead.

In this section we broaden our vision on the energy savings issue. Savings on lighting have to be correlated to the thermal effect of the facade, i.e. solar heat gains and, to a lesser extent, correlated to the electrical consumption of the facade's actuators.

### 3.1 About daylight and solar heat gains

We cannot go through the entire thermal analysis in this thesis but as a major importance performance aspect, we will use comparison with existing systems acknowledged to be efficient to indirectly evaluate our system.

For this purpose, the transmission reduction operated by the blinds (shading coefficient called  $F_c$ -value) is a good measure, giving an order of magnitude of potential solar gain reduction.

3.1.1 A short reminder from buildings' physics

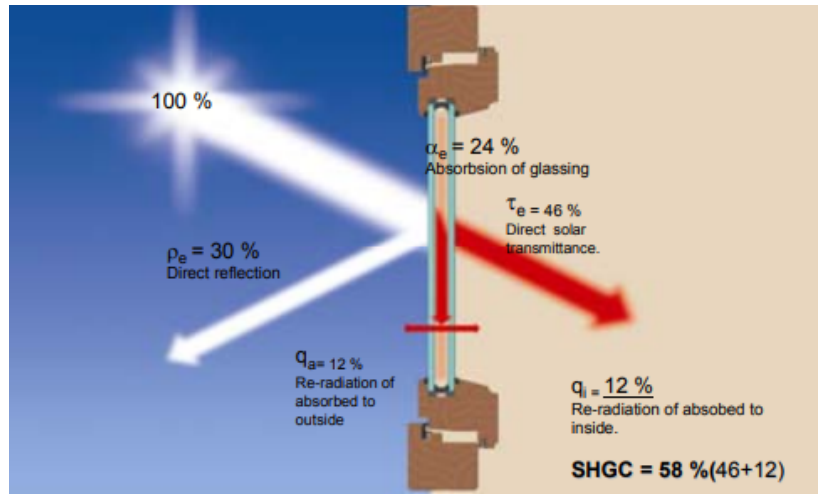


Figure 140 - Solar Heat Gain Coefficient  
 (source: <https://www.petermeyerblinds.com.au/pdf/exterior-metal-venetians-technical.pdf>)

American Standards use the Solar Heat Gain Coefficient (SHGC) – similar to European  $g$ -value – defined as the fraction of incident solar radiation (energy) that effectively enters the building (heat gain) through the {shading system + glazing} combination. Then when the SHGC (or the  $g_{tot}$ -value) of this combination is known, the shading factor  $F_c$  can be calculated as  $F_c = g_{tot}/g$  where  $g$  is the  $g$ -value of the glazing alone.

3.1.2 Shading coefficient

A reference product to compare with as been selected and corresponds to external Venetian (horizontal) blinds, with 80mm aluminium slats. Data are from the German supplier Warema .

80 mm slats with double glazing

Reference values for the combination with a double heat protection glazing with  $g=0.63$  and  $U_g=1.1 \text{ W/(m}^2\text{K)}$

Colour	Slat angle	Sun angle	$g_{tot}$	$F_c$
white	closed	0°	0.07	0.11
	45°	30°	0.12	0.19
silver	closed	0°	0.07	0.11
	45°	30°	0.10	0.16
anthracite	closed	0°	0.08	0.13
	45°	30°	0.08	0.13

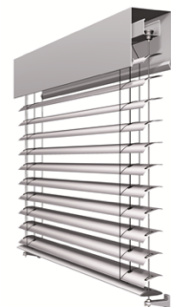


Table 40 - Typical  $F_c$  values for horizontal aluminium exterior blinds, studied as a reference system [44]

NB: the glazing used in the Rhino model and DIVA calculation model has a  $g$ -value  $g=0.72$  while the Table 40 above is based on measurements with  $g=0.63$ . We will still use their  $F_c$  values as we study external blinds, moreover without "special glazing" behind.

To calculate the  $F_c$  value with the twisted blinds system, we created a model containing only the blinds geometry (without thickness) of about 15 blinds. We defined very fine random grid of sensors behind the whole and a sensor point ahead to measure the amount of solar radiation passing through the system. Note that for this purpose, the East orientation is kept but there is no real sky,

the sun is set perpendicular to the facade's plane. Also note that the to-the-inside re-radiation of absorbed solar radiation is zero (Figure 140) as Radiance considers absorption, but not in a thermal "way" (absorbed energy is not a heat gain) ; the  $F_c$  value calculated is the reduction of the visible solar radiation by the shading:

$$F_c = \frac{\text{illuminance on the front sensor}}{\text{average illuminance on sensors behind the blinds}}$$

Blinds position	No blinds (ref.)	90-90	90-0	135-0	0-90	45-0	0-0
$F_c$	1	1	0.491	0.518	0.499	0.260	<b>0.148</b>

Table 41 -  $F_c$  shading coefficient calculated for six blinds' positions (sun is considered normal to the facade)

For a perpendicular sun, the protective state is 0-0. Its  $F_c$  value is around 0.15, higher than for closed venetian blinds (around 0.12 depending on the colour), because the system is not fully opaque. We proved in Chapter I that the translucency (causing the 15% transmittance) was a good point in terms of illuminance. Further applications of the facade should investigate solar heat gains and check that they are not too high with such a translucent system, depending on local climates.

The  $F_c$  of the other states are provided as a scaling of the results. The sun azimuth must be adapted to measure a relevant shading coefficient, as adapted for the 45° slat angle in venetian blinds data Table 40. However those  $F_c$  values give a comparison scale and information on the 3D effect of curved shapes: the 135-0, i.e. the more warped one, has a higher  $F_c$  than the top or bottom 90° twisted states while it closed more in terms of view access (Chapter I section 2.2.1, Table 16). It exhibits again the "light-catching" effect of 3D curved elements.

### 3.2 About (the hidden face of) daylight efficiency

We are realizing energy savings as we optimize the artificial lighting demand of the building. But the facade actuators also consume electricity.

The employed methodology is similar than for solar heat gains. We first estimate the electrical power needed for the actuation of broadly used systems as Venetian blinds and then compare to our motors' consumption. Calculations were carried out considering a facade height to be covered equal to 2.5m, and then normed by unitary surface of facade. We considered 4 actuation cycles per day, i.e. 2 full openings and 2 full closures of the blinds. Final results are summarized below:

Shading system	Exterior Venetian blinds	Twisting GFRP facade
Annual electrical consumption [kWh/(year.m <sup>2</sup> of glazing)]	0.7	120

Table 42 - Comparison of electrical energy consumption of the actuators for exterior Venetian blinds and twisting GFRP facade

Typical electrical consumption for (artificial) lighting ranges between 10 and 30 [kWh/(year.m<sup>2</sup> of floor area)]. The studied zone of the SG Foyer (depth 11.2m) would use 112 to 336 [kWh/year.linear meter] for artificial lighting, while the actuation of the facade would need 300 [kWh/year.linear meter] (2.5m height continuous window).

The actuators currently consume as much energy as the maximum savings that could be achieved on lighting if the building could work with natural light only.

A solution imagined to reduce the consumption is to actuate several blinds with one motor. This is valid if the electrical power consumption increases slower than the mechanical power of the motors, unfortunately it is the opposite according to technical data for hydraulic orbital motors\*. This solution also discards some creative freedom as the blinds are not all independent anymore.

\*Source: data HT500 motors on <https://www.brevinfluidpower.ie/hydraulic-motor-systems/hydraulic-motors/orbital-motors>

The development of a dedicated actuation system is a challenging mechanical engineering topic, as high torque forces are needed but only for a few seconds a day. If hydraulic orbital motors meet requirement for the high torque, they are definitely underused in this facade implementation and bring unreasonable extra-cost, without mentioning weight and size issues.

Solar productive cells embedded in the GFRP are an option to counterbalance the power used for actuation, nevertheless they have a cost too.

Calculation details for shading systems' consumption in Table 42 are provided:

- Exterior Venetian blinds: calculation note in Appendix XII
- GFRP twisting facade:

From ANSYS calculations we know that a twisted GFRP element (of height 2.5m, width 15cm and with fixed support conditions) requires a torque force  $T=507.8[\text{N.m}]$  to achieve a  $135^\circ$  rotation.

Low speed hydraulic orbital motor necessary to achieve T have electrical power  $P\sim 8[\text{kW}]^*$

\*Source: data for BR315 and HR315 motors on <https://www.brevinfluidpower.ie/hydraulic-motor-systems/hydraulic-motors/orbital-motors>

From laboratory torsion tests on 1:5 samples,  $v = 10^\circ / \text{sec}$  is a convenient rotation speed to avoid dynamic shocks in the supports. Hence to complete 4 cycles per day, each motor (one at each end of the module) uses power during  $4[\text{cycles}] * 70^\circ / 10^\circ / \text{sec} = 28[\text{sec}]$ . We assume that once the rotation is completed, the blinds are locked by a mechanical system that does not require power.

We have 2 motors per blind element, and about  $1/0.15=6.6$  [blinds/linear meter of facade]. The annual electrical consumption per unitary surface of glazing is:

$$(6.6)[\text{blinds/linear m of facade}] / 2.5[\text{m}] * 365[\text{d}] * 28[\text{sec/day}] * 2[\text{motors}] * 8[\text{kW}]$$

$$= \mathbf{120 \text{ [kWh/year.m}^2 \text{ of glazing]}}$$

## 4 Conclusion of Chapter III

This chapter addressed the side but still important issues in relation to the developed adaptive facade. The expected diffuse transmittance of real-size elements (25 GFRP layers) was estimated to 26.6% based on the density of fiber reinforcement ([43]) and measured to 27.5% on a hand-laminated specimen made of C-type material. It was shown that white and black resin dyes used in volumic fractions  $1 \cdot 10^{-4}$  to  $4 \cdot 10^{-4}$  provided sufficient drops of transmittance in epoxy resin to reach the targeted 15%. Further tests should consolidate this result for dyed laminates as well as investigate surface treatment to get appropriate roughness and specularity, and finally deal with the angle-dependency of optical properties.

In terms of motion, the strength of the architectural concept goes beyond the few intermediate twisted states studied in Chapter I, as a plethora of patterns are achievable by combining rigid and flexible rotations. The possibility of revolving the blinds around their axis and adding torsional deformations makes even more sense with independently actuated blinds, and motions that the author imagined parametrically handled by means of control curves. The increase of the creative freedom brought the question of having multiple pieces over the height of the facade. Regarding the view out, facades with shorter pieces lead to thinner blinds but involved the add of intermediates actuators somehow splitting the view horizontally. In terms of pure cost evaluation between all the four variations ( $H_i=0.625\text{m}$  to  $H_i=2.5\text{m}$ ), facades with shorter pieces were cheaper. Because the necessary torque load was higher, the longer elements required more powerful motors, so more expensive ones. However a decision based on the absolute cost requires to precise the exact balance between mechanical power and actuators' cost. Moreover the relative parts of expenditures for actuators appeared to reach minimum 80% of the total cost in any case. Given the cost of raw material (366[CHF/m<sup>2</sup> of facade] for the resin and the fibers) it would require to decrease by a factor 10 the cost of the actuation system to maintain it below 50% of the total cost of the facade.

Adaptive facades target higher sustainability regarding energy demand for modern buildings. In this vein, a daylighting control system influences solar heat gains along with the electrical consumption for (artificial) lighting. The  $F_c$  shading coefficient was evaluated to 0.15, against 0.12 for traditional exterior Venetian blinds, indicating further need to assess the impact of the facade on the thermal balance. It would require a full modelling of the GFRP material, including absorption and radiation properties which play a major role in heating and cooling loads. Regarding daylight efficiency, it must be underlined that the actuators currently consume as much energy as the maximum savings that could be achieved on lighting if the building could work with natural light only.

Unreasonable cost and energy consumption of the actuators must be seen as the next challenges of this adaptive facade concept. The simultaneous need for high torque force with low and continuous rotation speed brought to investigating hydraulic orbital motors among commercially available products. However we need their actuation only a few seconds a day! The development of a dedicated actuation system is a challenging mechanical engineering topic.

# CONCLUSION

The project to engineer a concept of adaptive facade system emerged from the desire to explore an innovative research branch in the field of the built environment, gathering structural engineering along with architecture and building physics. This chapter synthesizes the conclusions from the interdisciplinary research work performed throughout this master thesis.

In relation to the implication of the building envelope for occupants comfort, the exterior facade system was developed for daylighting control purposes. As an adaptive shading system, it was designed to make the best use of available natural light while ensuring a good glare protection for the users. Moreover, it had the further aim to enhance perceptual impressions of the space, recognized as a major shortcoming in traditional shading systems controls.

It was proposed to heighten the potential of flat striped blinds by introducing torsional deformations generating surface and edges curvatures likely to increase the visual interest of the scene, while further immersive studies should collect precisely people's reaction to twisted patterns. A facade mockup helped a lot to appreciate the various twist possibilities and to capture practical limitations. By means of 3D parametrical modeling, the concept was applied to a multi-used space with large glazed area. Annual daylight simulations were performed to measure its performance and provide a visual mapping of it, thus facilitating the comparison of several variations. It was demonstrated that intermediate twisted shapes allowed a balance between glare protection and light penetration while preserving some view access. Subjective parameters like the atmosphere were correlated to changes in quantifiable metrics and integrated along with user comfort in a state choice algorithm scheduling the blinds' motions, as a step toward multiple assessment criteria. More specifically, the concept enabled new daylighting control strategies for spaces where closure is badly tolerated and occupants' glare sensitivity diminishes in return for higher pleasantness.

Fiber reinforced polymers were selected for the implementation of the adaptive facade because they offered customizable and directional structural properties. Glass fibers were especially chosen for their translucent aspect and their durability against environmental attacks. Structural stability requirements were checked as an essential performance of any building envelope, starting with the definition of adequate support condition. The targeted torsional motion involved flexibility on elements supposed to resist wind loads. Unidirectional fiberglass laminates were providing a sufficient rotation capacity according to analytical linear elastic calculations. However the theory validity was questioned regarding this unusual application that largely deformed the material. An experimental investigation process was specifically developed. It confirmed the feasibility of the torsional motion and showed an even greater rotation capacity but exhibited a viscoelastic material behavior with partial recovery, leading to permanent plastic strains. Those phenomena could be integrated in the design, provided evaluation of their criticality by calibration of appropriate constitutive law and study of the long-time and cyclic behaviors of the facade modules. Coming back to the material, the facade's functionality as a shading system asked for a control on the optical properties. Options preserving the structural characteristics were explored; playing at the level of the polymeric matrix gave encouraging results.

System-wide issues were underlined as well, related to the combination of specific material properties, loads and support conditions. Results from laboratory testings and numerical FEM calculations unequivocally converged to the evidence of geometric non-linearities in the behavior

of the system from the point when elements tended to show slow off-axis buckling, leading to an exponential increase of the torque force necessary to rotate. The main concern shifted from the twist feasibility, acknowledged from this point onward, to what effort it cost to perform this motion. Wind resistance criterion, translated in the form of a maximum deflection, had been applied uncompromisingly, imposing element thickness responsible for the mechanical difficulty to twist them. As is, the design required powerful actuators which showed up not to be acceptable regarding an estimation of both the facade cost and the electrical consumption for the actuation. There is an underlying stake to value all design criteria in relation to each other.

The highlighted interrelationship between design criteria from technical and aesthetical fields extends to the overall adaptive facades world. The achievement of a paradigm shift towards more human and environment sensitive buildings cannot happen at the expense of all performance requirements but is not realistic without compromises. An integrated design is the key to manage multi-level criteria ; the main challenge was and remains to integrate subjectivity and sustainability as stakeholders in the process.

## Acknowledgments

This interdisciplinary master thesis would not have been possible without the support, availability and collaboration of the Composite Construction Laboratory (CCLAB) and the Laboratory of Integrated Performance in Design (LIPID), along with other people occasionally involved in the project. Especially I would like to thank:

- Prof. M. Andersen, Dr. A. P. Vassilopoulos and Dr. K. Chamilothoni, who have been enthusiastic about the proposed research topic and put effort to frame it as a master thesis, offering me the chance to work on this project.
- Dr. A. P. Vassilopoulos for his supervision and motivation to investigate this uncommon application of composites, especially with the experimental resources he provided me and his trust regarding the processes.
- Dr. J. Wienold for the time he consecrated sharing his experience about daylighting, for closely following-up of the development of daylight performance assesment methods and for his precious help with Radiance calculations.
- Dr. K. Chamilothoni for her enthusiam about the project since the earliest stage and the passion she had sharing her experiments on perceptual impressions, for supervising the pre-study and also for her precious guidance with DIVA simulations.
- A. Krkic, S. Despont and G. Guignet, technicians at the Civil Engineering Insitute (IIC), for their help with the building of dedicated laboratory setups, the cutting of GFRP elements and the experimental measurements.
- N. Vahedi, PhD candidate (CCLAB), for her help running the laboratory shear tests.
- Prof. J-F. Molinari and Dr. A. Cameselle Molares for general advice on numerical modeling issues.
- V. Lestang, civil engineering master student, for being my coworker on the composite course project that defined the structural pre-design base, and for pushing me to develop it further.
- The prototyping studio (ENAC-AM) for providing material and support in the mockup realization.

## References

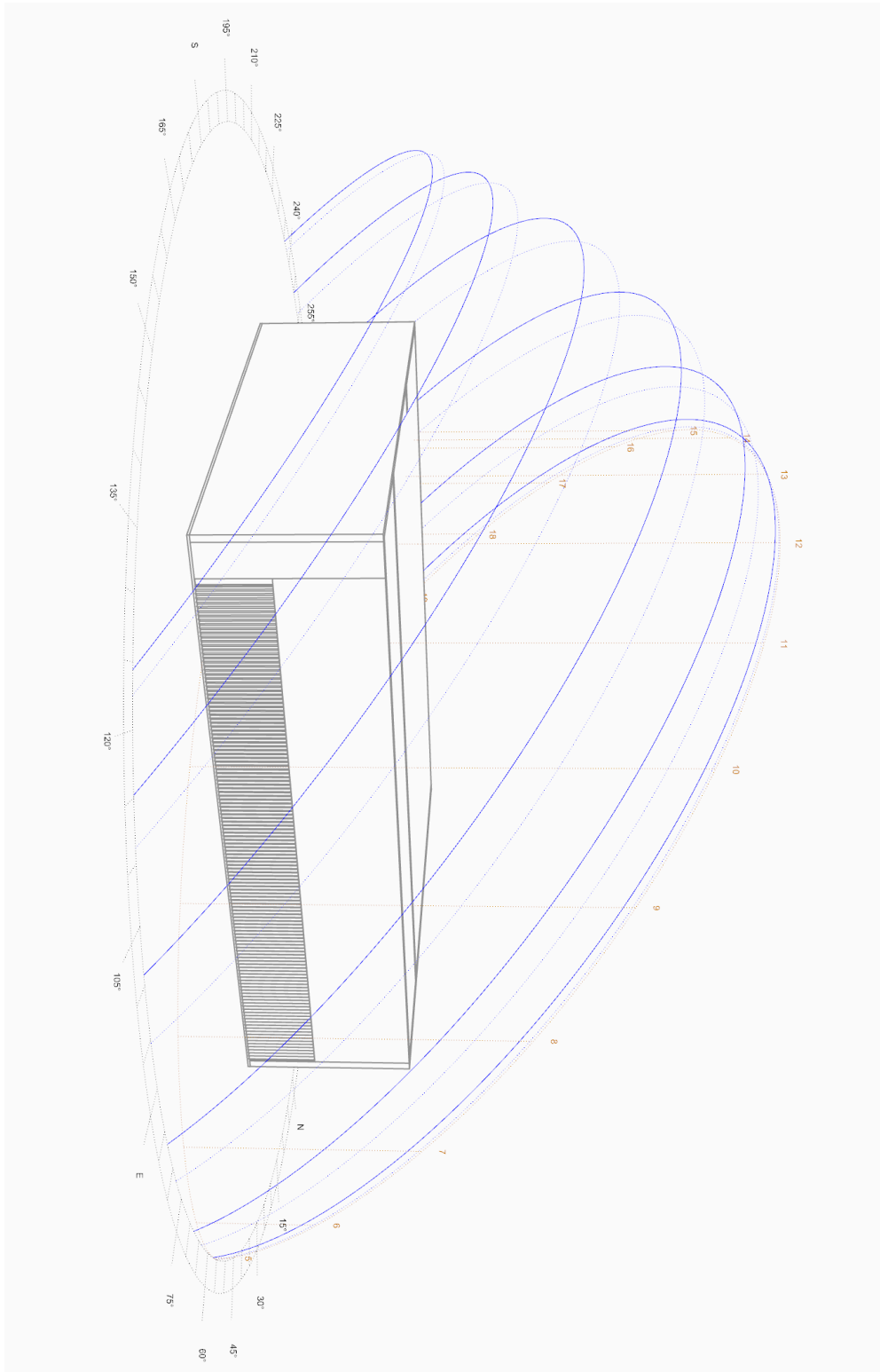
- [1] J. Butterfield, *The Art of Light and Space*. Abbeville Press, 1996.
- [2] U. Knaack, T. Klein, M. Bilow, and T. Auer, *Facades: Principles of Construction*. Birkhäuser, 2014.
- [3] R. K. Pachauri, L. Mayer, and Intergovernmental Panel on Climate Change, Eds., *Climate change 2014: synthesis report*. Geneva, Switzerland: Intergovernmental Panel on Climate Change, 2015.
- [4] *Loi sur l'énergie (LEne)*. 2016.
- [5] 'SIA 380/1 / 2016 F - Besoins de chaleur pour le chauffage'.
- [6] 'SIA 380/4 / 2006 F - L'énergie électrique dans le bâtiment'.
- [7] Z. Nagy & al., 'The Adaptive Solar Facade: From concept to prototypes', *Frontiers of Architectural Research*, vol. 5, no. 2, pp. 143–156, Jun. 2016.
- [8] M. I. Nkandu and H. Z. Alibaba, 'Biomimicry as an Alternative Approach to Sustainability', *Bulletin of the Polytechnic Institute of Jassy*, Jan. 2018.
- [9] S. Attia, 'Evaluation of adaptive facades: The case study of Al Bahr Towers in the UAE', *QScience Connect*, vol. 2017, no. 2, Oct. 2017.
- [10] S. Attia, S. Bilir, T. Safy, C. Struck, R. Loonen, and F. Goia, 'Current trends and future challenges in the performance assessment of adaptive facade systems', *Energy and Buildings*, vol. 179, pp. 165–182, Nov. 2018.
- [11] B. Abboushi, I. Elzeyadi, K. Van Den Wymelenberg, and G. Jacobsen, 'Do Visually Interesting Sunlight Patterns Impact Occupants' Perceived Glare in Daylit Offices?', in *Proceedings of IES Research Symposium 2018*, Atlanta, GA, 2018.
- [12] Fidinam, 'The challenges of office workplace design in the future', *Fidinam Group Worldwide*, 20-Apr-2018.
- [13] A. O. Sawyer, M. Niermann, and L. Groat, 'The use of environmental aesthetics in subjective evaluation of daylight quality in office buildings', in *Proceedings of IES Research Symposium 2015*, Indianapolis, 2015.
- [14] K. Chamilothoni, G. Chinazzo, J. Rodrigues, M. Andersen, J. Wienold, and E. Dan-Glauser, 'Subjective and physiological responses to facade and sunlight pattern geometry in virtual reality', *Building and Environment*, vol. 150, pp. 144–155, Mar. 2019.
- [15] K. Chamilothoni, 'Perceptual effects of daylight patterns in architecture', Ph.D. thesis, Ecole polytechnique fédérale de Lausanne, Lausanne, Switzerland, 2019.
- [16] K. J. Narayana and R. Gupta Burela, 'A review of recent research on multifunctional composite materials and structures with their applications', *Materials Today: Proceedings*, vol. 5, no. 2, Part 1, pp. 5580–5590, Jan. 2018.

- [17] A. Körner, A. Mader, S. Saffarian, and J. Knippers, 'Bio-Inspired Kinetic Curved-Line Folding for Architectural Applications', in *Proceedings of the 36th Annual Conference of the Association for Computer Aided Design in Architecture (ACADIA)*, Ann Arbor, Michigan.
- [18] J. Lienhard, C. Gengnanel, J. Knippers, and H. Alpermann, 'Active Bending, A Review on Structures where Bending is used as a Self-Formation Process', *International Journal of Space Structures*, vol. 28, pp. 187–196, Dec. 2013.
- [19] 'Reference Office | MIT Sustainable Design Lab', *web.mit.edu*.
- [20] S. Crone, 'Radiance Users Manual', vol. 2. Nov-1992.
- [21] J. A. Jakubiec and C. F. Reinhart, 'DIVA 2.0: Integrating Daylight and Thermal Simulations using Rhinoceros 3D, DAYSIM, and EnergyPlus', in *In Proceedings of Building Simulation*, 2011.
- [22] 'European Committee for Standardization CEN. EN17037:2019 Daylight in buildings'.
- [23] 'European Committee for Standardization CEN. prEN14501:2019 Blinds and shutters – thermal and visual comfort – performance characteristics and classification'.
- [24] 'Weather Data by Location | EnergyPlus'. [Online]. Available: [https://energyplus.net/weather-location/europe\\_wmo\\_region\\_6/CHE//CHE\\_Geneva.067000\\_IWEC](https://energyplus.net/weather-location/europe_wmo_region_6/CHE//CHE_Geneva.067000_IWEC). [Accessed: 10-May-2019].
- [25] J. Wienold, 'Daylight glare in offices', Fraunhofer Verlag, Stuttgart, 2010.
- [26] C. Reinhart and K. Voss, 'Monitoring manual control of electric lighting and blinds', *Lighting Research & Technology*, vol. 35, no. 3, pp. 243–258, Sep. 2003.
- [27] M. Sivak & al., 'Discomfort glare is task dependent', *UMTRI Report No. 89-27*, The University of Michigan, 1989.
- [28] C. Pierson, J. Wienold, and M. Bodart, 'Discomfort glare perception in daylighting: influencing factors', *Energy Procedia*, vol. 122, pp. 331–336, Sep. 2017.
- [29] K. Chamilothoni, J. Wienold, and M. Andersen, 'Daylight patterns as a means to influence the spatial ambience: a preliminary study', *Proceedings of the 3rd International Congress on Ambiances*, 2016.
- [30] Y. K. Yi, 'Building facade multi-objective optimization for daylight and aesthetical perception', *Building and Environment*, vol. 156, pp. 178–190, Jun. 2019.
- [31] 'SIA 260:2013 - Bases pour l'élaboration des projets de structures porteuses'.
- [32] 'SIA 261:2014 - Actions sur les structures porteuses'.
- [33] 'Baehr-Bruyère J., Lestang V., Advanced Composites Course, Project Report, Jan. 2019'.
- [34] H. Honickman, J. Johrendt, and P. Frise, 'On the torsional stiffness of thick laminated plates', *Journal of Composite Materials*, vol. 48, no. 21, pp. 2639–2655, Sep. 2014.
- [35] U. A. Khashaba, 'In-plane shear properties of cross-ply composite laminates with different off-axis angles', *Composite Structures*, vol. 65, no. 2, pp. 167–177, Aug. 2004.

- [36] C. B. York, 'On Bending-Twisting coupled laminates', *Composite Structures*, vol. 160, pp. 887–900, Jan. 2017.
- [37] A. Chateauneuf, 'La méthode des éléments finis – Calcul non-linéaire géométrique', *Techniques de l'Ingénieur*, Aug. 2016.
- [38] I. M. Ward and J. Sweeney, *An Introduction to the Mechanical Properties of Solid Polymers*. John Wiley & Sons, 2005.
- [39] D. L. Logan, *A First Course in the Finite Element Method*. Cengage Learning, 2016.
- [40] M. Osei-Antwi, 'Structural performance of complex core systems for FRP-balsa composite sandwich bridge decks'.
- [41] G. Odegard and M. Kumosa, 'Determination of shear strength of unidirectional composite materials with the Iosipescu and 10° off-axis shear tests', *Composites Science and Technology*, p. 27, 2000.
- [42] V. Cech, E. Palesch, and J. Lukes, 'The glass fiber–polymer matrix interface/interphase characterized by nanoscale imaging techniques', *Composites Science and Technology*, vol. 83, pp. 22–26, Jun. 2013.
- [43] C. Pascual Agullo, T. Keller, and J. De Castro, 'Translucent load-bearing GFRP envelopes for daylighting and solar cell integration in building construction', Lausanne, EPFL, 2014.
- [44] Warema, 'Reference values for shading factors - External venetian blinds'.
- [45] 'SHARCNet: ANSYS user guide - Element Quality metric'. [Online]. Available: [https://www.sharcnet.ca/Software/Ansys/17.0/en-us/help/wb\\_msh/msh\\_Element\\_Quality\\_Metric.html](https://www.sharcnet.ca/Software/Ansys/17.0/en-us/help/wb_msh/msh_Element_Quality_Metric.html). [Accessed: 07-Jun-2019].
- [46] E. J. Barbero, *Finite Element Analysis of Composite Materials Using ANSYS®*. CRC Press, 2013.

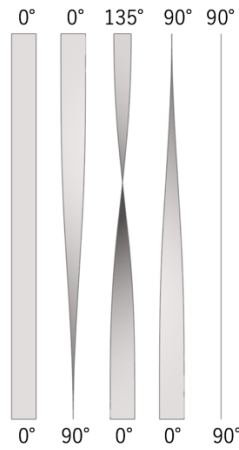
# APPENDIX I

## Annual sunpath diagram

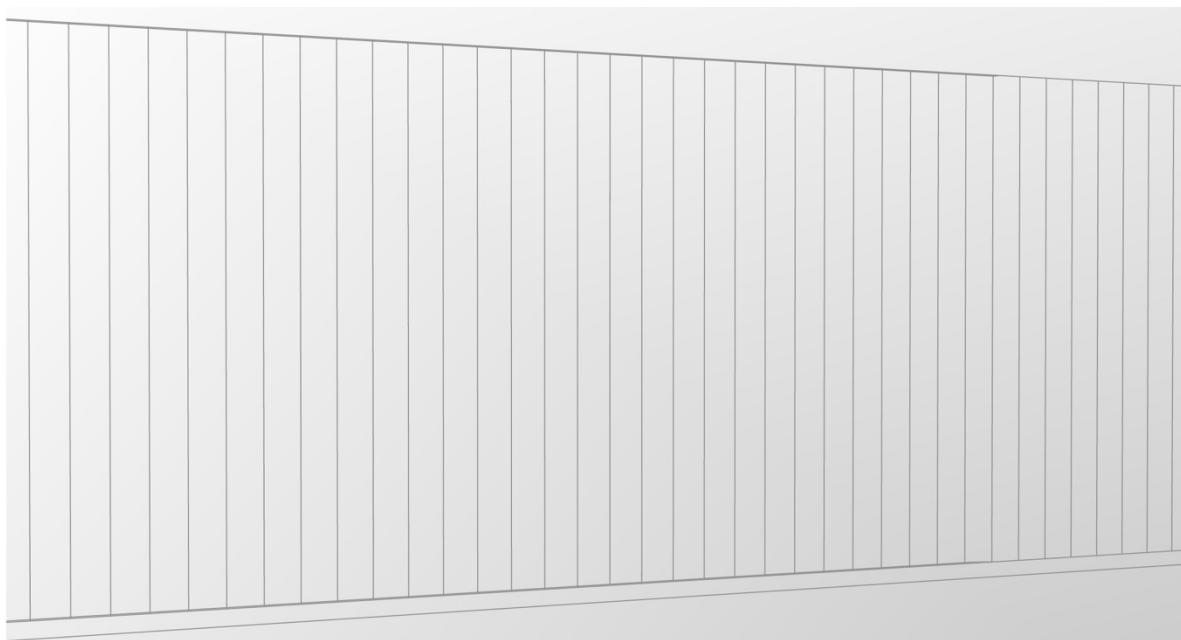


# APPENDIX II

Visualizations of the space with the blinds in the different configurations studied, recalled below:



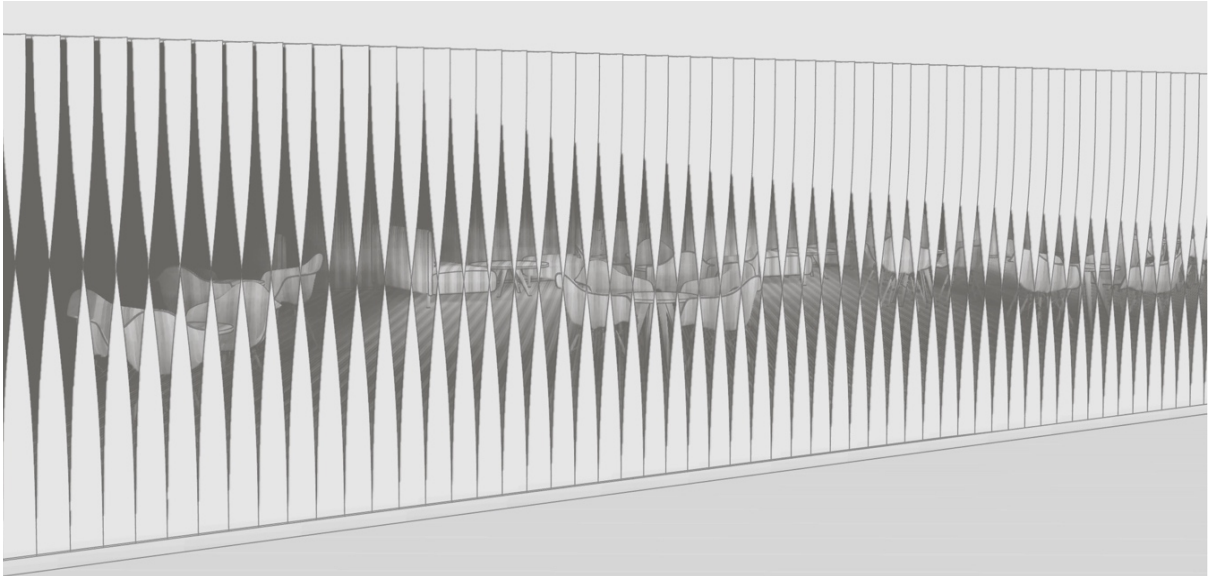
State: closed 0-0°



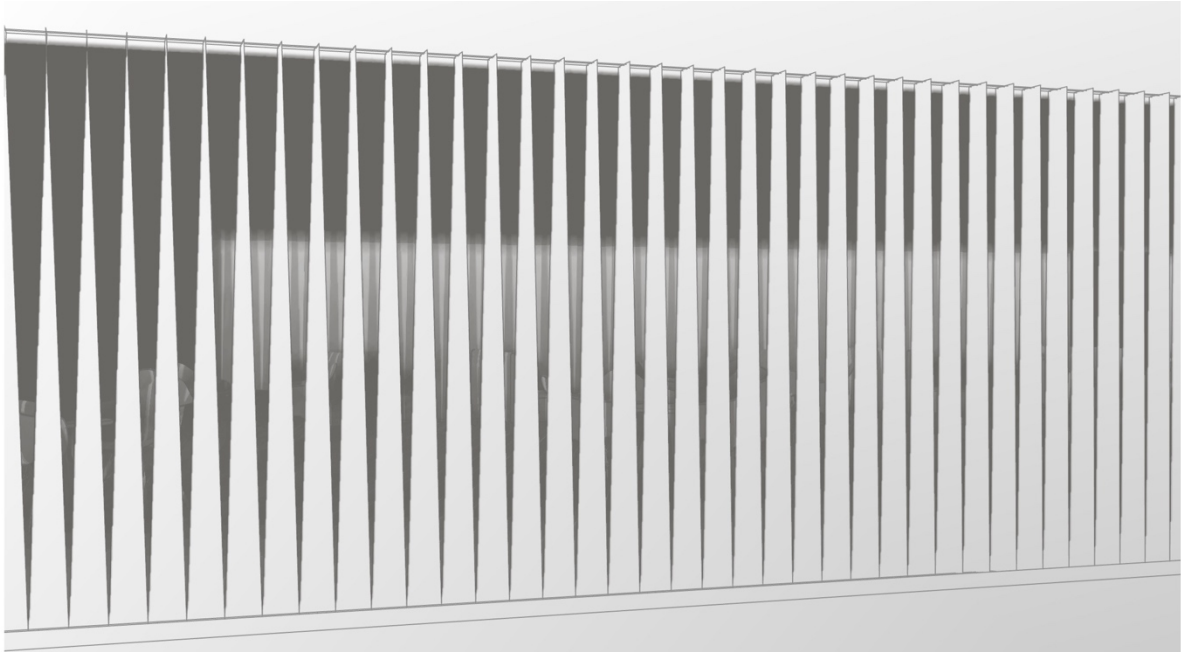
State: 0-90° (outside and inside views)



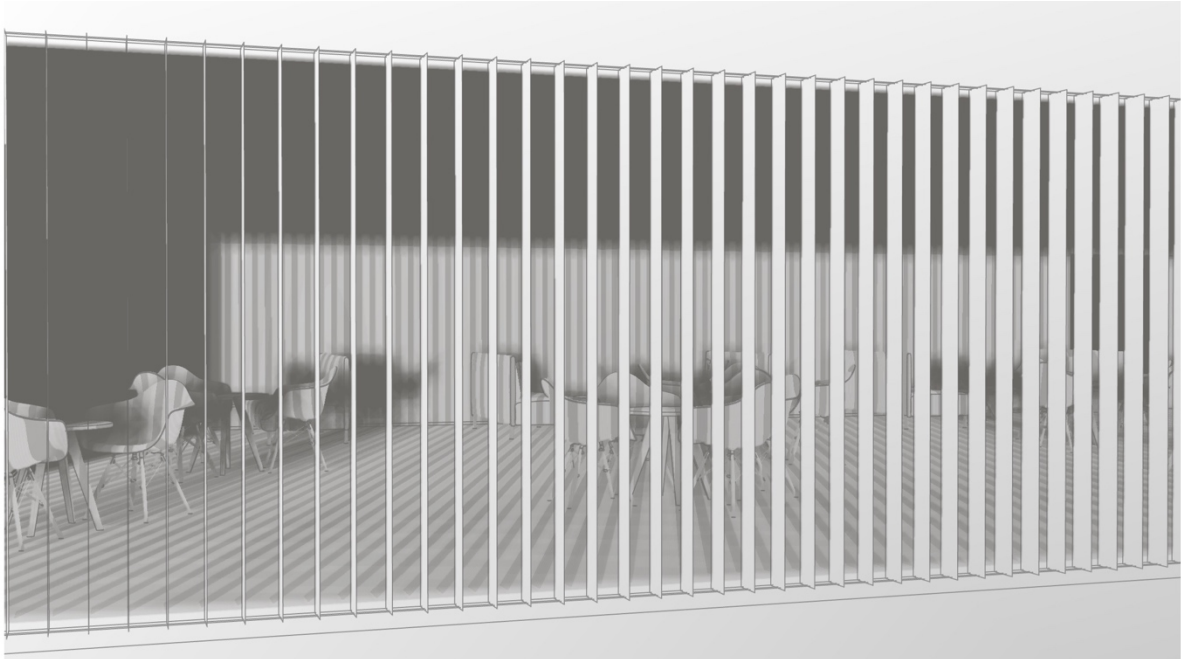
State: open at the bottom 135-0° (outside and inside views)



State: 90-0° (outside and inside views)



State: open 90-90° (outside view)



# APPENDIX III

Individual annual glare maps for the different blinds states investigated (15% transmittance and 50% reflectance material) ; the DGP metric is evaluated on occupied hours.

\*clockwise rotation

\*\*counter-clockwise rotation

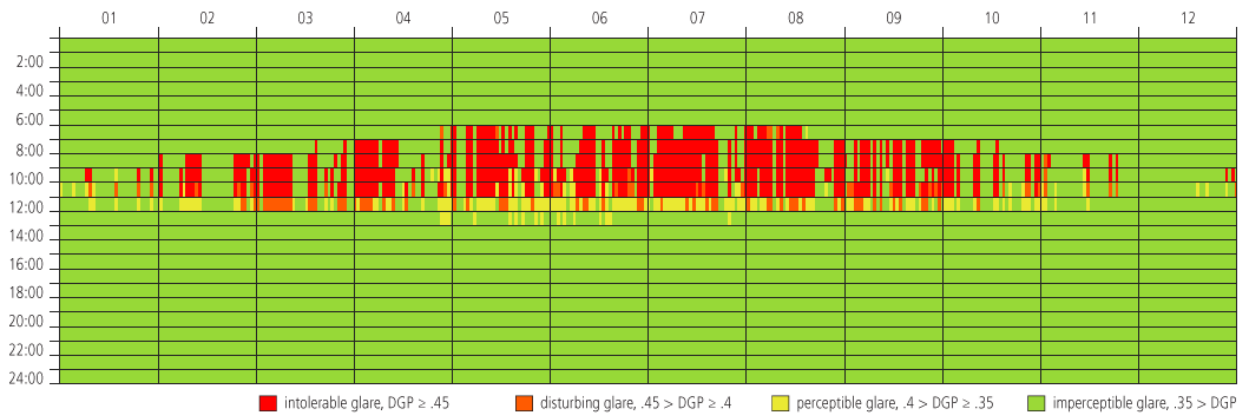
State: No blinds,  $DGP_{e<5\%,annual} = 0.89$



State: 90-90,  $DGP_{e<5\%,annual} = 0.59$



State: 90-0 \*\*,  $DGP_{e<5\%,annual} = 0.62$



State: 90-0 \*,  $DGP_{e<5\%,annual} = 0.53$



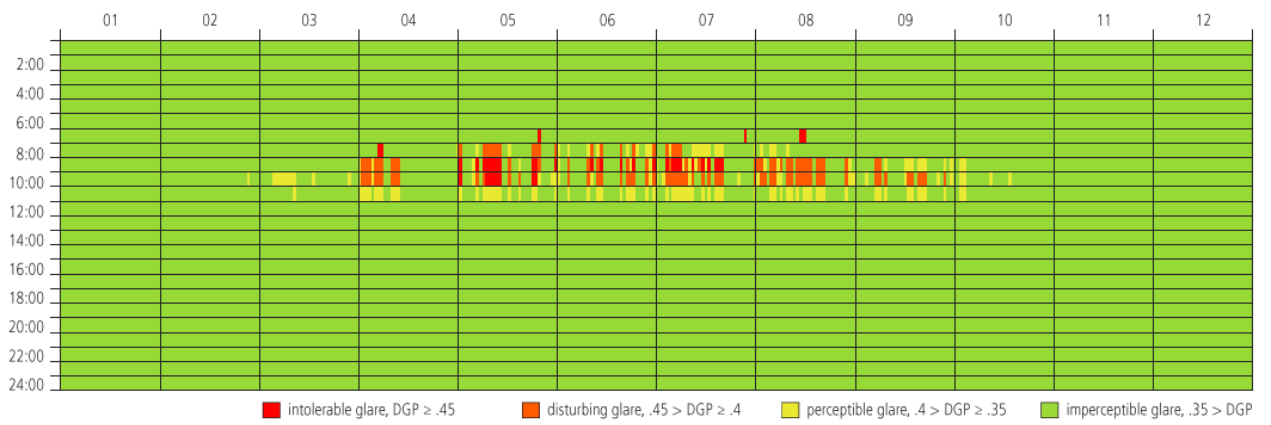
State: 135-0 \*\*,  $DGP_{e<5\%,annual} = 0.46$



State: 0-90 \*\*,  $DGP_{e<5\%,annual} = 0.43$



State: 0-90 \*,  $DGP_{e<5\%,annual} = 0.37$

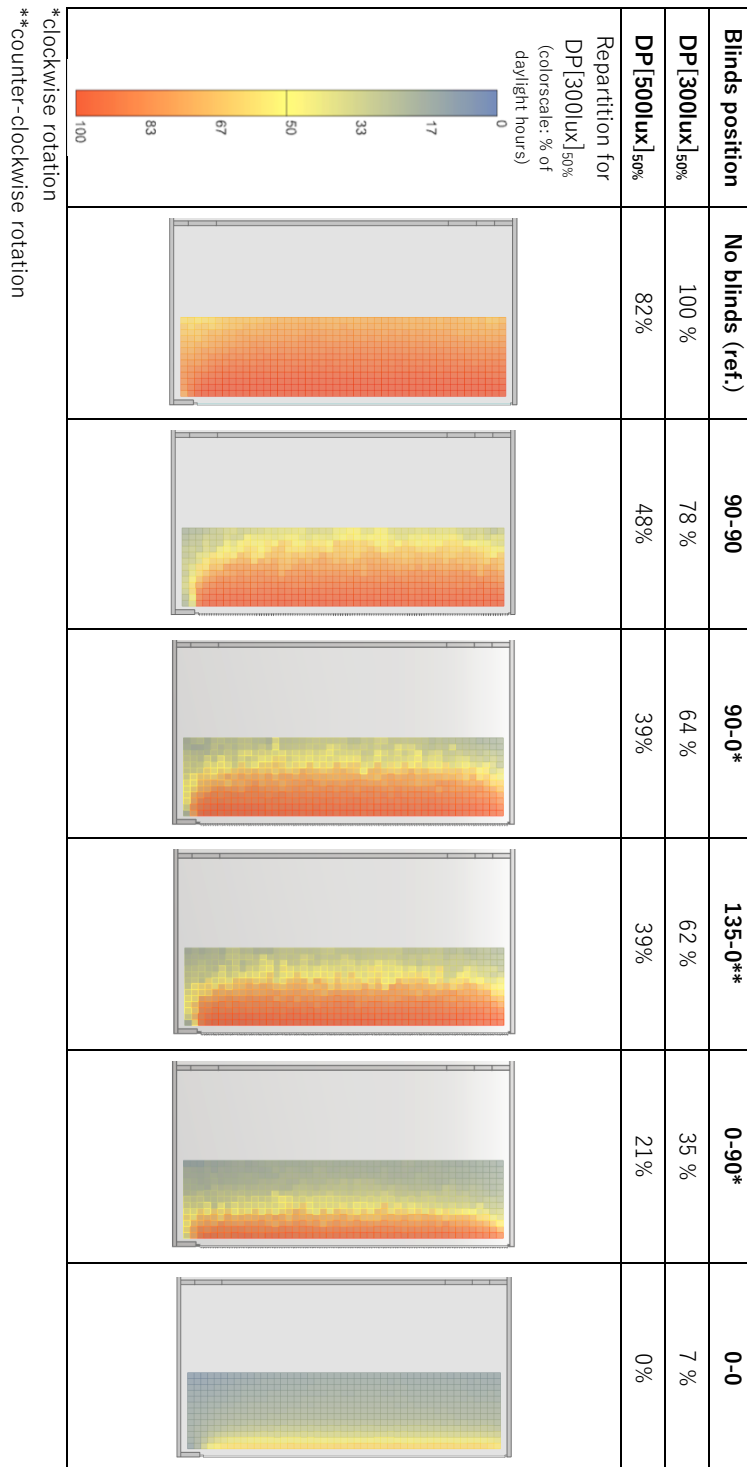


State: 0-0,  $DGP_{e<5\%,annual} = 0.35$



# APPENDIX IV

Evaluation and visualization of the annual DP for the set of investigated blinds states (t=15%, r=50%)



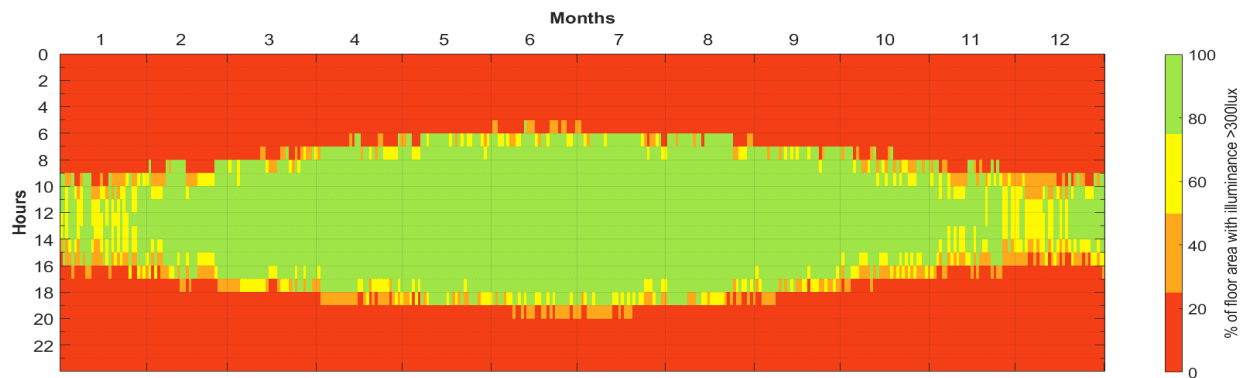
# APPENDIX V

Individual annual daylight provision maps for the different blinds states investigated (t=15%, r=50%) ; the DP[300lux]<sub>50%</sub> metric is evaluated on daylight hours

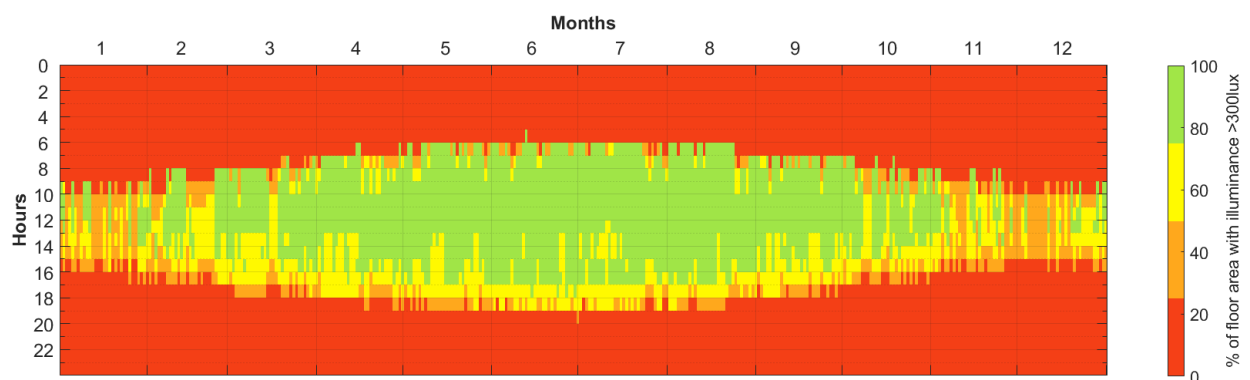
\*clockwise rotation

\*\*counter-clockwise rotation

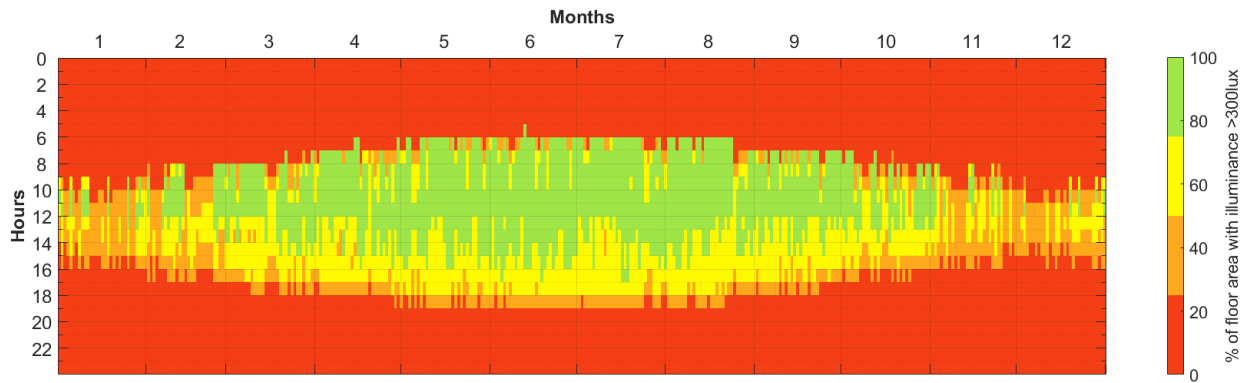
State: No blinds, DP[300lux]<sub>50%</sub> = 100%



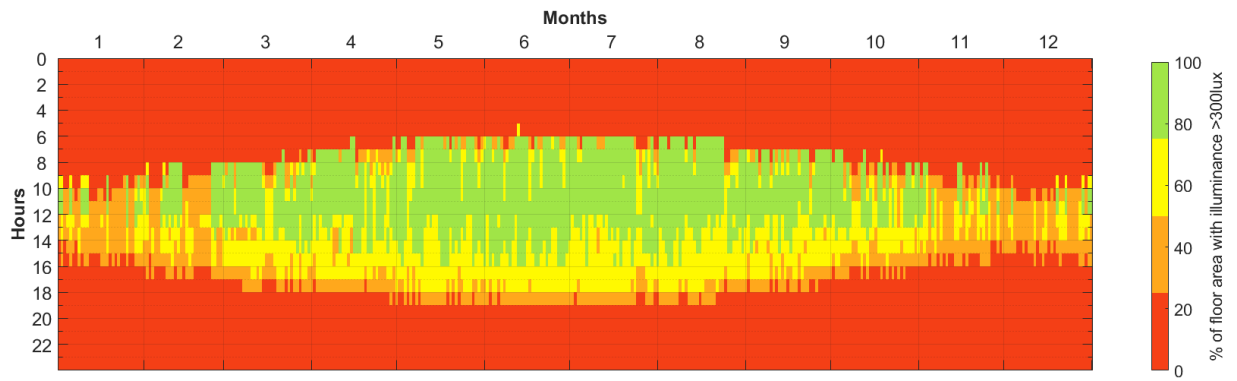
State: 90-90, DP[300lux]<sub>50%</sub> = 78%



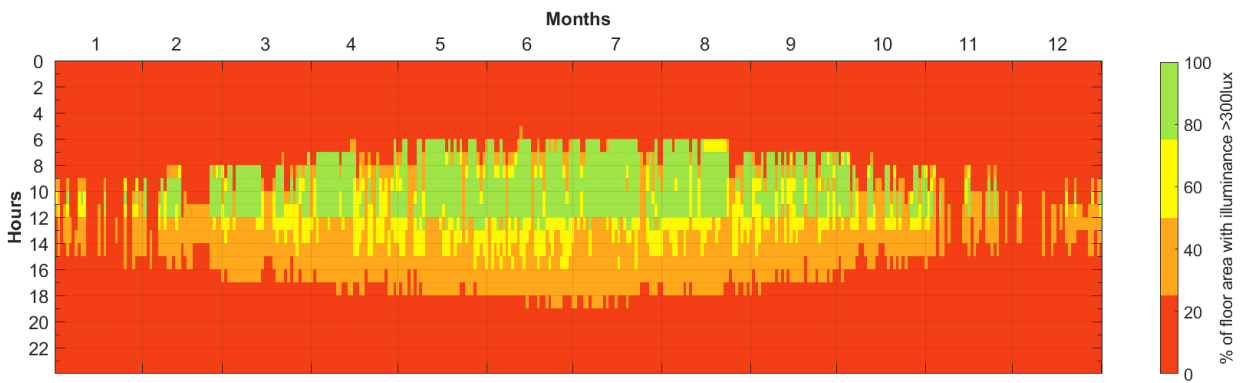
State: 90-0 \*, DP[300lux]<sub>50%</sub> = 64%



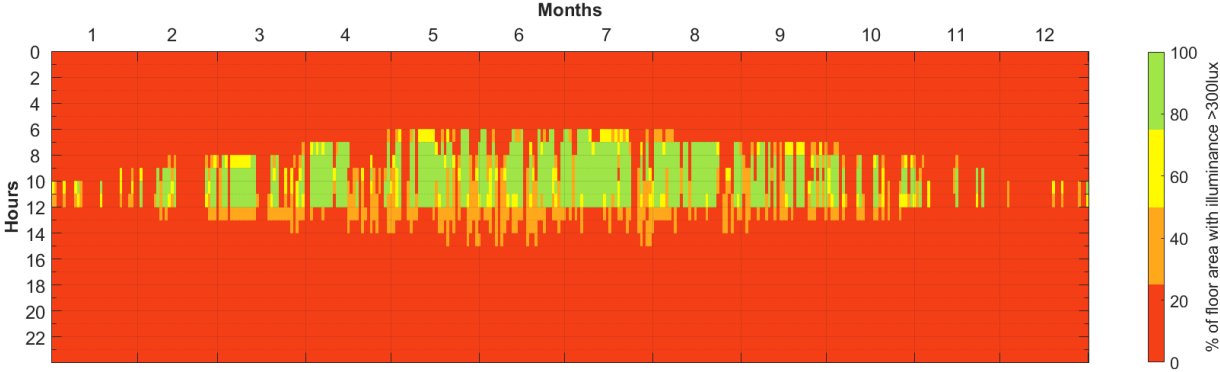
State: 135-0 \*\*, DP[300lux]<sub>50%</sub> = 62%



State: 0-90 \*, DP[300lux]<sub>50%</sub> = 35%



State: 0-0 \*, DP[300lux]<sub>50%</sub> = 7%



# APPENDIX VI

## FEM mesh quality and computation time

The ANSYS Academic licence has limitations, among which a numerical limit of 32000 nodes and elements for the structural package. This is quite high, however composites elements are made of very thin layers (~0.5mm here). We need at least one mesh element through the thickness of each layer (and ideally 4 to 5 mesh elements through this same thickness). The in-plane dimensions of the mesh should be similar to the through-thickness dimension, to obtain a good Element Quality (EQ)\*. We can roughly estimate the minimum in-plane dimension  $m$  allowed for our quadrilateral mesh, knowing the maximum number  $n_{elements,max}$  of elements allowed by the Academic License, for the modeling of the real scale GRFP module. Assuming square geometry of the mesh,

$$\frac{L * b}{m^2} \leq \frac{n_{elements,max}}{n_{layers}} \leftrightarrow m \geq \sqrt{\frac{2500 * 150}{\frac{32000}{25}}} = 17.11 \text{ mm}$$

For a square mesh of side 17.11 mm and thickness 0.50 mm, EQ=0.035<<1.

\*'Element Quality' is a metric ranging between 0 and 1. "This metric is based on the ratio of the volume to the sum of the square of the edge lengths for 2D quad/tri elements, or the square root of the cube of the sum of the square of the edge lengths for 3D elements. A value of 1 indicates a perfect cube or square while a value of 0 indicates that the element has a zero or negative volume" [45].

An insufficient EQ becomes problematic close to edges and supports, where high stress concentrations and rearrangements are expected. The most straightforward solution to get mesh refinement possibilities remains to diminish the size of the model. It is common to take advantage of symmetry\* conditions [46]. If it exists a plane of symmetry, displacement normal to this plane and rotations in this plane are zero. The model can be "cut" at the plane's location, the effect of the deleted part is replaced by the previously mentioned boundary conditions. If it exists a plane of antisymmetry\*, displacements in this plane and rotation normal to this plane are zero.

\*symmetry requires geometry, boundary conditions, material and loads to be simultaneously symmetric ; antisymmetry requires antisymmetry of loads and symmetry of geometry, boundary conditions and material.

The bending load case is symmetric. The torsional load case is antisymmetric. As soon as they are studied in separate models, it is possible to divide the size of the model by two. However we previously discussed the superposition of the results and its validity in section 3.2. It is not recommended to proceed by superposition for this specific application involving large deformations.

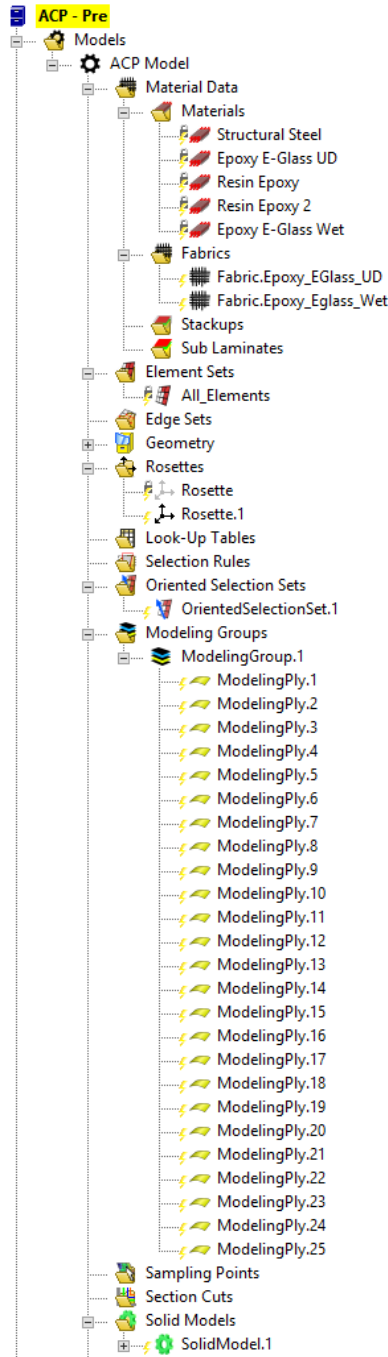
Another option is to work on a scaled model. We choose to go from the 1:1 rectangular geometry to a 1:5 rectangular geometry. Scaling of the structural behavior was discussed in section 4.1. The estimated minimum in-plane dimension  $m$  allowed for the quadrilateral mesh is now:

$$\frac{L * b}{m^2} \leq \frac{n_{elements,max}}{n_{layers}} \leftrightarrow m \geq \sqrt{\frac{500 * 30}{\frac{32000}{5}}} = 1.53 \text{ mm}$$

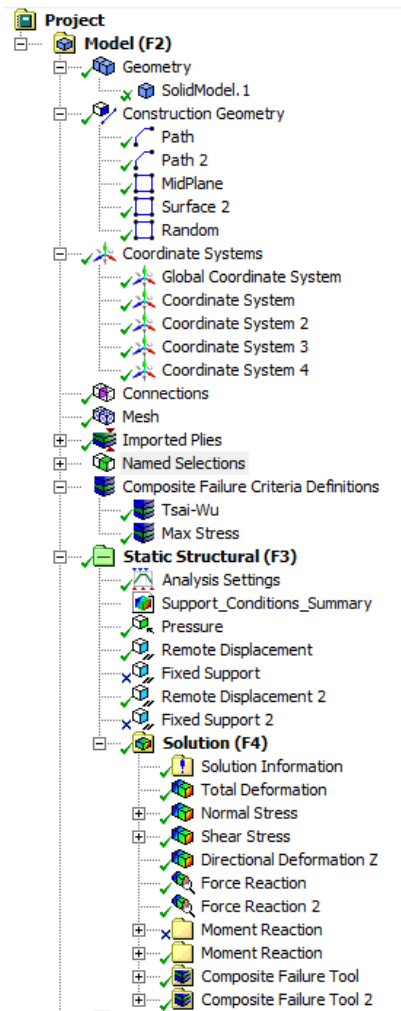
The Element Quality is 10 times better.

# APPENDIX VII

## ANSYS setup menus



Detailing of the ACP Pre setup menu

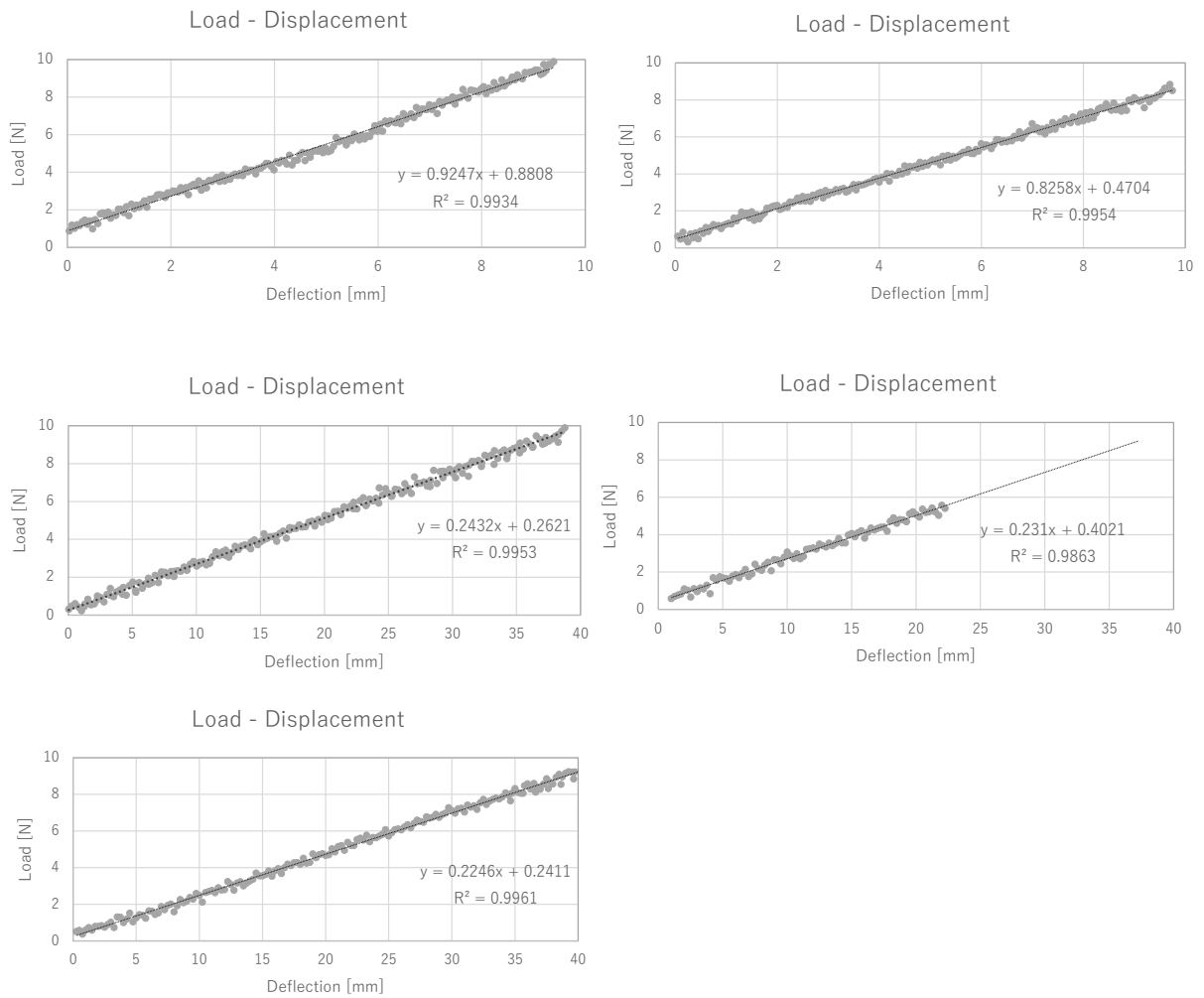


Detailing of the Static Structural setup menu

# APPENDIX VIII

## Experimental Force-Displacement curves from 3 points Bending Tests

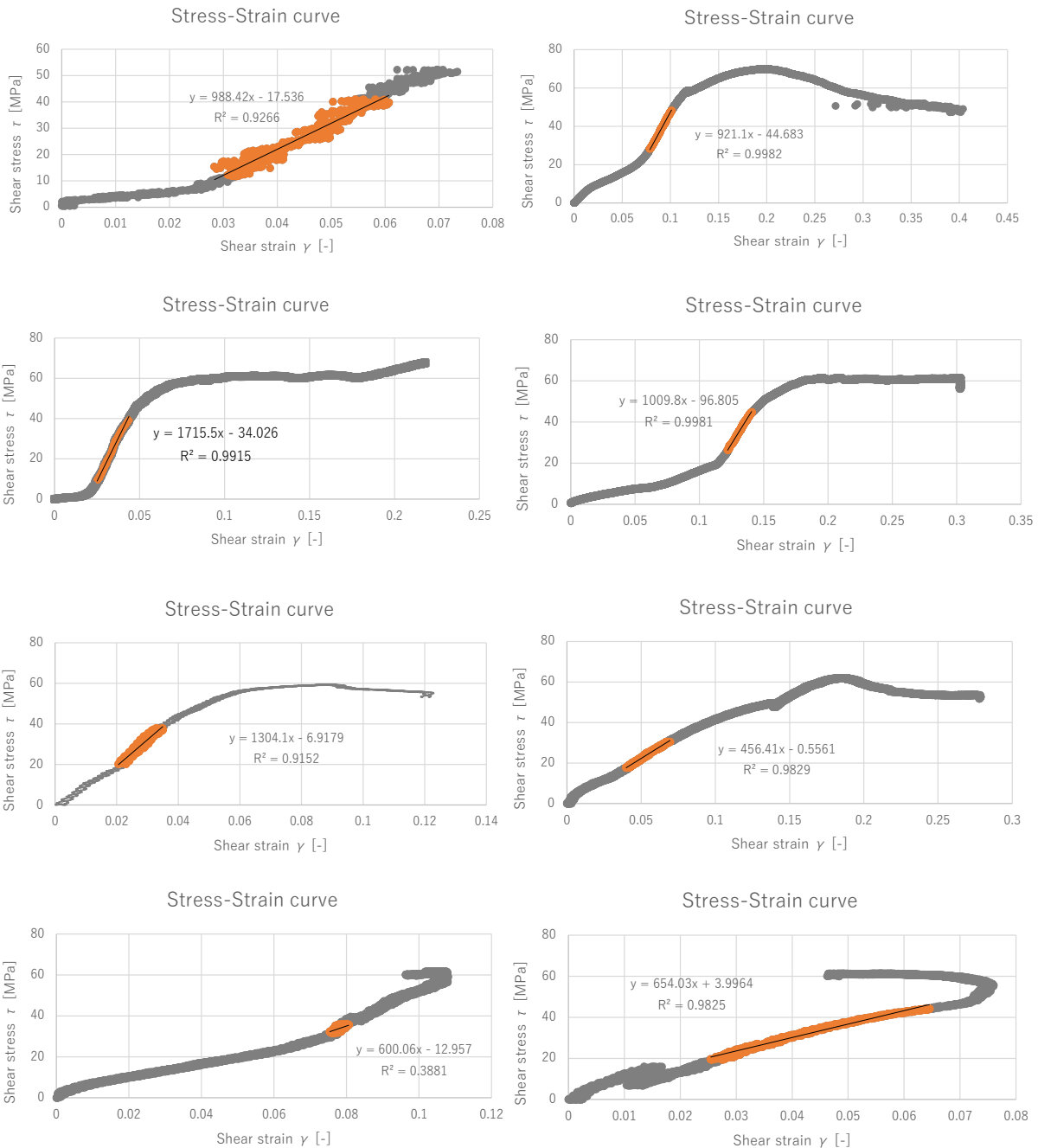
Plots correspond, in that order, to samples V3-V4 and C1-C4-C5



# APPENDIX IX

## Experimental Stress-Strain curves from Shear Tests

Plots correspond, in that order, to samples Sv1-Sv4-Sv5-Sv6 and Sc1-Sc2-Sc3-Sc4.  
 Those plots are mainly provided to illustrate encountered problems in the measurements with the test fixture.



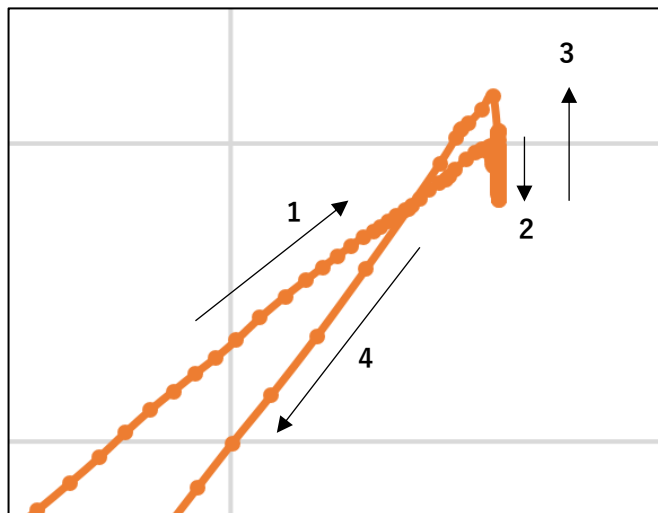
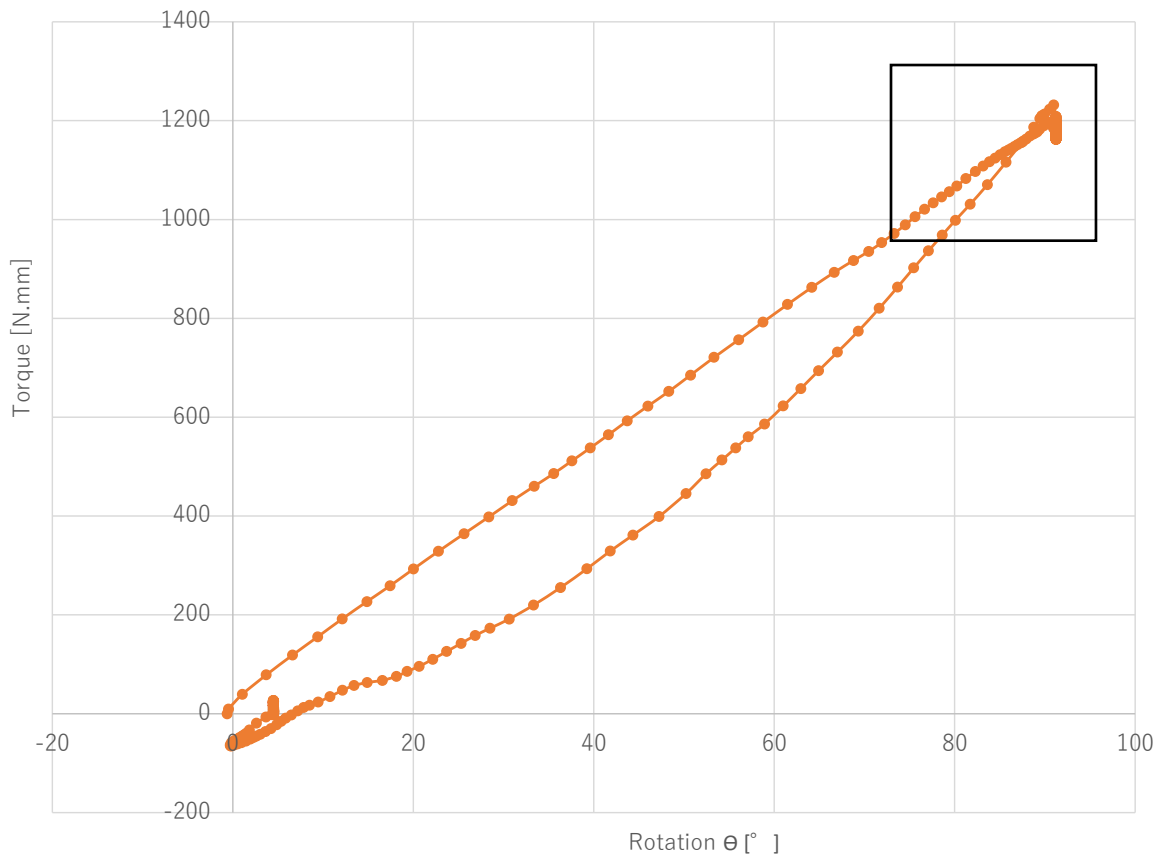
# APPENDIX X

## Cyclic torsion diagram from raw experimental data

Relaxation test n° 2, loading/unloading cycle n° 1/3

This plot is provided to illustrate the data treatment process, especially correcting for the fixture's effect on the raw measurements.

Cyclic loading up to 90° ; Cycle 1



- 1: loading up to 90° and locking of the system in this position
  - 2: torque loss because of relaxation (duration=5 minutes)
  - 3: unlocking of the system ; part of the fixture's friction is transferred to the element and so interfere in the torque measurement
  - 4: unloading back to 0°
- The jump in the torque introduced by step 3 must be corrected by shifting the unloading curve down.

# APPENDIX XI

## Angle-dependency of optical measurements on the mockup GFRP strips



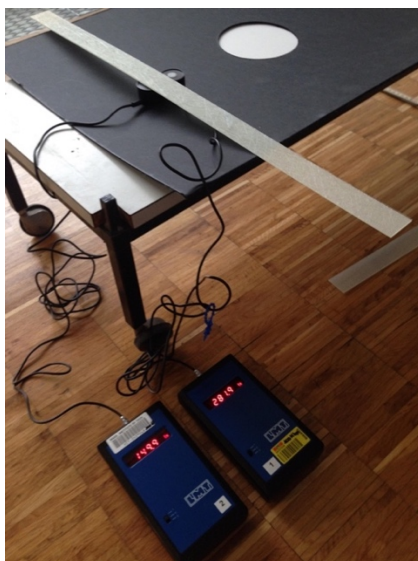
### Specimens:

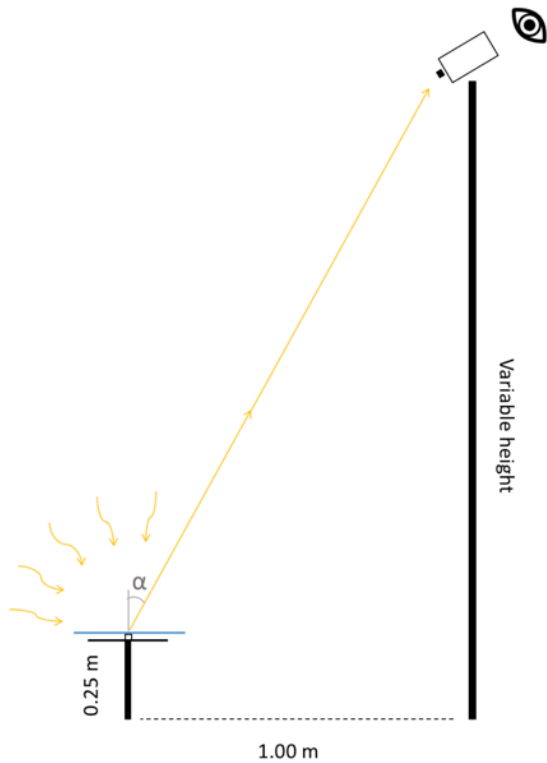
- W50/50: woven material (fabric with an equivalent amount of fibres woven in two perpendicular directions). The reinforcement weight is 390 [g/m<sup>2</sup>.layer]. The laminate is made up of 2 layers, for a mean thickness measured after curing equal to 1.2mm.

- CFM: mat material (continuous fiberglass filaments randomly oriented). The reinforcement weight is 300 [g/m<sup>2</sup>.layer]. The laminate is made up of 4 layers, for a mean thickness measured after curing equal to 1.8mm.

### Material and process:

- specimens to test (a GFRP strip from the mockup on pictures above)
- black plate to absorb parasit reflections
- support and tripod
- 2 lux-meters to measure the Illuminance
- 1 luminance-meter to measure the Luminance





Transmittance: it is the ratio of the Illuminance  $I_{spec}$  [Lux] measured by the lux-meter sensor under the specimen over the Illuminance  $I_{room}$  in the room (measured by a sensor as close as possible from the other one).

$$T = \frac{I_{spec}}{I_{room}} [-]$$

Reflectance: it can be calculated as follows, with  $L_{spec}$  the Luminance [ $cd/m^2$ ] read by the observer on the Luminance-meter (for a given angle  $\alpha$  to the normal of the specimen's surface) and  $I_{room}$  the Illuminance [Lux] in the room.

$$R = \frac{L_{spec} * \pi}{I_{room}} [-]$$

Absorption: it can be calculated with

$$A = 1 - T - R [-]$$

Results:

- Transmittance
- Reflectance
- Absorption

		Mat (CFM)	Woven (W50.50)
Angle $\alpha$ to the normal	30°	0.52	0.55
		0.40	0.30
		0.08	0.15
	45°	0.54	0.65
		0.42	0.31
		0.04	0.04

Comments:

The experimental setup only allows to measure total transmittance without separation between direct and diffuse components. Assumption was made that the light inside the room was diffuse and homogeneous over half a sphere centered on the objects. The optical measurements tend to show that mat material exhibits better transmittance properties than fabrics. But we know from the structural calculations that this material is not stiff enough to handle the wind deflection with an acceptable thickness. The optical requirements on the laminate are considered as a criteria of choice only between structurally feasible solutions.

# APPENDIX XII

## Calculation note for the annual electrical consumption of exterior Venetian blinds

Exterior blinds modules are raised/lowered and tilted by motorized rewinders (2 per module), similarly to roller shutters blinds. For aluminium ('dim-out') slats with mean width 80 mm, the weight of the shading system is about 3kg/m<sup>2</sup>, so that one square unit module (2.5\*2.5m) weights 3\*2.5<sup>2</sup>=18.8 kg, let's say ~20 kg.

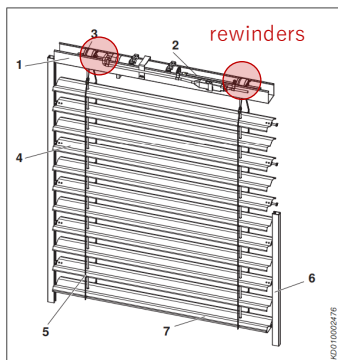


fig. 31: External venetian blind E 93 A6

- 1 Top rail
- 2 Tilt rod
- 3 Bearing
- 4 Slats
- 5 Slat suspension and lifting tape
- 6 Lateral guidance
- 7 Bottom rail

Types	Construction limit values in mm <sup>1)</sup>								Average weight in kg/m <sup>2,2)</sup>	Operation
	Individual units				Group unit					
	Width <sup>3)</sup>		Height	Area <sup>4)</sup> in m <sup>2</sup>	Max. width	Area <sup>5)</sup> in m <sup>2</sup>	left/right of drive product max. coupl. each side			
min. <sup>6)</sup>	max.	Area in m <sup>2</sup>					Number of blinds			
<b>External venetian blinds, beaded slats with cable or rail guidance</b>										
C 60/80 A2 S	450	5000 <sup>8)</sup>	4000	12	12000	12	12	2	2.7/2.8	Crank
E 60/80 A2 S	600	5000 <sup>8)</sup>	4000	20	12000	26-30	13	2	3.0/3.1	Motor
C 60/80 A6 S	450	5000	5000	12	12000	12	12	2	2.7/2.8	Crank
E 60/80 A6 S	600	5000	5000	25	12000	26-30	13	2	3.0/3.1	Motor
<b>External venetian blinds, flat slats with cable guidance</b>										
C 50/60/80/100 AF	450	5000 <sup>8)</sup>	4000	13	12000	13	13	2	2.3 - 2.5	Crank
E 50/60/80/100 AF	600	5000 <sup>8)</sup>	4000	20	12000	32-35	13	2	2.5 - 2.7	Motor
E 150 AF	600	5000 <sup>8)</sup>	4000	20	12000	24-26	13	2	2.9	Motor
<b>External venetian blinds, flat slats with rail guidance</b>										
C 60/80/100 AF A6	450	5000 <sup>7)</sup>	4000	13	12000	13	13	2	2.3 - 2.5	Crank
E 60/80/100 AF A6	600	5000 <sup>7)</sup>	4000	20	12000	32-35	13	2	2.5 - 2.7	Motor
<b>External venetian blinds, dim-out slats with rail guidance</b>										
C 73/90/93 A6	450	4500	4300	10	12000	10	10	2	2.9	Crank
E 73/90/93 A6	600	4500	4300	15	12000	23-24	13	2	3.2	Motor
<b>External venetian blinds, dim-out slats with rail guidance</b>										
C 73/90/93 A2	450	4500	4000	10	12000	10	10	2	2.9	Crank
E 73/90/93 A2	600	4500	4000	15	12000	23-24	13	2	3.2	Motor
<b>External venetian blinds with ProVisio</b>										
E 80 A2 S/A6 S PV	600	4000	3000	12	10000	30	12	1	3.0/3.1	Motor
E 90/93 A2/A6 PV	600	4000	3000	12	10000	24	12	1	3.2	Motor
<b>Wind-stable external venetian blinds with rail guidance</b>										
E 80 A6 S wind-stable	600	3000 <sup>9)</sup>	3600	7	9000	20	7	1	4.0	Motor
E 93 A6 wind-stable	600	3000 <sup>9)</sup>	3600	8	9000	20	8	1	4.2	Motor
<b>Self-supporting external venetian blinds</b>										
E 80 A6 S	600	4000	5000	13	12000	26-30	13	1	3.1	Motor
E 80 AF A6	600	4000 <sup>10)</sup>	4000	13	12000	32-35	13	1	2.7	Motor
E 90/93 A6	600	4000	4300	13	12000	24-25	13	1	3.2	Motor
<b>External venetian blinds with cable guidance</b>										
C 50 A1	450	5000 <sup>8)</sup>	4000	20	12000	30	20	2	2.3	Crank
E 50 A1	600	5000 <sup>8)</sup>	4000	20	12000	36-39	20	2	2.5	Motor
K 50 A1	400	4000 <sup>8)</sup>	3000	7	-	-	-	-	2.0	Crank
Q 50 A1 S	400	4000 <sup>8)</sup>	2800	6	-	-	-	-	2.0	Cord

<sup>1)</sup> Construction limit values for solar drive see Page 413  
<sup>2)</sup> Cable force: 350 N per tension cable.  
<sup>3)</sup> Width dimension - slat size (for A6 model: slat size = dimension of back edge of the guide rail - 65 mm (for guide rail types 1 and 2))  
<sup>4)</sup> The maximum areas indicated depend on the height; see "Height-to-width ratio of external venetian blinds" on page 446.  
<sup>5)</sup> Asymmetrical running of slats cannot be prevented for small widths. (Please pay attention to the external venetian blind guideline ITRS Industrieverband Technische Textilien - Rollladen - Sonnenschutz e.V.)  
<sup>6)</sup> Additional tension cables are required for slat sizes exceeding 3001 mm.  
<sup>7)</sup> Additional tension cables are required for slat sizes exceeding 2401 mm.  
<sup>8)</sup> Additional tension cables are required for slat sizes exceeding 1501 mm.  
<sup>9)</sup> Additional tension cables are required for slat sizes exceeding 1501 mm.  
<sup>10)</sup> Additional tension cables are required for slat sizes exceeding 2401 mm. Standard cover panel depth is 150 mm.

Source: [https://www.warema.com/en/planning/architects/downloads.php#DL\\_Raffstoren](https://www.warema.com/en/planning/architects/downloads.php#DL_Raffstoren) ;  
 'Technical\_data\_external\_venetian\_blinds-pdf'

Given the system's weight and height, it is identified with the help of technical charts\* for roller shutters rewinders that the revider diameter should be about Ø=6cm. The mechanical couple required to raised the blinds is then C=M.g.Ø=20[kg]\*10[m.s<sup>-2</sup>]\*0.6[m] = 12 [N.m], partitioned on the two rewinders i.e. 6 [N.m/rewinder].

\*Source: <https://www.guide-volet-roulant.fr/index.php/motoriser-volet-roulant/abaque-des-puissances-en-nm-pour-volet-roulant/>

The power consumption of rewinders' motors is estimated about 90 W per motor according to the previous estimation of the mechanical couple (torque) and the technical data right after.

# Roller shutter and sun protection drives with mechanical limit switching



for barrels with diameters of 50 mm and above

R7/17M – R50/11C M



**Mechanical limit switching**

Highlight: "Short" drive  
R7/17M for narrow roller shutter applications.

Highlight: Zip version –  
Drive adapters from various manufacturers can be adapted directly, and therefore fit the zip drive adapters from various manufacturers

**Motor protected against overheating**

Motor head can be overwrapped

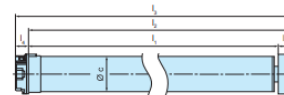
**Suitable for left and right installation**

Classic limit position adjustment by means of setting tools

Technical data	Item number	Item number zip	Torque (Nm)	Speed (min <sup>-1</sup> )	Limit switch range (revolutions)	Nominal current (A)	Power consumption (W)	Connecting cable (m)
R7/17M	2010 110 041 0		7	17	17	0.45	90	3
R8/17C M	2010 110 100 0		8	17	38	0.45	100	*
R12/17C M	2010 110 101 0	2010 110 103 0	12	17	38	0.50	110	*
R20/17C M	2020 110 100 0	2020 110 102 0	20	17	38	0.75	160	*
R30/17C M	2030 110 100 0	2030 110 101 0	30	17	38	0.90	205	*
R40/17C M	2040 110 100 0	2040 110 101 0	40	17	38	1.15	260	*
R50/11C M	2050 110 100 0		50	11	38	1.10	240	*

Rated voltage: 230 V AC/50 Hz      Operating mode: S2 4 min      Degree of protection: IP44

Dimensions (in mm)	l <sub>1</sub>	l <sub>2</sub> **	l <sub>3</sub> **	l <sub>4</sub>	l <sub>5</sub> **	dia. c
R7/17M	354	394	411	17	40	45
R8/17C M	414	454	471	17	40	45
R12/17C M	414	454	471	17	40	45
R20/17C M	443	483	500	17	40	45
R30/17C M	567	607	624	17	40	45
R40/17C M	587	627	644	17	40	45
R50/11C M	514	554	571	17	40	45



Source: Becker technical documentation for Roller Shutter Wired Drives (<http://en.becker-antriebe-partner.de/cgi-bin/?id=223>)

Number of actions per day is estimated to 4 (2 full openings and 2 full closings).

One action required to consume electrical power during 50 seconds, let's say ~1 min.

Explanation: the motor makes 17spins/min, one action implied to raise H=2.5m long wires and the rod diameter is Ø=6cm. The motor needs to complete  $H/(\pi \cdot \varnothing) = 13.3$  spins to fully raise the blinds. It takes  $13.3/17 = 0.8$  min (=50 sec).

The daily power consumption of a 2.5m\*2.5m module is:

$$2[\text{motors}] * 4[\text{actions}] * 90[\text{Watts}] * 60[\text{sec}] = 43200 [\text{W.s}] = 12.10^{-3} [\text{kWh/day}]$$

The annual electrical consumption per 2.5m\*2.5m module is:

$$12.10^{-3} [\text{kWh/day}] * 365[\text{days}] = 4.4 [\text{kWh/year}], \text{ equivalent to } \mathbf{0.7 [\text{kWh/year.m}^2 \text{ of glazing}]}$$